ENANTIOSELECTIVE QUANTUM OPTICAL EFFECTS IN CHIRAL MOLECULES

Somasree Pal

UNIVERSITÀ DEGLI STUDI DELL'AQUILA

DSFC

European Innovation Council

UNIVERSITÀ DEGLI STUDI DELL'AQUILA

DIPARTIMENTO DI Scienze Fisiche e Chimiche

Dottorato di Ricerca in **SCIENZE FISICHE E CHIMICHE**

Curriculum _____

XXXVIII ciclo

Titolo della tesi

Enantioselective Quantum Optical Effects in Chiral Molecules

SSD PHYS-04/A

Dottorando

Somasree Pal

Somasree Pal

Coordinatore del corso	Advisor
Prof. Massimiliano Aschi	Prof. Andrea Marini

a.a. 2024/2025

TwistedNano

European Innovation Council Funded by the European Union

This project has received funding from the European Union under grant agreement No 101046424. Views and opinions expressed are however those of the author(s) only and do not necessarily reflect those of the European Union or the European Innovation Council. Neither the European Union nor the European Innovation Council can be held responsible for them.

Dedicated to...

My Parents

Acknowledgement

I would like to express my sincere gratitude to my supervisor, Prof. Andrea Marini, for his constant guidance and support throughout my Ph.D. journey. *Grazie mille, Professore!* Observing you work happily for hours every day has deeply inspired me; at first, I was astonished, and now I find myself able to dedicate the same commitment to research. Beyond science, I am especially grateful for your support during my initial days in L'Aquila, which made adapting to a new country much easier. Thank you for guiding me with patience and kindness throughout this journey.

I am very grateful to my Ph.D. coordinator, Prof. Massimiliano Aschi, for his continuous support. You were always present and responsive by email, and whenever I approached you with a request, you handled it promptly, which has been much needed for the progress of my Ph.D. degree.

Special thanks to Carino Ferrante, Davide Tedeschi, Paola Benassi, Alessandro Ciattoni, and Antonio Mecozzi for their support and for many insightful discussions. Your ideas and feedback have significantly improved my understanding of Physics.

To all my groupmates—Leone D.M., Ashis P., Raju A., Matteo V., Matteo S., Giovanna S., Andrea A., Federico P., and Luca A.—thank you for making this journey memorable. *Grazie, Giovanna!* for the many meaningful conversations about both research and life. I would also like to thank Ambaresh da for the opportunity to work with you during my first year, for everything I learned from

you, and Ashis da for many valuable discussions and constant encouragement. Special thanks to Andrea A., although we had only a short time to work together, it was truly a pleasure. Thanks to Matteo S. for the support and collaboration on a project that could not be included in this thesis—hopefully, we will complete it soon. Thank you, Raju and Matteo V., beyond sharing the same office, our many discussions—both professional and personal—have been truly valuable to me.

I am grateful to Visva-Bharati University, where, during my M.Sc. days, I was inspired to pursue research. I sincerely thank Prof. Amitabha Sir, my M.Sc. supervisor, for his guidance during my first research project and Prof. Swapan Sir for his valuable advice and research suggestions. I am also thankful to Prof. Arani Sir and Prof. Rajkumar Sir for their support during difficult times. Special thanks to Suman Da, co-supervisor of my M.Sc. thesis, and to Dolon Da for their guidance. I am equally grateful to the University of Calcutta, where I completed my B.Sc. and first developed an interest in pursuing research in Physics.

I would like to thank my dear friends Tamalika, Debolina, Nilay, and Shubhadip for their support and for inspiring me in different ways. I am deeply grateful to my friends in L'Aquila, especially our small Indian group, who became like a second family away from home, supporting me in both life and research and making it feel like home through small celebrations and discussions about our work. Special thanks also go to Arianna, Massimo, Lorenzo, and Simone for all their support, and thanks to Lucia for helping me so much in the initial days in L'Aquila.

Most of all, I want to thank my parents for giving me the opportunity to pursue higher studies. Maa, thank you for being my best friend, philosopher, and guide. Your unconditional love and faith have supported me throughout these years.

Finally, and above all, I am deeply grateful to the University of L'Aquila. I also sincerely thank the TwistedNano project for providing me the opportunity to pursue my P.hD. and grow as a researcher.

Abstract

Chiroptical sensing is challenging due to the inherent weak chiral-light-matter interactions, but in the pharmaceutical industry, chiral sensing plays a key role because specific enantiomeric forms of drugs can simultaneously affect functionality and toxicity. Current techniques are inefficient for real-time analysis and lab-on-a-chip integration platforms. In this thesis, we developed a quantum-optical effect that overcomes these limitations and improves chiral sensing by utilizing nonlinear optical techniques and operating chiral-light-matter interactions in a nanophotonic environment that amplifies the inherent weak chiroptical sensitivity. We use a perturbative approach within the density-matrix formalism to calculate molecular observables using Time-dependent Density Functional Theory (TDDFT) and quantum-chemical methods. We observe that the nonlinear optical technique based on Electromagnetically Induced Transparency (EIT) and Lasing Without Inversion (LWI) significantly enhances the differential absorption cross-section of the chiral molecule upon optical pumping and probing by circularly polarized (CP) radiations, with great potential for the development of novel nonlinear spectroscopic techniques capable of detecting chirality at the single molecule level. Additionally, we investigate Spontaneous Emission (SE) of polarized radiation in a chiral cavity, where results suggest that a strain-engineered solid-state emitter with an advanced microcavity can effectively manipulate CP-SE, with clear potential for integrated CP single-photon sources.

List of abbreviations

ACS Absorption Cross-Section

CD Circular Dichroism

CP Circular Polarization

CW Continuous Wave

DACS Differential Absorption Cross-Section

DSF Dissymmetry Factor

DGF Dyadic Green's Function

EIT Electromagnetically Induced Transparency

IR Infrared

LCP Left Circular Polarization

LDOS Local Density of Optical States

LP Linear Polarization

LWI Lasing Without Inversion

NL Nonlinear

OR Optical Rotation

ORD Optical Rotatory Dispersion

PCCD Plasmon-Coupled Circular Dichroism

QED Quantum Electrodynamics

RCP Right Circular Polarization

SE Spontaneous Emission

SFG Sum-Frequency Generation

SHG Second-Harmonic Generation

SPP Surface Plasmon Polariton

TAPCs Twisted Anisotropic Photonic Crystals

TE Transverse Electric

THG Third-Harmonic Generation

TM Transverse Magnetic

TMA Transfer Matrix Approach

UV Ultraviolet

VCD Vibrational Circular Dichroism

Contents

List of Figures

Chapter 1

Introduction

"True chirality is exhibited by systems that exist in two distinct enantiomeric states that are interconverted by space inversion, but not by time reversal combined with any proper spatial rotation."

— L. D. Barron, *Chem. Phys. Lett.* **123**, 423 (1986)

The story of chiroptical spectroscopy starts with attempts to answer a simple question: What is light? Previously, geometrical optics was developed with modern astronomy. Later, in the seventeenth century, according to Newton's corpuscular model and Huygens' wave theory, the nature of light was explained by the optical phenomena of reflection and refraction [1, 2]. In the nineteenth century, Fresnel [3, 4] explained interference and diffraction, declaring light as a transverse wave with the help of Huygens' ideas. In the meantime, Biot, Faraday, and others made combined work on optical phenomena, electric currents, and magnetic fields, and the progress made was significant [5, 6, 7]. Eventually, Maxwell provided the electromagnetic theory, which declares that light is a propagating wave consisting of mutually orthogonal electric and magnetic fields [6, 8]. Further, Planck and Einstein added the photon concept, giving the idea of quanta without the field

picture, which is important for describing light–matter interaction [9, 10].

In classical–quantum physics, polarization is defined as a key property of the electromagnetic field. A monochromatic beam can be considered as linear, circular, or elliptical polarization depending on how the electric and magnetic field vectors oscillate in time [2, 4]. In 1936, Beth's experiment [11] showed that circularly polarized light carries angular momentum corresponding to photon spin (± 1) [12, 13]. The connection between polarization and angular momentum [14] is important for chiral interactions because it allows a definite handedness to light itself. As a result, Left Circular Polarization (LCP) and Right Circular Polarization (RCP) modes, which are mirror images of each other, experience different interactions when propagating through chiral media [15]. Later, in the mid-twentieth century, with the development of lasers [16, 17] and semiclassical radiation theory, it became possible to produce strong optical fields to describe absorption, stimulated emission, and Nonlinear (NL) interactions [18], giving a basic idea of chiroptical spectroscopy [19].

Experimentally, the optical activity was well developed before chirality was defined. In 1811, Arago observed that certain quartz crystals [20] produce colour patterns when placed between polarizers, indicating that the plane of polarization of transmitted light is rotated. Later, Biot [21] developed that sugar and other organic solutions also rotate linearly polarized light, establishing Optical Rotation (OR) as a bulk property of specific liquids and crystals, and Fresnel observed this effect in terms of different refractive indices for LCP and RCP, with differential absorption of these modes giving rise to CD [22]. The origin of these macroscopic effects was explained by Pasteur, who made a connection between opposite OR of tartrate crystals with their non-superimposable mirror-image shapes [5]. In molecular stereochemistry, Kelvin [23] later developed this by defining a body as chiral if it cannot be superimposed on its mirror image by any combination of rotations and translations. The term chiral originates from the Greek word $\chi\varepsilon\iota\rho$,

which means hand [24], an example of a chiral entity. Historically, enantiomorphs (chiral twin structures) are typically defined as left- or right-handed due to this connection with the word hand.

Later in the twentieth century, a general theory of chiroptical interactions was developed using quantum chemistry and electrodynamics. In the macroscopic description, optically active media are considered bi-isotropic (Pasteur) materials [25], in which electric and magnetic fields are coupled by a chirality parameter, so that LCP and RCP waves propagate with different complex refractive indices. In the macroscopic description, quantum mechanical treatments show that chiroptical signals such as ORD and CD [26] originate from interference between electric and magnetic transition dipole moments, providing a direct connection between spectra and the three-dimensional arrangement of atoms in chiral molecules. These developments, together with advances in instrumentation, established linear chiroptical methods as a convincing method for determining absolute configuration and observing biomolecular structure in chemistry, biology, and pharmacology [27, 28].

In recent days, chiral light-matter interaction, in turn, "new age of molecular chirality," [29] has been measured by ultrafast lasers, strong high-intensity fields, and nanophotonic control of electromagnetic modes [30, 31]. Modern concepts such as optical chirality and electromagnetic helicity measure the handedness of general, structured fields and make it possible to design super chiral and optimally chiral light that enhances weak chiroptical responses [32]. Also, with the help of nanofabrication and metamaterials, which make chiral near fields and resonant environments that selectively amplify the response of one enantiomer over the other and, in turn, focus on chiral sensing at low concentrations and measure enantioselectivity of electronic molecular structure [33, 34, 35]. Against this historical backdrop, this thesis explains how modified environments and NL excitation can be used to measure chirality in areas previously inaccessible to optical activity,

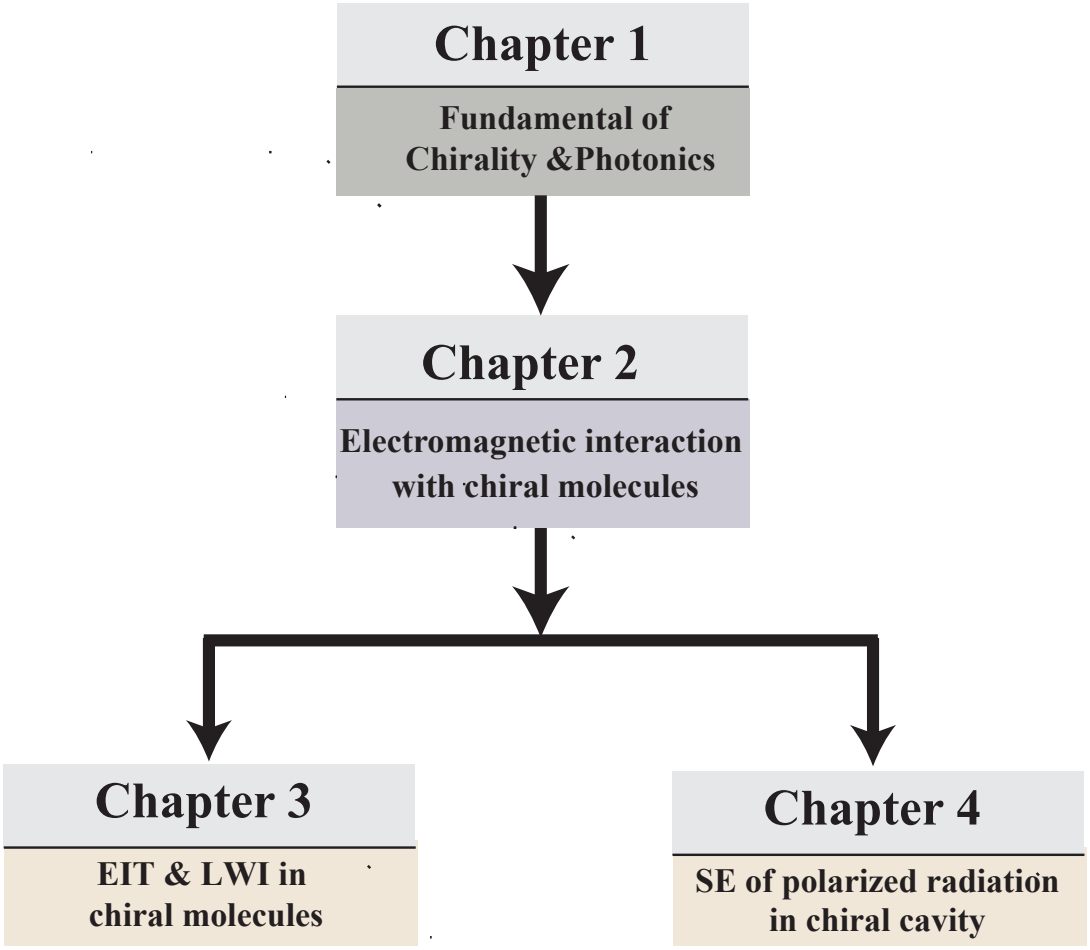

Figure 1.1 Schematic representation of thesis outline.

making them important for future research in molecular and nanophotonic chiroptics.

1.1 Outline

This thesis focuses on the theoretical modeling of chiral light-matter interactions using NL optical spectroscopy, also in a nanophotonic environment.

The thesis is organized as follows:

- Chapter 1 presents the fundamental concepts of chirality and, for measuring it, introduces basic linear optical spectroscopy. First, we describe pulse propagation in optical media by introducing the macroscopic Maxwell equa-

tions and the constitutive relations and by giving a basic idea of the linear and NL contributions arising from the total polarization. Then we discuss the basic concepts of light, considering it as a plane wave and its polarization, review the Stokes parameters, and establish the CP states as a natural basis for describing light-matter interaction in chiral media. Then, a brief description of chiroptical activity was introduced, discussing the CD and ORD methods for measuring the chirality of drug solutions. Then, we provided a basic overview of analytical and separation-based techniques that can also measure chirality and addressed the challenges of measuring chirality at low concentrations. Then, we present theoretical modeling to study the enhancement of inherently weak chiroptical signals through NL chiroptical spectroscopy in a nanophotonic environment. In the first section, we present theoretical modeling of NL and ultrafast techniques such as Sum-Frequency Generation (SFG), Second-Harmonic Generation (SHG), the optical Kerr effect, and pump-probe spectroscopy, and we study the possibilities outlined in some articles to enhance molecular chirality. In the following section of this chapter, we discuss the nanophotonics environment, including plasmonic, dielectric, and hybrid nanostructures, as well as Plasmon-Coupled Circular Dichroism (PCCD) and Surface Plasmon Polariton (SPP), and how these amplify chiroptical sensitivity at reduced sample volumes using nanodevices.

- In Chapter 2, we describe the theoretical modeling of the interaction between chiral molecules and light, which is important for chiroptical sensing. First, we introduce the fundamental concepts necessary for developing a mathematical framework. In the following section, we describe chiroptical interactions theoretically within the density-matrix formalism. Upon excitation with external radiation, we evaluate the field-induced dipole moments and orientational-averaged microscopic responses through the Euler rota-

tion matrix approach. Then, we calculate the macroscopic response and bianisotropic constitutive relation of the chiral drug solution. In the following section, we eventually discuss the enantioselective properties of chiral molecules. The theoretical framework will be helpful for studying the chapters that follow in detail.

- In Chapter 3, we present a theoretical modeling of EIT and LWI in chiral molecules and study how these two NL optical techniques can enhance weak chiroptical signals. First, we discuss the EIT and LWI in a standard three-level atomic system; then we discuss how the polarity and chirality of the chiral molecule fluoroxirane enable optical pumping to excite a virtual state in a two-level system. First. We present a theoretical model of the NL chiroptical interaction using the density-matrix formalism and the Lindblad operator approach, and then provide a perturbative solution for the density matrix from which it is possible to derive the electric and magnetic dipole moments, which are incorporated with the coefficients of the pump and signal field obtained at zero-order and first-order response in the multiscale expansion, respectively. Then, using the chiral optical theorem, we calculate the molecule's absorption cross-section and investigate it as a function of different optical parameters. In MATLAB, using the analytical expressions based on the calculated electronic structure and spectroscopic quantities of fluoroxirane, we perform some simulations. In the results and discussion section, we first study linear response, obtaining the absorption at resonance for signal-field excitation only. Then we introduce a NL response that includes the interaction between the pump and signal fields, in which we observe transparency or amplification rather than absorption. Then we study the transparency or gain for the molecular orientation. Finally, we evaluate the NL-Dissymmetry Factor (DSF), which gives the enhancement rate of

the weak chiroptical signal. We study it as a function of polarization and molecular orientation. Then, we present the most important threshold pump intensity, which is required to obtain the transparency or amplification, and with that threshold pump intensity, we calculate the orientation-averaged NL-DSF by averaging over impinging signal orientations.

- In Chapter 4, we present a theoretical modeling of polarization-dependent SE. First, we provide an overview of SE, including in free space and across different environments, and discuss how it can be enhanced or inhibited using the Quantum Electrodynamics (QED) and DGF approaches. Then we focus on the main concept of this chapter: studying SE in a chiral cavity. First, we characterize the cavity wall made of TAPCs and, using TMA, we evaluate the scattered field. Then we study reflectance and transmittance at a particular incident wavelength and study them for different molecular orientations, and establish that the cavity wall exhibits helicity-preserving reflectance for one CP and very high transmittance for another CP. Then, we evaluate the total DGF to define the right and left CP-SE rates. Then, considering Rubidium as a quantum emitter by using the calculated electronic structure, we perform some simulations in MATLAB. First, in the results and discussion, we evaluate the SE in free space; then we present the dependence of the CP-SE rate on the cavity width; and, finally, we observe the dependence on specific dipolar positions/orientations.

  Finally, Chapter 5 concludes the thesis with a summary and a discussion of the future scope of the thesis work. A schematic map that links the chapters of this thesis outline is presented in Fig 1.1.

1.2 Chirality

As discussed at the beginning of this chapter, chirality is a fundamental geometrical property that arises when an object cannot be superimposed with its mirror image by any combination of rotations and translations [21]. Two such mirror-related forms are said to be left and right-handed structures of chiral matter. Although this definition is purely geometric, its consequences are well established in chemistry, biology, and optics because chiral objects interact differently with other chiral systems and with fields that themselves possess a sense of handedness, such as CP of light [36, 37]. Physically, chirality refers to the breaking of mirror-image symmetry, which means an achiral system is indistinguishable from its mirror image, whereas a chiral system is not. This symmetry breaking concept provides an idea for the chiral matter to interact with the helicity of electromagnetic fields, so that LCP and RCP light can experience different absorption, refraction, or scattering. These differences give rise to chiroptical phenomena, which provide key tools for the detection and characterization of chirality [21].

1.2.1 Chirality in nature

In our lives, one of the most common examples of chirality is provided by our hands and feet; though they are similar in shape and proportions, they are not identical. If we look at our mirror image of the left hand, it appears identical to the right hand. In everyday life, some objects, such as screws and propellers, are chiral. A right-handed screw is the mirror image of a left-handed screw, and the two cannot be made to coincide by any rotation or translation. If we compare propellers, the situation is similar. A right-handed and a left-handed propeller turning with the same sense of rotation will push a boat in opposite directions, while a right-handed propeller turning clockwise and a left-handed propeller turn-

ing counterclockwise both drive the boat forward. In both screws and propellers, a rotation around an axis is always linked with a translation along that axis, and the way these two motions are combined depends on the handedness of the object. This simple example shows how chirality naturally combines rotational and translational motion, which is helpful in understanding dynamic chirality [24].

In the macroscopic scale, chirality is also visible in the coiling direction of plant tendrils, the spiral shells of certain mollusks, and helical growth patterns in vines and microorganisms [21]. In our biological function molecular chirality plays an important role especially in the case of deoxyribonucleic acid (DNA), which contains a right handed double helix structure, which is important for the replication and transcription of genetic information [37, 38]. Also, proteins responsible for catalysis and structural support in living systems are made from L-configured amino acids, while nucleic acids and many carbohydrates are made from D-sugars [39, 40]. This global homochirality of biomolecular building blocks is believed to be important for specific molecular recognition because enzymes and receptors are chiral and therefore differentiate between enantiomers of substrates [41, 42].

There are a lot of natural products; for example, many alkaloids, terpenes, steroids, and antibiotics are biosynthesized in a single enantiomeric form, and their biological activity is directly linked to their stereochemistry [41, 43]. Previously, the medicines derived from plants and animals had already revealed the chiral nature of their active components [44, 45] before the molecular origins of their efficacy were understood. The connection between molecular handedness and macroscopic biological response only became clear in the nineteenth century. This clarity came with the development of stereochemistry and the work of Louis Pasteur, Jacobus Henricus van't Hoff, and Joseph Achille Le Bel [44].

1.2.2 Enantiomers

The two mirror-image forms of a chiral molecule are termed enantiomers. They possess identical atomic composition and bonding connectivity but differ in their arrangement, such that the two structures are non-superimposable mirror images [21]. An achiral environment exhibits the same physical properties, such as melting point, vapor pressure, and electronic transition energies. However, they respond differently to chiral environments and exhibit distinct biological and chemical behaviors [21, 41]. A racemic mixture is defined as an equal amount of both enantiomers.

For distinguishing enantiomers, the widely used structural scheme is the Cahn-Ingold-Prelog (CIP) system, which assigns each stereogenic center an absolute configuration denoted as R (from rectus, right) or S (from sinister, left) according to the priority ordering and spatial orientation of its substituents [46]. Also, experimentally determined classification is based on optical activity: enantiomers are described as (+) or (–) depending on whether they rotate the plane of Linear Polarization (LP) of light clockwise or counterclockwise in an OR experiment [21]. This sign does not follow directly from the R/S configuration and must be measured for each compound. In biochemical contexts, the D/L notation, defined according to the stereochemistry of glyceraldehyde, is used to specify the configuration of sugars and amino acids. In the present work, the CIP R/S convention is used to identify molecular enantiomers.

In biochemical systems, chiral molecules occur in a single enantiomeric form. Amino acids incorporated into proteins are almost exclusively L-enantiomers, while the saccharides in nucleic acids and many polysaccharides are predominantly D-enantiomers [37, 47]. Numerous antibiotics, steroids, and other bioactive natural products are also synthesized as single enantiomers. Despite such homochirality, the ability to discriminate between opposite enantiomers remains

important because they can function distinctly in living organisms [48].

1.2.3 Chirality in medicine

The importance of enantiomer discrimination is particularly evident in pharmacology. Biological targets such as enzymes, transporters, ion channels, and receptors are chiral macromolecules and therefore often bind selectively to only one enantiomer of a chiral drug [41]. As a result, the two enantiomers of a pharmaceutical compound may exhibit different pharmacodynamics. In many cases, one enantiomer exhibits the expected therapeutic effect, whereas the other is less active or inactive [41].

In the case of thalidomide, the R-enantiomer has sedative and anti-nausea effects, while the S-enantiomer has been associated with teratogenic effects leading to severe birth defects during pregnancy [49, 50]. Another example is methamphetamine: the L-enantiomer (levomethamphetamine) has been used as a relatively mild nasal decongestant, while the D-enantiomer (dextromethamphetamine) is a powerful stimulant for the central nervous system with high abuse potential and strong addictive properties [51, 52]. Ketamine, used in anesthesia and analgesia, is considered to be a racemic mixture, but its R- and S-enantiomers exhibit different properties for NMDA receptors, giving rise to the motivation for the development of single-enantiomer formulations to improve the therapeutic index [53, 54].

These and many other cases have led regulatory agencies to require the separate evaluation of each enantiomer of new chiral drugs [27, 55]. Therefore, precise chirality analysis and accurate determination of enantiomeric excess are essential for drug development [56].

1.2.4 Current techniques for measuring chirality

In the following sections, we first discuss linear chiroptical spectroscopy in section 1.4 and some analytical techniques in section 1.5 for measuring chirality, focusing on their capabilities and limitations, see section 1.6. We then introduce NL chiroptical methods in section 1.8 and nanophotonic environments in section 1.9 that overcome these challenges and enhance the sensitivity of chirality measurements.

1.3 Pulse propagation in optical media

The propagation of light in an optical medium can be explained in the framework of macroscopic Maxwell equations [6]:

$$\begin{cases} \nabla \cdot \mathbf{D} = \rho, \\ \nabla \cdot \mathbf{B} = 0, \\ \nabla \times \mathbf{E} = -\dfrac{\partial \mathbf{B}}{\partial t}, \\ \nabla \times \mathbf{H} = \mathbf{J} + \dfrac{\partial \mathbf{D}}{\partial t}, \end{cases} \tag{1.1}$$

where $\mathbf{E}$ and $\mathbf{H}$ are the electric and magnetic fields, $\mathbf{D}$ is the electric displacement vector, $\mathbf{B}$ is the magnetic flux density, ρ is the free charge density, and $\mathbf{J}$ is the free current density.

For source-free optical media ($\rho = 0$, $\mathbf{J} = 0$) the dependence of the electric displacement vector $\mathbf{D}$ and the magnetic flux density $\mathbf{B}$ on the electric $\mathbf{E}$ and magnetic $\mathbf{H}$ fields is described by the macroscopic constitutive relations as

$$\begin{aligned} \mathbf{D} &= \varepsilon_0 \, \mathbf{E} + \mathbf{P}, \\ \mathbf{B} &= \mu_0 \, (\mathbf{H} + \mathbf{M}), \end{aligned} \tag{1.2}$$

where $\mathbf{P}$ is the material-induced polarization and $\mathbf{M}$ is the induced magnetization. In general, the polarization depends nonlinearly on the electric field strength [18], while ε_0 and μ_0 are the permittivity and permeability of vacuum, respectively.

1.3.1 Linear response

In a homogeneous, isotropic medium, the linear response of the material, that is, the polarization and magnetization, can be expressed as temporal convolutions of the electric and magnetic fields with the response functions [57] respectively, as follows:

$$\mathbf{P}(\mathbf{r},t) = \epsilon_0 \int_{-\infty}^{+\infty} dt' \chi_e(t-t')\mathbf{E}(\mathbf{r},t), \tag{1.3a}$$

$$\mathbf{M}(\mathbf{r},t) = \int_{-\infty}^{+\infty} dt' \chi_m(t-t')\mathbf{H}(\mathbf{r},t). \tag{1.3b}$$

Here, $\chi_e(t-t')$ and $\chi_m(t-t')$ are the temporal response functions that depend only on the time difference $(t-t')$ because the system is time invariant, and spatial locality is assumed so that $\mathbf{P}(\mathbf{r},t)$ and $\mathbf{M}(\mathbf{r},t)$ depend only on $\mathbf{E}$ and $\mathbf{H}$ at the same position $\mathbf{r}$. For a homogeneous, isotropic medium, $\chi_e(t-t')$ and $\chi_m(t-t')$ are position independent, and the integrals in Eq. 1.3 extend from $-\infty$ to $+\infty$. In turn, it is necessary that $\chi_e(t-t') = 0$ and $\chi_m(t-t') = 0$ for $t' > t$, which leads to the Kramers-Kronig relations [6] and is responsible for the analytic properties of the frequency-dependent electric and magnetic susceptibilities $\chi_e(\omega)$ and $\chi_m(\omega)$ respectively.

Introducing the Fourier representation

$$F(t) = \frac{1}{2\pi} \int_{-\infty}^{+\infty} \mathrm{d}\omega\, F(\omega)\, \exp(-i\omega t), \tag{1.4}$$

for $F(t) = \mathbf{E}(t), \mathbf{H}(t), \mathbf{P}(t), \mathbf{M}(t)$ the convolution theorem [58], converts Eq. 1.3

into the algebraic relations:

$$\mathbf{P}(\mathbf{r},\omega) = \varepsilon_0\,\chi_e(\omega)\,\mathbf{E}(\mathbf{r},\omega), \tag{1.5a}$$

$$\mathbf{M}(\mathbf{r},\omega) = \mu_0\,\chi_m(\omega)\,\mathbf{H}(\mathbf{r},\omega), \tag{1.5b}$$

with $\chi_e(\omega)$ and $\chi_m(\omega)$ are the linear electric and magnetic susceptibilities [18] respectively. Inserting Eq. 1.5 into Eq. 1.2 gives the frequency dependent constitutive relations as

$$\mathbf{D}(\mathbf{r},\omega) = \epsilon_0\epsilon(\omega)\mathbf{E}(\mathbf{r},\omega), \tag{1.6a}$$

$$\mathbf{B}(\mathbf{r},\omega) = \mu_0\mu(\omega)\mathbf{H}(\mathbf{r},\omega), \tag{1.6b}$$

where $\varepsilon(\omega) = 1 + \chi_e(\omega)$ and $\mu(\omega) = 1 + \chi_m(\omega)$, so that $\varepsilon(\omega)$ and $\mu(\omega)$ are the frequency-dependent relative dielectric permittivity and relative magnetic permeability of the medium, respectively.

Combining Maxwell's equations 1.1 with the constitutive relations 1.2 and using the vector identity $\nabla\times\nabla\times\mathbf{E} = \nabla(\nabla\cdot\mathbf{E}) - \nabla^2\mathbf{E}$, which reduces to $-\nabla^2\mathbf{E}$ in a homogeneous, source-free isotropic medium where $\nabla\cdot\mathbf{E} = 0$, one obtains the time-domain wave equation for the electric field [6, 18]:

$$\nabla^2\mathbf{E}(\mathbf{r},t) - \frac{1}{c^2}\frac{\partial^2\mathbf{E}(\mathbf{r},t)}{\partial t^2} = \frac{1}{\varepsilon_0 c^2}\frac{\partial^2\mathbf{P}(\mathbf{r},t)}{\partial t^2}, \tag{1.7}$$

where $c = 1/\sqrt{\varepsilon_0\mu_0}$ is the speed of light in vacuum. This equation declares that the polarization acts as a source of the propagating wave through its contribution to the displacement field.

1.3.2 Nonlinear response and effective wave equation

Taking the temporal Fourier transform of Eq. 1.7 according to Eq. 1.4 yields the frequency-domain vector wave equation

$$\nabla^2\mathbf{E}(\mathbf{r},\omega) + \frac{\omega^2}{c^2}\,\mu_(\omega)\,\varepsilon(\omega)\,\mathbf{E}(\mathbf{r},\omega) = -\frac{\omega^2}{\varepsilon_0 c^2}\,\mu(\omega)\,\mathbf{P}(\mathbf{r},\omega). \tag{1.8}$$

Now, splitting the polarization into linear and NL contributions,

$$\mathbf{P}(\mathbf{r},\omega) = \mathbf{P}_{\mathrm{L}}(\mathbf{r},\omega) + \mathbf{P}_{\mathrm{NL}}(\mathbf{r},\omega), \tag{1.9}$$

and using the linear constitutive relation $\mathbf{P}_{\mathrm{L}}(\mathbf{r},\omega) = \varepsilon_0\chi^{(1)}(\omega)\mathbf{E}(\mathbf{r},\omega)$ as discussed in the previous section 1.3.1, and absorbing the linear response into $\varepsilon(\omega)$ and $\mu(\omega)$, one obtains the NL wave equation

$$\nabla^2\mathbf{E}(\mathbf{r},\omega) + \frac{\omega^2}{c^2}\,\mu(\omega)\,\varepsilon(\omega)\,\mathbf{E}(\mathbf{r},\omega) = -\frac{\omega^2}{\varepsilon_0 c^2}\,\mu(\omega)\,\mathbf{P}_{\mathrm{NL}}(\mathbf{r},\omega), \tag{1.10}$$

where, $\mathbf{P}_{\mathrm{NL}}$ contains all higher-order contributions in the electric field.

If the NL response is neglected ($\mathbf{P}_{\mathrm{NL}} = 0$), Eq. 1.10 reduces to the homogeneous Helmholtz equation

$$\nabla^2\mathbf{E}(\mathbf{r},\omega) + \frac{\omega^2}{c^2}\,n^2(\omega)\,\mathbf{E}(\mathbf{r},\omega) = 0, \tag{1.11}$$

where we introduce $n^2(\omega) = \varepsilon(\omega)\mu_(\omega)$. Thus, in the linear regime, from the refractive index, $n(\omega)$ we obtain information about dispersion and absorption in linear spectroscopic propagation, while the NL polarization $\mathbf{P}_{\mathrm{NL}}$ acts as a source term, giving rise to new frequencies in the field in case of NL optical processes [18].

1.3.2.1 Plane waves and polarisation states

A particularly important solution of the homogeneous wave equation corresponds to plane waves, for which the electromagnetic fields are uniform over planes perpendicular to the direction of propagation. We consider a monochromatic plane wave propagating in a homogeneous isotropic medium, whose electric field in the time domain may be written as

$$\mathbf{E}(\mathbf{r},t) = \mathrm{Re}\{\mathbf{E_0}\, e^{i\mathbf{k}\cdot\mathbf{r}-i\omega t}\}\,, \tag{1.12}$$

where $\mathbf{E_0}$ is the complex field amplitude, $\mathbf{k}$ is the wavevector, and ω is the angular frequency. Substitution of Eq. 1.12 into the linear wave equation 1.11 derived in the previous section, we obtain the dispersion relation

$$k = \frac{n(\omega)\,\omega}{c}, \tag{1.13}$$

which describes the propagation of monochromatic waves in the medium. The refractive index $n(\omega)$ therefore fully determines the phase velocity and dispersive properties of the propagating field.

The polarization state of an electromagnetic wave is defined by the direction and the time evolution of the electric field vector in the plane which is transverse to the direction of propagation.

In the transverse plane, we consider propagation along the $+z$ direction, $\mathbf{k} = k\,\hat{\mathbf{z}}$. The electric field then lies in the transverse (x,y) plane and may be written as

$$\mathbf{E}(\mathbf{r},t) = \mathrm{Re}\{\left[E_x\,\hat{\mathbf{e}}_x + E_y\,e^{i\phi}\,\hat{\mathbf{e}}_y\right] e^{ikz-i\omega t}\}\,, \tag{1.14}$$

where E_x and E_y are the complex amplitudes of the orthogonal field components and ϕ is their relative phase difference. When the relative phase satisfies $\phi = 0$

(or an integer multiple of 2π), the two transverse components oscillate in phase, and the field reduces to

$$\mathbf{E}_{\mathrm{LP}}(\mathbf{r},t) = \mathrm{Re}\left\{ (E_x\,\hat{\mathbf{e}}_x + E_y\,\hat{\mathbf{e}}_y)\, e^{ikz-i\omega t} \right\}, \tag{1.15}$$

which represents LP light. In this case, the electric field oscillates along a fixed direction in the transverse plane.

We define CP as when the two orthogonal components have equal magnitudes, $|E_x| = |E_y| = E/\sqrt{2}$, and a relative phase difference $\phi = \pm\pi/2$. Using the identity $e^{\pm i\pi/2} = \pm i$, the electric field becomes

$$\mathbf{E}_{\pm}(\mathbf{r},t) = \mathrm{Re}\left\{ \frac{E}{\sqrt{2}} (\hat{\mathbf{e}}_x \pm i\,\hat{\mathbf{e}}_y)\, e^{ikz-i\omega t} \right\}, \tag{1.16}$$

which describes a field which rotates uniformly in the transverse plane. The CP unit vectors can be defined as below

$$\hat{\mathbf{e}}_{\pm} = \frac{1}{\sqrt{2}} (\hat{\mathbf{e}}_x \pm i\,\hat{\mathbf{e}}_y), \tag{1.17}$$

so that the RCP and LCP states may be written as

$$\mathbf{E}_{\mathrm{RCP}}(\mathbf{r},t) = \mathrm{Re}\left\{ E\,\hat{\mathbf{e}}_+\, e^{ikz-i\omega t} \right\}, \tag{1.18a}$$

$$\mathbf{E}_{\mathrm{LCP}}(\mathbf{r},t) = \mathrm{Re}\left\{ E\,\hat{\mathbf{e}}_-\, e^{ikz-i\omega t} \right\}. \tag{1.18b}$$

These two CP states are orthogonal and form a natural basis for describing light–matter interactions in isotropic and chiral media.

1.4 Linear chiroptical spectroscopy

Chiral media respond differently to LCP and RCP of light, giving rise to linear chiroptical effects such as OR, ORD, and CD [59, 60]. These phenomena can be understood at the macroscopic level with bi-isotropic (Pasteur) constitutive relations and at the microscopic level as interference between electric and magnetic transition dipole moments. This section introduces the basic field description of isotropic chiral media, and then we discuss ORD and CD as the two observables of linear chiroptical spectroscopy.

In general, a bi-isotropic medium is characterized by the property that the polarization state of light changes as it propagates through the material. The constitutive relation for these chiral media for the electric displacement vector $\mathbf{D}$ and induction magnetic field $\mathbf{B}$ in terms of electric $\mathbf{E}$ and magnetic $\mathbf{H}$ fields can be expressed as:

$$\begin{cases} \mathbf{D}(\mathbf{r},t) = \varepsilon_0\,\varepsilon\,\mathbf{E}(\mathbf{r},t) - \dfrac{i\kappa}{c}\,\mathbf{H}(\mathbf{r},t), \\ \mathbf{B}(\mathbf{r},t) = \mu_0\,\mu\,\mathbf{H}(\mathbf{r},t) + \dfrac{i\kappa}{c}\,\mathbf{E}(\mathbf{r},t). \end{cases} \tag{1.19}$$

where ε and μ denote the relative permittivity and relative permeability of the medium, while ε_0 and μ_0 are the permittivity and permeability of free space, respectively and c represents the speed of light in vacuum. The measurement of the degree of chiral handedness is given by the chirality parameter κ, and its sign reverses for opposite enantiomers.

By combining Maxwell's equations 1.1 with the constitutive equations 1.19 above, the wave equation can be obtained as below

$$\nabla^2\mathbf{E} + 2\kappa\,\frac{\omega}{c}\,\nabla\times\mathbf{E} + \left(\varepsilon\mu - \kappa^2\right)\frac{\omega^2}{c^2}\,\mathbf{E} = 0. \tag{1.20}$$

The above expression 1.20 contains an additional curl term proportional to κ

with angular frequency ω. This term denotes the distinct propagation of different polarization states.

For a homogeneous medium, we choose the plane wave propagated along the z direction, and the eigenmodes of the wave equation, which are in CP mode can be written as

$$\mathbf{E}^{(\mathrm{RCP})} = [E_x\,\hat{\mathbf{e}}_x + i\,E_y\,\hat{\mathbf{e}}_y]\,e^{ik^{(\mathrm{RCP})}z}, \tag{1.21a}$$

$$\mathbf{E}^{(\mathrm{LCP})} = [E_x\,\hat{\mathbf{e}}_x - i\,E_y\,\hat{\mathbf{e}}_y]\,e^{ik^{(\mathrm{LCP})}z}, \tag{1.21b}$$

corresponding to RCP and LCP waves with amplitudes E_x and E_y in the direction defined by unit vectors $\hat{\mathbf{e}}_x$ and $\hat{\mathbf{e}}_y$, respectively, where the propagation constant k satisfies the equation below:

$$k^2 = \left(\frac{\omega}{c}\right)^2 (\sqrt{\varepsilon\mu} \pm \kappa)^2\,. \tag{1.22}$$

The wave vectors for two CP eigenmodes are obtained as:

$$k^{(\mathrm{RCP})} = \frac{\omega}{c}\,(\sqrt{\varepsilon\mu} + \kappa)\,, \qquad k^{(\mathrm{LCP})} = \frac{\omega}{c}\,(\sqrt{\varepsilon\mu} - \kappa)\,. \tag{1.23}$$

Therefore, as a result, these double mode propagation RCP and LCP waves experience different refractive indices, $n^{(\mathrm{RCP})} = \sqrt{\varepsilon\mu} + \kappa$, $n^{(\mathrm{LCP})} = \sqrt{\varepsilon\mu} - \kappa$ and consequently propagate with different phase velocities, $v^{(\mathrm{RCP})} = \frac{c}{\mathrm{Re}\left[n^{(\mathrm{RCP})}\right]}$, $v^{(\mathrm{LCP})} = \frac{c}{\mathrm{Re}\left[n^{(\mathrm{LCP})}\right]}$.

1.4.1 Optical rotatory dispersion (ORD) and polarimetry

When a linearly polarized electromagnetic wave propagates through a chiral medium, its plane of polarization generally rotates about the direction of propagation. This phenomenon, called OR, is characterized by the two CP of the medium, RCP and

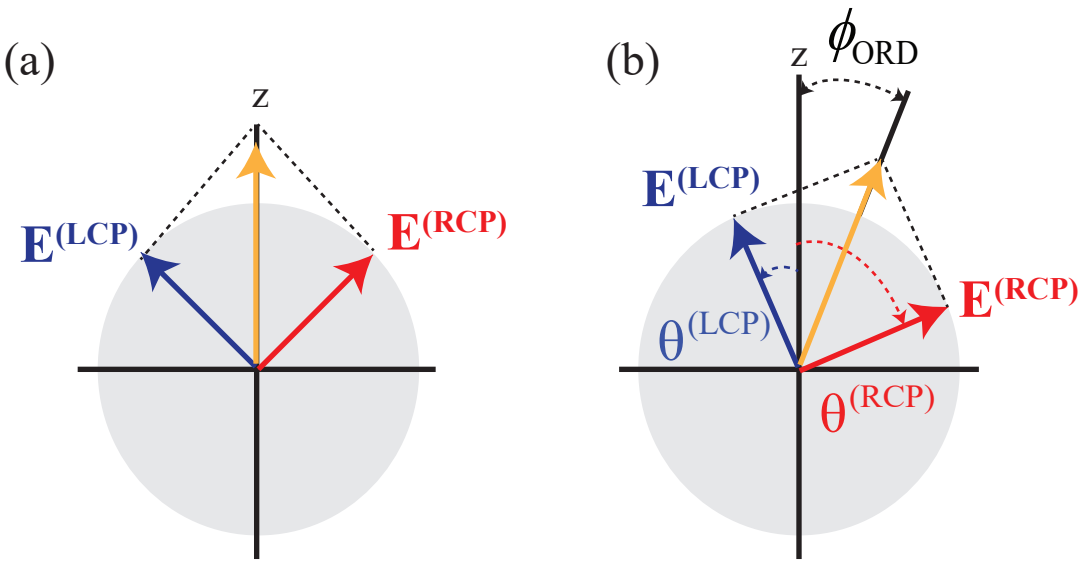

Figure 1.2 (**a**) In an achiral medium, a linearly polarized electric field **E** can be decomposed into coherent RCP and LCP components, $\mathbf{E}^{(\mathrm{RCP})}$ and $\mathbf{E}^{(\mathrm{LCP})}$. (**b**) In a chiral medium, the recombination of these components after propagation leads to a rotation of the polarization plane by the optical rotatory dispersion angle Φ_{ORD}, arising from the different orientations $\theta^{(\mathrm{RCP})}$ and $\theta^{(\mathrm{LCP})}$ of the CP excitations.

LCP of waves, propagating with different phase velocities due to circular birefringence [21, 59, 60]. As described in the previous section 1.4, we see that this birefringence comes from the splitting of the refractive indices $n^{(\mathrm{RCP})}$ and $n^{(\mathrm{LCP})}$, or equivalently, from the difference in propagation constants $k^{(\mathrm{RCP})}$ and $k^{(\mathrm{LCP})}$.

A LP of a field is considered as an equal superposition of RCP and LCP eigenmodes. In an achiral medium, these components propagate with identical phases and, upon recombination, reproduce the original polarization state. Within a chiral medium, there is a relative phase difference between the two CP components that comes from the difference in propagation constants. After propagating a distance d, the differential phase shift $\Delta\phi$ is given by:

$$\Delta\phi = (k^{(\mathrm{RCP})} - k^{(\mathrm{LCP})})d, \tag{1.24}$$

which causes the recombined field to remain as in LP state, but rotated relative to the incident polarization direction.

As shown, schematically in Fig. 1.2, see Fig. 1.2(a), the incident linearly polarized field is decomposed into its RCP and LCP components, whose electric-field vectors rotate with equal magnitude but opposite handedness. In an achiral medium, the two components remain phase-matched and recombine without rotation. But in a chiral medium, see Fig. 1.2(b), the RCP and LCP field components propagate with different phases. At a given propagation distance and time, their electric-field vectors are oriented at angles $\theta^{(\mathrm{RCP})}$ and $\theta^{(\mathrm{LCP})}$ relative to the initial polarization direction. The resulting LP is oriented midway between these two circular components. Hence, the net rotation Φ_{ORD} of the polarization plane in radians can be written as

$$\Phi_{\mathrm{ORD}}(\lambda) = \frac{\theta^{(\mathrm{RCP})} + \theta^{(\mathrm{LCP})}}{2}. \tag{1.25}$$

The rotation angle depends on wavelength and propagation length and can be expressed in terms of the refractive indices of the two circular eigenmodes. We write the refractive indices as complex quantities, $n^{(\mathrm{RCP})} = n^{(\mathrm{R})} + in^{(\mathrm{R})''}$ and $n^{(\mathrm{LCP})} = n^{(\mathrm{L})} + in^{(\mathrm{L})''}$, the OR arises from the difference in their real parts. For a propagation length d, the rotation angle is given by

$$\Phi_{\mathrm{ORD}}(\lambda) = \frac{\pi d}{\lambda}\left(n^{(\mathrm{R})} - n^{(\mathrm{L})}\right), \tag{1.26}$$

where λ is the vacuum wavelength. This wavelength dependence of the OR defines ORD. The real parts of $n^{(\mathrm{RCP})}$ and $n^{(\mathrm{LCP})}$ determine the phase velocities $v^{(\mathrm{RCP})} = c/\mathrm{Re}[n^{(\mathrm{RCP})}]$ and $v^{(\mathrm{LCP})} = c/\mathrm{Re}[n^{(\mathrm{LCP})}]$.

Also, we express $\Phi_{\mathrm{ORD}}(\lambda)$ in terms of the transmitted complex phases of RCP and LCP of fields, using

$$\Phi_{\mathrm{ORD}}(\lambda) = \tfrac{1}{2}\left[\arg(T^{(\mathrm{RCP})}) - \arg(T^{(\mathrm{LCP})})\right], \tag{1.27}$$

where $T^{(\mathrm{RCP})}$ and $T^{(\mathrm{LCP})}$ are the complex transmission coefficients for the two CP states. This form denotes that ORD directly probes the phase response of the medium and is therefore sensitive to the real part of the chirality parameter $\mathrm{Re}(\kappa)$.

We measure the ORD spectrum experimentally by using polarimetry, where an incident linearly polarized beam passes through the chiral sample, and an analyzer (a second linear polarizer) is rotated until the transmitted intensity is maximized to determine $\Phi(\lambda)$ as a function of wavelength and thereby obtain the ORD spectrum. This ORD spectrum is particularly sensitive to dispersive changes in the real part of the chiral refractive index and complements CD measurements, which probe the imaginary part.

1.4.2 Circular dichroism

When LCP and RCP of light experience different attenuation upon propagation through a chiral medium, the resulting differential absorption gives rise to CD. As shown in Fig. 1.3(a), a linearly polarized wave entering a chiral sample can be decomposed into RCP and LCP components that propagate with different phase velocities, leading to OR, whereas in Fig. 1.3(b) the same two components are absorbed at different rates so that their transmitted amplitudes no longer match, which defines CD.

In this case, as discussed in the section. 1.4, when the imaginary parts of the refractive indices differ, $n^{(\mathrm{R})\prime\prime} \neq n^{(\mathrm{L})\prime\prime}$, the two CP eigenmodes are attenuated at unequal rates as they propagate through the chiral medium.

As the RCP and LCP states are absorbed at different rates, the CD signal is expressed in terms of the differential absorbance

$$\Delta A(\lambda) = A^{(\mathrm{RCP})}(\lambda) - A^{(\mathrm{LCP})}(\lambda), \tag{1.28}$$

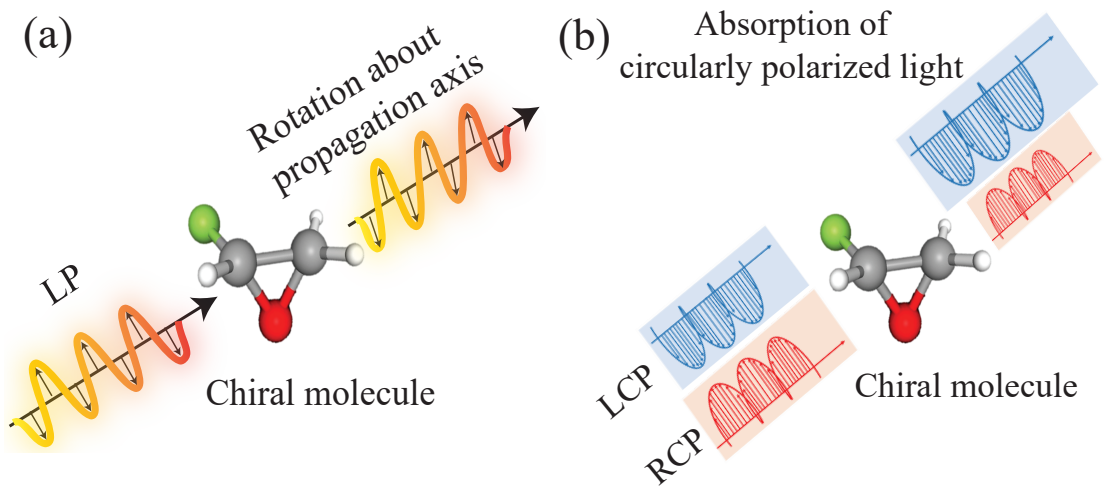

Figure 1.3 (**a**) Schematic diagram of OR where a linearly polarized wave propagating through a chiral medium experiences a rotation of its polarization plane due to different phase velocities of the RCP and LCP components. (**b**) Schematic diagram of CD where RCP and LCP waves are absorbed at different rates by a chiral medium, resulting in unequal transmitted amplitudes for the two different polarizations.

while the mean absorbance

$$A(\lambda) = \frac{A^{(\mathrm{RCP})}(\lambda) + A^{(\mathrm{LCP})}(\lambda)}{2} \tag{1.29}$$

where $A^{(\mathrm{RCP})}(\lambda)$ and $A^{(\mathrm{LCP})}(\lambda)$ denote the absorbance of RCP and LCP of light, which explains the total absorption independent of chirality [60].

The corresponding intensity transmission coefficients of RCP and LCP of light waves after propagating a distance d through the chiral medium are defined as $T^{(\mathrm{RCP})}(\lambda) = \frac{I^{(\mathrm{RCP})}(d)}{I_0}$, $T^{(\mathrm{LCP})}(\lambda) = \frac{I^{(\mathrm{LCP})}(d)}{I_0}$, where I_0 is the incident intensity.

According to the Beer-Lambert law, the intensity of a monochromatic wave propagating through an absorbing medium decays exponentially,

$$I(d) = I_0 \exp\left[-2\frac{\omega}{c} n'' d\right], \tag{1.30}$$

with n'' denoting the imaginary part of the refractive index. In a chiral medium,

the RCP and LCP eigenmodes experience different transmitted intensities,

$$I^{(\mathrm{RCP})}(d) = I_0 \exp\big[-2(\omega/c)\, n^{(\mathrm{R})\prime\prime} d\big], \qquad I^{(\mathrm{LCP})}(d) = I_0 \exp\big[-2(\omega/c)\, n^{(\mathrm{L})\prime\prime} d\big], \tag{1.31}$$

which explains the microscopic asymmetry of light–matter interaction that defines CD.

We measure CD using the dissymmetry (anisotropy) factor $g(\lambda)$ [61], first introduced by Kuhn in 1930. Considering the interaction between a chiral molecule and CP of light, the molecular chirality is revealed in the difference between the differential absorbance for two CP of light waves, normalized to their average as below:

$$g(\lambda) = 2\,\frac{\Delta A(\lambda)}{A^{(\mathrm{RCP})}(\lambda) + A^{(\mathrm{LCP})}(\lambda)}. \tag{1.32}$$

Also, the strength of CD is expressed in terms of ellipticity, because unequal attenuation of the RCP and LCP components converts an initially LP of wave into an elliptically polarized one. The ellipticity η can be expressed in terms of the transmission amplitudes for RCP and LCP as

$$\eta = \frac{1}{2}\sin^{-1}\left(\frac{\left|T^{(\mathrm{RCP})}\right|^2 - \left|T^{(\mathrm{LCP})}\right|^2}{\left|T^{(\mathrm{RCP})}\right|^2 + \left|T^{(\mathrm{LCP})}\right|^2}\right), \tag{1.33}$$

and is reported in degrees or millidegrees in conventional CD spectroscopy. Also, it is converted to molar ellipticity to determine the concentration and path length [60]. Modern CD spectrometers use this by modulating between RCP and LCP using a photoelastic modulator and recording the corresponding transmitted intensities as a function of wavelength.

Within the Pasteur description of chiral media, CD is directly related to the

imaginary part of the differential refractive index,

$$\mathrm{CD}(\lambda) \propto \mathrm{Im}\left[n^{(\mathrm{RCP})}(\lambda) - n^{(\mathrm{LCP})}(\lambda)\right] \propto \mathrm{Im}[\kappa(\lambda)]\,, \tag{1.34}$$

and therefore probes the absorptive component of the chiral magnetoelectric coupling. Together, CD and ORD provide a complete characterization of the linear chiroptical response of a chiral medium [59, 60]. Thus, CD probes the imaginary part of the chiral coupling parameter κ. At the same time, ORD is directly proportional to its real part, making CD and ORD two standard methods for the linear chiroptical response.

1.5 Analytical and separation-based techniques

With the above optical methods, there are also some separation-based analytical techniques that are useful for measuring chirality in the pharmaceutical industry, such as High-performance liquid chromatography (HPLC) , capillary electrochromatography, gas chromatography, and NMR-based methods, which are commonly used for measuring chirality. HPLC is an analytical technique used to separate and identify the R- and S-enantiomers of chiral compounds [62]. NMR spectroscopy can differentiate enantiomers of chiral solvents, giving both structural information and accurate enantiomeric ratios [63]. These techniques are highly sensitive but need careful sample preparation for a long time; also, in the case of in situ or on-chip measurements, they can measure chirality up to milliliter volume.

1.6 Challenges in measuring chirality at low concentration

Measuring chirality with linear chiroptical spectroscopy (CD and ORD) 1.4 faces some challenges [1]. These techniques produce noisy signals with inherently low sensitivity, arising from interference between oscillating electric-dipole and much weaker magnetic-dipole (or electric-quadrupole) moments in organic molecules. Also, in linear chiroptical spectroscopy, the material's response does not depend on the intensity of light. Additionally, the separation-based methods 1.5 can measure chirality with large milliliter-scale sample volumes with long preparation times, where these chiroptical signals suffer from limited sensitivity and are too weak to be detected. Therefore, the above methods are not suitable for precision medicine and nanomedicine, which are innovative solutions for tailored treatment and in-situ analysis of genetic variations, where chirality should be measured at nanoliter volumes.

1.7 Nonlinear and ultrafast spectroscopy and nanophotonic environments for chiral sensing

The inherently weak chiroptical response can be enhanced by using NL ultrafast techniques, which provide much higher sensitivity to molecular chirality. In addition, nanophotonic environments can amplify chiroptical signals far better than what is achievable with conventional linear chiroptical spectroscopy.

In linear optical activity, the polarization angle of a light beam cannot change with the intensity of light. When a high-intensity electric field interacts with atoms or molecules, the valence electrons are strongly driven by the applied field. As a result, the induced polarization of the medium depends nonlinearly on the electric

field amplitude. This NL polarization gives rise to new frequency components and phenomena, and this is the origin of NL optics. Additionally, chiral sensing in a nanophotonic environment depends on the interaction between chiral molecules and appropriately designed nanostructures. By engineering the near field around these structures, linear CD signals can be strongly enhanced. The nanostructures act as binding sites for the analyte and support resonance modes that further enhance the chiral response. Moreover, near-field scattering in such systems can modify the molecular transition frequencies; in turn, the chiral molecules can modify the effective surface properties and resonances of the nanophotonic structures.

1.8 Nonlinear and ultrafast chiroptical spectroscopy

To study the NL optical effect with high-intensity electromagnetic field, the polarization is expanded in powers of the electric field. The total polarization can be written as

$$\mathbf{P}_{\mathrm{NL}}(\mathbf{r},\omega) = \varepsilon_0 \Big[\chi^{(1)}(\omega)\mathbf{E}(\mathbf{r},\omega) + (\chi^{(2)}(\omega)\mathbf{E}(\mathbf{r},\omega)\mathbf{E}(\mathbf{r},\omega) + (\chi^{(3)}(\omega)\mathbf{E}(\mathbf{r},\omega)\mathbf{E}(\mathbf{r},\omega)\mathbf{E}(\mathbf{r},\omega) + ...\Big] \tag{1.35}$$

The linear optical phenomena, such as refraction and absorption, are described by the first term, where $\chi^{(1)}$ is the linear susceptibility tensor. NL optical effects arise from higher-order terms in the Eq. 1.35. As the intensity of the field increases, the polarization drifts from its linear behaviour. Here, we focus on 2nd- and 3rd-order NL optical effects. The second-order susceptibility tensor $\chi^{(2)}$ depends quadratically on the electric field and gives rise to SHG and SFG, whereas the third-order NL susceptibility tensor $\chi^{(3)}$ depends nonlinearly on the electric field, giving rise to some NL optical effects like the optical Kerr effect and pump-probe

spectroscopy. These NL optical phenomena can be used to measure chirality with linear as well as CP of light, leading to NL chiroptical spectroscopy; however, the intensity will be much larger than in linear spectroscopy.

1.8.1 Sum Frequency Generation in chirality

SFG is the second-order NL optical process where the pulses with two different frequencies ω_1 and ω_2 overlap, and the output field is generated at frequency ω_3 as the sum of two incident fields as shown in the Fig. 1.4 with an induced NL polarization $\mathbf{P}^{(2)}$ at the sum frequency given below:

$$\omega_3 = \omega_1 + \omega_2 \tag{1.36}$$

Within the electric–dipole approximation, the second-order polarization at ω_3 is

$$\mathbf{P}^{(2)}(\mathbf{r}, \omega_3) = \varepsilon_0 \, \boldsymbol{\chi}^{(2)}(\omega_3; \omega_1, \omega_2) : \mathbf{E}(\mathbf{r}, \omega_1)\mathbf{E}(\mathbf{r}, \omega_2), \tag{1.37}$$

where, $\boldsymbol{\chi}^{(2)}$ is the second-order susceptibility tensor and $\mathbf{E}(\mathbf{r}, \omega_j)$ denotes the field amplitudes. In the case of centrosymmetric and isotropic achiral media, the electric dipole contribution to the second-order susceptibility tensor $\boldsymbol{\chi}^{(2)}$ does not exist, so SFG cannot be produced in that case. But in the case of isotropic chiral media, there is no inversion symmetry, so the second-order susceptibility tensor $\boldsymbol{\chi}^{(2)}$ is non-zero. If we take the orientational average for the randomly oriented chiral molecule, then the second-order polarization in chiral liquid [64] becomes

$$\mathbf{P}_{\mathrm{SFG}}(\mathbf{r}, \omega_3) = \varepsilon_0 \, \chi_{\chi}^{(2)}(\omega_3; \omega_1, \omega_2) \left[\mathbf{E}(\mathbf{r}, \omega_1) \times \mathbf{E}(\mathbf{r}, \omega_2)\right], \tag{1.38}$$

where $\chi_{\chi}^{(2)}$ is a pseudoscalar susceptibility, for opposite enantiomers, its sign reverses. In above equation 1.38 the polarization is perpendicular to the plane with

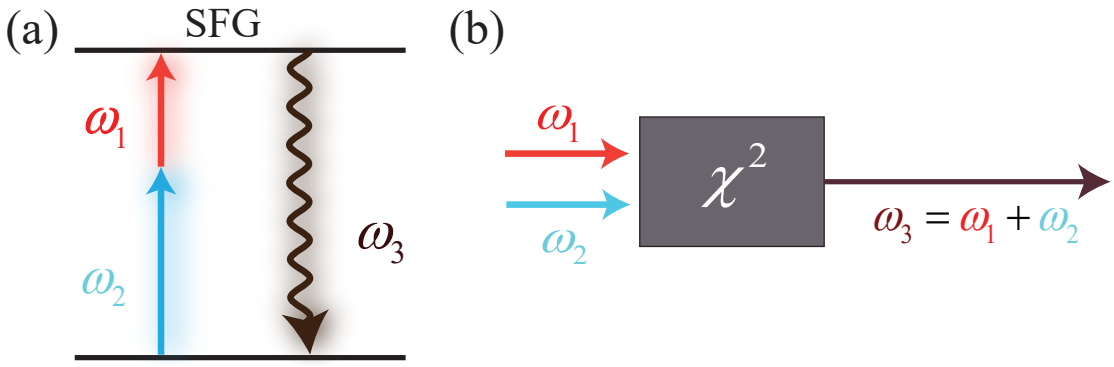

Figure 1.4 Schematic representation of SFG process. (**a**) Energy level diagram showing the absorption of photons at frequencies ω_1 and ω_2 and emission at the sum frequency $\omega_3 = \omega_1 + \omega_2$, (**b**) Schematic diagram of two input fields at ω_1 and ω_2 interacting in a nonlinear medium with χ^2 to produce the SFG output.

unit vectors $\hat{\mathbf{e}}_3 = \hat{\mathbf{e}}_1 \times \hat{\mathbf{e}}_2$ and the output SFG beam is emitted along the direction with phase matching condition $\mathbf{k}_3 = \mathbf{k}_1 + \mathbf{k}_2$.

As SFG is produced from the electric–dipole interactions, so a NL signal can be produced with SFG even at lower intensity lasers, but with high resolution in femtoseconds [65]. If we consider SFG in a randomly oriented chiral molecule of two color noncollinear fields at frequencies ω and 2ω, the total electric field can be written as below

$$\mathbf{E}(\mathbf{r},t) = \mathrm{Re}\Big\{\mathbf{E}_{\omega}^{(1)}\, e^{-i\omega t + i\mathbf{k}_1\cdot\mathbf{r}} + \mathbf{E}_{\omega}^{(2)}\, e^{-i\omega t + i\mathbf{k}_2\cdot\mathbf{r}} + \mathbf{E}_{2\omega}^{(2)}\, e^{-2i\omega t - i\phi_{2\omega} + 2i\mathbf{k}_2\cdot\mathbf{r}}\Big\}, \tag{1.39}$$

where the field components $\mathbf{E}_{\omega}^{(1)}$ and $\mathbf{E}_{\omega}^{(2)}$ are cross-polarized within the plane of propagation, $\mathbf{E}_{2\omega}^{(2)}$ is polarized perpendicular to that plane, and $\phi_{2\omega}$ is the two-color phase delay. For this chiral field, there are two electric-dipole pathways that lead to radiation at the third harmonic 3ω. One chiral SFG signal is produced with frequency $\omega + 2\omega \rightarrow 3\omega$ and polarization $\mathbf{P}_{\mathrm{SFG}}^{(2)}(3\omega) \propto \chi_{\chi}^{(2)}(3\omega;\omega,2\omega)\,\mathbf{E}(\omega)\mathbf{E}(2\omega)$, which have equal amplitudes and opposite phases for the two enantiomers. Also an achiral Third-Harmonic Generation (THG) signal is produced with frequency $\omega+\omega+\omega \rightarrow 3\omega$ and polarization $\mathbf{P}_{\mathrm{THG}}^{(3)}(3\omega) \propto \chi_{\mathrm{ach}}^{(3)}(3\omega;\omega,\omega,\omega)\,\mathbf{E}(\omega)^3$, which is identical for the two enantiomers $\mathbf{P}_{\mathrm{THG}}^{(3),\mathrm{L}} = \mathbf{P}_{\mathrm{THG}}^{(3),\mathrm{R}}$.

In a proper noncollinear geometry, THG has the same phase matching condition as chiral SFG. So the polarization at 3ω can be written as

$$\mathbf{P}^{\mathrm{L}}_{\mathrm{tot}}(3\omega) = \mathbf{P}^{(3)}_{\mathrm{THG}}(3\omega) + \mathbf{P}^{(2)}_{\mathrm{SFG}}(3\omega), \tag{1.40a}$$

$$\mathbf{P}^{\mathrm{R}}_{\mathrm{tot}}(3\omega) = \mathbf{P}^{(3)}_{\mathrm{THG}}(3\omega) - \mathbf{P}^{(2)}_{\mathrm{SFG}}(3\omega), \tag{1.40b}$$

where the far field intensities are expressed as $I^{\mathrm{L/R}}(3\omega) \propto \left|\mathbf{P}^{\mathrm{L/R}}_{\mathrm{tot}}(3\omega)\right|^2$. Because only the chiral SFG contribution changes sign, the interference term $2\,\mathrm{Re}[\mathbf{P}^{(2)}_{\mathrm{SFG}}(3\omega)\cdot \mathbf{P}^{(3)*}_{\mathrm{THG}}(3\omega)]$ is strongly enantiosensitive. By adjusting the relative amplitude of the 2ω field and the two-color phase $\phi_{2\omega}$, the interference can be controlled from constructive for one enantiomer to destructive for the other.

1.8.2 Second Harmonic Generation CD

SHG is a second-order nonlinear optical process in which two photons of the fundamental field at frequency ω are absorbed to produce a single photon at double the frequency 2ω [18].

The SHG field transmission intensity depends on SHG conversion efficiency, which includes the second-order susceptibility tensor $\boldsymbol{\chi}^{(2)}$, the incidence angle of radiation, and the properties of the sample. As discussed in the previous section 1.8.1, the second-order susceptibility tensor $\chi^{(2)}$ vanishes in centrosymmetric media, but in the case of surfaces, SHG perpendicular to the surface is symmetry-allowed. The second-order susceptibility tensor $\chi^{(2)}$ is made of achiral and chiral tensor elements. The achiral elements are electric quadrupole and magnetic dipole, but electric dipole is forbidden.

SHG, combined with CD, can measure chirality by producing different second-harmonic signals for RCP and LCP radiation. The anisotropy factor g [66] of SHG-CD can be defined by the difference of the second harmonic produced by left I^{LCP} and right I^{RCP} circularly polarized intensity, respectively, by normalizing

over their average as below:

$$g = 2\,\frac{\Delta I}{I^{(\mathrm{RCP})} + I^{(\mathrm{LCP})}}, \tag{1.41}$$

where $\Delta I = I^{(\mathrm{LCP})} - I^{(\mathrm{RCP})}$, and it is worth mentioning that SHG-CD is more sensitive [67] than linear chiroptical spectroscopy; also, SHG-CD, with the arrangement of transition dipole moments, depends on molecular orientation.

Also, it is reported in [68] that MoS_2 with SHG is very useful for integrated photonics and nonlinear optical devices. By fabricating for different chiralities and by studying their SHG performances, which is explained by the superposition theory of the second harmonic field, depending on certain chirality and diameter, SHG intensity can be greatly enhanced and used as a simple, nondestructive probe of the handedness of the nanoscrolls.

1.8.3 Optical Kerr effect

The third term associated with χ^3 in Eq. 1.35 is responsible for the optical Kerr effect, where the refractive index of the medium is modulated by the incident field intensity. In the presence of an χ^3 medium exhibits an intensity-dependent refractive index see Fig. 1.5 as below:

$$n = n_0 + n_2 I \tag{1.42}$$

where $n_2 = 3\chi^3/4n_0^2\varepsilon_0 c$ is the is the Kerr coefficient [69], n_0 is the linear refractive index and I is intensity of the incident fields. Self-focusing of light in some material is produced by this intensity-dependent refractive index, which is referred to as the Kerr effect [70].

Using the Kerr nonlinearity, various NL interactions can be explored, including self-phase modulation, self-focusing, and NL refraction. Additionally, we can

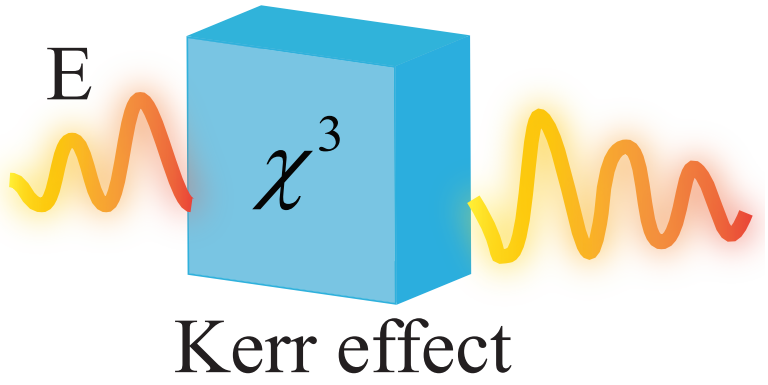

Figure 1.5 Schematic diagram of intensity-dependent refractive index by strong electric field intensity $I(\mathbf{E})$ through third-order nonlinear susceptibility χ^3 in an optical medium.

explore transient grating or self-diffraction using third-order Kerr nonlinear interaction. If we consider Transverse Electric (TE) and Transverse Magnetic (TM) waves incident on a glass surface, we can use the Kerr nonlinear interaction in a chiral medium with a bi-anisotropic dispersion relation as below:

$$\begin{aligned}\mathbf{D}(\mathbf{r},t) &= \varepsilon_0 \left[\varepsilon(\omega_0)\,\mathbf{E}(\mathbf{r},t) - i\,\mu_0 c\,\kappa(\omega_0)\,\mathbf{H}(\mathbf{r},t)\right] \\ &\quad + \varepsilon_0 \chi_3(\omega_0)\left[\mathbf{E}(\mathbf{r},t)\cdot\mathbf{E}(\mathbf{r},t)\right]\mathbf{E}(\mathbf{r},t), \\ \mathbf{B}(\mathbf{r},t) &= \mu_0\left[\frac{i\,\kappa(\omega_0)}{\mu_0 c}\,\mathbf{E}(\mathbf{r},t) + \mu(\omega_0)\,\mathbf{H}(\mathbf{r},t)\right].\end{aligned} \tag{1.43}$$

A standard transient grating forms when pump fields with the same polarization interfere, creating a modulation in the medium's refractive index. But in case of using orthogonal polarization in an achiral medium, TE and TM polarization will remain as TE and TM after interaction because a standard Kerr medium does not change the polarization state due to perpendicular incident fields; therefore, no cross-polarization effects occur, and standard transient grating formation is not possible with orthogonally polarized pump fields in an achiral medium. But a chiral medium has the ability to rotate the plane of polarization, which is why, by exploring Kerr nonlinear interaction in a chiral medium, it is possible to form

a transient grating or self-diffraction in the presence of two orthogonally polarized pump fields.

Hence, we can study the intensity-dependent refractive index in an optically active substance, and, using the Kerr NL interaction, the transient grating signal will be stronger than the linear chiroptical signal, so we can measure chirality at low concentrations.

1.8.4 Pump–probe nonlinear CD

Pump–probe spectroscopy is another NL optical technique used to study ultrafast carrier dynamics in a various range of materials, from semiconductors to molecular chromophores [18, 71]. A strong pump pulse prepares the system in a nonequilibrium excited state, while a weaker probe pulse investigates the optical response at a proper time delay. The weaker beam is often referred to as the probe or signal field, and the stronger beam as the pump or control field. By observing the pump-induced changes in probe transmission or absorption as a function of delay, one can study ultrafast NL optical phenomena such as EIT, LWI, transient gratings and Kerr effects.

To study nonlinear CD, we consider a chiral sample irradiated by a pump (P) and a signal (S) monochromatic field with vacuum wavelengths $\lambda_{\mathrm{P,S}}$. The total electric and magnetic induction fields are $\mathbf{E}_{\mathrm{T}}(t) = \mathbf{E}_{\mathrm{P}}(t) + \mathbf{E}_{\mathrm{S}}(t)$ and $\mathbf{B}_{\mathrm{T}}(t) = \mathbf{B}_{\mathrm{P}}(t) + \mathbf{B}_{\mathrm{S}}(t)$ where the individual pump and signal components are written as

$$\mathbf{E}_{\mathrm{P,S}}(t) = \mathrm{Re}\left[\mathbf{E}_0^{\mathrm{P,S}}\, e^{-i\omega_{\mathrm{P,S}}t}\right], \qquad \mathbf{B}_{\mathrm{P,S}}(t) = \mathrm{Re}\left[\mathbf{B}_0^{\mathrm{P,S}}\, e^{-i\omega_{\mathrm{P,S}}t}\right]. \tag{1.44}$$

Here $\mathbf{E}_0^{\mathrm{P,S}}$ and $\mathbf{B}_0^{\mathrm{P,S}}$ are complex vector field amplitudes at the molecule, $\omega_{\mathrm{P,S}} = 2\pi c/\lambda_{\mathrm{P,S}}$ are the angular frequencies of the pump and signal, and c is the speed of light in vacuum.

We can model this by using time-dependent density functional theory and

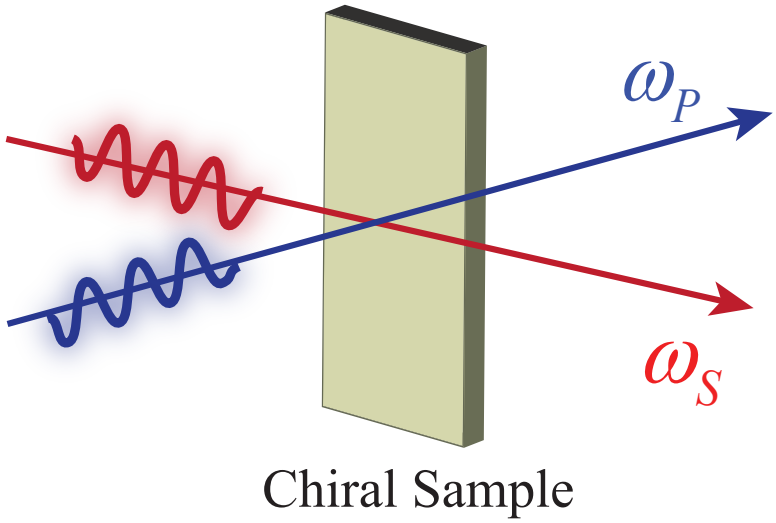

Figure 1.6 Schematic of the chiral pump-probe configuration, indicating the pump ω_P and signal ω_S beams interacting with the chiral sample.

using the chiroptical theorem in terms of the signal-field energy dissipation rate, $dU_{\rm S}/dt = \langle \int_\tau \mathbf{J}_{\rm S} \cdot \mathbf{E}_{\rm S}\, d\tau \rangle_{T_{\rm S}}$, the pump-induced nonlinear signal absorption cross section can be calculated as below:

$$\sigma_{\rm NL} = (1/I_{\rm S})(dU_{\rm S}/dt) \tag{1.45}$$

where $I_{\rm S} = (1/2)\epsilon_0 c|\mathbf{E}_0^{\rm S}|^2$ is the intensity of the impinging signal, energy dissipation rate.

By calculating $\sigma_{\rm NL}$ for LCP and RCP pump-induced signals, and comparing with the linear absorption cross section by putting the intensity of the pump field to zero, one obtains the pump-induced enhanced CD signal that is the intensity-dependent contribution to the differential absorption of LCP and RCP light in the chiral sample. From the enhancement factor, pump–probe spectroscopy in the NL EIT regime describes how much the CD is amplified by the pump, by which we can measure chirality and its polarization dependence. In Chapter 3, we present an enhanced chiroptical sensing approach by EIT and LWI in chiral molecules.

1.9 Nanophotonic environment for chiral sensing

At the subwavelength scale, nanophotonic platforms can enhance chirality. As molecular CD is weak because the molecular structures are comparable with the wavelength of light used for sensing. Additionally, Ultraviolet (UV) light is absorbed by chiral molecules; that is why it is more difficult to measure UV optics than the visible light range. So, to enhance weak CD signals, the nanomaterial environment can be used. Also, it shows strong CD because of localized surface plasmon, where the free electrons in the structure oscillate coherently with the external electromagnetic field, which occurs, in fact, in the visible or Infrared (IR) range. Therefore, a nanophotonic environment can produce a large chiroptical signal at resonance with the transition energy of the chiral molecule. We will discuss different nanophotonic platforms for sensing chirality.

1.9.1 Chiral sensing using differential absorption

We can measure the absorbance of the chiral molecule for different CP excitations, as below:

$$\Delta A(\lambda) = A^{(\mathrm{RCP})}(\lambda) - A^{(\mathrm{LCP})}(\lambda), \tag{1.46}$$

where $A^{(\mathrm{RCP})}(\lambda)$ and $A^{(\mathrm{LCP})}(\lambda)$ denote the absorbance of RCP and LCP of light, the corresponding transmission coefficient for the considered chiral medium of thickness d is given by

$$T^{(\mathrm{RCP})}(\lambda) = \frac{I^{(\mathrm{RCP})}(d)}{I_0}, T^{(\mathrm{LCP})}(\lambda) = \frac{I^{(\mathrm{LCP})}(d)}{I_0}, \tag{1.47}$$

where I_0 is the incident intensity.

For the chiral material, the transmittance and absorptance are different de-

pending on the two CP though the reflectance remains the same. For the chiral nanostructure, of course, we can measure CD in the same way as the chiral isolated molecules. But CD spectra of chiral nanophotonic structures are generated by the combined molecular and optical responses of the nanostructure. However, the chiral nanostructures exhibit complex interactions between molecular and optical resonances.

1.9.1.1 Chiral sensing in the near field or superchiral field

Optical chirality for a monochromatic electromagnetic field can be defined as

$$C \equiv \frac{\varepsilon_0}{2}\,\mathbf{E}\cdot\nabla\times\mathbf{E} + \frac{1}{2\mu_0}\,\mathbf{B}\cdot\nabla\times\mathbf{B} = -\frac{\omega}{2c^2}\,\mathrm{Im}(\mathbf{E}^*\cdot\mathbf{H}) \tag{1.48}$$

where $\mathbf{E}$ and $\mathbf{H}$ are the electric and magnetic fields, ε_0 and μ_0 are the permittivity and permeability of free space, ω is the angular frequency, and c is the speed of light in vacuum. For generating a large chiral density C, both the electric and magnetic fields should be parallel components; they should have a nonzero phase difference, and the field should be a high-intensity field.

In free space the optical chirality for CP excitation, the optical chirality C_{CPL} can be written as:

$$C_{\mathrm{CPL}} = \pm\frac{\varepsilon_0\omega}{2c}\,E_0^2 \tag{1.49}$$

The superchiral field is generated when regions satisfies $|C| > |C_{\mathrm{CPL}}|$. The absorption rates of LCP and RCP excitation by a chiral molecule can be written as

$$A^{(\mathrm{LCP,RCP})} = \omega\Big[\alpha''\,|\mathbf{E}|^2 \pm G''\,C\Big], \tag{1.50}$$

where α_{ee} is the imaginary part of the electric–dipole polarisability and G'' is the imaginary part of the mixed electric–magnetic (chiral) polarisability. The CD

signal is then

$$\Delta A = A_L - A_R = 2\omega\, G''\, C, \tag{1.51}$$

If we increase the local optical chirality C, it enhances the chiral absorption difference for different CP excitations.

1.9.1.2 Plasmonic chiral sensing

Plasmonic nanostructures are a promising area for nanophotonic devices used to enhance chirality. Due to the large electric polarizability, localized surface plasmon resonances interact with the electric field of light [72] intensely. But because they lack magnetic polarizability, they cannot interact with the magnetic field and thus fail to enhance chiral density. But these structures still produce enhanced optical chirality through superchiral field generation, which supports the circulation of electric charges and induces magnetic near-field enhancement [73].

In the case of chiral plasmonic nanostructures for containing the intrinsic chirality, there is an advantage for these materials to enhance chirality measurements. But in some cases, the RCP and LCP respond simultaneously, and their effects cancel, resulting in weak chiral response. But it has already been reported in [74], where they propose a way to overcome these challenges by fabricating a 3D chiral material in which the fundamental modes of the plasmonic nanostructure contain electric and magnetic dipoles that are not perpendicular to each other; they are parallel. Thus, this structure can enhance chirality by containing multiple helices. If we change the chirality, the relative direction of the field vectors will change. For example, in the case of fabricating 3D structures that suffer from some making procedure mistakes, like they have large size, they need a long processing time, the group [75] reported making an asymmetric bent split-ring resonator based on ion-beam matter interaction. CD enhancement increases with increasing bending angle of the split ring. Also, numerical analysis confirms the enhancement in

CD resulting from the cross-coupling of the parallel electric and magnetic fields. Also, the 2D planar chiral nanostructures [76], which are known as pseudochiral nanostructures, exhibit chiral response and interact with circularly polarized light at normal incidence. There is no need for 3D characteristics; these structures exhibit chirality through symmetry-breaking.

In the case of achiral plasmonic nanostructures, which have the advantage of no background CD, though they lack magnetic-field enhancement [77], they can still produce superchiral near fields. It is reported in [78], where they propose a double-spiral ring resonator by generating superchiral near fields, which provides strong evidence for an achiral plasmonic nanostructure. Another achiral nanostructure was reported in [79], where gold nanorods, which are essentially patterned nanostructures, produce large CD enhancements, playing important roles in the generation of optical chiral responses. Also, optical chirality was reported in a symmetric plasmonic nanostructure, produced by considering three gold nanodisks [80], in which optical chirality arises from near-field interference between plasmon modes.

1.9.1.3 Dielectric nanostructures

Dielectric nanostructures are also another promising nanophotonic platform. Though the electric field enhancement is somewhat weaker than that of plasmonic nanostructures, high-index dielectric materials can support electric and magnetic resonances for chirality sensing. Also, dielectric nanostructures exhibit low optical losses [81] which can help protect materials from heating. Additionally, another drawback of dielectric nanostructures is that the electric and magnetic Mie resonances at similar frequencies occur in the IR region, which is why they failed to enhance CD in the UV region.

For achiral dielectric nanostructures, it was proposed to use achiral Si nanodisk material for sensing chirality. The Kerker-like condition [82] was introduced, in

which the electric and magnetic fields are spatially overlapped and transmitted at that frequency. Chiral density is enhanced up to 138-fold with a phase lag of 90 degrees between the electric and magnetic dipoles around the disk. Also, it was found [83] that off-axis LP excitation produces strong superchiral localized hotspots within dimer gaps, which, when using CP excitation to generate a superchiral field, is unnecessary. The optical chiral field was enhanced 300-fold, as reported. Also, Ge-treated [84] resonators successfully generated a strong superchiral field via strong electric and magnetic fields via Mie resonance.

In the case of dielectric chiral metamaterials such as all-dielectric waveguides and polarimeters, it was shown that chiral crossed-bowtie Si nanoantennas can create strong hotspots of enhancement C in the bowtie junction [85], which is promising for enhancing CD signals from nearby molecules. Later, chiral-slotted Si nanodisks were introduced, in which a parallelogram-shaped slot supports electric and magnetic resonances that hybridize with those of the disk, thereby increasing C. Although experimental demonstrations of fully dielectric chiral metasurfaces for sensing remain limited, dielectric material mixing with plasmonic nanostructures will make a promising nanophotonic platform, as we'll see in the next section.

1.9.1.4 Plasmonic and Dielectric hybrid nanostructures

Plasmonic nanostructures exhibit a strong enhancement in the electric field but a weak response in the magnetic field. So, a hybrid platform provides strong electric and magnetic responses and can achieve a strong near-field, producing strong optical chirality. To achieve maximum optical chiral density, the electric and magnetic fields must be parallel with a $\pi/2$ phase difference. It is reported in Ref. [86] that a hybrid composition of gold metallic and silicon dielectric particles with a high refractive index exhibits electric and magnetic resonance, maintaining the $\pi/2$ phase difference in the electric and magnetic field components. Also, Ref [87] reports chiral density enhancement using a combination

of hexagonal Au-GaAs nanowires. Another enhancement was reported in Ref. [88]for the hybrid nanostructure composed of graphene ribbons and Si rods on Cu substrate. Additionally, plasmonic hybrid nanostructures show a strong response to magnetic particles [89, 90, 91]. These nanostructures were applied to enhance the vibration CD for chiral molecules. It was reported in Ref. [92] that a cavity-coupled achiral material was presented for sensing surface-enhanced vibration CD. Therefore, a hybrid nanostructure is definitely a promising platform for measuring chirality.

1.9.2 Plasmon-coupled CD

Chiral-molecule sensing is also possible using PCCD. The dipolar and multipolar Coulomb interaction between a chiral molecule and an achiral plasmonic structure generates the CD here [93]. The PCCD mechanism proposes a theoretical explanation based on the quasistatic approximation and a general equation for the CD of a chiral molecule and a metallic nanophotonic structure. Some mechanisms by which PCCD can be generated were proposed, including near-field dipole-dipole interactions and far-field electromagnetic coupling. For low-concentration analytes, PCCD can be understood in terms of near-field interactions [94, 95, 96, 97], in which the electromagnetic field enhances CD at a nearby achiral plasmonic nanophotonic structure. Using far-field electromagnetic coupling [98], molecular chirality can be measured for an achiral plasmonic substrate, where this CD is obtained from the differential refractive index of CP excitation.

Theoretically, PCCD can be explained by the equation that describes the interaction of the plasmonic field enhancement matrix and the electric magnetic

transition dipole element, as given below:

$$\begin{aligned} \mathrm{CD}_{\mathrm{mol+pl}} &= \mathrm{CD}_{\mathrm{mol}} + \mathrm{CD}_{\mathrm{pl}}, \\ \mathrm{CD}_{\mathrm{mol}} &\propto E_0^2 \frac{\gamma_0}{\left|\hbar\omega - \hbar\omega_0 + i\Gamma_0\right|^2} \mathrm{Im}\left[\left(\hat{\mathbf{P}}\cdot\boldsymbol{d}_{12}\right)\cdot\boldsymbol{m}_{12}\right]. \end{aligned} \tag{1.52}$$

where $\mathrm{CD}_{\mathrm{mol+pl}}$ is the total CD of the molecule–plasmon complex, $\mathrm{CD}_{\mathrm{mol}}$ is the intrinsic molecular CD, and $\mathrm{CD}_{\mathrm{pl}}$ is the PCCD contribution. The molecular term becomes maximum near the molecular resonance frequency ω_0. Here, E_0 is the local electric-field amplitude, γ_0 and Γ_0 describe the damping and broadening of the molecular transition, and $\boldsymbol{d}_{12}$ and $\boldsymbol{m}_{12}$ are the electric and magnetic transition dipole moments. The imaginary part of $\left(\hat{\mathbf{P}}\cdot\boldsymbol{d}_{12}\right)\cdot\boldsymbol{m}_{12}$ gives the chiral interference between the electric and magnetic transition channels, which is the origin of the molecular CD.

PCCD has been reported experimentally and theoretically for various nanostructures containing chiral molecules, including proteins [99, 100, 101], DNA [102, 103], and peptides [104, 105]. Therefore, this mechanism has been explored by various researchers for achiral plasmonic nanostructures with different compositions and optical parameters.

1.9.3 Surface plasmon polariton

A SPP is described as an electromagnetic wave that is locally confined to a metal-dielectric interface propagating along a planar interface [106, 107, 108]. This wave is generated by the coupling of free-electron oscillations in the metal with the optical field, which enhances the electromagnetic field intensity near the metal surface. SPPs are generally well-suited to the dielectric properties of the media used in biosensor devices [109, 110, 111]. Also, the field enhancement can be used in single nanoparticles for detecting the spectroscopy of a single molecule. The propagation of SPP waves has a limitation of ohmic loss in the metal. So,

a special material composition and geometric configuration are needed to excite surface modes. A metal–dielectric interface with permittivities of metal $\epsilon_m(\omega)$ and permittivities of dielectric $\epsilon_d(\omega)$ supports SPPs when $\mathrm{Re}[\epsilon_m(\omega)] < 0$ and $\mathrm{Re}[\epsilon_d(\omega)] > 0$.

Theoretically, we can explain the propagation of SPP along the x direction through the dispersion relation [112] as follows:

$$k_x^{\mathrm{SPP}}(\omega) = \frac{\omega}{c}\sqrt{\frac{\epsilon_m(\omega)\,\epsilon_d(\omega)}{\epsilon_m(\omega)+\epsilon_d(\omega)}}\,. \tag{1.53}$$

Here, k_x^{SPP} denotes the in-plane wave vector of the SPP mode, ω is the angular frequency, and c is the speed of light in vacuum. For any given ω and neglecting losses, the SPP wave vector is larger than that of a plane wave in free space, $k_x^{\mathrm{SPP}} > k_{\mathrm{light}}$, where $k_{\mathrm{light}} = \omega/c$. Consequently, the SPP wavelength $\lambda_{\mathrm{SPP}} = 2\pi/k_x^{\mathrm{SPP}}$ is smaller than the free-space wavelength.

SPP excitation is highly sensitive to variations in the dielectric environment. The strong light-molecule interaction can be achieved through unique features of SPP, such as subwavelength confinement, and through strongly enhanced local fields [113, 114, 115]. That can significantly enhance the CD signal for chiral drug solutions.

1.9.4 Chiral sensing using differential emission

The nanophotonic structure can modify the characteristics of the photon emitter. For photon emission, the cavity modification is known as the Purcell effect. For a resonant chiral nanostructure, the Purcell effect becomes effective. In free space, there will be no imbalance in SE between two CPs. However, when using a chiral nanostructure, we can study CP-SE manipulation, which we discuss in detail in Chapter 4.

1.10 Concluding remarks

In this introductory chapter, basic concepts of optical propagation in chiral media are briefly described. After introducing chirality, the basic linear spectroscopy methods, CD and ORD, for measuring chirality were described.

For the inherently weak chiroptical signal, which failed to measure chirality at low concentration, the chiroptical sensitivity can be further amplified by ultrafast enantioselective NL optical techniques and a nanophotonic environment that overcomes these challenges and enhances the sensitivity of chirality measurements to achieve advanced levels of detection and selectivity, as discussed in the following sections of this chapter.

Chapter 2

Electromagnetic interaction with chiral molecules

"Symmetry principles illuminate the profound laws of physics; the breaking of symmetry often unlocks the precious secrets of nature."

— Adapted from L. D. Landau and E. M. Lifshitz, *Quantum Mechanics*

The history of chirality and optics was well introduced before in the 19th century with the introduction of polarization and chirality, which is well known and already discussed in Chapter 1. In this chapter, we discuss the theoretical modeling of chiral light-matter interaction. Basically, the response of the optical medium to the external radiation depends on how the charged particles of an atom, like electrons or protons, are bound to the nucleus and interact with external electromagnetic radiation. The microscopic response of any material is defined by an ensemble of atoms and molecules with discrete electronic, vibrational, and rotational levels, which primarily determine light–matter interactions. Also, the strength of this chiral light-matter interaction depends on the internal energy of the spectrum, the intensity of the incident field, and the degree of resonance be-

tween the driving frequency and the material eigenmodes. Therefore, we apply electromagnetic radiation to study the response of an optical medium, though this is difficult because a material has many degrees of freedom, making it impossible to solve many dynamical equations. Therefore, we introduce some systematic approximations, such as a weak-coupling regime and slowly varying envelopes, to study chiral light-matter interactions. By using these approximations, we treat the optical field as a classical quasi-monochromatic wave that interacts with the molecular system quantum mechanically, allowing us to work with only those degrees of freedom in resonance with the incident field. The remaining degrees of freedom, which are off-resonant and weakly coupled to the system, are included through damping and dephasing rates that describe the energy flow into a thermal bath composed of these degrees of freedom. Consequently, we introduce the density-matrix description, in which relaxation is included through the Lindblad operator. We observe that electronic transitions dominate in the ultraviolet and visible regions, vibrational transitions give rise to infrared frequencies, and rotational modes contribute in the far-infrared or microwave regions of electromagnetic radiation. In the case of indirect resonance, two-photon processes such as Raman and Brillouin scattering [116] provide a different idea of how the higher-order light-matter interaction excites low-frequency modes.

In this chapter, we present a theoretical model of chiral light-matter interactions by first applying a semiclassical approach, treating electromagnetic radiation classically and the chiral molecule quantum mechanically through the density-matrix formalism. This theoretical framework is very useful in describing how electromagnetic radiation interacts with the dipole moments of chiral molecules.

2.1 Fundamental concepts

This chapter develops such a framework, beginning with a multilevel description of the molecular Hamiltonian and using perturbations introduced by the electric and magnetic components of externally applied radiation. A complete treatment of coherence, population dynamics, and dissipative processes—all important for characterizing the time-dependent response—is made possible by the subsequent introduction of the density matrix formalism. Moreover, rotational averaging is performed across molecular orientations to relate microscopic molecular properties to the macroscopic response. This statistical approach is important given the random orientations in most experimental samples and is performed via Euler angle rotations of the molecular dipole moments into the laboratory frame. With this approach, we obtain essential quantities, including electric and magnetic polarizabilities and their cross-coupling terms, which together characterize the medium's chiral and bianisotropic properties. These parameters completely describe how electromagnetic waves propagate through chiral materials when they are included in modified Maxwell's equations and constitutive relations. Computational methods that combine electronic and vibrational states provide a clear understanding of how chirality changes the optical properties of reparixin in aqueous solution, which is a chemically and biologically essential compound. A comprehensive understanding will become clear upon examining the detailed discussion of the theoretical approach presented in the following sections of this chapter.

2.2 Multilevel chiroptical interaction

We consider the interaction of a chiral sample with electromagnetic radiation. We start our analysis with the unperturbed Hamiltonian of the system with some discrete molecular energy levels.

The unperturbed Hamiltonian for the system can be defined in the N-level approximation as follows:

$$\hat{\mathcal{H}}_0 = \sum_{n=1}^{N} \hbar\omega_n |n\rangle\langle n|, \tag{2.1}$$

where $|n\rangle$ represents the eigenstates of the molecule with the corresponding energy value $\hbar\omega_n$.

Now we can find an approximate solution to the system by applying a perturbation in the form of external radiation driving the molecule. Therefore, we write the general form of the Hamiltonian as below:

$$\hat{\mathcal{H}}(t) = \sum_{n=1}^{N} \hbar\omega_n |n\rangle\langle n| - \hat{V}, \tag{2.2}$$

where $\hat{V}$ denotes the perturbation due to external electromagnetic radiation.

Also, we consider the electric and magnetic dipolar approximation, and the interaction energy $\hat{\mathcal{H}}_{\text{INT}}$ of the system can be expressed in the following way:

$$\hat{\mathcal{H}}_{\text{INT}} = -\mathbf{E}(t) \cdot \hat{\mathbf{d}} - \mathbf{B}(t) \cdot \hat{\mathbf{m}}. \tag{2.3}$$

Now, the total Hamiltonian of the system, see Fig. 2.1 can be defined as below:

$$\hat{\mathcal{H}}(t) = \sum_{n=1}^{N} \hbar\omega_n \, |n\rangle \, \langle n| - \mathbf{E}(t) \cdot \hat{\mathbf{d}} - \mathbf{B}(t) \cdot \hat{\mathbf{m}}. \tag{2.4}$$

The expression above includes both intrinsic molecular energy and electric/-magnetic dipolar interaction, which describe how the external field perturbs the system.

In the expression of the total Hamiltonian, see Eq. 2.4, these two terms $\mathbf{E}(t)\cdot\hat{\mathbf{d}}$ and $\mathbf{B}(t)\cdot\hat{\mathbf{m}}$ arise because we assume that the system is excited by monochromatic

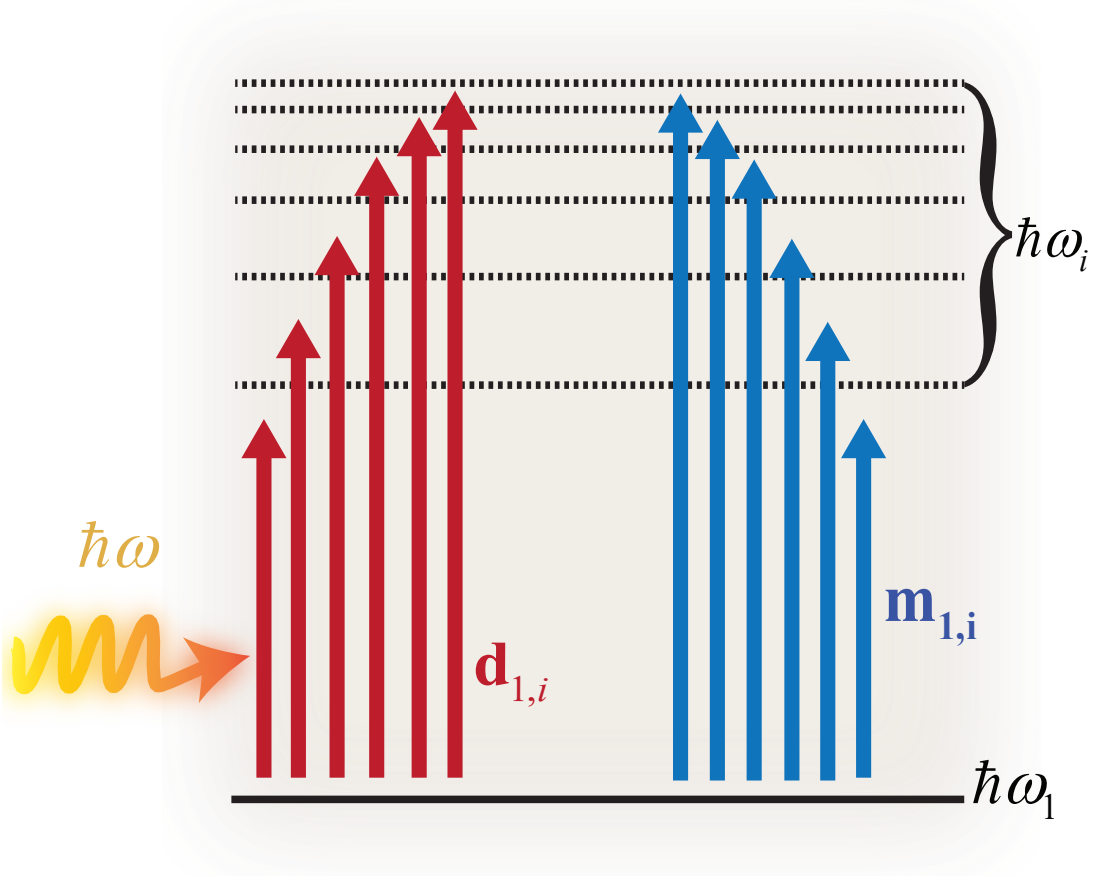

Figure 2.1 Schematic illustration of a multilevel molecular system with discrete energy states $|n\rangle$, when illuminated by a monochromatic field with energy $\hbar\omega$. However, owing to chirality, the molecule possesses non-orthogonal transition electric $\mathbf{d}_{1,i}$ and magnetic $\mathbf{m}_{1,i}$ dipole moments through which chiroptical interaction occurs, and there is a transition from initial states with energy $\hbar\omega_1$ to different excited states with energy $\hbar\omega_i$.

external radiation fields consisting of electric and magnetic fields as follows:

$$\mathbf{E}(t) = \mathrm{Re}\left[\mathbf{E}_0 e^{-i\omega t}\right], \tag{2.5a}$$

$$\mathbf{B}(t) = \mathrm{Re}\left[\mathbf{B}_0 e^{-i\omega t}\right], \tag{2.5b}$$

where ω is the angular frequency and $\lambda = (2\pi c)/\omega$ denotes the carrier vacuum wavelength, where c is the speed of light in vacuum.

Also, the electric transition dipole moment operator $\hat{\mathbf{d}}$ and magnetic transition

dipole moment operator $\hat{\mathbf{m}}$ in dyadic representation are given by

$$\hat{\mathbf{d}} = \sum_{n,m=1}^{N} \mathbf{d}_{n,m} \, |n\rangle\langle m|, \tag{2.6a}$$

$$\hat{\mathbf{m}} = \sum_{n,m=1}^{N} \mathbf{m}_{n,m} \, |n\rangle\langle m|, \tag{2.6b}$$

where the matrix elements $\mathbf{d}_{n,m}$ and $\mathbf{m}_{n,m}$ denote the electric and the magnetic transition dipole moments, respectively, between the states, which can be defined as below:

$$\mathbf{d}_{n,m} = \langle n|\hat{\mathbf{d}}|m\rangle, \tag{2.7a}$$

$$\mathbf{m}_{n,m} = \langle n|\hat{\mathbf{m}}|m\rangle, \tag{2.7b}$$

where $|n\rangle\langle m|$ denotes the projection operator, which defines whether $n = m$, that is, the diagonal component represents the static electric dipole moment within a single state $|n\rangle$, while if $n \neq m$, that is, the off-diagonal component represents the transition between the molecular states $|n\rangle$ and $|m\rangle$.

2.2.1 Density matrix formalism

The density matrix approach is used to define how the quantum state of the system changes with time when it interacts with external electromagnetic radiation. The density matrix describes not only the pure quantum states but also the mixed states [18, 117].

At any time, the state of a system can be described by a density matrix, usually denoted as

$$\hat{\rho} = \sum_{n,m=1}^{N} \rho_{n,m} |n\rangle\langle m|, \tag{2.8}$$

where $|n\rangle$ and $\langle m|$ represent the discrete quantum states of the molecule, and the coefficients $\rho_{n,m}$ denote the populations (n=m) and coherence ($n \neq m$) between

these states.

2.2.2 Lindblad operator approach

A physical system will interact with its environment because any real physical system cannot be perfectly isolated. To treat such interaction of a quantum system with the environment, the mathematical technique using the Lindblad operator [118] is very important to describe the non-unitary processes from dissipation to decoherence [119] for the quantum system.

In the case of our considered system, the temporal evolution of the density matrix is governed by the Liouville-von Neumann equation, which can be written in the following way:

$$\frac{d\hat{\rho}}{dt} = \frac{1}{i\hbar}\left[\hat{\mathcal{H}}(t), \hat{\rho}\right] + \hat{L}(\hat{\rho}), \tag{2.9}$$

where the coherent quantum evolution of the system is included through the total Hamiltonian term $\hat{H}(t)$, also, $\hat{L}(\hat{\rho})$ is the Lindblad operator that accounts for the dissipative processes, such as non-radiative recombination to the ground state or decoherence in the system, which can be expressed mathematically as follows:

$$\hat{L}(\hat{\rho}) = \sum_{n=2}^{N} \frac{\gamma_n}{2}\Big[2\rho_{n,n}|1\rangle\langle 1| - |n\rangle\langle n|\hat{\rho} - \hat{\rho}|n\rangle\langle n|, \tag{2.10}$$

where, γ_n denotes the decoherence of the system.

Therefore, using the density matrix formalism and the Lindblad operator approach, from Eq. 2.9 and Eq. 2.10, the system can be described by the general form of the equation:

$$\frac{d\hat{\rho}}{dt} = \frac{1}{i\hbar}\left[\hat{\mathcal{H}}(t), \hat{\rho}\right] + \sum_{n=2}^{N} \frac{\gamma_n}{2}\Big[2\rho_{n,n}|1\rangle\langle 1| - |n\rangle\langle n|\hat{\rho} - \hat{\rho}|n\rangle\langle n|. \tag{2.11}$$

Above Eq. 2.11 defines how the system evolves in time as a result of these interactions. Now, the general form of the density matrix equation provides the

following:

$$\begin{aligned}\dot{\rho}_{i,j} &= -i\left(\omega_i - \omega_j\right)\rho_{i,j} \\ &+ \frac{1}{i\hbar}\sum_{n=1}^{N}\Big\{\rho_{i,n}\Big[\mathbf{E}(t)\cdot\mathbf{d}_{n,j} + \mathbf{B}(t)\cdot\mathbf{m}_{n,j}\Big] - \rho_{n,j}\Big[\mathbf{E}(t)\cdot\mathbf{d}_{i,n} + \mathbf{B}(t)\cdot\mathbf{m}_{i,n}\Big]\Big\} \\ &+ \Big\{\sum_{n=2}^{N}\gamma_n\rho_{n,n}\Big\}\delta_{i,1}\delta_{j,1} - \frac{\gamma_i}{2}\rho_{i,j}\left(1-\delta_{i,1}\right) - \frac{\gamma_j}{2}\rho_{i,j}\left(1-\delta_{j,1}\right). \end{aligned} \tag{2.12}$$

In the above Eq. 2.12, $\delta_{i,j}$ the Kronecker delta is defined as $\delta_{i,j} = 1$ if $i = j$, and 0 if $i \neq j$. The dynamics of the system are described through the above equation for the temporal evolution of each matrix element, $\rho_{i,j}$, where the indices i and j refer to the quantum states that represent how population (diagonal terms) and coherences (off-diagonal terms) vary with time due to external fields.

For the diagonal terms, we obtain from the above equation

$$\begin{aligned}\dot{\rho}_{1,1} &= \frac{2}{\hbar}\sum_{n=2}^{N}\mathrm{Im}\left\{\rho_{1,n}\left[\mathbf{E}(t)\cdot\mathbf{d}_{n,1} + \mathbf{B}(t)\cdot\mathbf{m}_{n,1}\right]\right\} + \sum_{n=2}^{N}\gamma_n\rho_{n,n}, \\ \dot{\rho}_{i,i} &= -\frac{2}{\hbar}\mathrm{Im}\left\{\rho_{1,i}\left[\mathbf{E}(t)\cdot\mathbf{d}_{i,1} + \mathbf{B}(t)\cdot\mathbf{m}_{i,1}\right]\right\} - \gamma_i\rho_{i,i}, \quad (i \neq 1). \end{aligned} \tag{2.13}$$

These equations describe how the populations of the molecular ground and excited states are influenced by coherent interactions with the ground and excited states mediated by external fields, as well as by spontaneous non-radiative decay, represented by γ_i.

For the off-diagonal elements, we get

$$\begin{aligned}\dot{\rho}_{1,i} &= \Big[i(\omega_i - \omega_1) - \frac{\gamma_i}{2}\Big]\rho_{1,i} + \frac{i}{\hbar}\Big\{\left[\mathbf{E}(t)\cdot\mathbf{d}_{1,i} + \mathbf{B}(t)\cdot\mathbf{m}_{1,i}\right]\left(\rho_{i,i} - \rho_{1,1}\right) \\ &+ \left[\mathbf{E}(t)\cdot\left(\mathbf{d}_{1,1} - \mathbf{d}_{i,i}\right) + \mathbf{B}(t)\cdot\left(\mathbf{m}_{1,1} - \mathbf{m}_{i,i}\right)\right]\rho_{1,i}\Big\} \\ &- \frac{i}{\hbar}\sum_{\substack{n=2 \\ n\neq i}}^{N}\rho_{1,n}\left[\mathbf{E}(t)\cdot\mathbf{d}_{n,i} + \mathbf{B}(t)\cdot\mathbf{m}_{n,i}\right], \quad (i \neq 1). \end{aligned} \tag{2.14}$$

The above equation 2.14 describes how the quantum mechanical superpositions between the ground and excited states change with time under an external driving field and population differences with the other coherences.

In general, Eq. 2.12 is a bit difficult to solve analytically. Using perturbation theory [18], we introduce a small parameter λ that varies from 0 to 1, which characterizes the strength of the perturbations, with $\lambda = 1$ corresponding to the physical situation.

Applying perturbation series expansion, we can write the density matrix elements $\rho_{i,j}$ in the following form:

$$\rho_{i,j} = \rho_{i,j}^{(0)} + \lambda\rho_{i,j}^{(1)} + \lambda^2\rho_{i,j}^{(2)}. \tag{2.15}$$

Since this solution should hold for any value of the perturbation density parameter λ, each term in the expansion must independently satisfy the resultant equation at each order in λ. Thus, multiscale expansion up to the second order provides

$$\rho_{1,i}^{(i\neq 1)} = \rho_{1i}^{(1)} + \rho_{1i}^{(2)} \tag{2.16a}$$

$$\rho_{11} = 1 + \rho_{11}^{(2)} \tag{2.16b}$$

$$\rho_{ii} = \rho_{ii}^{(2)} \tag{2.16c}$$

. This expansion helps us to calculate the linear response (at first order) of the system upon excitation by electromagnetic radiation.

2.2.3 Linear response

We apply the perturbation solution to the density-matrix equation of motion and calculate the linear response of the molecular system. By solving the density

matrix at first order, we obtain:

$$\rho_{1i}^{(1)}(t) = -\frac{i\left(\mathbf{d}_{1,i}\cdot\mathbf{E}_0^* + \mathbf{m}_{1,i}\cdot\mathbf{B}_0^*\right)}{\hbar\left\{\gamma_i + 2i\Big[\omega - (\omega_i - \omega_1)\Big]\right\}}e^{i\omega t} - \frac{i\left(\mathbf{d}_{1,i}\cdot\mathbf{E}_0 + \mathbf{m}_{1,i}\cdot\mathbf{B}_0\right)}{\hbar\left\{\gamma_i - 2i\Big[\omega + (\omega_i - \omega_1)\Big]\right\}}e^{-i\omega t},$$
$$\equiv \mathrm{P}_{1i}^{(+\omega)}e^{i\omega t} + \mathrm{P}_{1i}^{(-\omega)}e^{-i\omega t}. \tag{2.17}$$

The above equation describes the first-order coherence term in the molecular system in the quantum states $|1\rangle$ and $|i\rangle$ interacting with an external electromagnetic field. It defines the linear quantum response of the molecule to the electric and magnetic field at frequency ω, and $\mathrm{P}_{1i}^{(\pm\omega)}$ denotes the amplitudes corresponding to $\pm\omega$.

2.2.4 Induced dipole moment

The expectation values of electric and magnetic dipole moment operators can be derived from density matrix formalism discussed in the previous section 2.2.1. Therefore, we calculate the expectation values of induced electric $\mathbf{d}(t)$ and magnetic $\mathbf{m}(t)$ dipole moment operators as follows:

$$\mathbf{d}(t) = \mathrm{Tr}\{\hat{\mathbf{d}}\hat{\rho}\} = \sum_{i,j=1}^{N}\rho_{i,j}\mathbf{d}_{j,i}$$
$$= \rho_{1,1}\mathbf{d}_{1,1} + \sum_{i=2}^{N}\rho_{i,i}\mathbf{d}_{i,i} + 2\sum_{i=2}^{N}\mathrm{Re}\left[\rho_{i,1}\mathbf{d}_{1,i}\right], \tag{2.18a}$$
$$\mathbf{m}(t) = \mathrm{Tr}\{\hat{\mathbf{m}}\hat{\rho}\} = \sum_{i,j=1}^{N}\rho_{i,j}\mathbf{m}_{j,i}$$
$$= \rho_{1,1}\mathbf{m}_{1,1} + \sum_{i=2}^{N}\rho_{i,i}\mathbf{m}_{i,i} + 2\sum_{i=2}^{N}\mathrm{Re}\left[\rho_{i,1}\mathbf{m}_{1,i}\right]. \tag{2.18b}$$

Upon substituting the obtained first-order solution described in Eq. 2.17 for the density matrix coherence see Eq.2.16, we simplify this expression Eq.2.18 to:

$$\begin{aligned}\mathbf{d}(t) &= \mathbf{d}_{1,1} + \sum_{i=2}^{N} \mathrm{Re}\left\{\left[2\mathbf{d}_{1,i}\left[P_{1i}^{(+\omega)}\right]^{*} + 2\mathbf{d}_{i,1}P_{1i}^{(-\omega)}\right]e^{-i\omega t}\right\},\\ \mathbf{m}(t) &= \mathbf{m}_{1,1} + \sum_{i=2}^{N} \mathrm{Re}\left\{\left[2\mathbf{m}_{1,i}\left[P_{1i}^{(+\omega)}\right]^{*} + 2\mathbf{m}_{i,1}P_{1i}^{(-\omega)}\right]e^{-i\omega t}\right\}.\end{aligned} \tag{2.19}$$

These equations clearly indicate how external electromagnetic fields induce oscillating electric and magnetic dipole moments within the chiral molecule. Specifically, it explains contributions from the static electric $\mathbf{d}_{1,1}$ and magnetic $\mathbf{m}_{1,1}$ dipole moments and electric $\mathbf{d}_{1,i}$ and magnetic $\mathbf{m}_{1,i}$ transition dipole moments between the states.

2.2.5 The evaluation of molecular orientation

Generally, in various branches of nonlinear optical spectroscopy, such as CD or pump-probe experiments, the molecular sample is randomly oriented, so we average over all possible molecular orientations to relate microscopic molecular properties to macroscopic ones. We can sum the response over all molecules and divide by the total number of molecules, a process known as ensemble averaging [120]. Simultaneously, we can average the response of a single molecule over all orientations, a process known as rotational averaging. We consider two coordinate systems, described in Fig. 2.2, namely the molecular frame with axes x, y, and z, and the laboratory frame with axes X, Y, and Z, for calculating the rotational averaging. Here, Euler's angles are used to define the orientation of the molecule in the laboratory frame, where ϕ is the polar angle between the molecular z-axis and the laboratory Z-axis, and θ is the azimuthal angle between the projection of the molecular z-axis onto the XY plane and the X-axis and χ denotes the rotation around the molecular z-axis.

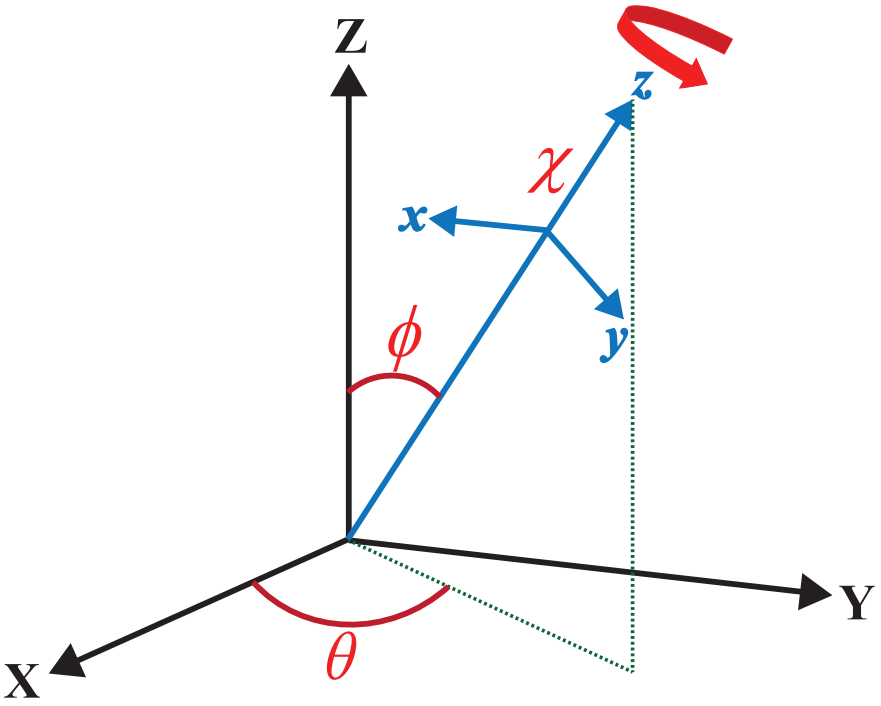

Figure 2.2 Schematic of the molecular frame with axes x, y, and z and laboratory frame with axes X, Y, and Z with Euler's angle θ, ϕ, and χ.

In the macroscopic system, we can calculate the dependence of the molecular response by averaging over molecular orientations. We use the direction cosine matrix, also known as the rotation matrix [121], which transforms vector and tensor quantities from the molecular frame to the laboratory frame, to perform this averaging.

The matrix is defined as below:

$$\hat{R}(\phi,\theta,\chi) = \begin{bmatrix} \cos\phi\cos\theta\cos\chi - \sin\phi\sin\chi & -\cos\phi\cos\theta\sin\chi - \sin\phi\cos\chi & \cos\phi\sin\theta \\ \sin\phi\cos\theta\cos\chi + \cos\phi\sin\chi & -\sin\phi\cos\theta\sin\chi + \cos\phi\cos\chi & \sin\phi\sin\theta \\ -\sin\theta\cos\chi & \sin\theta\sin\chi & \cos\theta \end{bmatrix}. \tag{2.20}$$

Using $\hat{R}(\phi,\theta,\chi)$, it is possible to compute transformed induced electric and magnetic dipole moments from the molecular frame to the laboratory frame.

Therefore, to define the orientation-dependent response of a function $f(\theta,\phi,\chi)$, to calculate the total response, we need to take the average of this function as given

below:

$$\langle f \rangle = \frac{1}{8\pi^2} \int_0^{2\pi} d\phi \int_0^{\pi} \sin\theta \, d\theta \int_0^{2\pi} d\chi \, f(\theta, \phi, \chi). \tag{2.21}$$

This way, we can easily calculate the average electric or magnetic dipole moment after rotational averaging.

2.2.6 Dipole Moment Transformation via Euler Rotations

To calculate the average electric/magnetic dipole moment in the laboratory frame, we take an orientational average for the randomly oriented molecules over all directions. First, the individual dipole moment rotates using the direction cosine matrix, denoted as $\hat{R}(\phi, \theta, \chi)$, where (ϕ, θ, χ) are the Euler angles that describe the molecular orientation. Upon molecular rotation, the diagonal and transition electric and magnetic dipole moments rotate as:

$$\begin{cases} \mathbf{D}_{1,i}(\alpha,\beta,\gamma) = \hat{R}(\phi,\theta,\chi)\mathbf{d}_{1,i} \\ \mathbf{D}_{n,i}(\alpha,\beta,\gamma) = \hat{R}(\phi,\theta,\chi)\mathbf{d}_{n,i} \\ \mathbf{D}_{i,i}(\alpha,\beta,\gamma) = \hat{R}(\phi,\theta,\chi)\mathbf{d}_{i,i} \end{cases} \quad \begin{cases} \mathbf{M}_{1,i}(\alpha,\beta,\gamma) = \hat{R}(\phi,\theta,\chi)\mathbf{m}_{1,i} \\ \mathbf{M}_{n,i}(\alpha,\beta,\gamma) = \hat{R}(\phi,\theta,\chi)\mathbf{m}_{n,i} \\ \mathbf{M}_{i,i}(\alpha,\beta,\gamma) = \hat{R}(\phi,\theta,\chi)\mathbf{m}_{i,i} \end{cases} . \tag{2.22}$$

Now these transformed dipole vectors can be averaged over all molecular orientations; therefore, from the above equation Eq 2.22, the average electric/magnetic dipole moment using rotational averaging integrals can be expressed as follows:

$$\begin{aligned} \langle \mathbf{d}(t) \rangle &= \frac{1}{8\pi^2} \int_0^{2\pi} d\phi \int_0^{\pi} d\theta \int_0^{2\pi} d\chi \sin\theta \, \mathbf{D}(t), \\ \langle \mathbf{m}(t) \rangle &= \frac{1}{8\pi^2} \int_0^{2\pi} d\phi \int_0^{\pi} d\theta \int_0^{2\pi} d\chi \sin\theta \, \mathbf{M}(t). \end{aligned} \tag{2.23}$$

2.2.7 Microscopic response

We consider the linear dependence of the applied electromagnetic field; therefore, the above dipolar responses are simplified as follows.

$$\begin{aligned}\langle \mathbf{d}(t)\rangle &= \mathrm{Re}\left\{[\mathrm{A_{d,E}}\mathbf{E}_0 + \mathrm{A_{d,B}}\mathbf{B}_0]\, e^{-i\omega t}\right\},\\ \langle \mathbf{m}(t)\rangle &= \mathrm{Re}\left\{[\mathrm{A_{m,B}}\mathbf{B}_0 + \mathrm{A_{m,E}}\mathbf{E}_0]\, e^{-i\omega t}\right\}.\end{aligned} \tag{2.24}$$

Here, $\mathrm{A_{d,E}}$ and $\mathrm{A_{m,B}}$ are the linear isotropic electric and magnetic polarizabilities, respectively, and $\mathrm{A_{d,B}}$ and $\mathrm{A_{m,E}}$ denote the linear isotropic mixing polarizabilities that characterize the chiral bi-anisotropic response of the molecule. The linear polarizability coefficients in the microscopic system [122] are defined in terms of the transition dipole matrix element as:

$$\mathrm{A_{d,E}} = \sum_{n=2}^{N} \frac{|\mathbf{d}_{1,n}|^2}{3\hbar}\left\{\frac{1}{[\omega + (\omega_n - \omega_1) + i\gamma_n/2]} - \frac{1}{[\omega - (\omega_n - \omega_1) + i\gamma_n/2]}\right\}, \tag{2.25a}$$

$$\mathrm{A_{d,B}} = \sum_{n=2}^{N} \frac{(\mathbf{d}_{1,n}\cdot\mathbf{m}_{1,n})}{3\hbar}\left\{\frac{1}{[\omega + (\omega_n - \omega_1) + i\gamma_n/2]} + \frac{1}{[\omega - (\omega_n - \omega_1) + i\gamma_n/2]}\right\}, \tag{2.25b}$$

$$\mathrm{A_{m,B}} = \sum_{n=2}^{N} \frac{|\mathbf{m}_{1,n}|^2}{3\hbar}\left\{\frac{1}{[\omega + (\omega_n - \omega_1) + i\gamma_n/2]} - \frac{1}{[\omega - (\omega_n - \omega_1) + i\gamma_n/2]}\right\}, \tag{2.25c}$$

$$\mathrm{A_{m,E}} = \sum_{n=2}^{N} \frac{2\,(\mathbf{d}_{1,n}\cdot\mathbf{m}_{1,n})}{3\hbar}\left\{\frac{-2[\omega + (\omega_n - \omega_1) + i\gamma_n}{4[\omega + (\omega_n - \omega_1)]^2 + \gamma_n^2} + \frac{-2[\omega - (\omega_n - \omega_1) + i\gamma_n}{4[\omega - (\omega_n - \omega_1)]^2 + \gamma_n^2}\right\}, \tag{2.25d}$$

where $(\omega_n - \omega_1)$ is the transition frequency between the excited state and ground state, n and 1, respectively, and γ_n denotes the corresponding decay rate. We observe from the above equations that electric polarizability $\mathrm{A_{d,E}}$ is dependent on

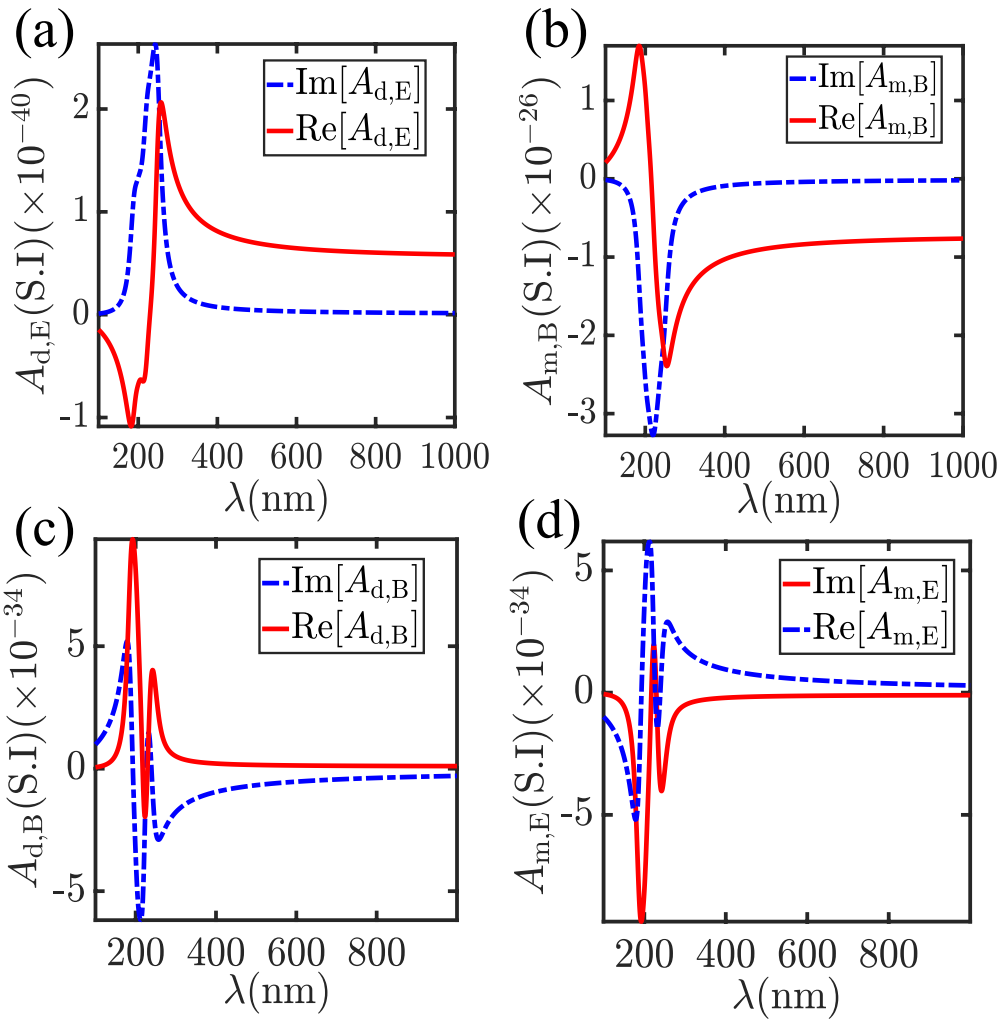

Figure 2.3 Dependence of real (shown in red solid curve) and imaginary (shown in blue dashed curve) parts of (**a**) linear isotropic electric polarizability $\mathrm{A_{d,E}}$, (**b**) magnetic polarizability $\mathrm{A_{m,B}}$, and (**c**, **d**) linear isotropic mixing polarizabilities $\mathrm{A_{m,B}}, \mathrm{A_{m,B}}$ on vacuum wavelength λ. These results are obtained for aqueous solutions of pure S Reparixin enantiomer at fixed molecular number density $n_{\mathrm{mol}} = 10^{-2}\mathrm{nm}^{-3}$.

the electric transition dipole moment, and magnetic polarizability $\mathrm{A_{m,B}}$ is determined by the magnetic transition dipole moment and the mixed linear isotropic polarizabilities $\mathrm{A_{d,B}}$, $\mathrm{A_{m,E}}$ depend on the scalar product $\mathbf{d}_{1,n} \cdot \mathbf{m}_{1,n}$, which defines the chirality of the considered molecular transition.

Additionally, as the equation 2.25d can be simplified to $\mathrm{A_{m,E}} = -\mathrm{A_{d,B}}$ therefore, this reciprocity is important for studying the enantioselective behavior of the chiral molecule, which is discussed in the following section 2.2.13 of this chapter.

To study the bi-anisotropic response of the considered chiral molecule, we illustrate the dependence of the microscopic response in terms of polarizabilities on vacuum wavelength λ, see Fig. 2.3). We observe a strong wavelength dependence of the polarizabilities, with the polarizabilities highest at resonance. In the Fig. 2.3(a), the linear isotropic polarizability for the electric part $A_{d,E}$ shows a dispersive real part (shown in the solid red curve) and a peak imaginary part (shown in the dashed blue curve) in resonance, which denotes the absorption and dispersion for the microscopic response of the aqueous solution of reparixin. The Fig. 2.3(b) shows the corresponding behavior of magnetic polarizability, which is smaller than $A_{d,E}$ as expected.

Also, the mixed polarizabilities are most important, as they determine the magneto-electrocoupling of the chiral response. As shown in the Fig.2.3(c,d), where the electric and magnetic transition dipole moments interfere effectively, we observe an intense chiral response. Also, we observe that the reciprocity is satisfied in the Fig. 2.3(c,d) as they show opposite natures. Next, we study the macroscopic response.

2.2.8 Macroscopic response

The macroscopic chiral molecular response can be determined by averaging the full microscopic polarizability over time. By individually averaging the electric/-magnetic dipole moments, the dipolar contribution should be multiplied by the molecular number density to obtain the polarization $\mathbf{P}(\mathbf{r}, t)$) and magnetization $\mathbf{M}(\mathbf{r}, t)$ fields.

The macroscopic polarization and magnetization in the limit of low molecular density can be expressed by averaging microscopic electric and magnetic dipole

moments as:

$$\begin{aligned}\mathbf{P}(\mathbf{r},t) &= \varepsilon_0 \mathrm{Re}\left\{\left[\frac{n_{mol}A_{dE}}{\varepsilon_0}\mathbf{E}_0 + \frac{n_{mol}A_{dB}}{\varepsilon_0}\mathbf{B}_0\right]e^{-i\omega t}\right\} \\ &= \mathrm{Re}\{\mathbf{P}_0(\mathbf{r})e^{-i\omega t}\} \qquad (2.26a)\end{aligned}$$

$$\begin{aligned}\mathbf{M}(\mathbf{r},t) &= \mathrm{Re}\left\{n_{mol}\left(A_{mE}\mathbf{E}_0 + A_{mB}\mathbf{B}_0\right)e^{-i\omega t}\right\} \\ &= \mathrm{Re}\{\mathbf{M}_0(\mathbf{r})e^{-i\omega t}\} \qquad (2.26b)\end{aligned}$$

where these time-dependent fields are as mentioned below:

$$\begin{cases}\mathbf{P}_0 = n_{mol}A_{d,E}\mathbf{E}_0 + A_{d,B}\mathbf{B}_0 \\ \mathbf{M}_0 = n_{mol}A_{m,E}\mathbf{E}_0 + A_{m,B}\mathbf{B}_0\end{cases} \qquad (2.27)$$

These polarization and magnetization fields, in turn, produce microscopic charge and current densities as

$$\rho_{\mathrm{P}}(\mathbf{r},t) = -\nabla\cdot\mathbf{P}(\mathbf{r},t), \qquad (2.28a)$$

$$\rho_{\mathrm{M}}(\mathbf{r},t) = 0, \qquad (2.28b)$$

$$\mathbf{J}_{\mathrm{P}}(\mathbf{r},t) = \partial_t\mathbf{P}(\mathbf{r},t), \qquad (2.28c)$$

$$\mathbf{J}_{\mathrm{M}}(\mathbf{r},t) = \nabla\times\mathbf{M}(\mathbf{r},t), \qquad (2.28d)$$

where $\rho_{\mathrm{P}}(\mathbf{r},t)$ and $\rho_{\mathrm{M}}(\mathbf{r},t)$ are the polarization and magnetization charge density respectively, while $\mathbf{J}_{\mathrm{P}}(\mathbf{r},t)$ and $\mathbf{J}_{\mathrm{M}}(\mathbf{r},t)$ are the polarization and magnetization current densities, respectively.

2.2.9 Microscopic Maxwell Equations

Introducing these source terms, we obtain the microscopic Maxwell equations for the monochromatic field with angular frequency ω as described below:

$$\begin{cases} \nabla \cdot \mathbf{E}_0^{(\omega)}(\mathbf{r}) = \dfrac{1}{\varepsilon_0 \varepsilon_{\mathrm{sol}}(\omega)} \rho_P^{(\omega)}(\mathbf{r}) \\ \nabla \cdot \mathbf{B}_0^{(\omega)}(\mathbf{r}) = 0 \\ \nabla \times \mathbf{E}_0^{(\omega)}(\mathbf{r}) = i\omega \mathbf{B}_0^{(\omega)}(\mathbf{r}) \\ \nabla \times \mathbf{B}_0^{(\omega)}(\mathbf{r}) = \mu_0 \mathbf{J}_P^{(\omega)}(\mathbf{r}) + \mu_0 \mathbf{J}_M^{(\omega)}(\mathbf{r}) - \dfrac{i\omega}{c^2} \varepsilon_{\mathrm{sol}}(\omega) \mathbf{E}_0^{(\omega)}(\mathbf{r}) \end{cases} \tag{2.29}$$

where $\varepsilon_{\mathrm{sol}}(\omega)$ is the relative electric permittivity of the chiral medium. The above equations define how they influence the generation of electromagnetic fields in a chiral medium. In the macroscopic environment, these equations can be reformulated.

2.2.10 Macroscopic Maxwell Equations

Using the polarization $\mathbf{P}$ and magnetization $\mathbf{M}$ in the displacement field $\mathbf{D}$ and magnetic field vector $\mathbf{H}$, we calculate the macroscopic formulation.

$$\begin{cases} \nabla \cdot \mathbf{D}_0^{(\omega)}(\mathbf{r}) = 0 \\ \nabla \cdot \mathbf{B}_0^{(\omega)}(\mathbf{r}) = 0 \\ \nabla \times \mathbf{E}_0^{(\omega)}(\mathbf{r}) = i\omega \mathbf{B}_0^{(\omega)}(\mathbf{r}) \\ \nabla \times \mathbf{H}_0^{(\omega)}(\mathbf{r}) = -i\omega \mathbf{D}_0^{(\omega)}(\mathbf{r}) \end{cases} \tag{2.30}$$

This macroscopic formulation is more useful for studying bulk optical properties of chiral molecules.

2.2.11 Constitutive relation

The electromagnetic behavior of the chiral medium is described by constitutive relations, which are given by:

$$\begin{cases} \mathbf{D}_0^{(\omega)}(\mathbf{r}) = \varepsilon_0 \varepsilon_{\mathrm{sol}}(\omega)\mathbf{E}_0^{(\omega)}(\mathbf{r}) + \mathbf{P}_0^{(\omega)}(\mathbf{r}) \\ \mathbf{D}_0^{(\omega)}(\mathbf{r}) = \varepsilon_0 \left[\varepsilon(\omega)\mathbf{E}_0^{(\omega)}(\mathbf{r}) - i\mu_0 c\kappa(\omega)\mathbf{H}_0^{(\omega)}(\mathbf{r})\right] \\ \mathbf{B}_0^{(\omega)}(\mathbf{r}) = \mu_0 \mathbf{H}_0^{(\omega)}(\mathbf{r}) + \mu_0 \mathbf{M}_0^{(\omega)}(\mathbf{r}) \\ \mathbf{B}_0^{(\omega)}(\mathbf{r}) = \mu_0 \left[\frac{i\kappa(\omega)}{\mu_0 c}\mathbf{E}_0^{(\omega)}(\mathbf{r}) + \mu(\omega)\mathbf{H}_0^{(\omega)}(\mathbf{r})\right] \end{cases} \tag{2.31}$$

These equations reflect the bi-anisotropic nature of chiral media, where electric and magnetic fields are connected due to molecular chirality, and we introduce parameters through the constitutive relations.

To describe the response more clearly, the following effective material parameters are introduced:

$$\begin{cases} \epsilon_{\mathrm{r}}(\omega) = \varepsilon_{\mathrm{sol}}(\omega) + \dfrac{n_{\mathrm{mol}} A_{d,E}}{\varepsilon_0} + \dfrac{\mu_0 n_{\mathrm{mol}}^2 A_{m,E} A_{d,B}}{\varepsilon_0 \left(1 - \mu_0 n_{\mathrm{mol}} A_{m,E}\right)} \\ \kappa(\omega) = \dfrac{i n_{\mathrm{mol}} A_{d,B}}{\varepsilon_0 c \left(1 - \mu_0 n_{\mathrm{mol}} A_{m,B}\right)} \\ \mu_{\mathrm{r}}(\omega) = \dfrac{1}{1 - \mu_0 n_{\mathrm{mol}} A_{m,B}} \end{cases} \tag{2.32}$$

Here $\epsilon_{\mathrm{r}}(\omega)$ define the effective permittivity of the chiral medium and $\mu_{\mathrm{r}}(\omega)$ defines the effective permeability and $\kappa(\omega)$ is the chirality parameter, which is responsible for optical activity and circular birefringence.

These quantities define the full linear response of a chiral material and serve as input to wave equations for determining measurable optical phenomena such as optical rotatory dispersion and circular dichroism.

2.2.12 Macroscopic bi-anisotropic response

2.2.12.1 Reparixin in water

To study the interaction of radiation with Reparixin in water [123], we consider computational approaches to find quantum molecular observables (e.g., electric and magnetic moments, ground-state energy, and electronic and vibrational excitation energies), which provide us with an idea of finding the macroscopic bianisotropic response of Reparixin for different molecular conformations in an aqueous solution. Subsequently, we calculated the electric and magnetic transition dipoles and their associated UV/vibrational spectra for aqueous reparixin by taking an ensemble average. First, we consider the solvent interaction through the density matrix formalism. The unperturbed vibronic structure of each enantiomer is expressed by independent electronic/vibrational Hamiltonians as below:

$$\hat{\mathcal{H}}_0^{\mathrm{el}}(k,a) = \sum_{i=1}^{5} \hbar\omega_i(k)|i(k,a)\rangle\langle i(k,a)|, \tag{2.33a}$$

$$\hat{\mathcal{H}}_0^{\mathrm{vib}}(k,a) = \sum_{\nu=0,1} (\nu+1/2)\hbar\omega_\nu|\nu(a)\rangle\langle\nu(a)|, \tag{2.33b}$$

where two enantiomers of Reparixin are labeled with index a = R, S and $\hbar\omega_i(k)$ and $\hbar\omega_\nu(\nu+1/2)$ are the electronic and vibrational energy eigenvalues respectively with eigenstates $|i(k,a)\rangle$ and $|\nu(a)\rangle$.

By solving the density matrix equations perturbatively up to first order, the induced electric $\mathbf{d}_a$ and magnetic $\mathbf{m}_a$ dipole moments are expressed as below:

$$\mathbf{o}_a^{\mathrm{el,vib}} = \sum_{k=1}^{4} p(k)\mathrm{Tr}\left[\hat{\rho}_{k,a}^{\mathrm{el,vib}}\hat{\mathbf{o}}_a^{\mathrm{el,vib}}(k,a)\right], \tag{2.34}$$

where $\mathbf{o} = \mathbf{d}, \mathbf{m}$ denotes the induced electric/magnetic dipole moments, $p(k) = 0.25$ is the statistical weight for each conformation, and $\hat{\rho}_{k,a}^{\mathrm{el,vib}}$ denotes the density matrix for each state. Therefore, by applying the Euler angle rotation averaging,

the resultant isotropic electric, magnetic, and mixing polarizabilities are obtained as follows:

$$\alpha^{(a)}_{\mathrm{e,b,m}}(\omega) = \mathcal{C}^{(vib)}_{\mathrm{e,b,m}}(a)\mathcal{F}^{\mathrm{vib}}(\omega) + \sum_{k=1}^{4} p(k) \sum_{j=2}^{5} \mathcal{C}^{(el)}_{j,\mathrm{e,b,m}}(k,a)\mathcal{F}^{\mathrm{el}}_{j,k}(\omega) \tag{2.35}$$

where

$$\mathcal{C}^{(\mathrm{vib,el})}_{\mathrm{e}} = \frac{1}{3\hbar}\langle|\mathcal{D}^{(\mathrm{vib,el})}_{\mathrm{e}}|^2\rangle, \tag{2.36a}$$

$$\mathcal{C}^{(\mathrm{vib,el})}_{\mathrm{b}} = \frac{1}{3\hbar}\langle|\mathcal{M}^{(\mathrm{vib,el})}_{\mathrm{e}}|^2\rangle, \tag{2.36b}$$

$$\mathcal{C}^{(\mathrm{vib,el})}_{\mathrm{m}} = \frac{i}{3\hbar}\langle \mathrm{Im}\left[\mathcal{D}^{(\mathrm{vib,el})}_{\mathrm{e}} \cdot \mathcal{M}^{(\mathrm{vib,el})}_{\mathrm{e}}\right]\rangle, \tag{2.36c}$$

$$\mathcal{F}^{\mathrm{vib}}(\omega) = \sum_{\sigma=\pm1} \frac{\sigma}{\omega + \sigma\langle\omega_\nu\rangle + i\gamma/2}, \tag{2.36d}$$

$$\mathcal{F}^{\mathrm{el}}_{j,k}(\omega) = \sum_{\sigma=\pm1} \frac{\sigma}{\omega + \sigma\langle\omega_j(k) - \omega_1(k)\rangle + i\gamma^{\mathrm{el}}_j(k)/2}. \tag{2.36e}$$

Here, the notation $\langle(...)\rangle$ denotes the ensemble averaging; additionally, $\mathcal{D}^{\mathrm{vib}} = \mathbf{d}^{01}, \mathcal{D}^{\mathrm{el}}_j = \mathbf{d}^{1j}, \mathcal{M}^{\mathrm{vib}} = \mathbf{m}^{01}, \mathcal{M}^{\mathrm{el}} = \mathbf{m}^{1j}$. The relaxation rate $\gamma_\nu = 0.012$ fs^{-1} is denoted for the $\nu = 0 \to 1$ transition vibrating with energy $\hbar\omega_\nu = 0.218$ eV. The calculated vibrational dipole moduli are $\sqrt{\langle|\mathbf{d}^{01}|^2\rangle}/d_0 = 0.105$, $\sqrt{\langle|\mathbf{m}^{01}|^2\rangle}/m_0 = 0.398$, and the pseudoscalar chiral projection $\mathrm{Im}[\mathbf{d}^{01} \cdot \mathbf{m}^{01}]/(d_0 m_0) = 0.007$. Here, $d_0 = |e|a_0$ is the atomic unit of electric dipole, $m_0 = e\hbar/(2m_e)$ is the Bohr magneton, and $a_0 = \hbar/(m_e c\alpha)$ is the Bohr radius.

In the low molecular density limit, the bi-anisotropic response of reparixin can be expressed by the following constitutive relations:

$$\mathbf{D}(\mathbf{r},t) = \varepsilon_0 \mathrm{Re}\left\{\left[\varepsilon_{\mathrm{r}}(\lambda)\mathbf{E}_0(\mathbf{r}) - i\mu_0 c\kappa(\lambda)\mathbf{H}_0(\mathbf{r})\right] e^{-i\omega t}\right\}, \tag{2.37a}$$

$$\mathbf{B}(\mathbf{r},t) = \mu_0 \mathrm{Re}\left\{\left[\frac{i\kappa(\lambda)}{\mu_0 c}\mathbf{E}_0(\mathbf{r}) + \mu_{\mathrm{r}}(\lambda)\mathbf{H}_0(\mathbf{r})\right] e^{-i\omega t}\right\}, \tag{2.37b}$$

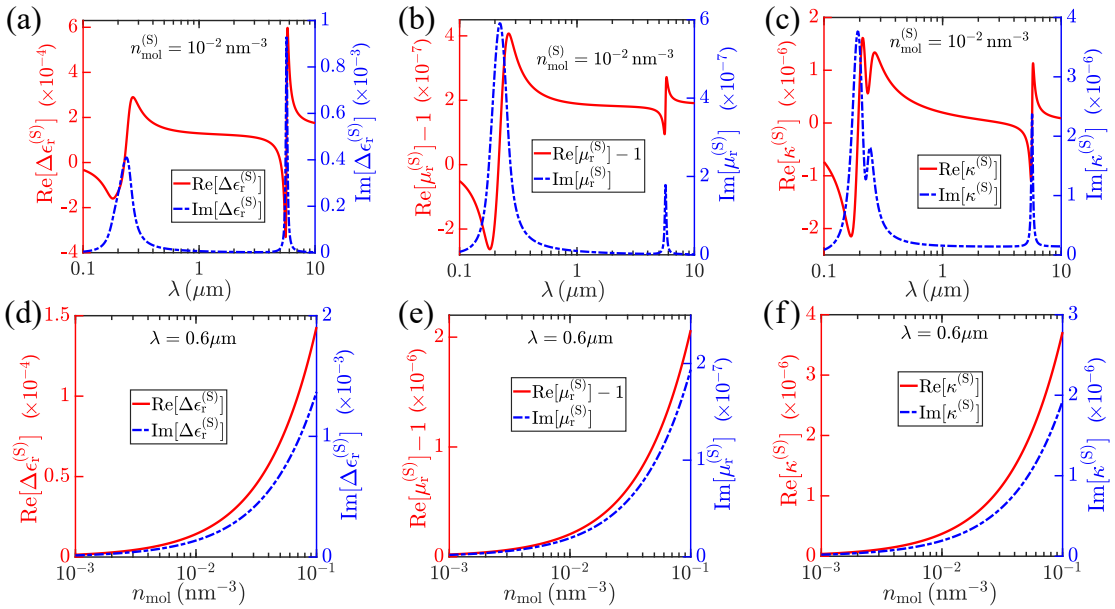

Figure 2.4 $(\mathbf{a}-\mathbf{f})$ Dependencies of the macroscopic bi-anisotropic response of an aqueous solution of pure S-Reparixin enantiomer on $(\mathbf{a}-\mathbf{c})$ vacuum wavelength λ and $(\mathbf{d}-\mathbf{f})$ molecular number density $n_{\rm mol}$ are shown for $(\mathbf{a},\mathbf{d})$ relative dielectric constant correction $\Delta\epsilon_{\rm r}$, $(\mathbf{b},\mathbf{e})$ relative magnetic permeability correction $\mu_{\rm r}-1$, and $(\mathbf{c},\mathbf{f})$ chiral parameter κ. These results are obtained for $(\mathbf{a}-\mathbf{c})$ fixed $n_{\rm mol} = 10^{-2}\,\rm nm^{-3}$ and $(\mathbf{d}-\mathbf{f})$ fixed $\lambda = 0.6\,\mu\rm m$. [*Courtesy of Matteo Venturi.*]

with the effective medium parameters defined as:

$$\varepsilon_{\rm r}(\lambda) = \varepsilon_{\rm H_2O}(\lambda) + \frac{n_{\rm mol}\alpha_{\rm e}(\lambda)}{\varepsilon_0}, \tag{2.38a}$$

$$\mu_{\rm r}(\lambda) = 1 + \mu_0 n_{\rm mol}\alpha_{\rm b}(\lambda), \tag{2.38b}$$

$$\kappa(\lambda) = \frac{i}{\varepsilon_0 c}\sum_{a=R,S} n_{\rm mol}^{(a)}\alpha_{\rm m}^{(a)}(\lambda). \tag{2.38c}$$

These relations illustrate that Reparixin in water shows a chiral bi-anisotropic response, which is described by relative dielectric permittivity $\varepsilon_{\rm r}(\lambda)$, relative dielectric permeability $\mu_{\rm r}(\lambda)$, and the chiral parameter $\kappa(\lambda)$ directly measures CD. Also, $\alpha_{\rm m}^{(R)} = -\alpha_{\rm m}^{(S)}$, hence optical activity vanishes for a racemic mixture ($n_{\rm mol}^{(R)} = n_{\rm mol}^{(S)}$).

To the overall chiroptical response of Reparixin, we observe both the contribution of the electronic transition $\approx 250nm$ and the vibrational transition around $\approx 6\mu m$. At lower concentrations, as illustrated in Fig. 2.4 (a-d), the real part

of the relative permittivity $\mathrm{Re}[\varepsilon_r(\lambda)]$ has a negligible effect on the refractive index dispersion, as it is influenced mainly by the water refractive index at these dilute levels. Simultaneously, the imaginary part $\mathrm{Im}[\varepsilon_r(\lambda)]$, which describes the light absorption, is not influenced by chirality but dominated by water absorption. The magnetic permeability $\mu_r(\lambda)$, which does not depend on the molecules' handedness, comes from the magnetic response of reparixin. The effects of absorption and dispersion are minimal, as seen in Fig. 2.4(b-e). Also, we observe the dependence of the chiral parameter $\kappa(\lambda)$ on wavelength, see Fig. 2.4(c), and molecular concentration, see Fig. 2.4(e), where we see the chiral parameter reaches its peak values close to the electronic and vibrational resonance wavelengths of Reparixin. The real part $\kappa(\lambda)$ determines the ORD, and the imaginary part of $\kappa(\lambda)$ denotes the CD.

2.2.12.2 Ladarixin in water

To study the interaction of radiation with Ladarixin in water [124], we present the following Figure: 2.5 shows the optical constants for aqueous Ladarixin, where we observe the dependence of some quantities on the vacuum wavelength λ and the molecular concentration n_{mol} for pure R-Ladarixin. From these results, we see that the chiroptical response of Ladarixin arises from electronic resonance near $\lambda \simeq 236$ nm and a vibrational resonance around $\lambda \simeq 5.4\ \mu$m. In the low concentration, it is dominated by the real part of the relative dielectric permittivity $\epsilon_{\mathrm{H_2O}}(\lambda)$ of water; also, water shows sufficient absorption, which is clear from the imaginary part of the permittivity of water ($\mathrm{Im}[\epsilon_{\mathrm{H_2O}}]$) dominates over the imaginary part of $\epsilon_{\mathrm{cs}}(\lambda)$.

Specifically, Fig. 2.5(a-c) display the wavelength dependence at a fixed molecular number density of $n_{\mathrm{mol}}^{(\mathrm{R})} = n_{\mathrm{mol}} = 10^{-2}\ \mathrm{nm}^{-3}$, illustrating 2.5(a) the change in relative permittivity $\Delta\epsilon_{\mathrm{cs}}(\lambda) = \epsilon_{\mathrm{cs}}(\lambda) - \epsilon_{\mathrm{H_2O}}(\lambda)$ compared to water, (b) the magnetic permeability difference $\mu_{\mathrm{cs}}(\lambda) - 1$, and (c) the chiral parameter, $\kappa_{\mathrm{cs}}(\lambda)$

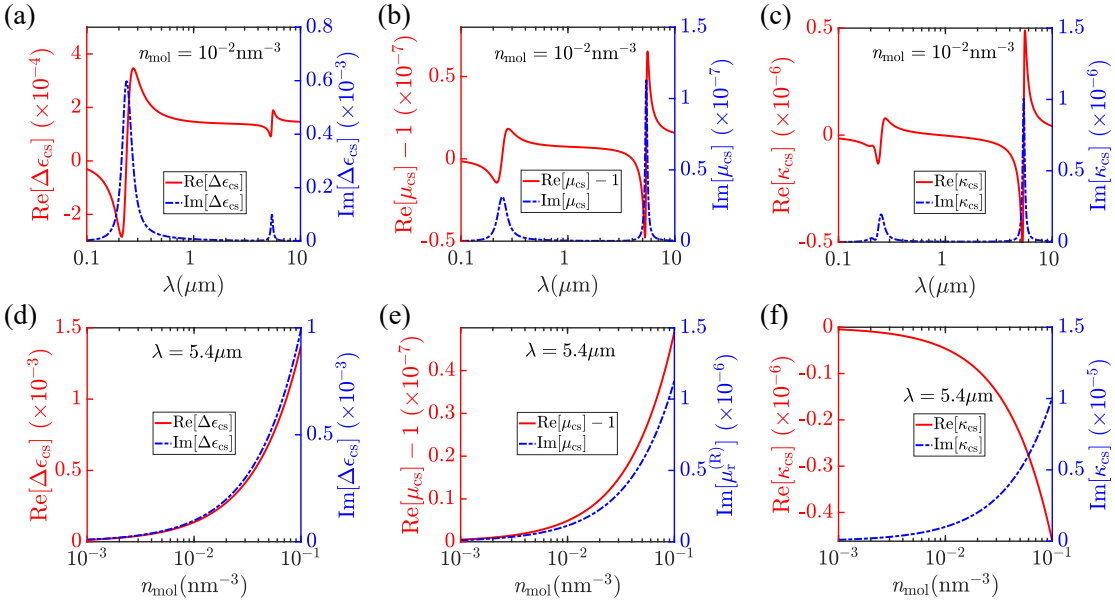

Figure 2.5 $(\mathbf{a}-\mathbf{f})$ Dependencies of the macroscopic bi-anisotropic response of an aqueous solution of pure R-Ladarixin enantiomer on $(\mathbf{a}-\mathbf{c})$ vacuum wavelength λ and $(\mathbf{d}-\mathbf{f})$ molecular number density n_{mol} are shown for $(\mathbf{a},\mathbf{d})$ relative dielectric constant correction $\Delta\epsilon_{\mathrm{r}}$, $(\mathbf{b},\mathbf{e})$ relative magnetic permeability correction $\mu_{\mathrm{r}}-1$, and $(\mathbf{c},\mathbf{f})$ chiral parameter κ. These results are obtained for fixed $n_{\mathrm{mol}} = 10^{-2}\,\mathrm{nm}^{-3}$ and $\lambda = 5.4\,\mu\mathrm{m}$. [*Courtesy of Raju Adhikary.*]

and the panels 2.5(d-f) determine how these same properties vary with molecular concentration $n_{\mathrm{mol}}^{(\mathrm{R})} = n_{\mathrm{mol}}$ at a fixed wavelength of $\lambda = 5.4\ \mu\mathrm{m}$.

From the results, we see that Ladarixin's chiroptical response arises from two main sources: an electronic resonance near 236 nm and a vibrational resonance around 5.4 μm. Due to the low concentrations considered here (between roughly 10^{-3} nm^{-3} and 10^{-3} nm^{-2}), the relative permittivity is dominated by water's real part, $\epsilon_{\mathrm{H_2O}}(\lambda)$, taking contribution from the molecules. Also, water's strong absorption in the mid-infrared region (as shown from the imaginary part of its permittivity (see $\mathrm{Im}[\epsilon_{\mathrm{H_2O}}]$), in Fig. 2.5(b) means that the imaginary component of $\epsilon_{\mathrm{cs}}(\lambda)$ is also mostly dependent on the solvent rather than Ladarixin. For the magnetic response, the relative permeability μ_{cs} appears from Ladarixin's molecular magnetism, but it is not sensitive to chirality. Its influence on the overall refractive index is minimal, as seen in Figs. 2.5(b,e). Importantly, at the vi-

brational resonance wavelength near 5.4 μm, Ladarixin shows a clear Vibrational Circular Dichroism (VCD), explained by the imaginary part of the chiral parameter $\kappa_{cs}(\lambda)$. In the following section, we will discuss the enantioselective properties of the considered chiral sample.

2.2.13 Enantioselective properties

In chiral molecules, the mirror-image forms of asymmetry are known as R and S enantiomers. They cannot be superimposed on each other with rotation or translation operations. The enantioselective properties determine different physical properties for the separate enantiomers due to differences in their electric and magnetic dipole moments.

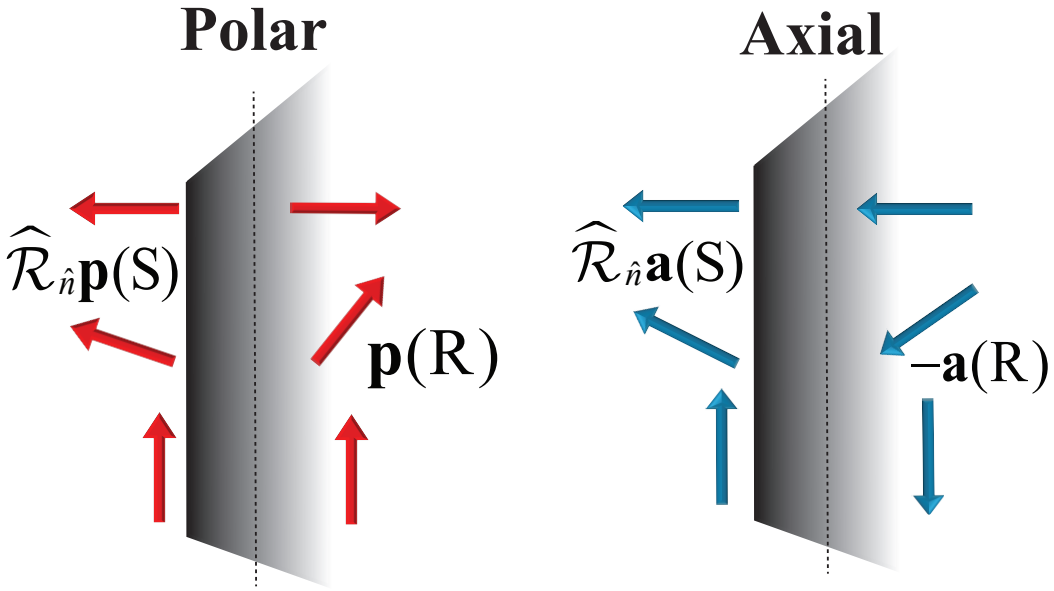

Figure 2.6 Schematic diagram of a (**a**) polar vector $\mathbf{p}(R)$ and an (**b**) axial vector $\mathbf{a}(R)$ transformed by the reflection operator $\mathbf{R}_{\hat{n}} = \mathbb{I} - 2\hat{\mathbf{n}}\hat{\mathbf{n}}$ where is $\hat{\mathbf{n}}$ the unit vector perpendicular to the mirror plane.

2.2.13.1 Dipole moment transformation

We introduce a reflection operator as follows:

$$\mathbf{R}_{\hat{n}} = \mathbb{I} - 2\hat{\mathbf{n}}\hat{\mathbf{n}} \tag{2.39}$$

where there is no reflection symmetry with the plane perpendicular to the unit vector $\hat{\mathbf{n}}$. Here $\mathbb{I}$ is the identity operator, which $\hat{\mathbf{n}}\hat{\mathbf{n}}$ represents the dyadic product of $\hat{\mathbf{n}}$ with itself. If we apply the reflection operation, the polar vector $\mathbf{p}(\mathrm{R})$ transforms according to

$$\mathbf{p}(\mathrm{R}) = \hat{\mathcal{R}}_{\hat{n}}\ \mathbf{p}(\mathrm{S}) = \mathbf{p}(\mathrm{S}) - 2[\mathbf{p}(\mathrm{S}) \cdot \hat{\mathbf{n}}]\hat{\mathbf{n}} \tag{2.40}$$

Also, under reflection, the axial vector $\mathbf{a}(\mathrm{R})$ transforms to

$$\mathbf{a}(\mathrm{R}) = -\hat{\mathcal{R}}_{\hat{n}}\ \mathbf{a}(\mathrm{S}) = -\mathbf{a}(\mathrm{S}) + 2[\mathbf{a}(\mathrm{S}) \cdot \hat{\mathbf{n}}]\hat{\mathbf{n}} \tag{2.41}$$

Therefore, the polar vector $\mathbf{a}(\mathrm{R})$ flips the component perpendicular to the mirror, while the axial vector $\mathbf{a}(\mathrm{R})$ changes sign under the reflection operation. For the R and S enantiomers, the polar vector $\mathbf{p}(\mathrm{R})$ and the axial vector $\mathbf{a}(\mathrm{R})$ undergo reflection, as shown in Fig. 2.6. It is worth mentioning that the magnitudes of the polar and axial vectors remain unchanged by enantiomeric inversion:

$$|\mathbf{p}(\mathrm{R})| = |\mathbf{p}(\mathrm{S})|, \tag{2.42a}$$

$$|\mathbf{a}(\mathrm{R})| = |\mathbf{a}(\mathrm{S})|. \tag{2.42b}$$

2.2.13.2 Dependence on Linear Polarizabilities

Now, we define the dependence of the linear polarizabilities using the reflection operator as follows:

$$\mathrm{A_{d,E}(R)} \propto |\mathbf{p}(\mathrm{R})|^2 \propto |\mathbf{p}(\mathrm{S})|^2 = \mathrm{A_{d,E}(S)}, \tag{2.43a}$$

$$\mathrm{A_{d,B}(R)} \propto \mathbf{p}(\mathrm{R}) \cdot \mathbf{a}(\mathrm{R}) \propto -\mathbf{p}(\mathrm{S}) \cdot \mathbf{a}(\mathrm{S}) = -\mathrm{A_{d,B}(S)}, \tag{2.43b}$$

$$\mathrm{A_{m,B}(R)} \propto |\mathbf{a}(\mathrm{R})|^2 \propto |\mathbf{a}(\mathrm{S})|^2 = \mathrm{A_{m,B}(S)}, \tag{2.43c}$$

$$\mathrm{A_{m,E}(R)} \propto \mathbf{p}(\mathrm{R}) \cdot \mathbf{a}(\mathrm{R}) \propto -\mathbf{p}(\mathrm{S}) \cdot \mathbf{a}(\mathrm{S}) = -\mathrm{A_{m,E}(S)}. \tag{2.43d}$$

This property is very important for many chiroptical effects, such as OR and CD, in which enantiomers interact differently with a polarized electromagnetic field. Therefore, we calculate the enantiomeric imbalance by the following expression

$$\frac{\Delta n_{\mathrm{mol}}}{n_{\mathrm{mol}}} = \frac{n_{\mathrm{mol}}^{(\mathrm{S})} - n_{\mathrm{mol}}^{(\mathrm{R})}}{n_{\mathrm{mol}}^{(\mathrm{S})} + n_{\mathrm{mol}}^{(\mathrm{R})}}, \tag{2.44}$$

where $n_{\mathrm{mol}}^{(\mathrm{R})}$ and $n_{\mathrm{mol}}^{(\mathrm{S})}$ are the molecular number densities for the R and S enantiomers, respectively.

To study the enantioselective properties for two pharmaceutical chiral drugs, reparixin and ladarixin, Fig. 2.7 shows the wavelength λ and enantiomeric imbalance $\frac{\Delta n_{\mathrm{mol}}}{n_{\mathrm{mol}}}$ dependence on the chiral response, which is denoted by the chiral parameter κ. In the expression Eq. 2.44, the ratio $+1$ denotes the purely S enantiomer, -1 denotes the purely R enantiomer, and for a racemic mixture, for an equal amount of R and S enantiomers, it is zero. We observe in the above Fig. 2.7 that κ changes from positive to negative for R and S enantiomers, meaning different enantiomers produce different chiral responses, as expected, which indicates the chiral parameter is enantioselective. For the racemic mixture, we observe that when equal amounts of R and S enantiomers are present, there is no chiral

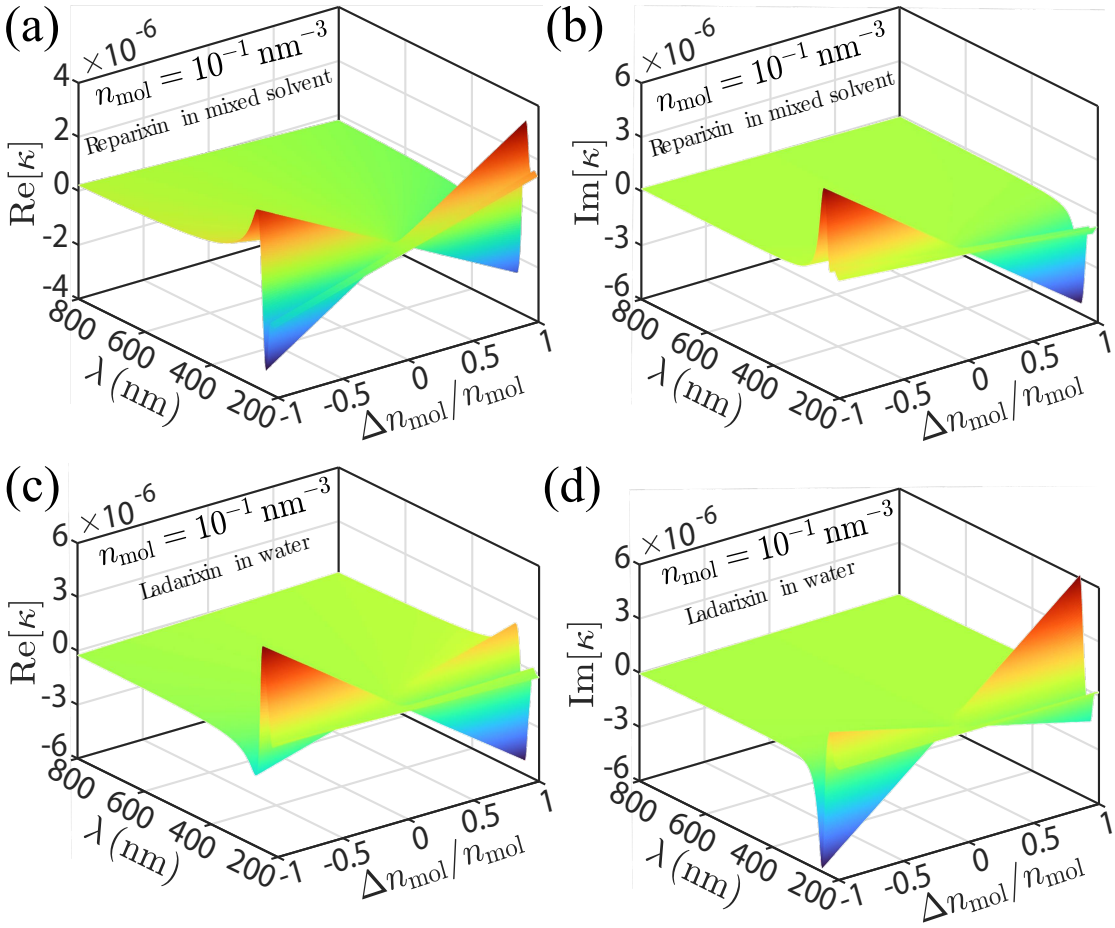

Figure 2.7 Dependence of the **(a,c)** Real and **(b,d)** imaginary parts of κ as a function of wavelength (λ) for relative concentration ($\Delta n_{mol}/n_{mol} = [n_{mol}^{(\mathrm{S})} - n_{mol}^{(\mathrm{R})}]/n_{mol}$) of two enantiomeric mixtures of R and S for **(a,b)** reparixin in mixed solvent and **(c,d)** ladarixin in water.

effect. At resonance with external electromagnetic radiation, the chiral response is strongest, as indicated by the peak in the lowest-wavelength region; off-resonance, the response is weak, as indicated by the flat region, which reflects the strong wavelength dependence of the chiral response. Most importantly, the real part of the chiral parameter $\mathrm{Re}[\kappa]$ in Fig. 2.7(a,c) determines the OR, which means how the phase response differs for the enantiomers of the chiral substance, and the imaginary part $\mathrm{Im}[\kappa]$ in Fig. 2.7(b,d) determines the CD, which determines the differential absorption of the chiral response. The rapatixin and ladarixin show different microscopic responses, of course, due to different molecular structures

and solvent environments.

2.3 Concluding remarks

In this chapter, we present a theoretical modeling of chiral light-matter interactions. We present a theoretical approach to determine multilevel chiroptical interactions using the density-matrix formalism. We solve the density-matrix equation perturbatively to calculate the induced electric and magnetic dipole moments. Then, using Euler's rotation matrix approach for randomly oriented molecules, we average over arbitrary orientations. Then, by calculating macroscopic polarization and magnetization, we obtain the constitutive relation that relates the microscopic and macroscopic responses. In the following chapter, we will use this relation to study the enhancement of the weak chiroptical signal by the nonlinear optical method, also by using a nanophotonic environment.

Chapter 3

Electromagnetically induced transparency and lasing without inversion in chiral molecule

"In quantum optics, opacity is not a property but a choice of driving field."

— Adapted from standard descriptions of coherent control in electromagnetically induced transparency, where tailored driving fields can transform an absorbing medium into a transparent or even amplifying one.

EIT and LWI are optical manifestations of quantum coherence control, a research frontier in modern photonics. Here we theoretically investigate these effects in a chiral molecule, fluoroxirane, in our calculations, coherently driven by an optical pump, finding that probe fields can undergo chiroptical absorption quenching or amplification within particular spectral windows at pump intensities as low as $\approx$ 1kW/cm^2. Our calculations reveal that molecular chirality has the capacity to dramatically alter quantum coherence phenomena at peculiar wavelength ranges, modulating efficiently CD depending on the polarization state of both pump and

probe fields and the molecular orientation. We find that, for a given molecular orientation, the DSF probed upon RCP/LCP excitation by the signal can get maximized by pump polarization tuning and the signal direction. By averaging over impinging signal orientations, we find that the orientation-averaged DSF can diverge owing to EIT producing vanishing averaged absorption cross-sections. Our results hold great potential for the development of novel NL spectroscopic techniques capable of detecting chirality at the single-molecule level.

3.1 Introduction

Arising from the destructive interference of distinct quantum excitation pathways, EIT lies in the quenching of optical absorption in an atomic system coherently driven by a pump laser field [125, 126, 127]. Practically, the transmission spectrum of probing light features a transparency resonance over a narrow spectral window within the wider absorption profile, resulting in a pronounced phase shift and a significant group delay produced by slow light regime [128, 129, 130].

Analogously, LWI also arises from quantum interference, coherently amplifying a probe field at the expense of the driving pump laser power without the necessity to attain population inversion [131]. As such, LWI is particularly relevant for achieving lasing action at wavelength ranges that are hardly accessible with existing laser systems.

Because EIT and LWI are merely *coherent* phenomena, whose quantum manifestation typically arises in gas-phase atomic systems [132] even with single photons [133] and atoms [134], they can also be simulated and exploited for diverse applications in analogue classical systems, e.g., waveguides [135], silicon-based resonators [136], drop-filter cavity-waveguide systems [137], plasmonic metamaterials/metasurfaces [138, 139, 140, 141], and optomechanical systems [142]. In the context of such all-optical analogues, the interplay between EIT and *chiral-*

ity – the handedness of a geometrical object with broken mirror symmetry – has been explored in non-Hermitian systems where transparency and absorption are modulated by chiral optical states at exceptional points in an indirectly coupled resonator system [143].

Chirality is crucial in diverse areas of science, and particularly for drug enantiomers – molecular forms with opposite handedness – presenting chirality-dependent interactions with biological tissues [41]. Chiroptical sensing techniques like polarimetry [144] and vibrational CD [145] currently enable the enantiomeric imbalance detection of dilute chiral drug solutions above ml volume owing to the inherently weak chiroptical signal. Nanophotonics, besides enabling effective chiroptical responses in artificial materials far exceeding those found in natural ones [146, 147, 148], amplifies chiroptical sensitivity to reduced sample volumes by nanodevices [149, 150, 151]. Metal-based nanostructures enable plasmon-enhanced chiroptical spectroscopy of chiral drugs [152, 153, 154], enhancing sensitivity to drug nanolitres thanks to surface plasmon polariton excitation at noble metal interfaces [123]. Chiroptical sensitivity can be further amplified by ultrafast enantioselective NL optical techniques, enabling advanced levels of detection and selectivity [155, 156].

3.2 Objectives and Hypothesis

Here, we investigate the interplay of EIT and LWI with chirality at the single-molecule level, exploring their potential for innovative chiroptical spectroscopy techniques. We observe that, conversely to atomic three-level systems where EIT and LWI arise from quantum interference of the distinct excitation pathways, in a chiral molecule such phenomena can also occur between two levels only, owing to virtual states and the coherences provided by static/transition electric/magnetic dipole moments; see Fig. 3.3. As such, starting from first principles, we

adopt a density matrix formalism to account for light-matter interaction beyond the standard electric dipole approximation to include also magnetic interaction, playing a crucial role in the chiroptical response due to molecular chirality. Adopting the two-level approximation for the chiral molecule electronic structure, fluoroxirane in our calculations, we evaluate the density matrix temporal evolution upon coherent driving by monochromatic pump and signal fields, calculating the signal ACS through the derivation of a generalized optical theorem. Our calculations reveal that, within the EIT and LWI spectral windows, the ACS heavily depends on both molecular orientation and the polarization of pump/signal fields. Orientation-averaged predictions indicate that EIT enables to attain a diverging DSF producing giant enhancement of standard CD. Our results are promising for advanced NL spectroscopic techniques capable of detecting chirality at the single-molecule level.

3.3 Electromagnetically induced transparency and Lasing without inversion overview

With the introduction of a new optical crystal, developed in the 1970s and 1980s from a material with advanced optical properties, the NL optical conversion efficiency increases in the UV region. Also, in optical media, the phase-matching condition, or coherence, is another important property of atomic or molecular media. When a coherent radiation field is allowed to pass through an atomic vapor, it is basically absorbed by the atomic system, but in the presence of another coherent radiation field having higher intensity, the absorption of the first field by the medium reduces, resulting in the optical properties of the medium being modified in the presence of another coherent radiation field. The field having higher intensity is called the pump field or control field, and the field having lower

intensity is called the probe field or signal field. EIT originates from the idea: E for *electromagnetic radiation*, I for *induced*, meaning this is the reason, and T for *transparency*, meaning that before EIT, light was absorbed by the media, and now it becomes transparent. In the absence of pumping, the usual absorption line-shape is observed, see Fig. 3.2(a), where the absorption peak is denoted in the blue curve. The introduction of a pump suppresses absorption at the resonance wavelength, leading to a dip in the absorption spectrum. We put this probe field at very low intensity so that all the electrons stay in the ground state, and the pump field is off-resonant around the transition, so, of course, it will not produce the population inversion but will still produce transparency by simply transferring coherence energy between the pump and signal fields due to quantum interference.

LWI is an application of EIT. If we achieve EIT, we just need to put some electrons in the upper excited state, and then lasing is possible even with a small population in that state. Usually, the gain medium of a laser works on the basis of a population inversion. Essentially, for a simple system, the upper laser level has a higher population than the lower laser level, so stimulated emission can provide a positive net gain. However, it was shown that optical amplification and, consequently, LWI are possible by using an additional optical or microwave field that induces quantum coherence in the atoms of the gain medium. The basic idea is to provide two different pathways for atoms to get from the ground state to the excited state—a direct one and another one via a third energy level—and to induce a quantum coherence so that the quantum-mechanical probability amplitudes for both processes cancel. In effect, this suppresses reabsorption, allowing a positive net gain even with a small population in the upper excited state. In principle, LWI could help, e.g., in realizing lasers operating on very short wavelengths, where a population inversion is difficult to achieve. So far, LWI has to be considered as a definitely interesting quantum-mechanical effect.

Historically, there is some evidence of EIT. In the 1960s, Fano showed that the

photoionization spectrum of multielectron atoms with autoionizing states shows asymmetric line shapes and even narrow transparency windows due to interference between direct excitation into the continuum and excitation through a discrete, strongly decaying state coupled to the same continuum [127]. Also, another experiment by Madden and Codling on helium confirmed that such autoionizing resonances can generate transparency regions inside a broad absorption band. Later, Armstrong and Wynne used interference between autoionizing resonances in strontium to enhance NL sum-frequency generation to the vacuum UV: absorption was suppressed in frequency regions where the NL response remained large, leading to more efficient frequency conversion [127]. This work already contained the main concept of EIT: cancel linear absorption by interference, but keep the NL susceptibility or even enhance it. In the late 1980s, Harris and co-workers realized that similar interference can be engineered with ordinary bound transitions using strong laser fields [127]. In 1990, Harris and collaborators used the term *electromagnetically induced transparency* to describe this cancellation of linear susceptibility in a laser-dressed medium, and Boller reported the first experimental observation of EIT in strontium vapour, soon after [125, 127].

Now we'll give a basic idea in the following section for achieving EIT and LWI in a standard three-level atomic system through quantum interference.

3.3.1 A three-level description of Electromagnetically induced transparency

A physical picture of EIT in a three-level atomic system is shown in Fig. 3.1. A weak probe field with angular frequency ω_S is applied to the $|1\rangle \leftrightarrow |2\rangle$ transition, while a strong coupling field drives the $|2\rangle \leftrightarrow |3\rangle$ transition. We consider the transition $|1\rangle \leftrightarrow |3\rangle$ to be dipole forbidden.

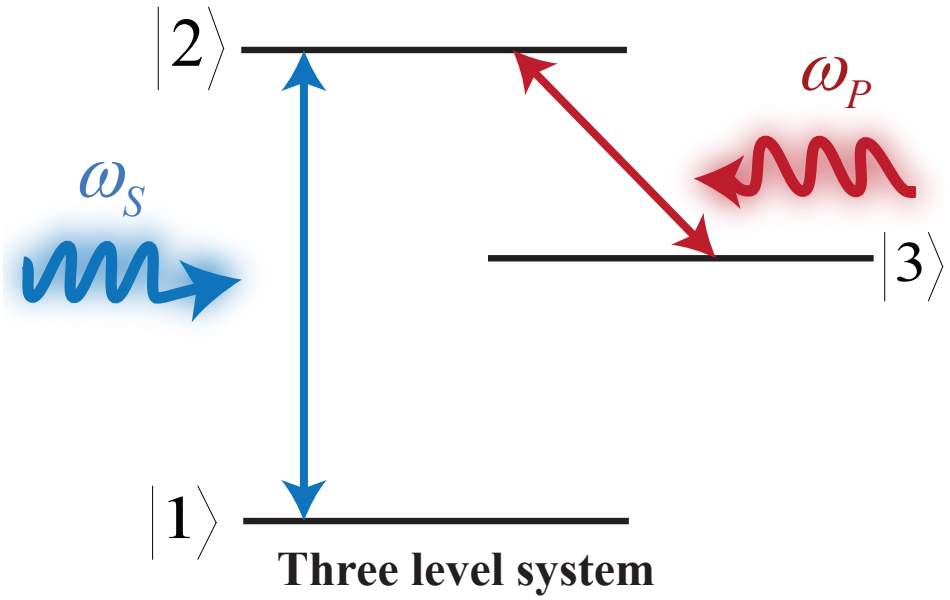

Figure 3.1 Schematic illustration of a three-level atomic system when illuminated by monochromatic pump and signal fields with angular frequencies $\omega_{\rm P}$ and $\omega_{\rm S}$, respectively.

We describe the unperturbed Hamiltonian of the atomic system as given below:

$$\hat{\mathcal{H}}_0 = \sum_{n=1}^{3} \hbar\,\omega_n\,|n\rangle\langle n|. \tag{3.1}$$

In the electric-dipole approximation, the interaction Hamiltonian can be written as, $\hat{\mathcal{H}}_{\rm int}(t) = -\mathbf{E}_{\rm T}(t)\cdot\hat{\mathbf{d}}$ where $\mathbf{E}_{\rm T}(t) = \mathbf{E}_{\rm P}(t) + \mathbf{E}_{\rm S}(t)$ denotes the total electric field, including contributions from the pump (P) and probe (S) fields.

We consider both pump and probe fields to be monochromatic excitations, given by

$$\mathbf{E}_{\rm P}(t) = {\rm Re}[\mathbf{E}_0^{\rm P}\,e^{-i\omega_{\rm P}\,t}], \tag{3.2a}$$

$$\mathbf{E}_{\rm S}(t) = {\rm Re}[\mathbf{E}_0^{\rm S}\,e^{-i\omega_{\rm S}\,t}]. \tag{3.2b}$$

Upon optical excitation, the time (t) dependent total Hamiltonian of the system is given by $\hat{\mathcal{H}}(t) = \hat{\mathcal{H}}_0 - \mathbf{E}_{\rm T}(t)\cdot\hat{\mathbf{d}}$.

Now we introduce pump and probe Rabi frequencies as

$$\Omega_{\mathrm{P}} = \frac{\mathbf{d}_{23} \cdot \mathbf{E}_0^{\mathrm{P}}}{\hbar}, \qquad \Omega_{\mathrm{S}} = \frac{\mathbf{d}_{21} \cdot \mathbf{E}_0^{\mathrm{S}}}{\hbar}. \tag{3.3}$$

Applying the rotating wave approximation, the interaction Hamiltonian can be written as

$$\hat{\mathcal{H}}_{\mathrm{int}}^{(\mathrm{RWA})} = -\frac{\hbar}{2}\left(\Omega_{\mathrm{S}} e^{-i\omega_{\mathrm{S}} t}\,|2\rangle\langle 1| + \Omega_{\mathrm{P}} e^{-i\omega_{\mathrm{P}} t}\,|2\rangle\langle 3| + \mathrm{H.c.}\right). \tag{3.4}$$

The total Hamiltonian of the system can be described as

$$\begin{aligned}\hat{\mathcal{H}}(t) = {} & \hbar\omega_1\,|1\rangle\langle 1| + \hbar\omega_2\,|2\rangle\langle 2| + \hbar\omega_3\,|3\rangle\langle 3| \\ & - \frac{\hbar}{2}\left(\Omega_{\mathrm{S}} e^{-i\omega_{\mathrm{S}} t}\,|2\rangle\langle 1| + \Omega_{\mathrm{P}} e^{-i\omega_{\mathrm{P}} t}\,|2\rangle\langle 3| + \mathrm{H.c.}\right).\end{aligned} \tag{3.5}$$

The temporal electron dynamics of the system are accounted for by the single-electron density matrix $\hat{\rho} = \sum_{n,m=1}^{3} \rho_{nm}(t)|n\rangle\langle m|$, satisfying the Liouville-von Neumann equation,

$$\frac{d\hat{\rho}}{dt} = \frac{1}{i\hbar}\left[\hat{\mathcal{H}}(t), \hat{\rho}\right] + \hat{\mathcal{L}}\left(\hat{\rho}\right), \tag{3.6}$$

where $\hbar$ is the reduced Planck constant and $\hat{\mathcal{L}}\left(\hat{\rho}\right)$ is the Lindblad operator that accounts for relaxation and dephasing.

We introduce Γ_{21} and Γ_{23} the as the spontaneous decay rates from $|2\rangle$ to $|1\rangle$ and $|3\rangle$, respectively. The corresponding coherence decay rates are denoted by Γ_{21}, Γ_{31}, and Γ_{23}. The optical Bloch equations for the density-matrix elements are

$$\dot{\rho}_{21} = -\big(i\omega_{21} + \Gamma_{21}\big)\rho_{21} + \frac{i}{2}\,\Omega_{\mathrm{S}}^{*} e^{-i\omega_{\mathrm{S}}t}(\rho_{11} - \rho_{22}) + \frac{i}{2}\,\Omega_{\mathrm{P}}^{*} e^{-i\omega_{\mathrm{P}}t}\,\rho_{31}, \tag{3.7a}$$

$$\dot{\rho}_{31} = -\big(i\omega_{31} + \Gamma_{31}\big)\rho_{31} + \frac{i}{2}\,\Omega_{\mathrm{S}}^{*} e^{-i\omega_{\mathrm{S}}t}\,\rho_{32} + \frac{i}{2}\,\Omega_{\mathrm{P}} e^{+i\omega_{\mathrm{P}}t}\,\rho_{21}, \tag{3.7b}$$

$$\dot{\rho}_{23} = -\big(i\omega_{23} + \Gamma_{23}\big)\rho_{23} + \frac{i}{2}\,\Omega_{\mathrm{P}}^{*} e^{-i\omega_{\mathrm{P}}t}(\rho_{33} - \rho_{22}) + \frac{i}{2}\,\Omega_{\mathrm{S}}^{*} e^{-i\omega_{\mathrm{S}}t}\,\rho_{13}. \tag{3.7c}$$

In the weak-probe regime, the pump field is assumed to be much stronger than the signal field and $\omega_P = \omega_{23}$, and initially almost all the population stays in the ground state $|1\rangle$. Also, we apply a perturbation interaction with Ω_{S}, therefore, by approximating, we obtain

$$\begin{aligned} \rho_{11}^{(0)} &= 1, \qquad \rho_{22}^{(0)} = 0, \\ \rho_{33}^{(0)} &= 0, \qquad \rho_{32}^{(0)} = 0. \end{aligned} \tag{3.8}$$

Assuming these, we can write

$$\rho_{21} = \tilde{\rho}_{21} e^{-i\omega_{\mathrm{S}}t}, \qquad \rho_{31} = \tilde{\rho}_{31} e^{-i(\omega_{\mathrm{S}} - \omega_{\mathrm{P}})t}. \tag{3.9}$$

Under this approximation, the weak signal field cannot establish an appreciable coherence ρ_{32} to first order,so we write

$$\dot{\tilde{\rho}}_{21} = -\big(\Gamma_{21} + i\Delta\big)\tilde{\rho}_{21} + \frac{i}{2}\,\Omega_{\mathrm{S}}^{*} + \frac{i}{2}\,\Omega_{\mathrm{P}}^{*}\,\tilde{\rho}_{31}, \tag{3.10a}$$

$$\dot{\tilde{\rho}}_{31} = -\big(\Gamma_{31} + i\Delta\big)\tilde{\rho}_{31} + \frac{i}{2}\,\Omega_{\mathrm{P}}\,\tilde{\rho}_{21}, \tag{3.10b}$$

The steady-state coherence equations then reduce to

$$0 = -\big(\Gamma_{21} + i\Delta\big)\tilde{\rho}_{21} + \frac{i}{2}\,\Omega_{\mathrm{S}}^{*} + \frac{i}{2}\,\Omega_{\mathrm{P}}^{*}\,\tilde{\rho}_{31}, \tag{3.11a}$$

$$0 = -\big(\Gamma_{31} + i\Delta\big)\tilde{\rho}_{31} + \frac{i}{2}\,\Omega_{\mathrm{P}}\,\tilde{\rho}_{21}, \tag{3.11b}$$

In steady state, $\dot{\tilde{\rho}}_{21} = \dot{\tilde{\rho}}_{31} = 0$ by solving the above equations, we obtain the microscopic polarization at the signal frequency as below:

$$\tilde{\rho}_{21} = \frac{\left(i\Omega_{\mathrm{S}}^{*}/2\right)\left(\Gamma_{31} + i\Delta\right)}{\left(\Gamma_{21} + i\Delta\right)\left(\Gamma_{31} + i\Delta\right) + |\Omega_{\mathrm{P}}|^{2}/4}. \tag{3.12}$$

where the probe detuning can be written as

$$\Delta = \omega_{21} - \omega_{\mathrm{S}} \tag{3.13}$$

The full time-dependent probe coherence is $\rho_{21}(t) = \tilde{\rho}_{21}\, e^{-i\omega_{\mathrm{S}}t}$. For an ensemble with atomic number density N, the macroscopic polarization induced at the probe frequency is

$$P_{\mathrm{S}}(t) = N\left(d_{21}\rho_{12}(t) + d_{12}\rho_{21}(t)\right) = N d_{12}\tilde{\rho}_{21}e^{-i\omega_{\mathrm{S}}t} + \text{c.c.}, \tag{3.14}$$

where $d_{21} = d_{12}^{*}$ is the electric dipole matrix element.

The polarization can also be expressed in terms of the electric susceptibility $\chi(\omega_{\mathrm{S}}) = \chi' + i\chi''$ as

$$P_{\mathrm{S}}(t) = \frac{1}{2}\,\varepsilon_0 E_{\mathrm{S}}\left[\chi(\omega_{\mathrm{S}})e^{-i\omega_{\mathrm{S}}t} + \chi(-\omega_{\mathrm{S}})e^{+i\omega_{\mathrm{S}}t}\right], \tag{3.15}$$

where E_{S} is the complex amplitude of the probe field.

Comparing Eqs. 3.14 and 3.15 we get the EIT-modified susceptibility at the probe frequency as below:

$$\chi(\omega_{\mathrm{S}}) = \frac{2N|d_{12}|^{2}}{\varepsilon_0\hbar}\frac{i\left(\Gamma_{31} + i\Delta\right)}{(\Gamma_{21} + i\Delta)(\Gamma_{31} + i\Delta) + |\Omega_{\mathrm{P}}|^{2}/4}. \tag{3.16}$$

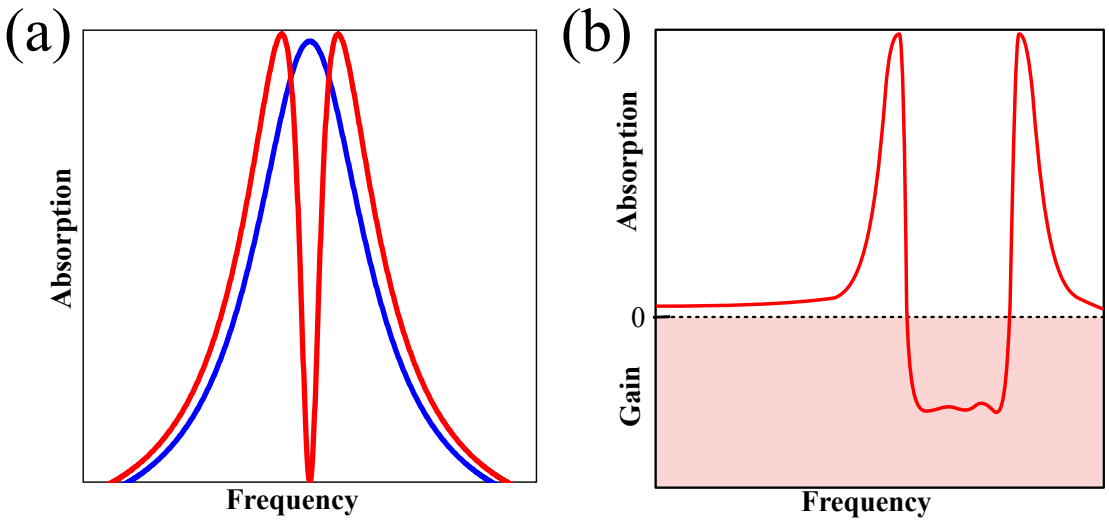

Figure 3.2 Schematic illustration of (a) EIT, where the blue curve represents the absorption window and the red curve denotes the transparency window, and (b) LWI, where the shaded region represents the amplification or gain region.

Separating real and imaginary parts of susceptibility, we obtain the following:

$$\chi' = \left(\frac{N|d_{12}|^2}{\varepsilon_0\hbar}\right)\frac{\Delta\left[\Gamma_{31}(\Gamma_{21}+\Gamma_{31})+(\Delta^2-\Gamma_{21}\Gamma_{31}-|\Omega_P|^2/4)\right]}{(\Delta^2-\Gamma_{21}\Gamma_{31}-|\Omega_P|^2/4)^2+\Delta^2(\Gamma_{21}+\Gamma_{31})^2}, \tag{3.17a}$$

$$\chi'' = \left(\frac{N|d_{12}|^2}{\varepsilon_0\hbar}\right)\frac{\Delta^2(\Gamma_{21}+\Gamma_{31})-\Gamma_{31}(\Delta^2-\Gamma_{21}\Gamma_{31}-|\Omega_P|^2/4)}{(\Delta^2-\Gamma_{21}\Gamma_{31}-|\Omega_P|^2/4)^2+\Delta^2(\Gamma_{21}+\Gamma_{31})^2}. \tag{3.17b}$$

The residual absorption at the probe resonance is then given by

$$\chi''(\Delta=0) = \left(\frac{N|d_{12}|^2}{\varepsilon_0\hbar}\right)\frac{\Gamma_{31}}{\Gamma_{21}\Gamma_{31}+|\Omega_P|^2/4}. \tag{3.18}$$

This vanishes when the pump Rabi frequency $|\Omega_P|$ exceeds the decay rate Γ_{21} of the probe transition.

At zero detuning, there is no absorption; that is, it becomes transparent under a strong, coherent pump field. See Fig. 3.2(a); there is an illustration of the absorption of the atomic system with the signal frequency. When there is only a signal field, an absorption peak is observed (blue curve); when there is coupling between the pump and probe fields, a transparency peak is observed (red curve).

3.3.2 Lasing without inversion description

In a multilevel system, however, absorption can be strongly reduced by destructive quantum interference, while emission is still possible. We obtain net gain even in the absence of conventional population inversion. This is the main physical idea behind LWI.

For the considered system, photon absorption to the upper state $|2\rangle$ occurs through two coherent pathways from the lower states $|1\rangle$ and $|3\rangle$, see Fig. 3.1. If the lower states are prepared in a coherent superposition with a fixed relative phase, these two absorption amplitudes interfere. Under suitable phase conditions, the total absorption amplitude vanishes, whereas emission from the upper state to the two lower states is not canceled in the same way; by using this approach LWI is possible.

First, we consider the atoms are in the two lower states as described by the initial conditions as below:

$$c_2(0) = 0, \qquad c_1(0) = \frac{1}{\sqrt{2}}, \qquad c_3(0) = \frac{1}{\sqrt{2}} e^{-i\psi}, \tag{3.19}$$

Using a perturbative approximation, the probability amplitude of the upper state $|2\rangle$ is then given by the coherent sum of the two excitation pathways,

$$c_2(t) \simeq \frac{i\,t}{2\sqrt{2}} \left[\Omega_{\mathrm{S}} e^{-i\phi_{\mathrm{S}}} + \Omega_{\mathrm{P}} e^{-i(\phi_{\mathrm{P}}+\psi)}\right], \tag{3.20}$$

where ϕ_{S} and ϕ_{P} denote the phases of the signal and pump fields, respectively.

For simplicity, we consider

$$\Omega_{\mathrm{S}} = \Omega_{\mathrm{P}} \equiv \Omega. \tag{3.21}$$

In that case, the population of the upper state becomes

$$|c_2(t)|^2 = \frac{t^2\Omega^2}{4}\left[1+\cos(\phi_S-\phi_P-\psi)\right]. \tag{3.22}$$

We see from the above Eq. 3.22 that the absorption probability depends on the relative phase between the two excitation pathways. Therefore, complete cancellation of absorption occurs when

$$\phi_S-\phi_P-\psi = \pm\pi. \tag{3.23}$$

Under this condition, the two optical amplitudes interfere destructively so that the atom cannot be excited into $|2\rangle$ by absorption.

Also, the emission from the upper state is not canceled in the same way. For this, let's consider that all the atoms are initially in the excited state,

$$c_2(0)=1, \qquad c_1(0)=c_3(0)=0. \tag{3.24}$$

For short times, the amplitudes of the two lower states are approximately equal

$$c_1(t) \simeq i\,\frac{\Omega_S^* t}{2}, \qquad c_3(t) \simeq i\,\frac{\Omega_P^* t}{2}, \tag{3.25}$$

so that the total emission probability is

$$|c_1(t)|^2+|c_3(t)|^2 = \frac{t^2}{4}\left(|\Omega_S|^2+|\Omega_P|^2\right), \tag{3.26}$$

which is always positive and independent of relative phase ψ. That is why absorption can be completely reduced by destructive interference, yet emission is still possible.

There is also a semiclassical approach reported in [157]. Based on our system,

let the field amplitude be denoted by $\mathcal{E}$. The emission probability is proportional to the upper-state population $\rho_{22}^{(0)}$, whereas the absorption probability from the lower-state doublet depends on the coherent sum of the lower-state amplitudes. The emission can be written as below:

$$P_{\text{emission}} = \left(|k_{2\to1}|^2\mathcal{E}^2 + |k_{2\to3}|^2\mathcal{E}^2\right)\rho_{22}^{(0)}, \tag{3.27}$$

while the absorption contribution is

$$P_{\text{absorption}} = \kappa\left(\rho_{11}^{(0)} + \rho_{33}^{(0)} + \rho_{13}^{(0)} + \rho_{31}^{(0)}\right)\mathcal{E}^2, \tag{3.28}$$

where κ, $k_{2\to1}$, and $k_{2\to3}$ are constants depending on the dipole matrix elements and the atom-field coupling strengths. So, we see the absorption probability depends not only on the lower-state populations $\rho_{11}^{(0)}$ and $\rho_{33}^{(0)}$, but also on the lower-state coherences $\rho_{13}^{(0)}$ and $\rho_{31}^{(0)}$.

Accordingly, the field amplitude may be written in the form

$$\dot{\mathcal{E}} = \frac{\mathcal{A}}{2}\left[\rho_{22}^{(0)} - \rho_{11}^{(0)} - \rho_{33}^{(0)} - \rho_{13}^{(0)} - \rho_{31}^{(0)}\right]\mathcal{E}, \tag{3.29}$$

where $\mathcal{A}$ is a proportionality constant. In an ordinary laser, the coherence terms $\rho_{13}^{(0)}$ and $\rho_{31}^{(0)}$ are absent, and we require $\rho_{22}^{(0)} > \rho_{11}^{(0)} + \rho_{33}^{(0)}$ in order to obtain gain, while in a coherent system, these extra terms can reduce or cancel the lower-state absorption. If the cancellation is complete, Eq. 3.29 reduces to

$$\dot{\mathcal{E}} = \frac{\mathcal{A}}{2}\rho_{22}^{(0)}\mathcal{E}, \tag{3.30}$$

which shows that the field amplitude can increase even if the upper-state population is smaller than the total lower-state population. This is the basic idea by which it is possible to achieve LWI in a three-level system. See Fig. 3.2;

the shaded region, where the absorption coefficient becomes negative, denoting the amplification or gain region, which occurs by simply coherent energy transfer between the pump and probe fields.

3.4 Electromagnetically induced transparency and Lasing without inversion in chirality

Until now, we have discussed the standard EIT and LWI in an atomic system. Now that we focus on the main concept of this chapter, we'll see the interplay between EIT and chirality and how this nonlinear technique can detect chirality at the single-molecule level. We'll first discuss this by describing the molecular spectral information, then present a theoretical approach, and, using the spectroscopic quantities, produce the results discussed in the following sections.

3.4.1 Electronic structure and spectroscopic quantities of fluoroxirane

We consider the chiral molecule fluoroxirane (C_2H_3FO). This is a model molecule, and it is not very stable. It was used only as a model of a rigid chiral scaffold.

The ground ($\hbar\omega_1$) and excited ($\hbar\omega_2$) fluoroxirane energy levels of states $|1\rangle, |2\rangle$ see Fig. 3.3, with energy gap $\hbar\omega_0 = \hbar(\omega_2 - \omega_1) \simeq 8.417$ eV, are calculated by time-dependent density functional theory complemented with molecular dynamics simulations, see Table 3.1. Such calculations also provide the transition electric ($|\mathbf{d}_{12}| \simeq 1.143 \times 10^{-30}$ Cm) and magnetic ($|\mathbf{m}_{12}| \simeq 9.883 \times 10^{-24}$ Am^2) dipole moments, as well as the static electric dipole moments in ground ($|\mathbf{d}_{11}| \simeq 8.391 \times 10^{-30}$ Cm) and excited ($|\mathbf{d}_{22}| \simeq 8.724 \times 10^{-30}$ Cm) states $|1\rangle, |2\rangle$, together with their orientation.

Because fluoroxirane is not a magnetic molecule, the static magnetic dipole mo-

ments of both ground and excited states are vanishing $\mathbf{m}_{11} = \mathbf{m}_{22} = 0$. However, due to its *polarity* and *chirality*, fluoroxirane has finite static electric ($\mathbf{d}_{11}, \mathbf{d}_{22}$) and transition magnetic ($\mathbf{m}_{12}$) dipole moments, respectively, which are not orthogonal to the transition electric dipole moment $\mathbf{d}_{12}$.

3.4.2 Theoretical Model

In this section, we outline the theoretical framework adopted to describe the NL interaction of electromagnetic radiation with a chiral molecule.

3.4.2.1 Nonlinear chiroptical interaction

Fig. 3.3 schematically illustrates the system under consideration, where a single molecule in vacuum is irradiated with pump (P) and signal (S) external monochromatic radiation with vacuum wavelengths $\lambda_{\mathrm{P,S}}$.

Upon optical excitation, the time (t) dependent total Hamiltonian of the system is given by

$$\hat{\mathcal{H}}(t) \;=\; \hat{\mathcal{H}}_0 - \mathbf{E}_{\mathrm{T}}(t)\cdot\hat{\mathbf{d}} - \mathbf{B}_{\mathrm{T}}(t)\cdot\hat{\mathbf{m}}, \tag{3.31}$$

where $\hat{\mathcal{H}}_0 = \sum_{n=1}^{2}\hbar\omega_n\,|n\rangle\langle n|$ is the unperturbed Hamiltonian, $\mathbf{E}_{\mathrm{T}}(t) = \mathbf{E}_{\mathrm{P}}(t) + \mathbf{E}_{\mathrm{S}}(t)$ and $\mathbf{B}_{\mathrm{T}}(t) = \mathbf{B}_{\mathrm{P}}(t) + \mathbf{B}_{\mathrm{S}}(t)$ are the total electric and induction magnetic fields.

The electric and induction magnetic pump/signal fields, assuming monochromatic field excitation, can be written as

$$\mathbf{E}_{\mathrm{P,S}}(t) = \mathrm{Re}[\mathbf{E}_0^{\mathrm{P,S}}\,e^{-i\omega_{\mathrm{P,S}}\,t}] \tag{3.32a}$$

$$\mathbf{B}_{\mathrm{P,S}}(t) = \mathrm{Re}[\mathbf{B}_0^{\mathrm{P,S}}\,e^{-i\omega_{\mathrm{P,S}}\,t}] \tag{3.32b}$$

with the vectorial field amplitudes $\mathbf{E}_0^{\mathrm{P,S}}$ and $\mathbf{B}_0^{\mathrm{P,S}}$ at the molecule position, $\omega_{\mathrm{P,S}} =$

Atomic positions (in Å)			
Atom	x	y	z
H	-1.8054	0.8354	0.6515
C	-0.9770	0.6222	-0.0221
C	0.2161	-0.0691	0.4542
H	-0.8986	1.2463	-0.9099
O	-0.7229	-0.7985	-0.2590
F	1.4055	0.1496	-0.1942
H	0.4029	-0.3582	1.4862

Permanent dipole moments (a.u.)			
Component	$\mathbf{d}_{11}$	$\mathbf{d}_{22}$	
x	-0.4653	-0.4286	
y	0.6245	0.6827	
z	0.6108	0.6395	

Transition dipole moments (a.u.)			
Component	$\mathbf{d}_{12}$	$\mathbf{m}_{12}$	
x	-0.0472	$-0.0282\times1i$	
y	0.0819	$0.5189\times1i$	
z	-0.0961	$0.1178\times1i$	

Spectroscopic parameters
Excitation energy $\hbar\omega_0 = 8.4167$ eV
Decay rate $\gamma = 1.1518 \times 10^7$ s^{-1}

Dipole moments (SI)
$\mathbf{d}_{11} = [-3.9447\hat{\mathbf{e}}_x + 5.2947\hat{\mathbf{e}}_y + 5.1786\hat{\mathbf{e}}_z] \times 10^{-30}$ Cm
$\mathbf{d}_{22} = [-3.6334\hat{\mathbf{e}}_x + 5.7880\hat{\mathbf{e}}_y + 5.4218\hat{\mathbf{e}}_z] \times 10^{-30}$ Cm
$\mathbf{d}_{12} = [-4.0018\hat{\mathbf{e}}_x + 6.9438\hat{\mathbf{e}}_y - 8.1477\hat{\mathbf{e}}_z] \times 10^{-31}$ Cm
$\mathbf{m}_{12} = i[-0.5230\hat{\mathbf{e}}_x + 9.6242\hat{\mathbf{e}}_y + 2.1849\hat{\mathbf{e}}_z] \times 10^{-24}$ Am^2

Table 3.1 Fluoroxirane S enantiomer: geometry, dipole vectors, spectroscopic parameters, and SI vector expressions.

$2\pi c/\lambda_{\mathrm{P,S}}$ are the pump/signal angular frequencies, c is the speed of light in vacuum, and $\hat{\mathbf{d}} = \sum_{n,m=1}^{2} \mathbf{d}_{nm} |n\rangle\langle m|$ and $\hat{\mathbf{m}} = \sum_{n,m=1}^{2} \mathbf{m}_{nm} |n\rangle\langle m|$ are the electric and magnetic dipole moment operators, respectively.

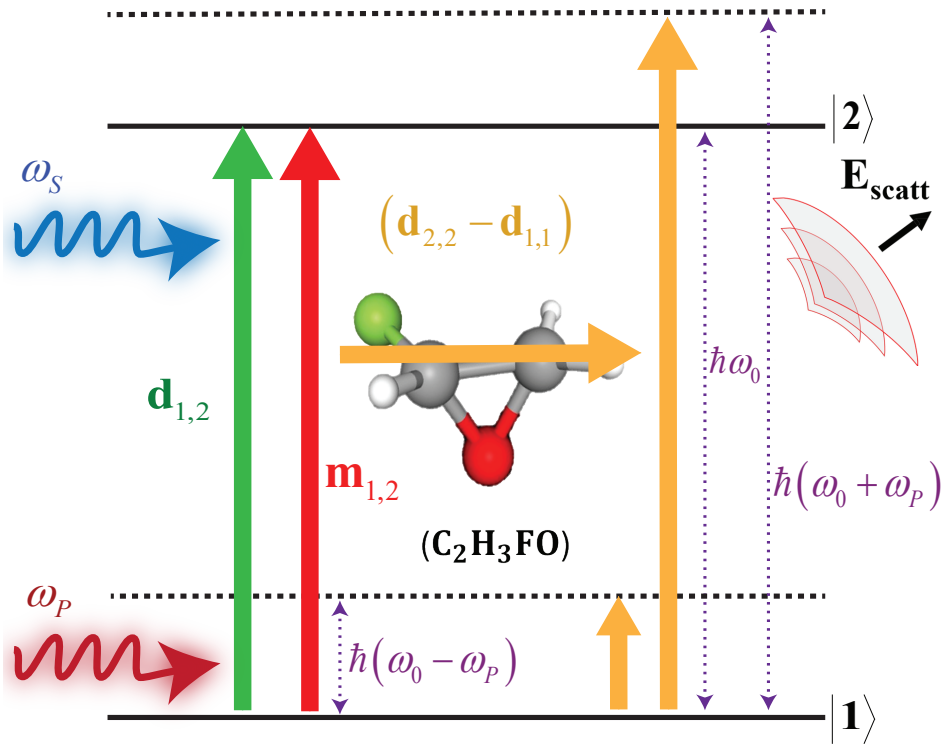

Figure 3.3 Schematic illustration of fluoroxirane (C_2H_3FO) electron dynamics in the two-level approximation when illuminated by monochromatic pump and signal fields with angular frequencies ω_P and ω_S, respectively. Because fluoroxirane is not a magnetic molecule, the static ground and excited magnetic dipole moments vanish $\mathbf{m}_{11} = \mathbf{m}_{22} = 0$. However, owing to chirality, fluoroxirane possesses non-orthogonal transition electric ($\mathbf{d}_{12}$) and magnetic ($\mathbf{m}_{12}$) dipole moments, as well as static electric ground ($\mathbf{d}_{11}$) and excited ($\mathbf{d}_{22}$) dipole moments arising from its polarity, all producing quantum interference.

The temporal electron dynamics of the system is accounted for by the single-electron density matrix $\hat{\rho} = \sum_{n,m=1}^{2} \rho_{nm}(t)|n\rangle\langle m|$, satisfying the Liouville-von Neumann equation; see Eq. 3.6 where the Lindblad operator can be written for a two-level system as below

$$\hat{\mathcal{L}}(\hat{\rho}) = \frac{\gamma}{2}\left[2\,\rho_{22}\,|1\rangle\langle 1| - |2\rangle\langle 2|\,\hat{\rho} - \hat{\rho}\,|2\rangle\langle 2|\right] \tag{3.33}$$

accounts for the dephasing ($\gamma/2$) and recombination (γ) rates, the spontaneous emission produces $\gamma = \gamma_{\text{rad}} \simeq 1.15 \times 10^7$ s^{-1} for fluoroxirane.

Explicitly, 3.6 provides

$$\dot{\rho}_{ij} = -i\left(\omega_i - \omega_j\right)\rho_{ij} + \gamma\rho_{22}\delta_{i,1}\delta_{j,1} + -\frac{\gamma}{2}\rho_{ij}\left(1-\delta_{i,1}\right) - \frac{\gamma}{2}\rho_{ij}\left(1-\delta_{j,1}\right) + \\ + \frac{1}{i\hbar}\sum_{n=1}^{2}\left\{\rho_{in}\left[\mathbf{E}_{\text{T}}(t)\cdot\mathbf{d}_{nj} + \mathbf{B}_{\text{T}}(t)\cdot\mathbf{m}_{nj}\right] - \rho_{nj}\left[\mathbf{E}_{\text{T}}(t)\cdot\mathbf{d}_{in} + \mathbf{B}_{\text{T}}(t)\cdot\mathbf{m}_{in}\right]\right\}, \tag{3.34}$$

where $i, j = 1, 2$, and $\delta_{i,j}$ indicates the Kronecker delta. Because in our calculations, see the Results and Discussion section 3.5 below, we consider a pump field with $\lambda_{\text{P}} \simeq 1000$ nm $>> \lambda_0$ heavily detuned from the largest fluoroxirane electronic resonance wavelength $\lambda_0 = 2\pi c/\omega_0 \simeq 147.3$ nm, we ignore electron population depletion from the ground level, approximating $\rho_{11} = 1$ and $\rho_{22} = 0$ in Eq. 3.34.

3.4.2.2 Perturbative solution of the density matrix equations

Moreover, following a perturbative approach in the signal field amplitude ($|\mathbf{E}_0^{\text{S}}|$), we express the coherence ρ_{12} as the superposition

$$\rho_{12} = \rho_{12}^{(0)} + \rho_{12}^{(1)}, \tag{3.35}$$

where the zero-order response can be written as

$$\rho_{12}^{(0)} = r_0^{\text{P}} + \sum_{f=\pm1} r_f^{\text{P}} e^{if\omega_{\text{P}}t} \tag{3.36}$$

which accounts non-perturbatively for the pump-induced coherences, neglecting harmonic generation, while the first-order is expressed as

$$\rho_{12}^{(1)} = \sum_{f,f'=\pm1} r_{ff'}^{\text{mix}} e^{i(f\omega_{\text{S}}+f'\omega_{\text{P}})t} + \sum_{f=\pm1} r_f^{\text{S}} e^{if\omega_{\text{S}}t} \tag{3.37}$$

which accounts for the wave-mixing and coherence-modulation produced by the pump on the weak signal field, neglecting its effect on the pump.

Inserting this Ansatz in Eq. 3.34, one gets the coefficients r_0^{P}, r_f^{P}, $r_{ff'}^{\mathrm{mix}}$ and r_f^{S}, which are reported below.

3.4.2.3 Zero order response

The zero-order optical coherences induced by the pump field are evaluated by neglecting the signal field and inserting the Ansatz as given below:

$$\rho_{12}^{(0)} = r_+^{\mathrm{P}} e^{i\omega_{\mathrm{P}} t} + r_-^{\mathrm{P}} e^{-i\omega_{\mathrm{P}} t} + r_0^{\mathrm{P}} \tag{3.38a}$$

$$\rho_{11} = 1 \tag{3.38b}$$

$$\rho_{22} = 0 \tag{3.38c}$$

Also, in Eq. 3.34, providing the pump-induced coherence amplitudes r_0^{P} and $r_\pm^{\mathrm{P}}$, explicitly given by

$$r_-^{\mathrm{P}} = -\frac{\mathcal{C}_0}{\mathcal{D}_0}\left(\mathbf{d}_{12}\cdot\mathbf{E}_0^{\mathrm{P}} + \mathbf{m}_{12}\cdot\mathbf{B}_0^{\mathrm{P}}\right) - \frac{(\mathbf{D}\cdot\mathbf{E}_0^{\mathrm{P}})^2}{\mathcal{D}_0}\left(\mathbf{d}_{12}\cdot\mathbf{E}_0^{\mathrm{P}*} + \mathbf{m}_{12}\cdot\mathbf{B}_0^{\mathrm{P}*}\right), \tag{3.39a}$$

$$r_+^{\mathrm{P}} = \frac{r_-^{\mathrm{P}}}{\mathcal{C}_0}(\mathbf{D}\cdot\mathbf{E}_0^{\mathrm{P}*})^2 + \frac{2\hbar\Omega}{\mathcal{C}_0}\left(\mathbf{d}_{12}\cdot\mathbf{E}_0^{\mathrm{P}*} + \mathbf{m}_{12}\cdot\mathbf{B}_0^{\mathrm{P}*}\right), \tag{3.39b}$$

$$r_0^{\mathrm{P}} = \frac{r_+^{\mathrm{P}}}{2\hbar\Omega}\left(\mathbf{D}\cdot\mathbf{E}_0^{\mathrm{P}}\right) + \frac{r_-^{\mathrm{P}}}{2\hbar\Omega}\left(\mathbf{D}\cdot\mathbf{E}_0^{\mathrm{P}*}\right), \tag{3.39c}$$

where $\Omega = \omega_0 + i\gamma/2$, $\mathbf{D} = \mathbf{d}_{22} - \mathbf{d}_{11}$, and

$$\begin{aligned} \mathcal{C}_0 &= 4\hbar^2\Omega(\Omega - \omega_{\mathrm{P}}) - \left|\mathbf{D}\cdot\mathbf{E}_0^{\mathrm{P}}\right|^2, \\ \mathcal{D}_0 &= 4\hbar\Omega\left[2\hbar^2(\omega_{\mathrm{P}}^2 - \Omega^2) + \left|\mathbf{D}\cdot\mathbf{E}_0^{\mathrm{P}}\right|^2\right]. \end{aligned} \tag{3.40}$$

3.4.2.4 First order response

At first order o($|E_0^{\mathrm{S}}|$) the optical coherences, resulting from the mixing of pump and signal fields, are evaluated by taking the Ansatz as given below:

$$\begin{aligned}\rho_{12}^{(1)} = r_{++}^{\mathrm{mix}} e^{i(\omega_{\mathrm{S}}+\omega_{\mathrm{P}})t} + r_{+-}^{\mathrm{mix}} e^{i(\omega_{\mathrm{S}}-\omega_{\mathrm{P}})t} + r_{-+}^{\mathrm{mix}} e^{-i(\omega_{\mathrm{S}}-\omega_{\mathrm{P}})t} \\ + r_{--}^{\mathrm{mix}} e^{-i(\omega_{\mathrm{S}}+\omega_{\mathrm{P}})t} + r_{+}^{\mathrm{S}} e^{i\omega_{\mathrm{S}}t} + r_{-}^{\mathrm{S}} e^{-i\omega_{\mathrm{S}}t}.\end{aligned} \quad , \tag{3.41}$$

Therefore, by neglecting higher order contributions o($|E_0^{\mathrm{S}}|^n$) with $n > 1$, provides

$$\begin{aligned} r_{+}^{\mathrm{S}} &= -\frac{2i\hbar}{\mathcal{D}_1}(\mathbf{d}_{12}\cdot\mathbf{E}_0^{\mathrm{S}*} + \mathbf{m}_{12}\cdot\mathbf{B}_0^{\mathrm{S}*} + r_0^{\mathrm{P}}\mathbf{D}\cdot\mathbf{E}_0^{\mathrm{S}*}) + \\ &- \frac{r_{+}^{\mathrm{P}}(\mathbf{D}\cdot\mathbf{E}_0^{\mathrm{P}})(\mathbf{D}\cdot\mathbf{E}_0^{\mathrm{S}*})}{[i(\omega_{\mathrm{S}}-\omega_{-})+\gamma/2]\,\mathcal{D}_1} - \frac{r_{-}^{\mathrm{P}}(\mathbf{D}\cdot\mathbf{E}_0^{\mathrm{P}*})(\mathbf{D}\cdot\mathbf{E}_0^{\mathrm{S}*})}{[i(\omega_{\mathrm{S}}-\omega_{+})+\gamma/2]\,\mathcal{D}_1} \equiv \\ &\equiv \mathbf{a}\cdot\mathbf{E}_0^{\mathrm{S}*} + \mathbf{b}\cdot\mathbf{B}_0^{\mathrm{S}*}, \end{aligned} \tag{3.42a}$$

$$\begin{aligned} r_{-}^{\mathrm{S}} &= -\frac{2i\hbar}{\mathcal{C}_1}(\mathbf{d}_{12}\cdot\mathbf{E}_0^{\mathrm{S}} + \mathbf{m}_{12}\cdot\mathbf{B}_0^{\mathrm{S}} + r_0^{\mathrm{P}}\mathbf{D}\cdot\mathbf{E}_0^{\mathrm{S}}) + \\ &+ \frac{r_{+}^{\mathrm{P}}(\mathbf{D}\cdot\mathbf{E}_0^{\mathrm{P}})(\mathbf{D}\cdot\mathbf{E}_0^{\mathrm{S}})}{[i(\omega_{\mathrm{S}}+\omega_{-})-\gamma/2]\,\mathcal{C}_1} + \frac{r_{-}^{\mathrm{P}}(\mathbf{D}\cdot\mathbf{E}_0^{\mathrm{P}*})(\mathbf{D}\cdot\mathbf{E}_0^{\mathrm{S}})}{[i(\omega_{\mathrm{S}}+\omega_{+})-\gamma/2]\,\mathcal{C}_1} \equiv \\ &\equiv \mathbf{c}\cdot\mathbf{E}_0^{\mathrm{S}} + \mathbf{d}\cdot\mathbf{B}_0^{\mathrm{S}}, \end{aligned} \tag{3.42b}$$

and

$$r_{++}^{\mathrm{mix}} = \frac{\mathbf{D}\cdot(r_{+}^{\mathrm{P}}\mathbf{E}_0^{\mathrm{S}*} + r_{+}^{\mathrm{S}}\mathbf{E}_0^{\mathrm{P}*})}{2i\hbar\,[i(\omega_{\mathrm{S}}-\omega_{-})+\gamma/2]}, \tag{3.43a}$$

$$r_{+-}^{\mathrm{mix}} = \frac{\mathbf{D}\cdot(r_{-}^{\mathrm{P}}\mathbf{E}_0^{\mathrm{S}*} + r_{+}^{\mathrm{S}}\mathbf{E}_0^{\mathrm{P}})}{2i\hbar\,[i(\omega_{\mathrm{S}}-\omega_{+})+\gamma/2]}, \tag{3.43b}$$

$$r_{-+}^{\mathrm{mix}} = \frac{\mathbf{D}\cdot(r_{+}^{\mathrm{P}}\mathbf{E}_0^{\mathrm{S}} + r_{-}^{\mathrm{S}}\mathbf{E}_0^{\mathrm{P}*})}{2i\hbar\,[-i(\omega_{\mathrm{S}}+\omega_{-})+\gamma/2]}, \tag{3.43c}$$

$$r_{--}^{\mathrm{mix}} = \frac{\mathbf{D}\cdot(r_{-}^{\mathrm{P}}\mathbf{E}_0^{\mathrm{S}} + r_{-}^{\mathrm{S}}\mathbf{E}_0^{\mathrm{P}})}{2i\hbar\,[-i(\omega_{\mathrm{S}}+\omega_{+})+\gamma/2]}, \tag{3.43d}$$

where $\omega_{\pm} = \omega_0 \pm \omega_{\mathrm{P}}$, and

$$\begin{aligned}\mathcal{D}_1 &= 4\hbar^2\left[i(\omega_{\mathrm{S}}-\omega_0)+\gamma/2\right] + \frac{\left|\mathbf{D}\cdot\mathbf{E}_0^{\mathrm{P}}\right|^2}{i(\omega_{\mathrm{S}}-\omega_-)+\gamma/2} + \frac{\left|\mathbf{D}\cdot\mathbf{E}_0^{\mathrm{P}}\right|^2}{i(\omega_{\mathrm{S}}-\omega_+)+\gamma/2},\\ \mathcal{C}_1 &= 4\hbar^2\left[-i(\omega_{\mathrm{S}}+\omega_0)+\gamma/2\right] + \frac{\left|\mathbf{D}\cdot\mathbf{E}_0^{\mathrm{P}}\right|^2}{-i(\omega_{\mathrm{S}}+\omega_-)+\gamma/2} + \frac{\left|\mathbf{D}\cdot\mathbf{E}_0^{\mathrm{P}}\right|^2}{-i(\omega_{\mathrm{S}}+\omega_+)+\gamma/2}.\end{aligned} \tag{3.44}$$

3.4.2.5 Evaluation of the induced electric/magnetic dipole moments

Thus, because we neglect the pump dynamics and here we focus on the CD enhancement produced by EIT and LWI, we calculate the induced electric and magnetic dipole moments only at the signal frequency, retaining only $\pm\omega_{\mathrm{S}}$ angular frequency terms as below:

$$\mathbf{d}_{\mathrm{S}} = \mathrm{Tr}\left[\hat{\rho}\,\hat{\mathbf{d}}\right]_{\omega=\pm\omega_{\mathrm{S}}}, \tag{3.45a}$$

$$\mathbf{m}_{\mathrm{S}} = \mathrm{Tr}[\hat{\rho}\,\hat{\mathbf{m}}]_{\omega=\pm\omega_{\mathrm{S}}}. \tag{3.45b}$$

The induced electric $\mathbf{d}_{\mathrm{S}}$ and magnetic $\mathbf{m}_{\mathrm{S}}$ dipole moments at the signal frequency are calculated as the expectation values of electric $\hat{\mathbf{d}} = \sum_{n,m=1}^{2}\mathbf{d}_{nm}\left|n\right\rangle\!\left\langle m\right|$ and $\hat{\mathbf{m}} = \sum_{n,m=1}^{2}\mathbf{m}_{nm}\left|n\right\rangle\!\left\langle m\right|$ magnetic dipole moment operators over the time-dependent density matrix oscillating with $\pm\omega_{\mathrm{S}}$ angular frequencies, i.e.,

$$\mathbf{d}_{\mathrm{S}} = 2\mathrm{Re}\left[\mathbf{d}_{12}\left(r_+^{\mathrm{S}*}+r_-^{\mathrm{S}}\right)e^{-i\omega_{\mathrm{S}}t}\right], \tag{3.46a}$$

$$\mathbf{m}_{\mathrm{S}} = 2\mathrm{Re}\left[\mathbf{m}_{12}\left(r_+^{\mathrm{S}*}-r_-^{\mathrm{S}}\right)e^{-i\omega_{\mathrm{S}}t}\right]. \tag{3.46b}$$

We obtain

$$\mathbf{d}_{\mathrm{S}}(t) = \mathrm{Re}\left\{[\hat{\alpha}_{\mathrm{dE}}:\mathbf{E}_0^{\mathrm{S}}+\hat{\alpha}_{\mathrm{dB}}:\mathbf{B}_0^{\mathrm{S}}]e^{-i\omega_{\mathrm{S}}t}\right\}, \tag{3.47a}$$

$$\mathbf{m}_{\mathrm{S}}(t) = \mathrm{Re}\left\{[\hat{\alpha}_{\mathrm{mE}}:\mathbf{E}_0^{\mathrm{S}}+\hat{\alpha}_{\mathrm{mB}}:\mathbf{B}_0^{\mathrm{S}}]e^{-i\omega_{\mathrm{S}}t}\right\}, \tag{3.47b}$$

where $\hat{\alpha}_{\mathrm{dE}}, \hat{\alpha}_{\mathrm{dB}}, \hat{\alpha}_{\mathrm{mE}}, \hat{\alpha}_{\mathrm{mB}}$ are electric, magnetic, and mixing hyperpolarisability tensors, respectively, reported below. Such tensors depend on the entire pump vectorial field amplitude $\mathbf{E}_0^{\mathrm{P}} = E_0^{\mathrm{P}}\hat{\mathbf{n}}_{\mathrm{P}}$, where $E_0^{\mathrm{P}} = |E_0^{\mathrm{P}}|e^{i\phi_{\mathrm{P}}}$ is the pump scalar amplitude with phase ϕ_{P} and modulus $|E_0^{\mathrm{P}}| = \sqrt{2I_{\mathrm{P}}/\epsilon_0 c}$ depending on its intensity I_{P}, ϵ_0 is the dielectric permittivity of vacuum, and $\hat{\mathbf{n}}_{\mathrm{P}}$ is the pump polarization unit vector.

Thus, $\mathbf{d}_{\mathrm{S}}$ and $\mathbf{m}_{\mathrm{S}}$ can get expressed as Eq. 3.47, where

$$\hat{\alpha}_{\mathrm{dE}} = 2\mathbf{d}_{12} \otimes (\mathbf{a}^* + \mathbf{c}), \tag{3.48a}$$

$$\hat{\alpha}_{\mathrm{dB}} = 2\mathbf{d}_{12} \otimes (\mathbf{b}^* + \mathbf{d}), \tag{3.48b}$$

$$\hat{\alpha}_{\mathrm{mE}} = 2\mathbf{m}_{12} \otimes (\mathbf{a}^* - \mathbf{c}), \tag{3.48c}$$

$$\hat{\alpha}_{\mathrm{mB}} = 2\mathbf{m}_{12} \otimes (\mathbf{b}^* - \mathbf{d}), \tag{3.48d}$$

the $\otimes$ operation indicates the dyadic product, and the vectors $\mathbf{a}, \mathbf{b}, \mathbf{c}, \mathbf{d}$ are defined in Eq 3.42.

3.4.2.6 Chiral optical theorem

In light-matter interactions, electromagnetic radiation exchanges energy with matter, maintaining energy conservation. We calculate the signal energy dissipation rate as below:

$$dU_{\mathrm{S}}/dt = \langle \int_{\tau} \mathbf{J}_{\mathrm{S}} \cdot \mathbf{E}_{\mathrm{S}}\, d\tau \rangle_{T_{\mathrm{S}}} \tag{3.49}$$

where $\mathbf{J}_{\mathrm{S}}$ is the current density radiating the electric field $\mathbf{E}_{\mathrm{S}}$.

Assuming monochromatic field excitation, one gets

$$\begin{aligned} \mathbf{J}_{\mathrm{S}}(\mathbf{r}, t) &= \mathrm{Re}\left[\mathbf{J}_0^{\mathrm{S}}(\mathbf{r})\, e^{-i\omega_{\mathrm{S}} t}\right], \\ \mathbf{E}_{\mathrm{S}}(\mathbf{r}, t) &= \mathrm{Re}\left[\mathbf{E}_0^{\mathrm{S}}(\mathbf{r})\, e^{-i\omega_{\mathrm{S}} t}\right]. \end{aligned} \tag{3.50}$$

The signal energy dissipation rate, assuming monochromatic field excitation, can

be expressed as,

$$\frac{dU_{\mathrm{S}}}{dt} = -\frac{1}{2}\int_{\tau} \mathrm{Re}\left[\mathbf{J}_0^{\mathrm{S}*}(\mathbf{r}) \cdot \mathbf{E}_0^{\mathrm{S}}(\mathbf{r})\right]\, d\tau \tag{3.51}$$

The signal current density within the molecular volume τ and averaged over the signal single-cycle $T_{\mathrm{S}} = 2\pi/\omega_{\mathrm{S}}$ can be calculated as

$$\mathbf{J}_{\mathrm{S}}(\mathbf{r}, t) = (d\mathbf{d}_{\mathrm{S}}/dt)\delta(\mathbf{r} - \mathbf{r}_0) + \nabla \times [\mathbf{m}_{\mathrm{S}}\delta(\mathbf{r} - \mathbf{r}_0)], \tag{3.52}$$

where $\mathbf{r}_0$ is the position vector indicating the molecule position, and $\delta(\mathbf{r} - \mathbf{r}_0)$ is the three-dimensional Dirac delta-function.

In turn, we obtain

$$\begin{aligned}\frac{dU_{\mathrm{S}}}{dt} = {} & \frac{\omega_{\mathrm{S}}}{2}\,\mathrm{Im}\{\mathbf{d}_{\mathrm{S}}^* \cdot \mathbf{E}_0^{\mathrm{S}}(\mathbf{r}_0)\} \\ & - \frac{1}{2}\,\mathrm{Re}\int_{\tau} \mathbf{E}_0^{\mathrm{S}}(\mathbf{r}) \cdot \{\delta(\mathbf{r} - \mathbf{r}_0)\,\nabla \times [\mathbf{m}_{\mathrm{S}}^*] + [\nabla\delta(\mathbf{r} - \mathbf{r}_0)] \times \mathbf{m}_{\mathrm{S}}^*(\mathbf{r})\}\, d\tau.\end{aligned} \tag{3.53}$$

We obtain the signal energy dissipation rate as below:

$$\frac{dU_{\mathrm{S}}}{dt} = \frac{\omega_{\mathrm{S}}}{2}\,\mathrm{Im}\left[\mathbf{d}_{\mathrm{S}}^* \cdot \mathbf{E}_0^{\mathrm{S}}(\mathbf{r}_0) + \mathbf{m}_{\mathrm{S}}^* \cdot \mathbf{B}_0^{\mathrm{S}}(\mathbf{r}_0)\right], \tag{3.54}$$

where $\mathbf{d}_{\mathrm{S}}$ and $\mathbf{m}_{\mathrm{S}}$ are expressed in Eq. 3.47.

The signal ACS is in turn calculated as

$$\sigma_{\mathrm{NL}} = (1/I_{\mathrm{S}})(dU_{\mathrm{S}}/dt), \tag{3.55}$$

where $I_{\mathrm{S}} = (1/2)\epsilon_0 c|\mathbf{E}_0^{\mathrm{S}}|^2$ is the intensity of the impinging signal, explicitly given by

$$\begin{aligned}\sigma_{\mathrm{NL}} = {} & \frac{\omega_{\mathrm{S}}}{\epsilon_0 c}\mathrm{Im}\left\{\hat{\mathbf{n}}_{\mathrm{S}}^* \cdot \left[\hat{\alpha}_{\mathrm{dE}} : \hat{\mathbf{n}}_{\mathrm{S}} + \frac{1}{c}\hat{\alpha}_{\mathrm{dB}} : \left(\hat{\mathbf{k}}_{\mathrm{S}} \times \hat{\mathbf{n}}_{\mathrm{S}}\right)\right] + \right. \\ & \left. + \frac{1}{c}\left(\hat{\mathbf{k}}_{\mathrm{S}} \times \hat{\mathbf{n}}_{\mathrm{S}}^*\right) \cdot \left[\frac{1}{c}\hat{\alpha}_{\mathrm{mB}} : \left(\hat{\mathbf{k}}_{\mathrm{S}} \times \hat{\mathbf{n}}_{\mathrm{S}}\right) + \hat{\alpha}_{\mathrm{mE}} : \hat{\mathbf{n}}_{\mathrm{S}}\right]\right\},\end{aligned} \tag{3.56}$$

where $\hat{\mathbf{n}}_{\mathrm{S}} = \mathbf{E}_0^{\mathrm{S}}/|\mathbf{E}_0^{\mathrm{S}}|$ and $\hat{\mathbf{k}}_{\mathrm{S}}$ are unit vectors of the signal electric field and wave vector, respectively. Note that, owing to the assumption of weak signal intensity, the ACS depends solely on the pump intensity I_{P} and not on the signal I_{S}, while depending on the polarization/propagation direction of both pump/signal waves and thus on molecular orientation.

We express the expression of the signal ACS below in a more simplified way

$$\begin{aligned}\sigma_{\mathrm{NL}} = 2\,\frac{\omega_{\mathrm{S}}}{\varepsilon_0 c}\,\mathrm{Im}\Bigg\{ & \left[\hat{\mathbf{n}}_{\mathrm{S}}^{*}\cdot\mathbf{d}_{12}\right]\left[(\mathbf{a}^{*}+\mathbf{c})\cdot\hat{\mathbf{n}}_{\mathrm{S}}\right] \\ & + \frac{1}{c^2}\left[(\hat{\mathbf{k}}_{\mathrm{S}}\times\hat{\mathbf{n}}_{\mathrm{S}}^{*})\cdot\mathbf{m}_{12}\right]\left[(\mathbf{b}^{*}-\mathbf{d})\cdot(\hat{\mathbf{k}}_{\mathrm{S}}\times\hat{\mathbf{n}}_{\mathrm{S}})\right] \\ & + \frac{1}{c}\left[\hat{\mathbf{n}}_{\mathrm{S}}^{*}\cdot\mathbf{d}_{12}\right]\left[(\mathbf{b}^{*}+\mathbf{d})\cdot(\hat{\mathbf{k}}_{\mathrm{S}}\times\hat{\mathbf{n}}_{\mathrm{S}})\right] \\ & + \frac{1}{c}\left[(\hat{\mathbf{k}}_{\mathrm{S}}\times\hat{\mathbf{n}}_{\mathrm{S}}^{*})\cdot\mathbf{m}_{12}\right]\left[(\mathbf{a}^{*}-\mathbf{c})\cdot\hat{\mathbf{n}}_{\mathrm{S}}\right]\Bigg\}.\end{aligned} \tag{3.57}$$

where $\mathbf{a}$, $\mathbf{b}$, $\mathbf{c}$, $\mathbf{d}$ is expressed above; see Eq. 3.42.

3.5 Results and Discussion

In this section, we first discuss the linear optical response of the chiral molecule. Next, we introduce the NL response and study how molecular orientation affects the corresponding observables. We then examine how the NL-DSF depends on different system parameters, and determine the minimum pump intensity required to achieve EIT and LWI. Finally, at this optimal intensity, we evaluate the NL-DSF to determine the enhancement of the chiroptical signal. In the following subsections, each point is discussed in detail.

The entire linear and NL chiroptical properties of the considered molecule upon pump excitation are incorporated in Eq. 3.56, as well as its inherent anisotropy. As a consequence, the chiral molecule experiences a modulated ACS upon pump/signal excitation.

Therefore, over distinct directions, in spherical coordinates, are accounted for by the unit vectors as given below:

$$\hat{\mathbf{k}}_{\mathrm{P,S}} = \sin\vartheta_{\mathrm{P,S}}\cos\varphi_{\mathrm{P,S}}\hat{\mathbf{e}}_x + \sin\vartheta_{\mathrm{P,S}}\sin\varphi_{\mathrm{P,S}}\hat{\mathbf{e}}_y + \cos\vartheta_{\mathrm{P,S}}\hat{\mathbf{e}}_z, l \tag{3.58}$$

where $\hat{\mathbf{e}}_{x,y,z}$ are Cartesian unit vectors spanning the x, y, z axes, and $\vartheta_{\mathrm{P,S}}, \varphi_{\mathrm{P,S}}$ are the pump/signal wavevector zenithal and azimuthal angles in the considered reference frame, respectively.

Moreover, the molecule experiences a NL DACS $\Delta\sigma_{\mathrm{NL}} = \left(\sigma_{\mathrm{NL}}^{\mathrm{LCP}} - \sigma_{\mathrm{NL}}^{\mathrm{RCP}}\right)$ upon RCP/LCP illumination by the signal, accounted for by the RCP/LCP unit vectors as given below:

$$\begin{aligned} \hat{\mathbf{n}}_{\mathrm{S}}^{(s)} &= \mathcal{N}^{-1}\left(\mathcal{N}_x\hat{\mathbf{e}}_x + \mathcal{N}_y^{(s)}\hat{\mathbf{e}}_y + \mathcal{N}_z^{(s)}\hat{\mathbf{e}}_z\right), \\ &\text{where, } s = +1 \quad \rightarrow \text{RCP}, \\ &\qquad\quad s = -1 \quad \rightarrow \text{LCP}. \end{aligned} \tag{3.59}$$

Upon arbitrary excitation direction as described by the equations below,

$$\mathcal{N}_x = 1 - \sin^2\vartheta\cos^2\varphi, \tag{3.60a}$$

$$\mathcal{N}_y^{(s)} = -\sin^2\vartheta\sin\varphi\cos\varphi + is\cos\vartheta, \tag{3.60b}$$

$$\mathcal{N}_z^{(s)} = -\sin\vartheta\Big(\cos\vartheta\cos\varphi + is\sin\varphi\Big). \tag{3.60c}$$

where the magnitude of the vector is denoted as $\mathcal{N} = \sqrt{|\mathcal{N}_x|^2 + |\mathcal{N}_y^{(s)}|^2 + |\mathcal{N}_z^{(s)}|^2}$.

3.5.1 Linear response

The linear molecular ACS can be straightforwardly calculated by setting $I_{\mathrm{P}} = 0$

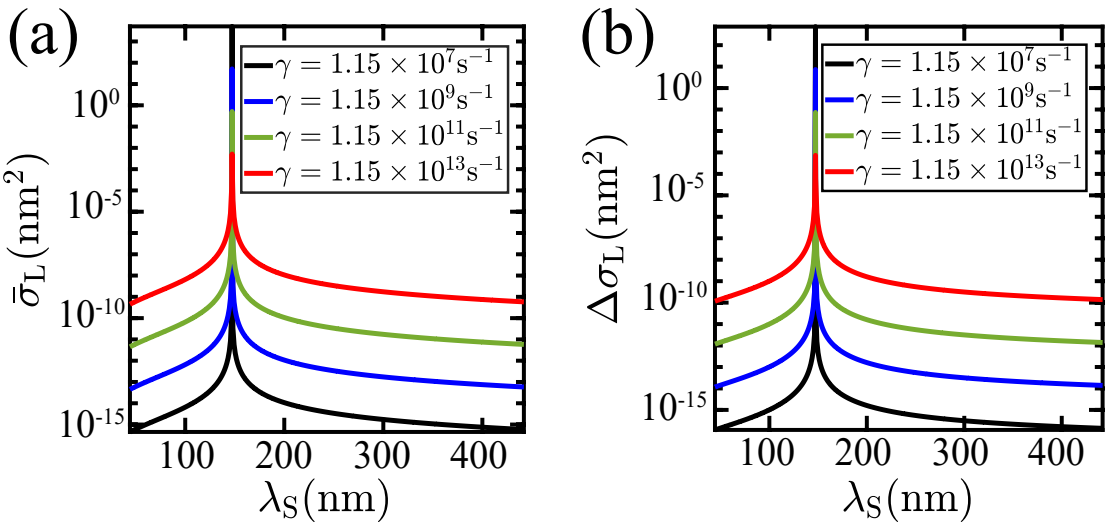

Figure 3.4 **(a)** Dependence of the average linear ACS $\bar{\sigma}_\mathrm{L} = (\sigma_\mathrm{L}^\mathrm{RCP} + \sigma_\mathrm{L}^\mathrm{LCP})/2$ on the signal wavelength λ_S for fixed propagation direction $\hat{\mathbf{k}}_\mathrm{S} = \hat{\mathbf{e}}_z$ and several distinct recombination rates $\gamma = \gamma_\mathrm{rad}$ (black curve), $10^2 \times \gamma_\mathrm{rad}$ (blue curve), $10^4 \times \gamma_\mathrm{rad}$ (green curve), and $10^6 \times \gamma_\mathrm{rad}$ (red curve). **(b)** Dependence of the linear DACS $\Delta\sigma_\mathrm{L} = \sigma_\mathrm{L}^\mathrm{LCP} - \sigma_\mathrm{L}^\mathrm{RCP}$ on the signal wavelength λ_S for identical signal propagation direction and electron recombination rates, with the same colour code as in **(a)**. The plots are obtained for the fluoroxirane S enantiomer.

in

$$\hat{\alpha}_{dE} = \left\{ -\frac{\mathbf{d}_{1,2} \otimes \mathbf{d}_{1,2}}{\hbar\,(\omega_\mathrm{S} - \Omega)} + \frac{\mathbf{d}_{1,2} \otimes \mathbf{d}_{1,2}}{\hbar\,(\omega_\mathrm{S} + \Omega)} \right\}, \tag{3.61a}$$

$$\hat{\alpha}_{dB} = \left\{ \frac{\mathbf{d}_{1,2} \otimes \mathbf{m}_{1,2}}{\hbar\,(\omega_\mathrm{S} - \Omega)} + \frac{\mathbf{d}_{1,2} \otimes \mathbf{m}_{1,2}}{\hbar\,(\omega_\mathrm{S} + \Omega)} \right\}, \tag{3.61b}$$

$$\hat{\alpha}_{mE} = \left\{ -\frac{\mathbf{m}_{1,2} \otimes \mathbf{d}_{1,2}}{\hbar\,(\omega_\mathrm{S} - \Omega)} - \frac{\mathbf{m}_{1,2} \otimes \mathbf{d}_{1,2}}{\hbar\,(\omega_\mathrm{S} + \Omega)} \right\}, \tag{3.61c}$$

$$\hat{\alpha}_{mB} = \left\{ \frac{\mathbf{m}_{1,2} \otimes \mathbf{m}_{1,2}}{\hbar\,(\omega_\mathrm{S} - \Omega)} - \frac{\mathbf{m}_{1,2} \otimes \mathbf{m}_{1,2}}{\hbar\,(\omega_\mathrm{S} + \Omega)} \right\}. \tag{3.61d}$$

where $\Omega = \omega_0 + i\gamma/2$ see Eq. 3.39, providing the linear ACS as

$$\sigma_\mathrm{L}(\omega_\mathrm{S}) = \frac{2\omega_\mathrm{S}^2\omega_0\gamma}{\varepsilon_0\hbar c\mathcal{D}}\{(|\tilde{d}_{12}|^2 + |\tilde{m}_{12}|^2) + \mathcal{N}\mathrm{Re}[\tilde{d}_{12}\tilde{m}_{12}]\}, \tag{3.62}$$

where $\mathcal{D}(\omega_\mathrm{S}) = (\omega_0^2 - \omega_\mathrm{S}^2 + \gamma^2/4)^2 + \gamma^2\omega_\mathrm{S}^2$, $\mathcal{N}(\omega_\mathrm{S}) = (\omega_0^2 + \omega_\mathrm{S}^2 + \gamma^2/4)/\omega_\mathrm{S}\omega_0$, $\tilde{d}_{12} = \mathbf{d}_{12} \cdot \hat{\mathbf{n}}_\mathrm{S}$, and $\tilde{m}_{12} = \mathbf{m}_{12} \cdot (\hat{\mathbf{k}}_\mathrm{S} \times \hat{\mathbf{n}}_\mathrm{S}^*)/c$.

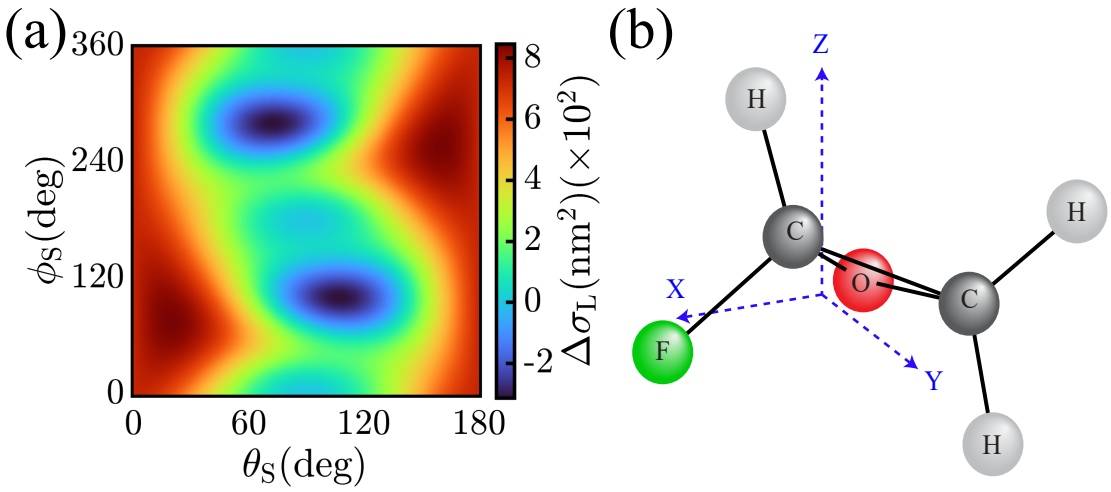

Figure 3.5 **(a)** Dependence of the linear DACS $\Delta\sigma_{\mathrm{L}} = \sigma_{\mathrm{L}}^{\mathrm{RCP}} - \sigma_{\mathrm{L}}^{\mathrm{LCP}}$ on the azimuthal φ_{S} and zenithal ϑ_{S} signal wavenumber angles for fixed resonant excitation wavelength $\lambda_{\mathrm{S}} = 147.3$ nm and decay rate $\gamma = \gamma_{\mathrm{rad}} = 1.15 \times 10^7$ s^{-1}. **(b)** Illustration of the molecule orientation in the considered $x-y-z$ cartesian reference frame spanned by the unit vectors $\hat{\mathbf{e}}_{x,y,z}$. The plots are obtained for the fluoroxirane S enantiomer orientation depicted in **(b)**.

In the linear limit, the DACS $\Delta\sigma_{\mathrm{L}} = \sigma_{\mathrm{L}}^{\mathrm{LCP}} - \sigma_{\mathrm{L}}^{\mathrm{RCP}}$ is in turn given by

$$\Delta\sigma_{\mathrm{L}} = \frac{4\omega_{\mathrm{S}}^2\omega_0\gamma\mathcal{N}}{\varepsilon_0\hbar c\mathcal{D}}\mathcal{F}, \tag{3.63}$$

where

$$\mathcal{F} = \frac{1}{c}\mathrm{Re}\left\{\left(\mathbf{d}_{12}\cdot\hat{\mathbf{n}}_{\mathrm{S}}^{(-)}\right)\left[\mathbf{m}_{12}\cdot\left(\hat{\mathbf{k}}_{\mathrm{S}}\times\hat{\mathbf{n}}_{\mathrm{S}}^{(-)*}\right)\right]\right\}. \tag{3.64}$$

Fluoroxirane ACS $\bar{\sigma}_{\mathrm{L}} = (\sigma_{\mathrm{L}}^{\mathrm{RCP}} + \sigma_{\mathrm{L}}^{\mathrm{LCP}})/2$ and DACS $\Delta\sigma_{\mathrm{L}} = \sigma_{\mathrm{L}}^{\mathrm{LCP}} - \sigma_{\mathrm{L}}^{\mathrm{RCP}}$ of the signal characterized by wavelength λ_{S} are illustrated in Figs. 3.4a,b for wave propagation $\hat{\mathbf{k}}_{\mathrm{S}}$ in $\hat{\mathbf{e}}_z$ direction, where the variation of several distinct recombination rates $\gamma = \gamma_{\mathrm{rad}}$ (black curve), $10^2 \times \gamma_{\mathrm{rad}}$ (blue curve), $10^4 \times \gamma_{\mathrm{rad}}$ (green curve), and $10^6 \times \gamma_{\mathrm{rad}}$ (red curve) are shown. Note that both the ACS and the DACS are resonant at $\lambda_0 \simeq 147.3$ nm, reaching values of the order of $\bar{\sigma}_{\mathrm{L}} = \left(\sigma_{\mathrm{L}}^{\mathrm{LCP}} + \sigma_{\mathrm{L}}^{\mathrm{RCP}}\right)/2 \simeq 10^3$ nm^2 and $\Delta\sigma_{\mathrm{L}} \simeq 10^2$ nm^2, producing resonant CD.

Moreover, the DACS heavily depends on the signal wavevector azimuthal and zenithal angles, as illustrated in Fig. 3.5a, which is plotted for a fixed resonant

excitation wavelength $\lambda_S = 147.3$ nm and decay rate $\gamma = \gamma_{rad} = 1.15 \times 10^7$ s^{-1}, and therefore the DACS heavily depends on molecular orientation, which in our calculations is fixed as illustrated in Fig. 3.5b. Note that, depending on the excitation direction, the DACS can be positive or negative, but with a positive average, which reflects the left-handed nature of the S-enantiomer; the opposite result is obtained for the R-enantiomer.

3.5.2 Nonlinear response

In the NL regime, EIT and LWI come into play after a particular pump intensity threshold dependent on the recombination rate γ, see below. Indeed, although the molecule possesses only two real energy states, $|1\rangle$ and $|2\rangle$ with transition energy $\hbar\omega_0 = \hbar(\omega_2 - \omega_1)$, the optical pump produces virtual states with transition energies $\hbar(\omega_0 + \omega_P)$ and $\hbar(\omega_0 - \omega_P)$, see Fig. 3.3. These virtual excitations mediate coherent processes in which energy is exchanged between pump and signal fields via molecular polarization without populating the real excited states. Indeed, the pump field substantially modifies the absorption profile beyond the primary resonance, as additional sidebands appear at $\lambda \simeq \lambda_\pm = 2\pi c/(\omega_0 \pm \omega_P)$ as a consequence of pump-induced virtual states.

3.5.2.1 Variation with signal field

Figs. 3.6a,b illustrate the NL-ACS dependence on the signal wavelength λ_S of the fluoroxirane S enantiomer for RCP/LCP (solid and dashed black curves, respectively) of the signal for fixed pump wavelength $\lambda_P = 1000$ nm, and pump intensities $I_P = 400$, 700, and 1000 TW/cm^2 are shown in blue, green, and red curves, respectively; see Fig. 3.6b. In Figs. 3.6a,b the pump and signal fields propagation directions are fixed to $\hat{\mathbf{k}}_{P,S} = \hat{\mathbf{e}}_z$, and the pump field is linearly polarized with unit vector $\hat{\mathbf{n}}_P = \hat{\mathbf{e}}_x$ and $\alpha_P = 0°$. Note that, for the considered

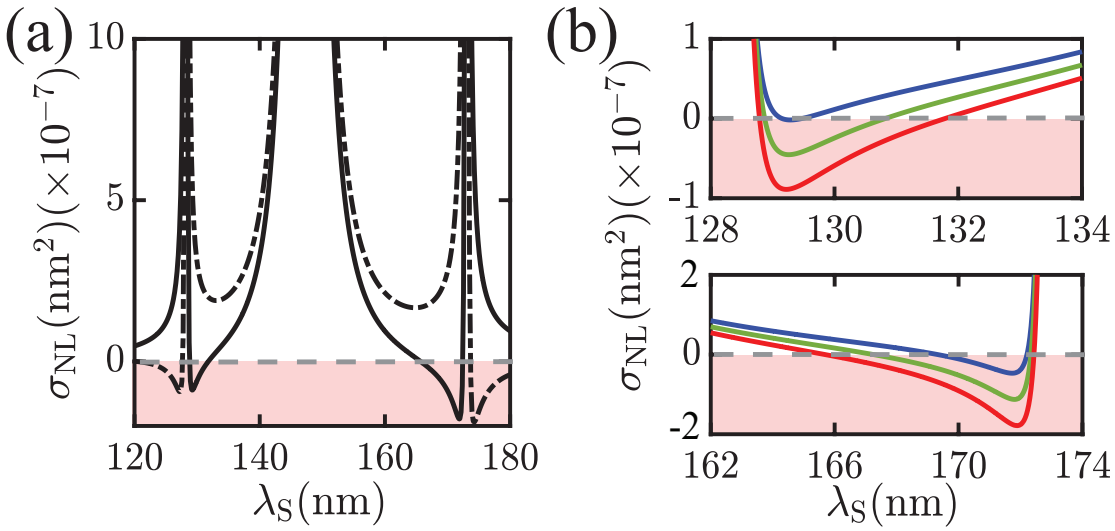

Figure 3.6 **(a-b)** NL-ACS σ_{NL} (in nm^2) as a function of the signal wavelength λ_{S} calculated at a fixed pump wavelength $\lambda_{\mathrm{P}} = 1000\,\mathrm{nm}$, for **(a)** RCP and LCP of the signal (solid and dashed black curves, respectively) and fixed pump intensity $I_{\mathrm{P}} = 1000\ \mathrm{TW/cm^2}$. **(b)** Zoom of the NL-ACS around the two wavelengths $\lambda_+ = 2\pi c/(\omega_0 + \omega_{\mathrm{P}})$ (top panel) and $\lambda_- = 2\pi c/(\omega_0 - \omega_{\mathrm{P}})$ (bottom panel), where EIT and LWI features appear, for RCP of the signal and pump intensities $I_{\mathrm{P}} = 400$, 700, and 1000 $\mathrm{TW/cm^2}$ (blue, green, and red curves, respectively). The plots are obtained for the fluoroxirane S enantiomer in vacuum, with a large damping rate $\gamma = 10^6 \times \gamma_{\mathrm{rad}}$ responsible for the large unphysical I_{P} involved (I_{P} can get heavily reduced to $\mathrm{kW/cm^2}$ for smaller damping, see Fig. 3.13 and the pump and signal fields propagation directions are fixed to $\hat{\mathbf{k}}_{\mathrm{P,S}} = \hat{\mathbf{e}}_z$, and the pump field is linearly polarized with $\alpha_{\mathrm{P}} = 0°$.

pump and signal fields, the NL-ACS vanishes at specific EIT wavelengths and becomes negative at peculiar LWI wavelength ranges around $\lambda_+ \simeq 127 - 129$ nm and $\lambda_- \simeq 171 - 174$ nm, depending on the signal RCP/LCP, see 3.6a. The sidebands lie around $\lambda \simeq \lambda_\pm$ because nonlinearity induces a resonance shift; see Fig. 3.6b. The zero baseline (gray line) in both figures denotes transparency, meaning that the molecule does not absorb the signal, whereas negative absorption indicates signal amplification that does not arise from population inversion, but rather from a coherent energy transfer from the optical pump. Such a coherence-mediated gain follows distinct dipole pathways incorporating $\mathbf{d}_{11} - \mathbf{d}_{22}$, $\mathbf{d}_{12}$, and $\mathbf{m}_{12}$, as schematically depicted in Fig. 3.3, and thus producing CP-dependent EIT and LWI owing to molecular chirality.

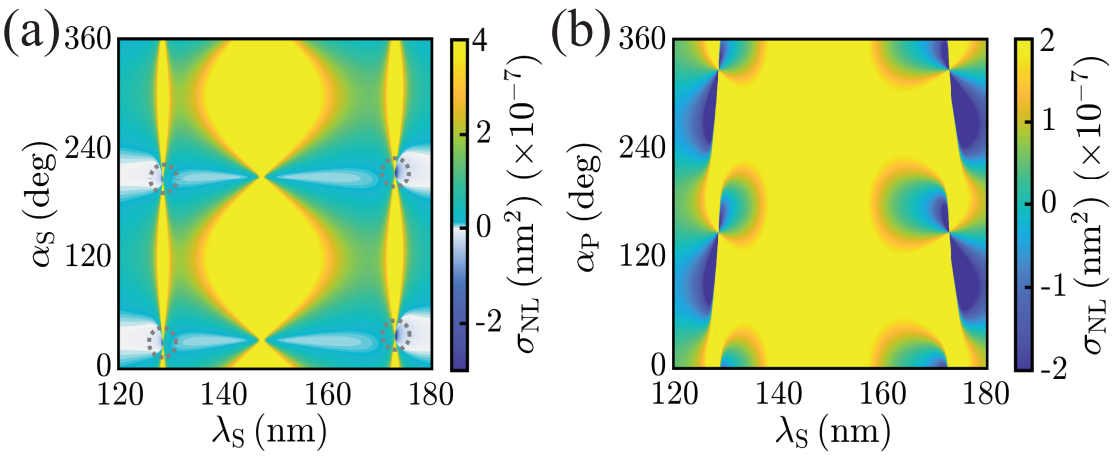

Figure 3.7 **(a,b)** NL-ACS dependence on λ_S and (**a**) the signal LP angle α_S (for fixed $\alpha_P = 0°$) or (**b**) the pump LP angle α_P (for fixed $\alpha_S = 0°$) for fixed RCP of the signal and pump intensity $I_P = 1000$ TW/cm^2. In **(a,b)** the colour bar is saturated in order to better illustrate EIT and LWI features. The plots are obtained for the fluoroxirane S enantiomer in vacuum, with a large damping rate $\gamma = 10^6 \times \gamma_{rad}$. In figures **(a-b)** the pump and signal fields propagation directions are fixed to $\hat{\mathbf{k}}_{P,S} = \hat{\mathbf{e}}_z$, and the pump field is linearly polarized with $\alpha_P = 0°$ but not in **(b)**, where α_P is modulated.

Figs. 3.7a,b illustrate the NL-ACS dependence on signal wavelength λ_S and also the signal LP angle α_S for a fixed pump LP angle $\alpha_P = 0°$ see Fig. 3.7a, and the pump LP angle α_P for a fixed signal LP angle $\alpha_S = 0°$ see Fig. 3.7b. Note also that, due to anisotropy, such coherent processes occur also for LP of the signal, see Fig. 3.7a. The signal polarization unit vector and pump polarization unit vector are defined as below:

$$\hat{\mathbf{n}}_S = \cos\alpha_S\,\hat{\mathbf{e}}_x + \sin\alpha_S\,\hat{\mathbf{e}}_y \tag{3.65a}$$

$$\hat{\mathbf{n}}_P = \cos\alpha_P\,\hat{\mathbf{e}}_x + \sin\alpha_P\,\hat{\mathbf{e}}_y \tag{3.65b}$$

These polarization unit vectors lie in the x-y plane for $\hat{\mathbf{k}}_S = \hat{\mathbf{e}}_z$, and are expressed in terms of a LP angle α_S with respect to the x-axis. Note that, at resonance, the NL-ACS is predominantly absorptive and only weakly dependent on α_S, producing the broad yellow band in the middle of 3.7a. Conversely, in the intensity- and CP-dependent sidebands around $\lambda_\pm$, σ_{NL} becomes highly sensitive to α_S, producing

absorption, amplification, or transparency (highlighted by the gray dashed circles), depending on the particular signal LP angle α_S. Analogously, also the pump polarization unit vector $\hat{\mathbf{n}}_P$ as denoted in Eq. 3.65 lies in the x-y plane for $\hat{\mathbf{k}}_P = \hat{\mathbf{e}}_z$ and can be expressed in terms of a LP angle α_P with respect to the x-axis. In 3.7b both signal and pump fields are assumed to propagate in the z direction with fixed RCP of the signal, and LP pump fields with fixed intensity $I_P = 1000$ TW/cm^2 and distinct LP angles α_P ranging from 0 to 2π. Note that, while the central resonant spectral region is almost insensitive to α_P, the sidebands show pronounced positive and negative lobes controlled by the pump LP. We emphasize that the colour bar in Figs. 3.7a,b is saturated in order to better illustrate the NL-ACS modulations, which are considerable at the sidebands' resonances $\lambda_\pm \simeq 128$ nm, 173 nm, but comparatively very weak at the electronic transition resonance $\lambda_0 \simeq 147.3$ nm denoted by the central region in Figs. 3.7a,b.

3.5.2.2 Variation with the pump field

In Fig. 3.8a the dependence of the NL-ACS on the pump intensity I_P for fixed $\alpha_P = 0°$ and $\lambda_P = 1000$ nm is examined for the two distinct signal wavelengths $\lambda_{S1} = 171$ nm and $\lambda_{S2} = 174$ nm, and for both RCP/LCP signal fields. Note that as I_P increases from 0 to 1000 TW/cm^2, the NL-ACS σ_{NL} increases or decreases linearly depending on the wavelength and the polarization and can cross the zero line, marking a transition from net absorption ($\sigma_{NL} > 0$) to net amplification ($\sigma_{NL} < 0$). For $\lambda_{S1} = 171$ nm, the LCP signal (dashed blue curve) exhibits an increasing positive σ_{NL}, whereas the corresponding RCP signal (solid blue curve) decreases with pump intensity, entering a gain regime highlighted by the shaded region. At $\lambda_{S2} = 174$ nm, the behaviour is reversed, as the LCP signal (dashed red curve) can get amplified while the RCP signal (solid red curve) remains absorbed. The crossings of the curves through $\sigma_{NL} = 0$ produce CP-dependent EIT, while regions with $\sigma_{NL} < 0$ label LWI regime. Indeed, we emphasize again that

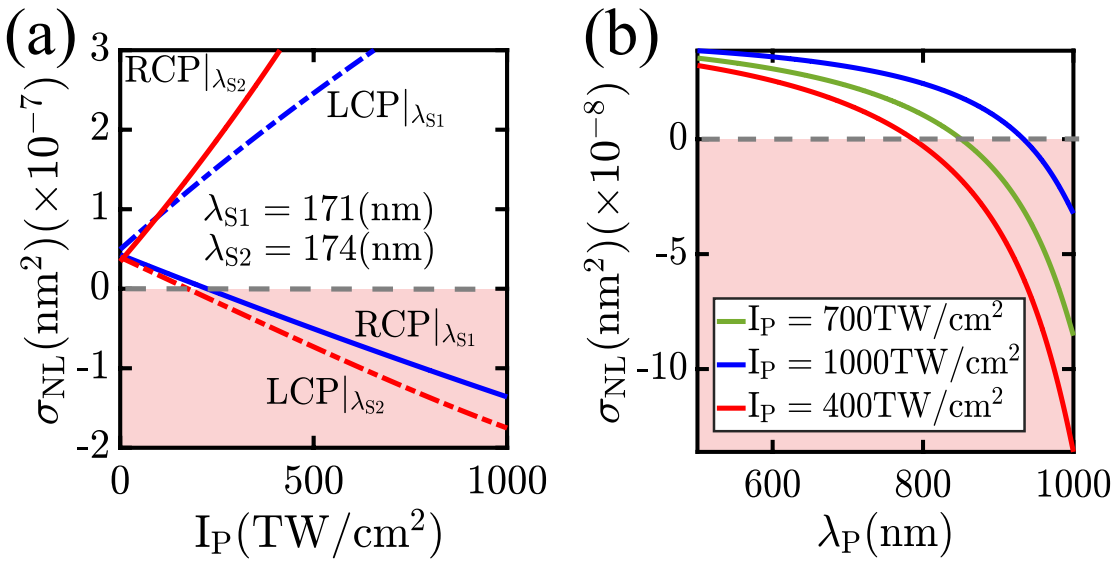

Figure 3.8 **(a)** NL-ACS dependence on the pump intensity I_P for fixed signal wavelengths $\lambda_S = 171\,\text{nm}$ (blue curves) and $\lambda_S = 174\,\text{nm}$ (red curves) and both RCP (solid curves) and LCP (dashed curves) of the signal. **(b)** Dependence of NL-ACS on the pump wavelength λ_P for fixed RCP of the signal with wavelength $\lambda_S = 171\,\text{nm}$ and several distinct pump intensities $I_P = 400$, 700, and 1000 TW/cm^2 (blue, green and red curves, respectively). The plots are obtained for the fluoroxirane S enantiomer in vacuum, with a large damping rate $\gamma = 10^6 \times \gamma_{rad}$ responsible for the large unphysical I_P involved (I_P can get heavily reduced to kW/cm^2 for smaller damping, see Fig. 3.13). In **(a-b)** the pump and signal fields propagation directions are fixed to $\hat{\mathbf{k}}_{P,S} = \hat{\mathbf{e}}_z$, and the pump field is LP with $\alpha_P = 0°$.

here amplification is achieved without resonant pumping, as $\lambda_P = 1000$ nm is far detuned from the UV signal transitions. Fig. 3.8b illustrates the NL-ACS σ_{NL} dependence on the pump wavelength λ_P for fixed RCP of the signal with wavelength $\lambda_S \simeq \lambda_- \simeq 171\,\text{nm}$ and several distinct pump intensities $I_P = 400$, 700, and 1000 TW/cm^2. Note that, in such $\lambda_S \simeq \lambda_-$ conditions, the NL-ACS decreases with the pump wavelength and becomes negative after an intensity-dependent wavelength threshold.

Note that all plots in Fig. 3.6, 3.7 and 3.8 are obtained for the fluoroxirane S enantiomer in vacuum, with a large damping rate $\gamma = 10^6 \times \gamma_{rad} \simeq 1.15 \times 10^{13}$ s^{-1}. Such a damping rate, typical for molecules in the gas phase at ambient temperature and pressure, is responsible for the large *unphysical* pump intensities

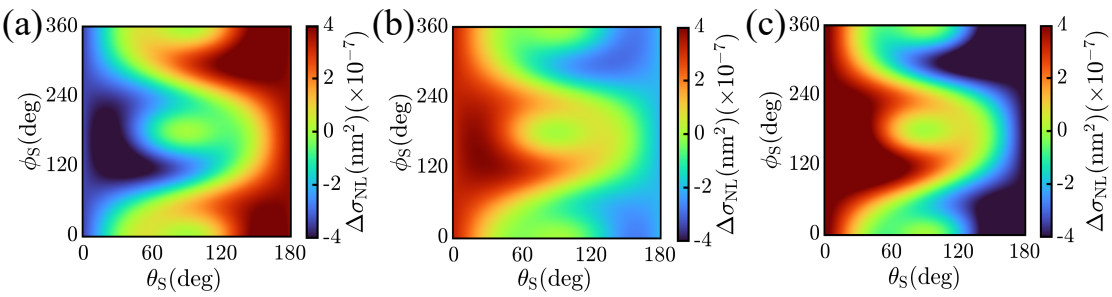

Figure 3.9 **(a-c)** Dependence of the NL-DACS $\Delta\sigma_{\rm NL} = \sigma_{\rm NL}^{\rm LCP} - \sigma_{\rm NL}^{\rm RCP}$ on the azimuthal $\varphi_{\rm S}$ and zenithal $\vartheta_{\rm S}$ angles of the signal normalized wavevector $\hat{\mathbf{k}}_{\rm S}$ for **(a)** LP with $\alpha_{\rm P} = 0°$, **(b)** RCP, and **(c)** LCP pump field with intensity $I_{\rm P} = 400$ TW/cm^2 and wavelength $\lambda_{\rm P} = 1000$ nm. All simulations are performed at a fixed signal wavelength $\lambda_{\rm S} = 174$ nm and damping rate $\gamma = 10^6 \times \gamma_{\rm rad} \simeq 1.15 \times 10^{13}$ s^{-1} for the S enantiomer of fluoroxirane in vacuum.

$I_{\rm P} > 500$ TW/cm^2 producing EIT and LWI above the molecular dissociation threshold [158]. However, such intensities can get heavily reduced to kW/cm^2 for smaller dampings, e.g., through laser cooling and trapping, producing $\gamma \simeq \gamma_{\rm rad}$, see below. In these plots we adopt a large damping in order to better illustrate the EIT and LWI spectral features, which become extremely narrow for $\gamma \simeq \gamma_{\rm rad}$ and thus it is difficult to grasp but maintain the same trends with $\lambda_{\rm S,P}$, $\hat{\mathbf{n}}_{\rm S,P}$, and $I_{\rm P}$.

3.5.3 Molecular orientation

Due to molecular anisotropy, the NL-DACS $\Delta\sigma_{\rm NL} = \sigma_{\rm NL}^{\rm LCP} - \sigma_{\rm NL}^{\rm RCP}$ depends on the zenithal angle $\vartheta_{\rm S}$ and the azimuthal angle $\varphi_{\rm S}$ of the impinging signal normalized wavevector $\hat{\mathbf{k}}_{\rm S}$. In 3.9 we illustrate the NL-DACS $\Delta\sigma_{\rm NL}(\vartheta_{\rm S}, \varphi_{\rm S})$ dependence on $\vartheta_{\rm S}, \varphi_{\rm S}$ for LP, RCP, and LCP of the pump at fixed pump intensity $I_{\rm P} = 400$ TW/cm^2, pump wavelength $\lambda_{\rm P} = 1000$ nm, signal wavelength $\lambda_{\rm S} = 174$ nm and damping rate $\gamma = 10^6 \times \gamma_{\rm rad} \simeq 1.15 \times 10^{13}$ s^{-1} for the S enantiomer of fluoroxirane in vacuum.

Note that, depending on the excitation angles $\vartheta_{\rm S}, \varphi_{\rm S}$, the signal LCP can get more absorbed than RCP in positive areas of the NL-DACS and vice versa. How-

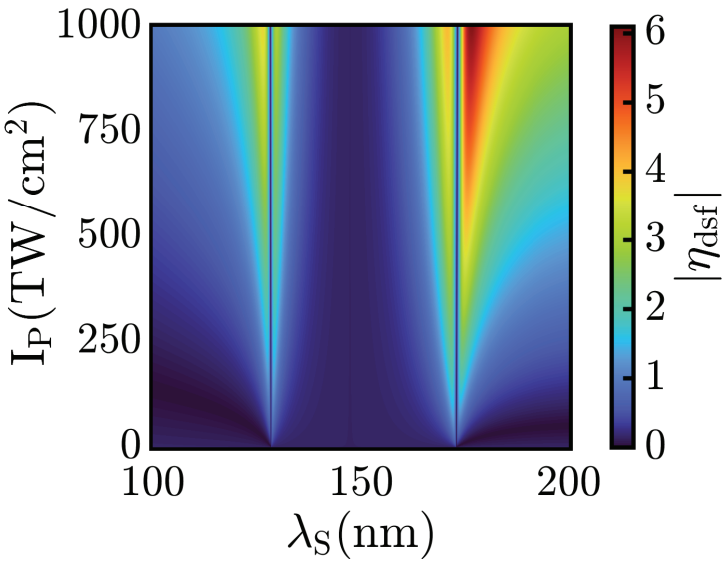

Figure 3.10 Dependence of the NL-DSF $\eta_{dsf} = \Delta\sigma_{NL}/\overline{\sigma}_{NL}$ on the signal wavelength λ_S and pump intensity I_P for fixed LP with $\alpha_P = 0°$, The plot is obtained for the S enantiomer of fluoroxirane with damping rate $\gamma = 10^6 \times \gamma_{rad} \simeq 1.15 \times 10^{13}$ s^{-1}, fixed pump wavelength $\lambda_P = 1000$ nm and the pump and signal excitation along the z-direction, i.e., $\hat{\mathbf{k}}_{P,S} = \hat{\mathbf{e}}_z$.

ever, such NL-DACS modulations with alternating sign, which exact shape depends on the particular pump polarization, see Figs. 3.9 a,b,c, do not average to zero as they are reminiscent of the left-handedness of the S fluoroxirane enantiomer, where the opposite result is obtained for the R enantiomer.

3.5.4 Evaluation nonlinear dissymmetry factor

To quantify the chiral sensitivity of the NL optical response, we evaluate the NL DSF $\eta_{dsf} = \Delta\sigma_{NL}/\overline{\sigma}_{NL}$, measuring the ratio between the NL-DACS $\Delta\sigma_{NL}$ and the average NL-ACS $\overline{\sigma}_{NL} = (\sigma_{NL}^{LCP} + \sigma_{NL}^{RCP})/2$.

Fig. 3.10 illustrates the dependence of the NL-DSF on both the pump intensity I_P and the signal wavelength λ_S. Note that the NL-DSF is greatly amplified at the virtual states resonances $\lambda_\pm = 2\pi c/(\omega_0 \pm \omega_P)$ and grows with increasing pump intensity, reflecting the central role played by pump-induced molecular coherence in amplifying the NL chiroptical signal.

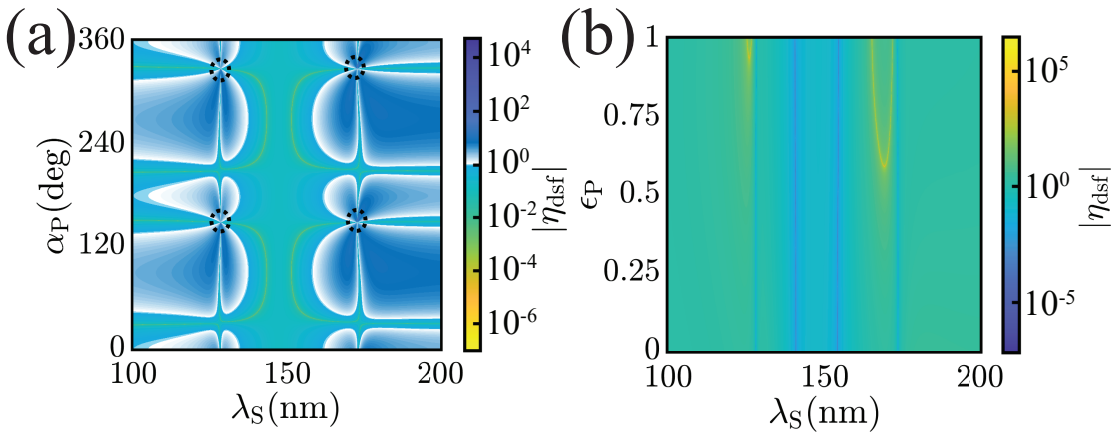

Figure 3.11 **(a-b)** Dependence of the NL-DSF $\eta_{dsf} = \Delta\sigma_{NL}/\overline{\sigma}_{NL}$ on the signal wavelength λ_S and pump **(a)** LP angle α_P for fixed intensity $I_P = 1000$ TW/cm^2, and **(b)** ellipticity ε_P (for fixed intensity $I_P = 1000$ TW/cm^2 also). The black dashed circles in **(a)** indicate maximum NL-DSF enhancement. The plots are obtained for the S enantiomer of fluoroxirane with damping rate $\gamma = 10^6 \times \gamma_{rad} \simeq 1.15 \times 10^{13}$ s^{-1}.

Similarly to the DACS, also the NL-DSF depends heavily on the pump polarization, as illustrated in Fig. 3.11a, depicting the NL-DSF dependence on the pump LP angle α_P for fixed intensity $I_P = 1000$ TW/cm^2 and wavelength $\lambda_P = 1000$ nm. Note that optimal NL-DSFs are attained around $\lambda_\pm$ and specific pump LP conditions, highlighted by the dashed black circles in Fig. 3.11a, due to the mutual direction of the pump electric $\mathbf{E}_0^P$ and magnetic $\mathbf{B}_0^P$ vectorial field amplitudes with respect to $\mathbf{D} = \mathbf{d}_{22} - \mathbf{d}_{11}$, $\mathbf{d}_{12}$, and $\mathbf{m}_{12}$, see Eq. 3.39, modulating the interference pathways producing the observed NL chiroptical response. To investigate more general pump polarization dependence, in Fig. 3.11b we depict the NL-DSF versus signal wavelength λ_S and pump ellipticity ε_P at fixed intensity $I_P = 1000$ TW/cm^2 and wavelength $\lambda_P = 1000$ nm. Elliptical pump polarization is accounted for by the unit vector $\hat{\mathbf{n}}_P = (\hat{\mathbf{e}}_x + e^{i\pi\varepsilon_P/2}\hat{\mathbf{e}}_y)/\sqrt{2}$, where the ellipticity ε_P varies from 0 (indicating LP with $\alpha_P = 45°$) to 1 RCP. Note that, similarly to LP, the NL-DSF is highly sensitive to ε_P, producing a NL-DSF exceeding the one observed for LP at particular excitation conditions identified by the yellow curve in Fig. 3.11b.

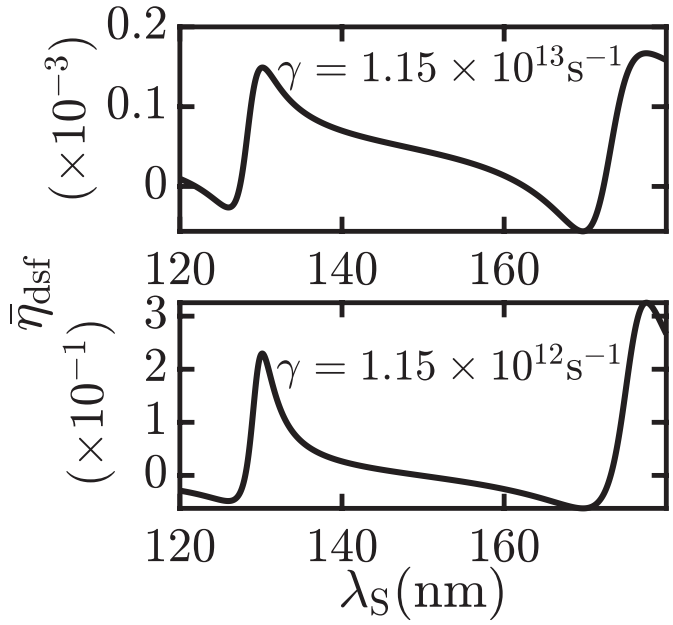

Figure 3.12 Orientation-averaged NL-DSF $\bar{\eta}_{\mathrm{dsf}}$ as a function of λ_{S} for different damping rates $\gamma = 1.15 \times 10^{13}$ s^{-1} (top panel) and $\gamma = 1.15 \times 10^{12}$ s^{-1} (bottom panel), and for fixed pump intensity $I_{\mathrm{P}} = 1000$ TW/cm^2 with LP angle $\alpha_{\mathrm{P}} = 0°$. The plot is obtained for the S enantiomer of fluoroxirane where γ is modified as described, and fixed pump wavelength $\lambda_{\mathrm{P}} = 1000$ nm. The NL-DSF is averaged over the signal-normalized wavevector zenithal ϑ_{S} and azimuthal φ_{S} angles.

We emphasize that Figs. 3.10 and 3.11 are obtained for pump and signal excitation along the z-direction, i.e., with normalized wavevectors $\hat{\mathbf{k}}_{\mathrm{P,S}} = \hat{\mathbf{e}}_z$. However, as illustrated in Fig. 3.5a and Figs. 3.9a-c, the chiroptical response heavily depends on the excitation direction. In turn, in order to quantify the average chiroptical response over molecular orientation, we calculate the averaged NL-DSF over the signal wavevector solid angle $\mathrm{d}^2\Omega_{\mathrm{S}} = \sin\vartheta_{\mathrm{S}}\mathrm{d}\vartheta_{\mathrm{S}}\mathrm{d}\varphi_{\mathrm{S}}$, explicitly given by $\bar{\eta}_{\mathrm{dsf}} = \langle\Delta\sigma_{\mathrm{NL}}\rangle_{\vartheta_{\mathrm{S}},\varphi_{\mathrm{S}}}/\langle\bar{\sigma}_{\mathrm{NL}}\rangle_{\vartheta_{\mathrm{S}},\varphi_{\mathrm{S}}}$, where $\langle(...)\rangle_{\vartheta_{\mathrm{S}},\varphi_{\mathrm{S}}} = \int_0^{2\pi}\mathrm{d}\varphi_{\mathrm{S}}\int_0^{\pi}\mathrm{d}\vartheta_{\mathrm{S}}\sin\vartheta_{\mathrm{S}}(...)/4\pi$. Fig. 3.12 illustrates the dependence of $\bar{\eta}_{\mathrm{dsf}}$ on the signal wavelength λ_{S} for two distinct damping rates $\gamma = 10^6 \times \gamma_{\mathrm{rad}} \simeq 1.15 \times 10^{13}$ s^{-1} (top panel) and $\gamma = 10^5 \times \gamma_{\mathrm{rad}} \simeq 1.15 \times 10^{12}$ s^{-1} (bottom panel). Note that smaller γ values produce sharper and larger NL-DSF features, consistent with longer coherence lifetimes that strengthen chiral wavemixing pathways. Indeed, by decreasing the decay rate by one order of magnitude, the NL-DSF amplitude increases by $\simeq 3$

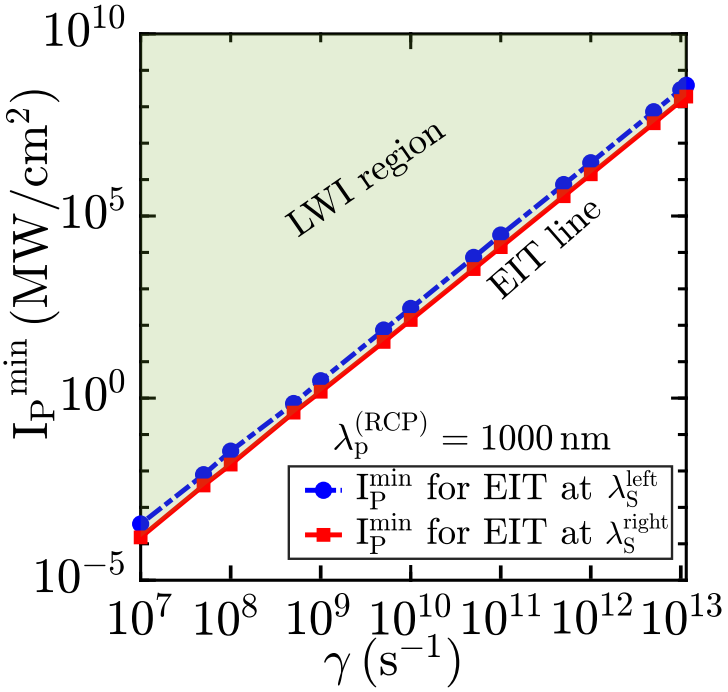

Figure 3.13 Dependence of the EIT pump intensity threshold I_P^{min} (pump propagating in the $\hat{\mathbf{e}}_z$ direction with fixed $\hat{\mathbf{n}}_P = \hat{\mathbf{e}}_x$ polarisation) on the damping rate γ for both LCP (blue circles) and RCP (red circles) signals propagating along $\hat{\mathbf{e}}_z$. The shaded region above the EIT intensity threshold line highlights the LWI regime producing net signal gain.

orders of magnitude and the resonances around $\lambda_\pm$ become more pronounced, see Fig. 3.12.

3.5.5 Evaluation of the threshold pump intensity for achieving EIT and LWI

As discussed above, decay rates $\simeq 10^{13}$ s^{-1} are typical for gas-phase molecular systems at ambient temperature and pressure. However, the decay rate of molecular systems can decrease down to the radiative one ($\gamma_{rad} \simeq 1.15 \times 10^7$ s^{-1} for the lowest-energy electronic transition of fluoroxirane considered here), e.g., by optical trapping combined with laser cooling techniques [159].

In turn, we systematically find the pump threshold intensity I_P^{min} producing EIT scanning the decay rate in the range $\gamma = 10^7 - 10^{13}$ s^{-1}, see Fig. 3.13, finding

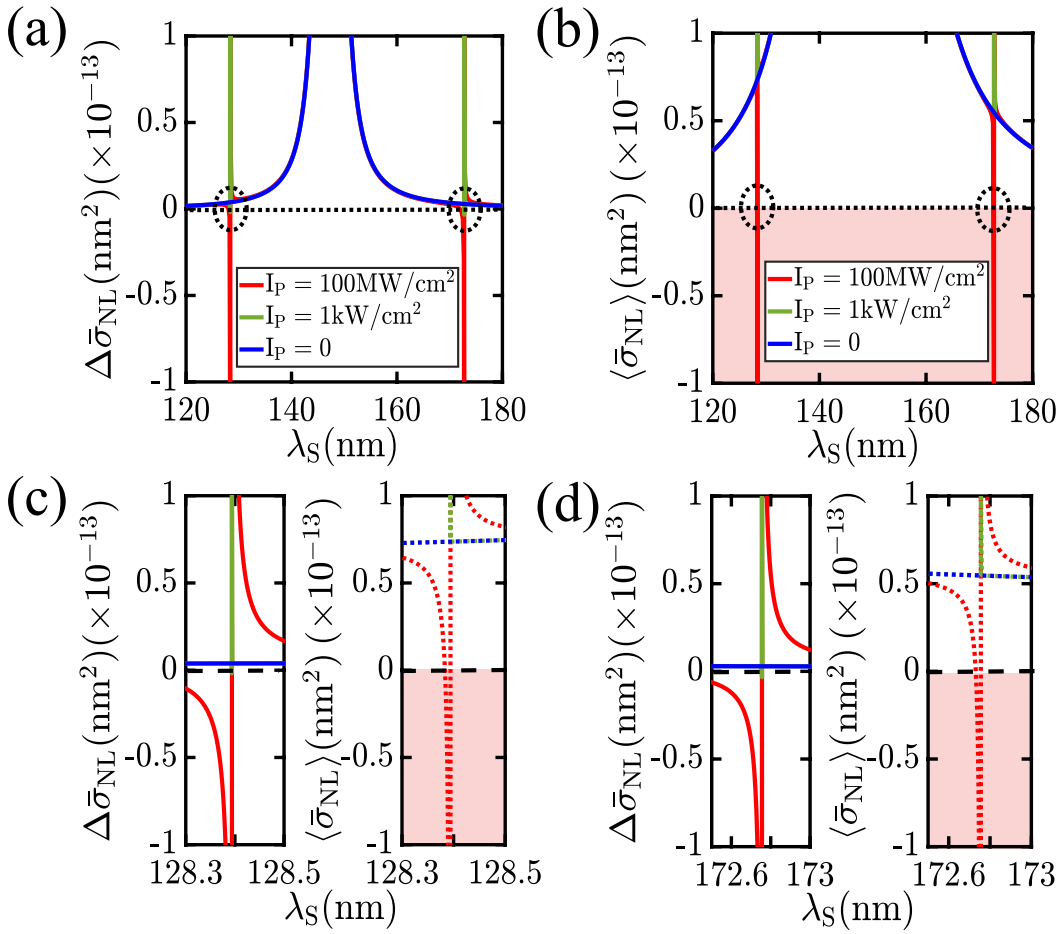

Figure 3.14 **(a,b)** Orientation-averaged **(a)** NL-DACS $\Delta\bar{\sigma}_{\rm NL}$ and **(b)** polarization-averaged NL-ACS $\langle\bar{\sigma}_{\rm NL}\rangle$ as a function of $\lambda_{\rm S}$ for several distinct pump intensities $I_{\rm P} = 0$, 1 kW/cm^2, and 100 MW/cm^2 (blue, green and red curves, respectively), and pump/signal excitation along the z-direction, such that $\hat{\mathbf{k}}_{\rm P,S} = \hat{\mathbf{e}}_z$ for fixed damping rate $\gamma = \gamma_{\rm rad} = 1.15 \times 10^7$ s^{-1}, **(c,d)** Zoom of **(a)** (left panel) and **(b)** (right panel) around the wavelength $\lambda_+ = 2\pi c/(\omega_0 + \omega_{\rm P})$ for RCP of the pump with intensities $I_{\rm P} = 0$, 1 kW/cm^2, and 100 MW/cm^2 (blue, green and red curves, respectively). All plots are obtained for the fluoroxirane S enantiomer pumped with fixed wavelength $\lambda_{\rm P} = 1000$ nm.

a remarkably low $I_{\rm P}^{\rm min} \simeq 1$ kW/cm^2 for $\lambda_{\rm P} = 1000$ nm and $\gamma = \gamma_{\rm rad}$, attainable with Continuous Wave (CW) laser systems. The EIT condition is attained at two distinct wavelengths $\lambda_{\rm S}^{\rm left}$ (for LCP) and $\lambda_{\rm S}^{\rm right}$ (for RCP) almost centered around λ_+ and weakly shifting with $I_{\rm P}$. The boundary separating the EIT and LWI regimes follows an approximate power-law relationship $I_{\rm P}^{\rm min} \propto \gamma^2$, reflecting the fact that stronger dephasing rate ($\gamma/2$) suppresses coherence and therefore requires higher

pump intensity to recover destructive interference in the absorption channel. The shaded region indicates conditions where the signal experiences LWI, while the line marks the EIT threshold.

3.5.6 Evaluation of enhancement factor

In Figs. 3.14 we illustrate the orientation-averaged **(a)** NL-DACS $\Delta\bar{\sigma}_{\rm NL}$ and **(b)** polarization-averaged NL-ACS $\langle\bar{\sigma}_{\rm NL}\rangle$ as a function of $\lambda_{\rm S}$ for several distinct pump intensities $I_{\rm P} = 0$, 1 kW/cm^2, and 100 MW/cm^2 (blue, green and red curves, respectively), and pump/signal excitation along the z-direction, such that $\hat{\mathbf{k}}_{\rm P,S} = \hat{\mathbf{e}}_z$ for fixed damping rate $\gamma = \gamma_{\rm rad} = 1.15 \times 10^7$ s^{-1}. Note that, owing to the reduced damping rate, the spectral EIT- and LWI-induced spectral features at $\lambda_{\rm S} \simeq \lambda_{\pm} = 2\pi c/(\omega_0 \pm \omega_{\rm P})$, which spectral behaviour is zoomed in Fig. 3.14c,d, become much more pronounced and narrower at CW laser intensities $\simeq 1$ kw/cm^2.

Remarkably, in contrast to any other chiroptical sensing technique to the best of our knowledge, EIT produces an orientation-averaged NL-DSF $\bar{\eta}_{\rm dsf}$ that can reach *diverging values* $\bar{\eta}_{\rm dsf} \to \infty$ owing to the vanishing of $\langle\bar{\sigma}_{\rm NL}\rangle$ around the virtual states resonances $\bar{\lambda}_{\pm} \simeq \lambda_{\pm}$.

In Figs. 3.15a,b we illustrate the dependence of the NL-ACS averaged over both molecular orientation and signal CP ($\langle\bar{\sigma}_{\rm NL}\rangle$) on the signal wavelength $\lambda_{\rm S}$ and pump intensity $I_{\rm P}$ around the wavelengths **(a)** $\lambda_+ = 2\pi c/(\omega_0 + \omega_{\rm P})$ and **(b)** $\lambda_- = 2\pi c/(\omega_0 - \omega_{\rm P})$ for fixed damping rate $\gamma = \gamma_{\rm rad} = 1.15 \times 10^7$ s^{-1}. The dashed black lines illustrate the diverging orientation-averaged NL-DSF curves, which can be obtained for $I_{\rm P} > 100$ kW/cm^2. Indeed, while for fixed molecular orientation the EIT intensity threshold can get as low as $I_{\rm P}^{\rm min} \simeq 1$ kW/cm^2, see Fig. 3.13, its average over molecular orientations increases to $I_{\rm P}^{\rm min} \simeq 100$ kW/cm^2 due to anisotropy.

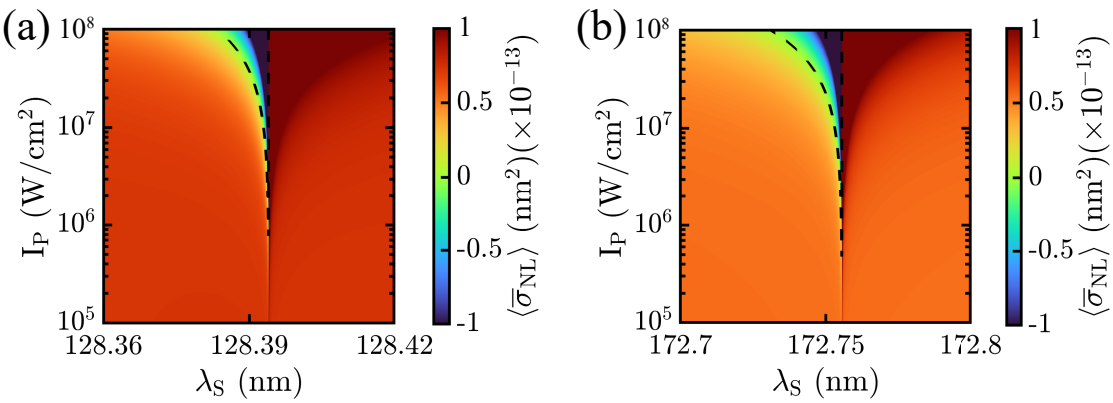

Figure 3.15 **(a-b)** Dependence of $\langle\bar{\sigma}_{\rm NL}\rangle$ (NL-ACS averaged over both molecular orientation and signal CP) on the signal wavelength $\lambda_{\rm S}$ and pump intensity $I_{\rm P}$ around the wavelengths **(a)** $\lambda_+ = 2\pi c/(\omega_0 + \omega_{\rm P})$ and **(b)** $\lambda_- = 2\pi c/(\omega_0 - \omega_{\rm P})$ for fixed damping rate $\gamma = \gamma_{\rm rad} = 1.15 \times 10^7$ s^{-1}. All plots are obtained for the fluoroxirane S enantiomer pumped with fixed wavelength $\lambda_{\rm P} = 1000$ nm.

In any case, the observed giant CD enhancement produced by quantum interference can be attained at intensities currently achievable through commercial CW laser systems.

3.6 Concluding remarks

In this paper we investigate the potential of EIT and LWI to enhance the DACS of fluoroxirane upon optical pumping and probing by RCP and LCP signals. We observe that, thanks to the polarity and chirality of fluoroxirane, EIT and LWI can occur also in the two-level approximation due to the excitation of virtual states produced by optical pumping. Because EIT and LWI are merely coherent phenomena, we find that the pump intensity threshold $I_{\rm P}^{\rm min}$ to observe such processes is highly dependent on the dephasing rate.

We find that, while one gets unphysical $I_{\rm P}^{\rm min} > 100$ TW/cm^2 for decay rates typical for gas-phase molecular systems at ambient temperature and pressure ($\gamma \simeq 10^{13}$ s^{-1}), by reducing the decay rate to the radiative one through optical trapping combined with laser cooling techniques ($\gamma_{\rm rad} \simeq 1.15 \times 10^7$ s^{-1} for the lowest energy electronic transition of fluoroxirane considered here), one gets $I_{\rm P}^{\rm min}$ as low as $I_{\rm P}^{\rm min} \simeq$

1 kW/cm^2 for fixed molecular orientation. Moreover, we systematically investigate EIT and LWI regimes, finding that they heavily depend on pump and signal polarization and molecular orientation. We find that, thanks to CP-sensitive EIT and LWI, one gets *diverging orientation-averaged CP dissymmetry factors* $\bar{\eta}_{\mathrm{dsf}} \to \infty$ *with* $I_{\mathrm{P}}^{\mathrm{min}} \simeq 1$ kW/cm^2, highlighting the great potential of EIT and LWI to probe chirality at the single-molecule level with current commercial CW laser systems.

3.7 Author contribution

The work presented in this chapter was carried out by the author. The author developed the research concept, implemented the theoretical and computational models, and performed all numerical simulations. She conducted the formal analysis and validation of the results, as well as data curation and visualization. The author also wrote the original draft of the manuscript and contributed to the presentation of the findings.

Chapter 4

Spontaneous emission of circularly polarized radiation in a chiral cavity

"Today, spontaneous emission is not a limit but a resource that we bend, split, and polarize, building new devices from the quantum field."

— Adapted from the ideas of Purcell, Novotny's *Principles of Nano-optics and contemporary quantum optics literature*

In nanophononics and quantum optics, the engineering of single-photon helicity has significant applications in chiral light-matter interactions for quantum communication. It was established that this purely quantum phenomenon is highly affected by the local environment of the quantum emitter. In this study, we explore the SE in a chiral cavity formed by two TAPCs structures. Given a specific vacuum wavelength, the considered mirror can be engineered to exhibit very high helicity-preserving reflectance for one CP and very high transmittance for the other CP for an incidence angle of 20° with respect to the optical axis. We con-

sider a two-level atomic quantum system in a cavity to calculate the complete DGF, taking into account both the inhomogeneous environment and scattering effects. We also analyze the impact of two CP on the SE rates induced by the chiral cavity; the effects differ by 3% after averaging over random dipole orientations. This approach can measure chirality and can provide insight into photonics devices that emit CP excitations at sub-micrometer scales.

4.1 Introduction

SE is an intrinsic radiative property of an atom or molecule in which the atom interacts with vacuum fields. Still, in a local environment, SE is influenced by the density of photonic states of the quantum emitter and the corresponding vacuum fluctuations of the electromagnetic field [160]. To observe this effect, one must design devices with dimensions on the order of the emission wavelength so that many relevant transitions occur in the optical range [161]. The atomic and molecular SE near different material structure has been reported in numerous articles, such as near a dielectric microsphere [162, 163, 164] and even near a cluster of two spherical nanoparticles [165, 166, 167]. Recent research has shifted its focus to study the SE in a chiral environment, such as a chiral nanoellipsoid [168], even near a cluster of two spherical chiral particles [169]. Additionally, it has been reported theoretically [170] and experimentally [171, 172, 173, 174] that the in-cavity environment can influence SE, which means that radiative properties can be altered using cavity walls [175, 176, 177]. In fact, SE can be inhibited [178, 179, 180, 181, 182] if the cavity is off-resonant or the cavity is located at the node of a mode function. Also, it can be enhanced if the cavity is in resonance and the atom is located at the antinode of the mode function [183, 184, 185, 186, 187, 188, 189, 190].

The cavity-emitter coupling is a promising area of research in quantum optics

that has a huge range of applications from low-threshold laser development to the development of brighter single-photon sources, which are important in quantum cryptographic systems [191]. Also, the manipulation of SE plays an important role in technologies, integrated photonic circuits, and even solar energy harvesting [192, 193, 194]. Nowadays, researchers focus on studying the SE rate in photonic crystal cavities and plasmonic metal nanoparticles [195, 196, 197] that can modify the electromagnetic modes to operate the emitter's radiative properties at the nanoscale.

In quantum communication [198], the field of chiral cavities is a new path. In Fabry-Pérot cavities [199, 200], the different chirality measurement techniques, such as CD or birefringence, provide a helpful method for molecular sensing [201, 202]. Additionally, by studying the various polarization effects of chiral matter, researchers can break the material symmetries, providing a clear idea of non-equilibrium phases of matter using ultrashort laser fields [203, 204].

SE different approaches from a theoretical point of view within quantum statistical theories [205], such as using Macroscopic QED [206, 207, 208, 209], which gives the representation of the electromagnetic field in a second-quantized formalism that describes the influence of dispersive and absorptive materials on light-matter interactions. Therefore, this approach gives all information about the quantized electromagnetic field within the classical DGF [210, 211], which determines how the environment influences the local density of states and, in turn, provides insight into the SE [212, 213, 214, 215, 216] rate.

The DGF provides an idea of the response of the whole system to a point-source excitation and, accordingly, provides the theoretical prediction and engineering of emitter properties in different nanophotonic devices. In fact, the effects of absorption, dispersion, and complex geometrical configurations can be explained by using macroscopic QED, which can overcome the limitations of simpler cavity QED models, which will be helpful for both finding out experimental data and

designing nanophotonic devices that can detect emission properties [217].

Therefore, the cavity-emitter system in chiral nanophononics is a strong area of quantum optics that uses macroscopic QED theory. Such systems offer promising techniques for controlling light-matter interactions and can enable the next generation of quantum devices for communication, energy conversion, and sensing.

4.2 Objectives and Hypothesis

In this study, theoretically, we investigate a particular form of Fabry-Pérot cavity mirrors composed of TAPCs. These mirrors are made of stacks of uniaxial anisotropic layers whose extraordinary axis is progressively tilted around the stacking direction [218].

In this study, the TAPCs mirrors act as efficient CP diodes, meaning the TAPCs mirrors can reflect one polarization with helicity preservation while transmitting the opposite polarization efficiently. These devices are particular realizations of Reusch piles [219, 220]. These materials can exert an optical torque on the polarization of the electromagnetic field [221]. The handedness selectivity within the cavity forms a resonant standing-wave excitation, depending on the cavity width and dipolar orientation/position.

We consider the atomic two-level quantum system and, in a chiral photonic crystal environment, study modifications to the SE rate in TAPCs-based microcavities, enabling LDOS manipulation for RCP and LCP excitation. Depending on cavity width and dipolar orientation/position, we find an imbalance of 3% in the CP excitation after averaging over random dipole orientations. We observed that, for a fixed dipolar orientation, the imbalance can reach up to 20%. The limited CP-SE imbalance we observe is due to constructive and destructive interference effects in an anisotropic environment and, secondarily, to the planar cavity geometry, which manipulates the LDOS efficiently for the particular waves

oriented around the cavity axis. We investigate the limitations of large CP-SE for a fixed dipolar orientation, which can be overcome by engineering advanced microcavities.

First, in this chapter, we give an overview of SE in different materials, then explain the chirality-induced imbalance in the SE rates between the two CP.

4.3 Spontaneous emission overview

As outlined in detail in [161], in QED, the interaction between the atomic transition and the quantized electromagnetic field can be distinguished based on whether it is a strong or weak coupling. These two regions are differentiated based on the atom-field coupling constant given below

$$k = \frac{d}{\hbar}\sqrt{\frac{\hbar\omega_0}{2\varepsilon_0 v}} \tag{4.1}$$

where, ω_0 is the atomic transition frequency, d denotes the dipole matrix element, and v is the volume of the cavity. In strong coupling, which satisfies $k \gg \gamma_{\text{cav}}$, where γ_{cav} represents the spontaneous emission rate, QED can give an accurate description. But in the weak coupling $k \ll \gamma_{\text{cav}}$, QED and classical electromagnetic theory provide almost the same result, so next we study the QED approach to the SE in detail.

4.3.1 QED of spontaneous emission

Here, we study the SE for a quantum two-level atomic system located at $\mathbf{r} = \mathbf{r}_0$ in free space. Applying the QED approach, we analyze the combined atom-field contribution. We consider a transition from the initial atomic state $|e, \{0\}\rangle$—where the atom is excited and the field is in its vacuum state—to the final states where the atom is in its ground state and the field contains a single photon, $|g, \{1_{\omega_{\mathbf{k}}}\}\rangle$.

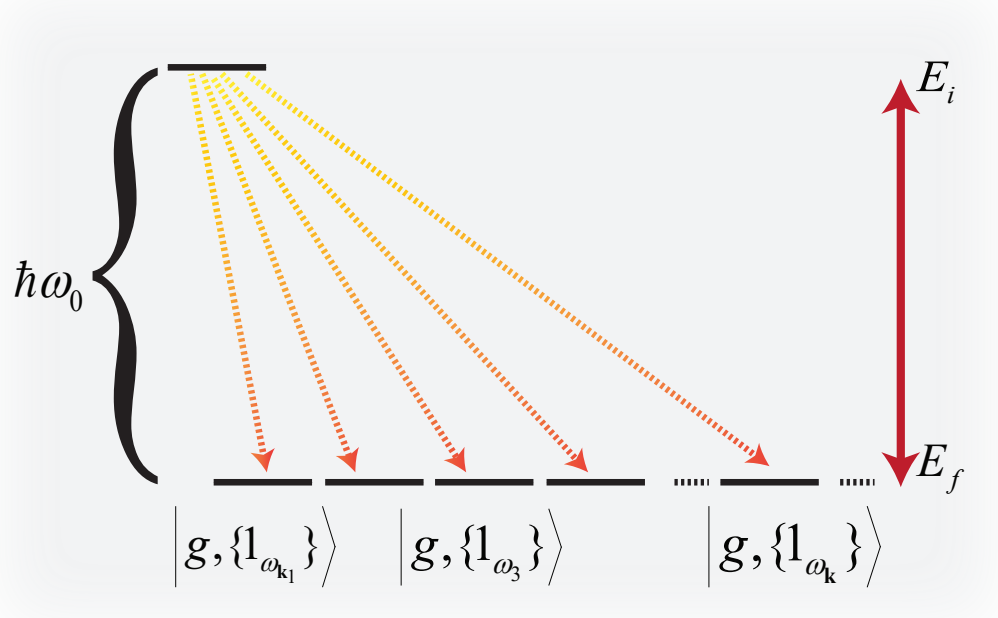

Figure 4.1 Schematic illustration of spontaneous decay of a two-level quantum atomic system, where transitions are shown by the range arrows from an initial state $|e,\{0\}\rangle$ to a set of final states$|g,\{1_{\omega_{\mathbf{k}}}\}\rangle$. The energy difference between initial and final states is $(E_i - E_f) = \hbar\omega_0$.

Each possible final state is defined by a photon with frequency $\omega_{\mathbf{k}}$ and mode index $\mathbf{k}$, as illustrated schematically in Fig. 4.1.

According to Fermi's Golden Rule, γ is given by:

$$\gamma = \frac{2\pi}{\hbar^2}\sum_f \left|\langle f|\hat{\mathcal{H}}_{\text{INT}}|i\rangle\right|^2 \delta(\omega_i - \omega_f) \tag{4.2}$$

where,

$$\hat{\mathcal{H}}_{\text{INT}} = -\hat{\mathbf{d}}\cdot\hat{\mathbf{E}} \tag{4.3}$$

is the interaction Hamiltonian in the dipole approximation.

In the above equation 4.3 the electric field operator $\hat{\mathbf{E}}$ can be written in terms of mode functions at $\mathbf{r} = \mathbf{r}_0$ as follows:

$$\hat{\mathbf{E}} = \sum_{\mathbf{k}}\left[\mathbf{E}^+_{\mathbf{k}}\hat{a}_{\mathbf{k}}(t) + \mathbf{E}^-_{\mathbf{k}}\hat{a}^\dagger_{\mathbf{k}}(t)\right] \tag{4.4}$$

where $\hat{a}_{\mathbf{k}}(t) = \hat{a}_{\mathbf{k}}(0)\exp(-i\omega_{\mathbf{k}}t)$, $\hat{a}^{\dagger}_{\mathbf{k}}(t) = \hat{a}^{\dagger}_{\mathbf{k}}(0)\exp(-i\omega_{\mathbf{k}}t)$, in which $\hat{a}_{\mathbf{k}}(0)$ and $\hat{a}^{\dagger}_{\mathbf{k}}(0)$ are the annihilation and creation operators of photons in mode $\mathbf{k}$ respectively and $\mathbf{E}^{+}_{\mathbf{k}} = \left(\mathbf{E}^{-}_{\mathbf{k}}\right)^{*}$ are the positive and negative part of the complex field $\mathbf{E}_{\mathbf{k}}$.

Also, in the same equation 4.3 the dipole moment operator $\hat{\mathbf{d}}$ can be written as:

$$\hat{\boldsymbol{d}} = \boldsymbol{d}\left(\hat{\sigma}^{+} + \hat{\sigma}^{-}\right) \tag{4.5}$$

where $\sigma^{+} = |e\rangle\langle g|$, $\sigma^{-} = |g\rangle\langle e|$ and $\hat{\boldsymbol{d}}$ is the transition dipole moment operator.

For the atom+ field combined system, the states are the product of the atomic state and the single-photon state, which can be expressed as below:

$$\begin{aligned} |i\rangle &= |e\rangle\,|\{0\}\rangle \\ |f\rangle &= |g\rangle\,|\{1_{\omega\mathbf{k}'}\}\rangle \end{aligned} \tag{4.6}$$

Here, $|\{0\}\rangle$ and $|\{1_{\omega\mathbf{k}'}\}\rangle$ denote the zero-photon state and one-photon state respectively and the difference between the initial and final states is given by $(E_i - E_f) = \hbar\omega_0$, it is worth mentioning that all the final states have the same energy.

Henceforth, we calculate $\hat{\mathbf{d}}\cdot\hat{\mathbf{E}}(\mathbf{r},t)$, express γ in equation 4.2 as below:

$$\gamma = \frac{2\pi}{\hbar^2}\sum_{\mathbf{k}}\left(\mathbf{d}\cdot{\mathbf{E}_{\mathbf{k}}}^{+}{\mathbf{E}_{\mathbf{k}}}^{-}\cdot\mathbf{d}\right)\delta(\omega_{\mathbf{k}} - \omega_0), \tag{4.7}$$

where the outer product ${\mathbf{E}_{\mathbf{k}}}^{+}{\mathbf{E}_{\mathbf{k}}}^{-}$ can be written in terms of normal mode $\mathbf{u}_{\mathbf{k}}$ as:

$${\mathbf{E}_{\mathbf{k}}}^{+} = \sqrt{\frac{\hbar\omega_{\mathbf{k}}}{2\varepsilon_0}}\mathbf{u}_{\mathbf{k}}, \quad {\mathbf{E}_{\mathbf{k}}}^{-} = \sqrt{\frac{\hbar\omega_{\mathbf{k}}}{2\varepsilon_0}}{\mathbf{u}_{\mathbf{k}}}^{*} \tag{4.8}$$

With the delta function ensuring $\omega_{\mathbf{k}} = \omega_0$ in the equation 4.7, the decay rate γ

and the partial local density $\rho_d(\mathbf{r}_0, \omega_0)$ can be expressed as

$$\gamma = \frac{2\omega}{3\varepsilon_0 \hbar} |d|^2 \rho_d(\mathbf{r}_0, \omega_0) \tag{4.9a}$$

$$\rho_d(\mathbf{r}_0, \omega_0) = 3 \sum_{\mathbf{k}} [\mathbf{n}_d \cdot (\mathbf{u_k} \mathbf{u_k}^*) \cdot \mathbf{n}_d \delta(\omega_k - \omega_0)] \tag{4.9b}$$

The dipole moment can be written as $\mathbf{d} = d\mathbf{n}_d$ in which $\mathbf{n}_d$ is the unit vector.

4.3.2 Approach of the Dyadic Green's Function

To avoid these singularities in the expression of partial local density in Eq. 4.9(b), it is better to build a relation between normal modes and the Green function, so that we can finally find out the SE rate and partial local density in terms of the Green function for a considered system. The normal modes satisfy the wave equation:

$$\nabla \times \nabla \times \mathbf{u_k}(\mathbf{r}, \omega_k) - \frac{\omega_k^2}{c^2} \mathbf{u_k}(\mathbf{r}, \omega_k) = 0, \tag{4.10}$$

and the modes are orthonormal over the field volume.

We can write the Green function $\overleftrightarrow{\mathbf{G}}$ in terms of normal mode as:

$$\overleftrightarrow{\mathbf{G}}(\mathbf{r}, \mathbf{r}'; \omega) = \sum_{\mathbf{K}} \mathbf{C_K}(\mathbf{r}', \omega) \mathbf{u_k}(\mathbf{r}, \omega_k) \tag{4.11}$$

where $\mathbf{C_K}$ is the coefficient whose value is to be determined. According to the definition of Green's function

$$\nabla \times \nabla \times \overleftrightarrow{\mathbf{G}}(\mathbf{r}, \mathbf{r}'; \omega) - \frac{\omega^2}{c^2} \overleftrightarrow{\mathbf{G}}(\mathbf{r}, \mathbf{r}'; \omega) = \overleftrightarrow{\mathbf{I}} \delta(\mathbf{r} - \mathbf{r}') \tag{4.12}$$

Now we can easily determine the value of $\mathbf{C_K}$ with help of equations 4.12, 4.12 and putting it in equation 4.11 we get

$$\overleftrightarrow{\mathbf{G}}(\mathbf{r}, \mathbf{r}'; \omega) = \sum_{\mathbf{k}} c^2 \frac{\mathbf{u_k^*}(\mathbf{r}', \omega_k) \mathbf{u_k}(\mathbf{r}, \omega_k)}{\omega_k^2 - \omega^2} \tag{4.13}$$

By using contour integration, we determine the imaginary part of the Green's function to evaluate the spontaneous emission of a dipole at position $\mathbf{r}_0$,

$$\mathrm{Im}\left\{\overleftrightarrow{\mathbf{G}}(\mathbf{r}_0,\mathbf{r}_0;\omega)\right\} = \frac{\pi c^2}{2\omega}\sum_{\mathbf{k}}\frac{1}{\omega_k}\mathbf{u}^*_{\mathbf{k}}(\mathbf{r}_0,\omega_k)\mathbf{u}_{\mathbf{k}}(\mathbf{r}_0,\omega_k)\,\delta(\omega-\omega_k) \tag{4.14}$$

Now we fix $\mathbf{r}=\mathbf{r}_0$ and $\omega=\omega_0$ and decay rate can be rewritten as

$$\gamma = \frac{2\omega}{3\varepsilon_0\hbar}|d|^2\rho_d\left(\mathbf{r}_0,\omega_0\right) \tag{4.15a}$$

$$\rho_d\left(\mathbf{r}_0,\omega_0\right) = \frac{6\omega_0}{\pi c^2}\left[\mathbf{n}_d\cdot\mathrm{Im}\left\{\overleftrightarrow{\mathbf{G}}\left(\mathbf{r}_0,\mathbf{r}_0;\omega_0\right)\right\}\cdot\mathbf{n}_d\right] \tag{4.15b}$$

Therefore, we establish the relation between the green dyadics and the partial local density, so it is now possible to find out the SE for a two-level quantum system with an arbitrary reference frame by just knowing the green dyadics of that reference frame.

In case of having no fixed dipole axis, we need to do an orientational averaging on the system.

$$\left\langle\left[\mathbf{n}_d\cdot\mathrm{Im}\left\{\overleftrightarrow{\mathbf{G}}\left(\mathbf{r}_0,\mathbf{r}_0;\omega_0\right)\right\}\cdot\mathbf{n}_d\right]\right\rangle = \frac{1}{3}\mathrm{Im}\left[Tr\left\{\overleftrightarrow{\mathbf{G}}_0\left(\mathbf{r}_0,\mathbf{r}_0;\omega_0\right)\right\}\right] \tag{4.16}$$

In free space, ($\overleftrightarrow{\mathbf{G}} = \overleftrightarrow{\mathbf{G}}_0$) leads to

$$\frac{1}{3}\mathrm{Im}\left[Tr\left\{\overleftrightarrow{\mathbf{G}}_0\left(\mathbf{r}_0,\mathbf{r}_0;\omega_0\right)\right\}\right] = \frac{\omega_0}{6\pi c} \tag{4.17}$$

The free space spontaneous decay can be rewritten as

$$\gamma_0 = \frac{\omega_0^3\,|\mathbf{d}|^2}{3\pi\varepsilon_0\hbar c^3}, \tag{4.18a}$$

$$\rho_0 = \frac{\omega_0^2}{\pi^2 c^3}. \tag{4.18b}$$

Therefore, the spontaneous decay rate depends on the partial local density of

states, which is determined by the orientation of the transition dipole between the two atomic levels involved. Only in homogeneous environments, or after averaging over all dipole orientations, can this partial density of states be replaced by the total local density of states. This explains why changes in the surroundings can strongly influence the decay rate.

It is well established that changing the photonic environment can significantly modify the SE of a quantum emitter. Different interfaces, photonic crystals, and plasmonic structures can either enhance or suppress the emission rate compared with free space [161]. Recent studies have also shown that the situation becomes even more interesting when a chiral molecule interacts with a structured chiral medium.

For example, see [168], where analytical expressions for the emission rate of an optically active molecule placed near a chiral nanoellipsoid are derived. Their results show that both the shape of the particle and its intrinsic chirality can lead to strong, enantioselective changes in the radiative decay rates of right- and left-handed molecules. These effects arise from chiral plasmonic resonances and from the combined roles of electric and magnetic dipole contributions in the emitter and its environment.

Also, it is reported in [222] that emission near a semi-infinite bi-isotropic material shows that the local photonic density of states can be heavily altered by the chiral and magnetoelectric properties of the medium. In more complex situations, such as clusters of two chiral particles, collective electromagnetic behavior enables controlled, enantioselective emission, which is helpful for chiral sensing [169].

Overall, these developments make it clear that by designing the electromagnetic environment—especially using chiral or plasmonic nanostructures the SE of quantum emitters can be tuned for various applications in nanophotonics, quantum optics, and chiral spectroscopy.

4.4 Spontaneous emission in chiral cavity

Until now, we have presented SE in free space; we have also presented the DGF approach to determine it in any other reference frame. In fact, we presented a literature review that focused on SE enhancement rather than the free-space decay rate, indicating that, depending on the environment, it can be enhanced. In this section, we study SE in a chiral cavity, as this allows us to study polarization-dependent results that will be helpful for measuring chirality with the provided nanophotonic structure. So in this section first, we investigate the characterization of the cavity walls, then evaluate the total DGF for the definition of right and left CP-SE rates, and then, in the results and discussion section, we study the different polarization effects in SE rates, which have a high dependence on the width of the cavity and the position of the quantum emitter.

4.4.1 Characterization of the cavity walls

The cavity we study is composed of two structures designed to exhibit chiral optical behavior. Each unit cell of the TAPCs is made of uniaxial anisotropic layers of calcite ($CaCO_3$). There are 30 unit cells; each unit cell has 4 layers of a stack of uniaxial anisotropic media.

Fig. 4.2 represents the schematic diagram of the cavity composed of chiral mirrors. A complete mathematical and physical description of these cavities made of chiral mirrors can be found in [223]. Here, we briefly describe the structure of these TAPCs and their optimization for normal incidence at a vacuum wavelength of $780, \mathrm{nm}$ see Fig. 4.2. Each unit cell of the TAPCs consists of four layers with thicknesses of $d_1 = 56.1, \mathrm{nm}$, $d_2 = 85.9, \mathrm{nm}$, $d_3 = 64.0, \mathrm{nm}$, and $d_4 = 45.1, \mathrm{nm}$, and a total of $N = 30$ unit cells. We consider the extraordinary and ordinary refractive indexes $n_\mathrm{E} = 1.4822$ and $n_\mathrm{O} = 1.6495$, respectively, at vacuum wavelength $\lambda = 780$

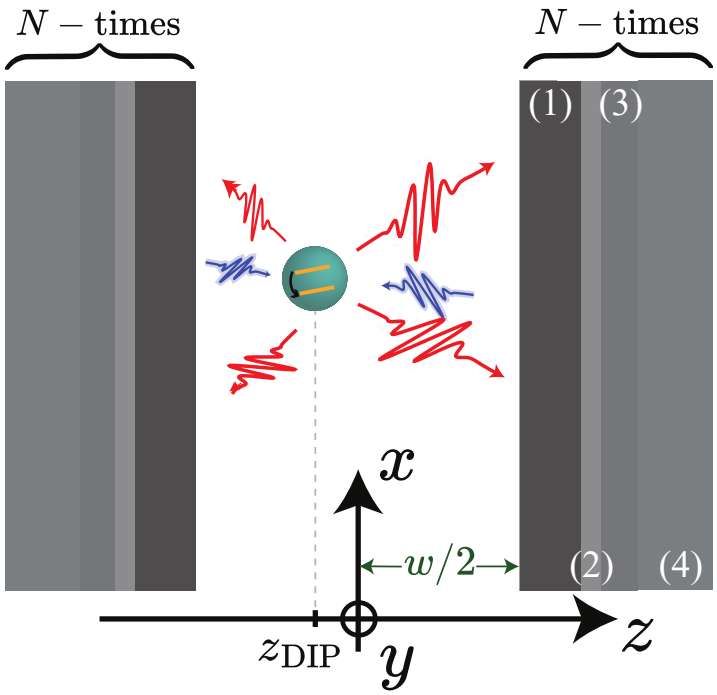

Figure 4.2 A two-level emitter at $z = z_{\text{DIP}}$ within a cavity of width w whose walls are the TAPCs described in [223] made of $(N = 30)\times$4-layers stack of uniaxial anisotropic media. The wall on the left is obtained through $\pi-$rotation of the right one around the $x-$axis. Moreover, in red we depict the propagating emitted field, while in blue the scattered one.

nm [224]. The extraordinary axes of the four uniaxial crystal layers lie in the $x-y$ plane, and each of them is chosen to be rotated by an angle of $\pi/4$ radians with respect to the nearest neighbors, starting from vertical (x-direction) for the first layer to $3\pi/4$ tilting with respect to the $x-$axis for the fourth layer in clockwise orientation along positive (negative) z for the mirror on the right (left) [223].

4.4.1.1 Transfer Matrix Approach

Generally, the TMA is used to determine the propagation of electromagnetic fields through a medium composed of a stack of layers. Here, in our study, we use the TMA to derive the scattered field within the cavity. For both mirrors of our system, the refraction/reflection at the different interfaces is accounted for by three transfer matrices, i.e., from vacuum to an anisotropic medium layer, between two distinct layers, and from the last layer to vacuum.

We adopt the index $k = 1, 2, 3, 4$ to label each layer in a single 4-layer stack; we can write each angular spectrum component of the electric field within the $k-$th anisotropic layer as

$$\mathbf{E}_{\mathrm{AN}}^{(k)}(\boldsymbol{k}_\perp, t) = \sum_{f=\pm 1} \sum_{\xi=x,y,z} \sum_{l=1,2} C_\xi^{(l,f,k)} e^{if\beta_l^{(k)} z} \hat{\mathbf{e}}_\xi e^{i\boldsymbol{k}_\perp \cdot \mathbf{r} - i\omega t}. \tag{4.19}$$

where $\boldsymbol{k}_\perp = (k_x, k_y)$, $f = 1$ is associated with forward propagating modes and $f = -1$ to backward ones. In particular, the two eigenmodes $l = 1, 2$, where the mode $l = 1$ denotes only the ordinary refractive index while the $l = 2$ mode is affected by both ordinary and extraordinary refractive indices are such that

$$\begin{aligned} C_x^{(1,f,k)} &= \sin\theta_{\mathrm{E}}^{(k)} \beta_1^{(k)} A_1^{(f,k)} / D_1^{(k)}, \\ C_y^{(1,f,k)} &= -\cos\theta_{\mathrm{E}}^{(k)} \beta_1^{(k)} A_1^{(f,k)} / D_1^{(k)}, \\ C_z^{(1,f,k)} &= f\gamma^{(k)} A_1^{(f,k)} / D_1^{(k)}, \end{aligned} \tag{4.20}$$

where,

$$\begin{aligned} D_1^{(k)} &= \left[\left(\frac{\omega^2}{c^2} \right) \varepsilon_{\mathrm{O}} - \left(\alpha^{(k)} \right)^2 \right]^{1/2}, \\ \theta_{\mathrm{E}}^{(k)} &= \frac{\pi}{4}(k-1), \\ \beta_1^{(k)} &= \left[\left(\frac{\omega^2}{c^2} \right) \varepsilon_{\mathrm{O}} - |\boldsymbol{k}_\perp|^2 \right]^{1/2}. \end{aligned}$$

similarly, for the $C_{x,y,z}^{(2,f,k)}$ mode we find

$$\begin{aligned} C_x^{(2,f,k)} &= \left[\frac{\omega^2}{c^2} \cos\theta_{\mathrm{E}}^{(k)} - \frac{k_x}{\varepsilon_{\mathrm{O}}} \alpha^{(k)} \right] A_2^{(f,k)} / D_2^{(k)}, \\ C_y^{(2,f,k)} &= \left[\frac{\omega^2}{c^2} \sin\theta_{\mathrm{E}}^{(k)} - \frac{k_y}{\varepsilon_{\mathrm{O}}} \alpha^{(k)} \right] A_2^{(f,k)} / D_2^{(k)}, \\ C_z^{(2,f,k)} &= -\frac{f}{\varepsilon_{\mathrm{O}}} \alpha^{(k)} \beta_2^{(k)} A_2^{(f,k)} / D_2^{(k)}, \end{aligned} \tag{4.21}$$

where

$$D_2^{(k)} = \left[\left(\frac{\omega^2}{c^2}\right) - \varepsilon_{\mathrm{O}}^{-1}\left(\alpha^{(k)}\right)^2\right]^{1/2} \times \left[\left(\frac{\omega^2}{c^2}\right) + \frac{\left(\varepsilon_{\mathrm{E}} - \varepsilon_{\mathrm{O}}\right)\left(\alpha^{(k)}\right)^2}{\varepsilon_{\mathrm{O}}^2}\right]^{1/2}. \tag{4.22}$$

and $\beta_2^{(k)} = \left[(\omega^2/c^2)\varepsilon_{\mathrm{E}} - (\varepsilon_{\mathrm{E}}/\varepsilon_{\mathrm{O}})\left(\alpha^{(k)}\right)^2 - \left(\gamma^{(k)}\right)^2\right]^{1/2}$.

We define the functions as below:

$$\begin{aligned} \alpha^{(k)} &= k_x \cos\theta_{\mathrm{E}}^{(k)} + k_y \sin\theta_{\mathrm{E}}^{(k)}, \\ \gamma^{(k)} &= -k_x \sin\theta_{\mathrm{E}}^{(k)} + k_y \cos\theta_{\mathrm{E}}^{(k)}. \end{aligned} \tag{4.23}$$

. Eventually, we observe that

$$\begin{aligned} \varepsilon_{\mathrm{O}} &= n_{\mathrm{O}}^2, \\ \varepsilon_{\mathrm{E}} &= n_{\mathrm{E}}^2. \end{aligned} \tag{4.24}$$

Now we put boundary conditions

$$\begin{aligned} \hat{\mathbf{e}}_z \cdot \mathbf{D}_j(\mathbf{r}, t) &= \hat{\mathbf{e}}_z \cdot \mathbf{D}_i(\mathbf{r}, t), \\ \hat{\mathbf{e}}_z \cdot \mathbf{B}_j(\mathbf{r}, t) &= \hat{\mathbf{e}}_z \cdot \mathbf{B}_i(\mathbf{r}, t), \\ \hat{\mathbf{t}} \cdot \mathbf{E}_j(\mathbf{r}, t) &= \hat{\mathbf{t}} \cdot \mathbf{E}_i(\mathbf{r}, t), \\ \hat{\mathbf{t}} \cdot \mathbf{H}_j(\mathbf{r}, t) &= \hat{\mathbf{t}} \cdot \mathbf{H}_i(\mathbf{r}, t), \end{aligned} \tag{4.25}$$

where $i, j = \mathrm{VAC}, k$ and $i \neq j$, we can write the following matrix relations:

$$\begin{aligned}
\hat{M}^f_{\mathrm{VAC}} \begin{bmatrix} E^{\mathrm{INC}}_{1,f} \\ E^{\mathrm{INC}}_{-1,f} \\ E^{\mathrm{REFL}}_{1,-f} \\ E^{\mathrm{REFL}}_{-1,-f} \end{bmatrix} &= \hat{M}_1 \begin{bmatrix} A_1^{(+,1)} \\ A_2^{(+,1)} \\ A_1^{(-,1)} \\ A_2^{(-,1)} \end{bmatrix}, \\
\hat{M}_i \begin{bmatrix} A_1^{(+,i)} \\ A_2^{(+,i)} \\ A_1^{(-,i)} \\ A_2^{(-,i)} \end{bmatrix} &= \hat{M}_j \begin{bmatrix} A_1^{(+,j)} \\ A_2^{(+,j)} \\ A_1^{(-,j)} \\ A_2^{(-,j)} \end{bmatrix}, \qquad (4.26) \\
\hat{M}_4 \begin{bmatrix} A_1^{(+,4)} \\ A_2^{(+,4)} \\ A_1^{(-,4)} \\ A_2^{(-,4)} \end{bmatrix} &= \hat{M}^f_{\mathrm{VAC}} \begin{bmatrix} E^{\mathrm{TRANSM}}_{1,f} \\ E^{\mathrm{TRANSM}}_{-1,f} \\ 0 \\ 0 \end{bmatrix}.
\end{aligned}$$

For the propagating modes, we have

$$\hat{M}^1_{\mathrm{VAC}} = \mathcal{N} \begin{bmatrix} 1 & 1 & 1 & 1 \\ M^{(-)}_{\mathrm{VAC}} & -M^{(+)}_{\mathrm{VAC}} & -M^{(+)}_{\mathrm{VAC}} & M^{(-)}_{\mathrm{VAC}} \\ -i & i & -i & i \\ -iM^{(-)}_{\mathrm{VAC}} & -iM^{(+)}_{\mathrm{VAC}} & iM^{(+)}_{\mathrm{VAC}} & iM^{(-)}_{\mathrm{VAC}} \end{bmatrix}, \qquad (4.27)$$

where

$$M^{(\pm)}_{\mathrm{VAC}} = \frac{ik_{\mathrm{VAC}}\beta \pm k_x k_y}{\beta^2 + k_y^2},$$

$$\mathcal{N} = \sqrt{\frac{\beta^2 + k_y^2}{2k^2_{\mathrm{VAC}}}}.$$

Also,

$$\hat{M}_k = \begin{bmatrix} \frac{\sin\theta_{\mathrm{E}}^{(k)}\beta_1^{(k)}}{D_1^{(k)}} & \frac{\frac{\omega^2}{c^2}\cos\theta_{\mathrm{E}}^{(k)} - \frac{k_x}{\varepsilon_{\mathrm{O}}^{(k)}}\alpha^{(k)}}{D_2^{(k)}} & \frac{\sin\theta_{\mathrm{E}}^{(k)}\beta_1^{(k)}}{D_1^{(k)}} & \frac{\frac{\omega^2}{c^2}\cos\theta_{\mathrm{E}}^{(k)} - \frac{k_x}{\varepsilon_{\mathrm{O}}^{(k)}}\alpha^{(k)}}{D_2^{(k)}} \\ -\frac{\cos\theta_{\mathrm{E}}^{(k)}\beta_1^{(k)}}{D_1^{(k)}} & \frac{\frac{\omega^2}{c^2}\sin\theta_{\mathrm{E}}^{(k)} - \frac{k_y}{\varepsilon_{\mathrm{O}}^{(k)}}\alpha^{(k)}}{D_2^{(k)}} & -\frac{\cos\theta_{\mathrm{E}}^{(k)}\beta_1^{(k)}}{D_1^{(k)}} & \frac{\frac{\omega^2}{c^2}\sin\theta_{\mathrm{E}}^{(k)} - \frac{k_y}{\varepsilon_{\mathrm{O}}^{(k)}}\alpha^{(k)}}{D_2^{(k)}} \\ \frac{\frac{\omega^2}{c^2}\varepsilon_{\mathrm{O}}^{(k)}\cos\theta_{\mathrm{E}}^{(k)} - k_x\alpha^{(k)}}{k_{\mathrm{VAC}}D_1^{(k)}} & -\frac{\frac{\omega}{c}\sin\theta_{\mathrm{E}}^{(k)}\beta_2^{(k)}}{D_2^{(k)}} & -\frac{\frac{\omega^2}{c^2}\varepsilon_{\mathrm{O}}^{(k)}\cos\theta_{\mathrm{E}}^{(k)} - k_x\alpha^{(k)}}{k_{\mathrm{VAC}}D_1^{(k)}} & \frac{\frac{\omega}{c}\sin\theta_{\mathrm{E}}^{(k)}\beta_2^{(k)}}{D_2^{(k)}} \\ \frac{\frac{\omega^2}{c^2}\varepsilon_{\mathrm{O}}^{(k)}\sin\theta_{\mathrm{E}}^{(k)} - k_y\alpha^{(k)}}{k_{\mathrm{VAC}}D_1^{(k)}} & \frac{\frac{\omega}{c}\cos\theta_{\mathrm{E}}^{(k)}\beta_2^{(k)}}{D_2^{(k)}} & -\frac{\frac{\omega^2}{c^2}\varepsilon_{\mathrm{O}}^{(k)}\sin\theta_{\mathrm{E}}^{(k)} - k_y\alpha^{(k)}}{k_{\mathrm{VAC}}D_1^{(k)}} & -\frac{\frac{\omega}{c}\cos\theta_{\mathrm{E}}^{(k)}\beta_2^{(k)}}{D_2^{(k)}} \end{bmatrix}. \tag{4.28}$$

For the anisotropic crystal mode basis, in-layer propagation matrices are easily obtained as

$$\hat{P}_k = \mathrm{diag}\left[e^{i\beta_1^{(k)}d_k}, e^{i\beta_2^{(k)}d_k}, e^{-i\beta_1^{(k)}d_k}, e^{-i\beta_2^{(k)}d_k}\right]. \tag{4.29}$$

We calculate the field on one side of the mirror in terms of the field on the other side by solving the linear problem for the amplitudes as given below:

$$\begin{bmatrix} E_{1,f}^{\mathrm{TRANSM}} \\ E_{-1,f}^{\mathrm{TRANSM}} \\ 0 \\ 0 \end{bmatrix} = \underbrace{\hat{M}_{4\to\mathrm{VAC}}^{1}\hat{P}_4\hat{M}_{3\to4}\hat{P}_3\hat{M}_{2\to3}\hat{P}_2\hat{M}_{1\to2}\hat{P}_1\left(\hat{M}_{4\to1}\hat{P}_4\hat{M}_{3\to4}\hat{P}_3\hat{M}_{2\to3}\hat{P}_2\hat{M}_{1\to2}\hat{P}_1\right)^{N-1}\hat{M}_{\mathrm{VAC}\to1}^{1}}_{\hat{M}_{\mathrm{TMA},1}} \times \begin{bmatrix} E_{1,f}^{\mathrm{INC}} \\ E_{-1,f}^{\mathrm{INC}} \\ E_{1,-f}^{\mathrm{REFL}} \\ E_{-1,-f}^{\mathrm{REFL}} \end{bmatrix}. \tag{4.30}$$

where

$$\hat{M}_{\mathrm{VAC}\to1}^{1} = \left(\hat{M}_1\right)^{-1}\hat{M}_{\mathrm{VAC}}^{1},$$

$$\hat{M}_{i\to j} = \left(\hat{M}_j\right)^{-1}\hat{M}_i,$$

$$\hat{M}_{4\to\mathrm{VAC}}^{1} = \left(\hat{M}_{\mathrm{VAC}}^{1}\right)^{-1}\hat{M}_4.$$

We consider the same for the left mirror, taking care to properly identify the impinging and reflected fields and modifying the involved matrices accordingly.

4.4.1.2 Evaluation of the scattered field with TMA

We use the TMA for birefringent layered media [225, 226] to express the fields on one side of the wall as a function of those on the other side as follows,

$$\begin{bmatrix} E^{\mathrm{TRANSM}}_{1,f} \\ E^{\mathrm{TRANSM}}_{-1,f} \\ 0 \\ 0 \end{bmatrix} = \hat{M}_{\mathrm{TMA},f} \begin{bmatrix} E^{\mathrm{INC}}_{1,f} \\ E^{\mathrm{INC}}_{-1,f} \\ E^{\mathrm{REFL}}_{1,-f} \\ E^{\mathrm{REFL}}_{-1,-f} \end{bmatrix},$$

$$\begin{bmatrix} E^{\mathrm{REFL}}_{1,-f} \\ E^{\mathrm{REFL}}_{-1,-f} \end{bmatrix} = \hat{M}^{f}_{\mathrm{REFL}} \begin{bmatrix} E^{\mathrm{INC}}_{1,f} \\ E^{\mathrm{INC}}_{-1,f} \end{bmatrix} = \frac{1}{\underbrace{M^f_{34}M^f_{43} - M^f_{33}M^f_{44}}_{\mathrm{D}^f}} \begin{bmatrix} M^f_{44} & -M^f_{34} \\ -M^f_{43} & M^f_{33} \end{bmatrix} \begin{bmatrix} M^f_{31} & M^f_{32} \\ M^f_{41} & M^f_{42} \end{bmatrix} \begin{bmatrix} E^{\mathrm{INC}}_{1,f} \\ E^{\mathrm{INC}}_{-1,f} \end{bmatrix},$$

$$\begin{bmatrix} E^{\mathrm{TRANSM}}_{1,f} \\ E^{\mathrm{TRANSM}}_{-1,f} \end{bmatrix} = \hat{M}^{f}_{\mathrm{TRANSM}} \begin{bmatrix} E^{\mathrm{INC}}_{1,f} \\ E^{\mathrm{INC}}_{-1,f} \end{bmatrix} = \left\{ \begin{bmatrix} M^f_{11} & M^f_{12} \\ M^f_{21} & M^f_{22} \end{bmatrix} + \frac{1}{\mathrm{D}^f} \begin{bmatrix} M^f_{13} & M^f_{14} \\ M^f_{23} & M^f_{24} \end{bmatrix} \begin{bmatrix} M^f_{44} & -M^f_{34} \\ -M^f_{43} & M^f_{33} \end{bmatrix} \begin{bmatrix} M^f_{31} & M^f_{32} \\ M^f_{41} & M^f_{42} \end{bmatrix} \right\} \begin{bmatrix} E^{\mathrm{INC}}_{1,f} \\ E^{\mathrm{INC}}_{-1,f} \end{bmatrix}. \quad (4.31)$$

where $M^f_{ij} = \left(\hat{M}_{\mathrm{TMA},f}\right)_{ij}$ are elements of the total transfer matrix, and $i,j = 1,2,3,4$ identify rows and columns, respectively, for both forward ($f = 1$) or backward ($f = -1$) impinging fields, depending on which cavity wall we consider; the forward fields $f = 1$ are reflected/transmitted by the right mirror, while the backward ones $f = -1$ by the left one. Moreover, $E^{\mathrm{TRANSM}}_{s,f}$, $E^{\mathrm{REFL}}_{s,-f}$, $E^{\mathrm{INC}}_{s,f}$ are the transmitted, reflected, and incident electric field amplitudes, respectively,

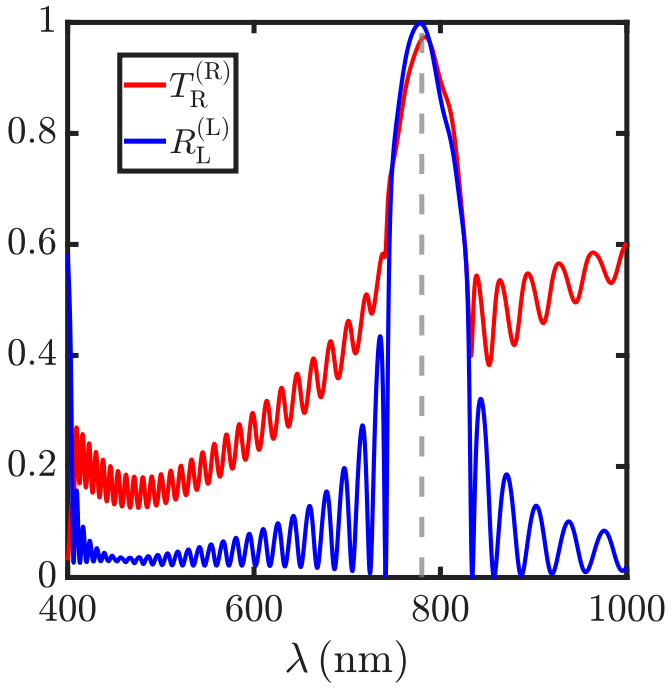

Figure 4.3 Wavelength dependence of the reflectance ($R_{\mathrm{L}}^{(\mathrm{L})}$) and transmittance ($T_{\mathrm{L}}^{(\mathrm{L})}$) for the two-level quantum emitter for LCP light with normally incident LCP light and RCP light with normally incident RCP lights, respectively, are shown in blue and red curves. The dashed line indicates the reflectance/transmittance at $\lambda_{\mathrm{VAC}} = 780$ nm. The plot is obtained for Rubidium-85 (^{85}Rb) as a quantum emitter, choosing the atomic transition to be $5S_{1/2} \rightarrow 5P_{3/2}$ with a reduced electric dipole matrix element $|\mathbf{d}_{ge}| = 5.98211 e a_0$, with e the absolute value of the electric charge, a_0 Bohr radius.

related to either RCP ($s = 1$) or LCP ($s = -1$), and $\hat{M}^f_{\mathrm{TRANSM}}$, $\hat{M}^f_{\mathrm{REFL}}$ are transmission and reflection matrices, respectively. We present the full derivation of the corresponding transfer matrix $\hat{M}_{\,rmTMA,f}$ in the section.

4.4.1.3 Evaluation of reflectance and transmittance

In Fig. 4.3 we present the wavelength dependence of the calculated reflectance and transmittance. We obtain $R_{\mathrm{L}}^{(\mathrm{L})} = 0.9971$ which denotes the reflectance of LCP excitation impinging with LCP excitation and $T_{\mathrm{R}}^{(\mathrm{R})} = 0.9700$ denoted in red curve. The blue curve denotes the transmittance of RCP excitation impinging on RCP excitation for a normally incident field with a vacuum wavelength $\lambda_{\mathrm{vac}} = 780\,\mathrm{nm}$. The dashed grey line indicates the chiral cavity simultaneously achieves

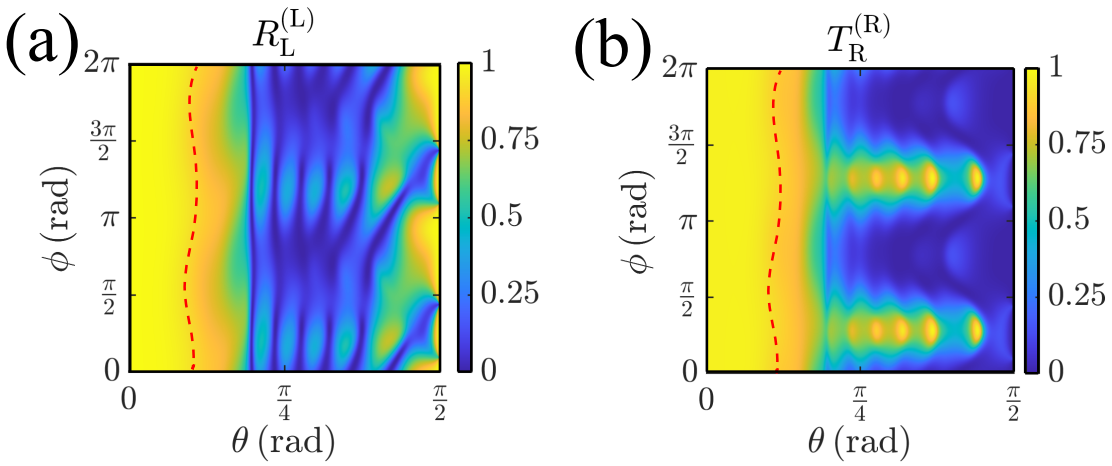

Figure 4.4 (**a**) Dependence of reflectance $R_{\mathrm{L}}^{(\mathrm{L})}$ and (**b**) transmittance $T_{\mathrm{R}}^{(\mathrm{R})}$ at $\lambda_{\mathrm{VAC}} = 780\,\mathrm{nm}$ over both the zenithal (θ) and azimuthal (ϕ) angles of incidence. Note that for θ ranging from zero to the red dashed lines in (**a,b**) $R_{\mathrm{L}}^{(\mathrm{L})}, T_{\mathrm{R}}^{(\mathrm{R})} > 0.90$. The plots are obtained for Rubidium-85 (^{85}Rb) as a quantum emitter, choosing the atomic transition to be $5S_{1/2} \rightarrow 5P_{3/2}$ with a reduced electric dipole matrix element $|\mathbf{d}_{ge}| = 5.98211ea_0$, with e the absolute value of the electric charge, a_0 Bohr radius.

$R_{\mathrm{L}}^{(\mathrm{L})} = 0.9971$ and $T_{\mathrm{R}}^{(\mathrm{R})} = 0.9700$, which confirms the structure provides high helicity-preserving reflection for LCP excitation and high transmission for RCP excitation at the operating wavelength.

4.4.1.4 Angular dependence of reflectance and transmittance

The Fig. 4.4 shows the angular response for the TAPCs for the corresponding vacuum wavelength $\lambda_{\mathrm{VAC}} = 780$ nm of the reflectance and transmittance. We observe that for the zenithal angle $|\theta| \lesssim 30^\circ$ and for almost all azimuthal angles ϕ, the reflectance remains larger than 0.90, as indicated by the red-shaded region. It signifies helicity-preserving reflection of LCP light by the TAPCs over a wide region around the normal incidence.

Also, we observe $T_{\mathrm{R}}^{(\mathrm{R})}$ also exceeds 0.90 for $|\theta| \lesssim 30^\circ$ for the full range of azimuthal angles ϕ, which declares the transmission of RCP excitation in the region. We see the cavity walls act as chiral Bragg mirrors that selectively reflect LCP and transmit RCP light for a wide region, not only in normal incidence.

4.4.2 Evaluation of the total DGF for the definition of right and left CP-SE rates

We investigate the SE of a two-level quantum emitter. Spontaneous decay, the process by which an excited quantum state transitions to a lower-energy state while emitting a photon, is a pure quantum mechanical phenomenon, and to investigate it requires the approach of QED. The atom and electromagnetic field together form a composite quantum state that evolves over time.

The energy of the two-level system's excited state $|e, \{0\}\rangle$ is given by

$$E_e = \hbar\omega_e \tag{4.32}$$

Transitions occur to a set of final states, $|g, \{1_{\omega_k,s}\}\rangle$ each with identical energy, denoted as below:

$$E_g = \hbar\omega_g \tag{4.33}$$

Here, E_g is the energy of the ground state, where the final states differ by mode wavevector $\mathbf{k}$ and polarization index s [227, 161].

We use Fermi's Golden Rule, which relates the transition probability per unit time to the matrix element of the interaction Hamiltonian $\hat{\mathcal{H}}_{\text{INT}}$ between the initial and final states, as well as to the density of available final electromagnetic field states. The SE rate, denoted by γ, is expressed as a sum over all allowed photon wavevectors and polarizations:

$$\gamma = \frac{2\pi}{\hbar^2} \sum_{\mathbf{k},s} \left| \langle g, \{1_{\omega_k,s}\}| \, \hat{\mathcal{H}}_{\text{INT}} \, |e, \{0\}\rangle \right|^2 \delta\left[\omega - (\omega_e - \omega_g)\right], \tag{4.34}$$

where, $\hat{\mathcal{H}}_{\text{INT}} = -\hat{\mathbf{d}} \cdot \hat{\mathbf{E}}(\mathbf{r}, t)$ is the interaction Hamiltonian is written in the dipole approximation where, $\hat{\mathbf{d}}$ is the atomic dipole operator, and $\hat{\mathbf{E}}$ is the electric field operator. The delta function in Eq. 4.34 defines energy conservation.

For the electric dipole (DIP) operator $\hat{\mathbf{d}}$ for a two-level system, we use a matrix that includes both ground and excited state terms given by:

$$\hat{\mathbf{d}} = \begin{bmatrix} \mathbf{d}_{gg} & \mathbf{d}_{ge} \\ \mathbf{d}_{eg} = \mathbf{d}_{ge}^{*} & \mathbf{d}_{ee} \end{bmatrix} \tag{4.35}$$

However, we consider a two-level quantum system for an atom with spherical symmetry, with a resonant transition that has a diagonal dipole matrix element that vanishes, i.e., $\mathbf{d}_{gg} = \mathbf{d}_{ee} = 0$. Simultaneously, only the off-diagonal elements of the transition dipole moments exist.

The quantum emitter now interacts not only with the emitted radiation but also with fields scattered and reflected by the cavity walls. To study the SE of a two-level system located at $\mathbf{r}_{\mathrm{DIP}} = (\mathbf{r}_{\perp}, z_{\mathrm{DIP}})$ $[\mathbf{r}_{\mathrm{DIP}} = (x, y)]$ within a chiral cavity, the electric field should take into account both emitted and scattered contributions.

Now we have to calculate the total electric field. As discussed earlier, using macroscopic QED [206, 207, 208, 209] it is possible to describe quantum effects in nanophotonic systems. This approach is can be used to study SE. The macroscopic QED contains all the important details about the quantized electromagnetic field are that are encoded in classical electromagnetic DGF [210, 211], which acts as a bridge between the quantum theory and classical field solutions.

We consider the dipolar contribution in vacuum within the cavity walls. We calculate the electromagnetic field of an oscillatory current as given below:

$$\mathbf{j}(\mathbf{r}, t) = \mathrm{Re}\left\{\mathbf{j}(\mathbf{r}, \omega)\, e^{-i\omega t}\right\} \tag{4.36}$$

which is located in the same nonmagnetic environment.

Now, according to Maxwell's equations and the superposition principle, the total electric field can be separated into the emitted (particular) field for which the solution corresponds to a source in an infinitely extended medium and the

scattered (homogeneous) field for which the solution is associated with the presence of boundaries.

In particular, the total electric field can be written as $\mathbf{E}(\mathbf{r},t) = \mathrm{Re}\{\mathbf{E}(\mathbf{r},\omega)\, e^{-i\omega t}\}$ can be written as

$$\mathbf{E}(\mathbf{r},\omega) = \mathbf{E}^{\mathrm{PART}}(\mathbf{r},\omega) + \mathbf{E}^{\mathrm{HOM}}(\mathbf{r},\omega), \tag{4.37}$$

separating the particular $\mathbf{E}^{\mathrm{PART}}(\mathbf{r},\omega)$ and homogeneous $\mathbf{E}^{\mathrm{HOM}}(\mathbf{r},\omega)$ solutions. The particular solution satisfies

$$\begin{aligned}
&\nabla\cdot\mathbf{D}^{\mathrm{PART}}(\mathbf{r},t) = \rho(\mathbf{r},t),\\
&\nabla\cdot\mathbf{B}^{\mathrm{PART}}(\mathbf{r},t) = 0,\\
&\nabla\times\mathbf{E}^{\mathrm{PART}}(\mathbf{r},t) = -\partial_t\mathbf{B}^{\mathrm{PART}}(\mathbf{r},t),\\
&\nabla\times\mathbf{B}^{\mathrm{PART}}(\mathbf{r},t) = \mu_0\mathbf{j}(\mathbf{r},t) + \mu_0\partial_t\mathbf{D}^{\mathrm{PART}}(\mathbf{r},t),
\end{aligned} \tag{4.38}$$

where $\mathbf{D}^{\mathrm{PART}}$ and $\mathbf{B}^{\mathrm{PART}}$ are the displacement and the induction magnetic fields, respectively, while $\rho(\mathbf{r},t)$ is the volume charge density satisfying the continuity equation $\partial_t\rho(\mathbf{r},t) + \nabla\cdot\mathbf{j}(\mathbf{r},t) = 0$.

From the above equations 4.38 we get

$$\begin{aligned}
&\nabla\times\mathbf{E}^{\mathrm{PART}}(\mathbf{r},t) = -\partial_t\mathbf{B}^{\mathrm{PART}}(\mathbf{r},t)\\
&\Rightarrow \nabla\times[\nabla\times\mathbf{E}^{\mathrm{PART}}(\mathbf{r},t)] = -\partial_t[\nabla\times\mathbf{B}^{\mathrm{PART}}(\mathbf{r},t)]\\
&\Rightarrow \nabla\times\nabla\times\mathbf{E}^{\mathrm{PART}}(\mathbf{r},t) + \mu_0\epsilon_0\partial_t^2\mathbf{E}^{\mathrm{PART}}(\mathbf{r},t) = -\mu_0\partial_t\mathbf{j}^{\mathrm{PART}}(\mathbf{r},t)
\end{aligned} \tag{4.39}$$

So in frequency space, the equation reads:

$$\left(\nabla\times\nabla\times - \frac{\omega^2}{c^2}\right)\mathbf{E}^{\mathrm{PART}}(\mathbf{r},\omega) = i\omega\mu_0\mathbf{j}^{\mathrm{PART}}(\mathbf{r},\omega) \tag{4.40}$$

From the system of equations 4.38, one easily retrieves the inhomogeneous Helmholtz

equation 4.40.

The homogeneous field solution can be found by setting the right-hand side of Eq. 4.40 to zero. Its amplitudes are fixed by the boundary conditions that encode the full geometry of the environment. We have to solve the above inhomogeneous Helmholtz equation 4.40 to find out the total electric field, see Eq. 4.37. In order to find a particular solution to the problem, the above equation 4.40 can be written in terms of DGF as follows:

$$\mathbf{E}^{\mathrm{PART}}(\mathbf{r},\omega) = i\omega\mu_0 \int_{\mathrm{V}} d^3r' \overleftrightarrow{\mathrm{G}}_{\mathrm{EMISS}}(\mathbf{r},\mathbf{r}',\omega)\cdot\mathbf{j}(\mathbf{r}',\omega), \tag{4.41}$$

where $\overleftrightarrow{\mathrm{G}}_{\mathrm{EMISS}}(\mathbf{r},\mathbf{r}',\omega)$ is the DGF satisfying

$$\left(\nabla\times\nabla\times-\frac{\omega^2}{c^2}\right)\overleftrightarrow{\mathrm{G}}_{\mathrm{EMISS}}(\mathbf{r},\mathbf{r}',\omega) = \mathbb{I}_3\delta(\mathbf{r}-\mathbf{r}'), \tag{4.42}$$

where V is the cavity volume. By using the condition of Eq. 4.42 and by substituting 4.41 in 4.40, we find Eq. 4.40 is satisfied.

In this study, the considered quantum system possesses translational invariance in the xy-plane; therefore, we write

$$\mathbf{r}_{\mathrm{DIP}} = (\mathbf{r}_\perp = 0,\ z_{\mathrm{DIP}}) \tag{4.43a}$$

$$\mathbf{j}(\mathbf{r}',\omega) = -i\omega\,\mathbf{d}_{ge}\,\delta(\mathbf{r}'-z_{\mathrm{DIP}}\hat{e}_z) \tag{4.43b}$$

where $\hat{e}_z$ is the unit vector along the $z-$direction that is chosen to be perpendicular with respect to the cavity walls and $\mathbf{d}_{ge}$ is the non-trivial dipole transition element.

Using equations 4.43 and 4.41 we express $\mathbf{E}^{\mathrm{PART}}(\mathbf{r},\omega)$ as below:

$$\begin{aligned}\mathbf{E}^{\mathrm{PART}}(\mathbf{r},\omega) &= \omega^2\mu_0\int_{\mathrm{V}} d^3r' \overleftrightarrow{\mathrm{G}}_{\mathrm{EMISS}}(\mathbf{r},\mathbf{r}',\omega)\,\delta(\mathbf{r}'-z_{\mathrm{DIP}}\hat{e}_z)\cdot\mathbf{d}_{ge}\\ \Rightarrow \mathbf{E}^{\mathrm{PART}}(\mathbf{r},\omega) &= \omega^2\mu_0\,\overleftrightarrow{\mathrm{G}}_{\mathrm{EMISS}}(\mathbf{r},z_{\mathrm{DIP}},\omega)\cdot\mathbf{d}_{ge}\end{aligned} \tag{4.44}$$

The DGF using the Fourier transform can be computed as:

$$\overleftrightarrow{\mathrm{G}}_{\mathrm{EMISS}}(\mathbf{r}, z_{\mathrm{DIP}}, \omega) = \int \frac{d^3k}{(2\pi)^3} \overleftrightarrow{\mathrm{G}}_{\mathrm{EMISS}}(\mathbf{k}, z_{\mathrm{DIP}}, \omega)\, e^{i\mathbf{k}\cdot\mathbf{r}} \tag{4.45}$$

where,

$$\delta(\mathbf{r} - z_{\mathrm{DIP}}\hat{e}_z) = \int \frac{d^3k}{(2\pi)^3} e^{i\mathbf{k}\cdot(\mathbf{r} - z_{\mathrm{DIP}}\hat{e}_z)} \tag{4.46}$$

Substituting Eq. 4.45 and Eq. 4.46 into Eq.4.41, we obtain the DGF in the angular spectrum decomposition through contour integration over k_z as follows:

4.4.2.1 Evaluation of the emission DGF for $z \neq z_{\mathrm{DIP}}$

Combining Eqs. 4.42, 4.45 and 4.46, and solving separately for the orthogonal subspaces $\mathbf{k}\otimes\mathbf{k}/k^2$ and $\mathbb{I}_3 - \mathbf{k}\otimes\mathbf{k}/k^2$, we retrieve

$$\begin{aligned}\overleftrightarrow{\mathrm{G}}_{\mathrm{EMISS}}(\mathbf{r}, z_{\mathrm{DIP}}, \omega) \int \frac{d\mathbf{k}}{(2\pi)^3} \frac{e^{i\mathbf{k}_\perp\cdot\mathbf{r}_\perp} e^{ik_z(z - z_{\mathrm{DIP}})}}{k_{\mathrm{VAC}}^2 (k^2 - k_{\mathrm{VAC}}^2)} \times \\ \times \begin{bmatrix} k_{\mathrm{VAC}}^2 - k_x^2 & -k_x k_y & -k_x k_z \\ -k_x k_y & k_{\mathrm{VAC}}^2 - k_y^2 & -k_y k_z \\ -k_x k_z & -k_y k_z & k_{\mathrm{VAC}}^2 - k_z^2 \end{bmatrix}.\end{aligned} \tag{4.47}$$

For $z \neq z_{\mathrm{DIP}}$, defining $\Delta z = z - z_{\mathrm{DIP}}$ and

$$I(\Delta z) = \int dk_z \frac{e^{ik_z\Delta z}}{k_z^2 - \beta^2} = i\pi \frac{e^{i\beta|\Delta z|}}{\beta}, \tag{4.48}$$

We can determine all the entries of the angular spectrum representation of the DGF. Eq. 4.48 describes the tensor's entries, whose numerator is proportional to k_z^0.

Therefore,

$$\int dk_z \frac{k_z e^{ik_z\Delta z}}{k_z^2 - \beta^2} = \frac{1}{i}\frac{\partial I}{\partial \Delta z} = i\pi \mathrm{sgn}(\Delta z) e^{i\beta|\Delta z|}, \tag{4.49}$$

and

$$\int dk_z \frac{k_z^2 e^{ik_z \Delta z}}{k_z^2 - \beta^2} = -\frac{\partial I}{\partial \Delta z} = 2\pi\delta(\Delta z) + i\pi\beta \mathrm{sgn}(\Delta z) e^{i\beta|\Delta z|}. \tag{4.50}$$

This allows us to determine the full angular spectrum decomposition of the DGF. For $\Delta z \neq 0$, the delta term in Eq. 4.50 vanishes, and we recover the standard evanescent DGF.

This leads to

$$\overleftrightarrow{\mathrm{G}}_{\mathrm{EMISS}}(\mathbf{r}, z_{\mathrm{DIP}}, \omega) = \sum_{f=\pm 1} \int \frac{d\mathbf{k}_\perp}{(2\pi)^2} e^{i\mathbf{k}_\perp \cdot \mathbf{r}_\perp} e^{i\beta|z - z_{\mathrm{DIP}}|} \times \underbrace{\times \frac{i\Theta\left[f(z - z_{\mathrm{DIP}})\right]}{2k_{\mathrm{VAC}}^2 \beta} \begin{bmatrix} k_{\mathrm{VAC}}^2 - k_x^2 & -k_x k_y & -f k_x \beta \\ -k_x k_y & k_{\mathrm{VAC}}^2 - k_y^2 & -f k_y \beta \\ -f k_x \beta & -f k_y \beta & k_{\mathrm{VAC}}^2 - \beta^2 \end{bmatrix}}_{\overleftrightarrow{\mathrm{G}}_f^{\mathrm{EMISS}}(\mathbf{k}_\perp)}, \tag{4.51}$$

where,

$$k_{\mathrm{VAC}} = \omega/c,$$

$$\mathbf{k}_\perp = k_x \hat{\mathbf{e}}_x + k_y \hat{\mathbf{e}}_y,$$

$$\beta = \sqrt{k_{\mathrm{VAC}}^2 - k_\perp^2 + i0^+},$$

and and $\Theta(x)$ is the Heaviside step function.

The above treatment for β declares that it always has a non-negative imaginary part. For evanescent waves ($k_{\mathrm{VAC}}^2 < k_\perp^2$), the argument of the square root is negative, and adding $+i0^+$ pushes the value into the second quadrant of the complex plane. We evaluate the positive imaginary part by calculating the square root, which is important for spatial decay.

However, the expression in Eq. 4.51 holds only for $z \neq z_{\mathrm{DIP}}$, while for the evaluation of the SE rate, we are interested in expressing the DGF at the dipole position [216]. We perform contour integration in the complex k_z plane by closing the integration path either in the upper half-plane (for $z > z_{\mathrm{DIP}}$) or in the lower

half-plane (for $z < z_{\mathrm{DIP}}$) by using the above condition.

4.4.2.2 Evaluation of the emission DGF for $z = z_{\mathrm{DIP}}$

Starting from Eq. 4.47 and using the Sokhotski-Plemelj relation, we now have

$$\begin{aligned} I(\Delta z) &= \int \frac{dk_z}{k_z^2 - \beta^2} = \\ &= \mathcal{P} \int \frac{dk_z}{k_z^2 - \beta^2 + i0^+} + i\pi \int dk_z \delta(k_z^2 - \beta^2 + i0^+) = \\ &= \frac{i\pi}{\beta}. \end{aligned} \tag{4.52}$$

The entries proportional to k_z are zero due to arguments related to the oddness of the integrand function. Eventually,

$$\begin{aligned} \int dk_z \frac{k_z^2}{k_z^2 - \beta^2} = \int dk_z + \beta^2 \int \frac{dk_z}{k_z^2 - \beta^2} = \\ = \infty + i\pi\beta. \end{aligned} \tag{4.53}$$

Therefore, the real part of the integral diverges.

But, for the evaluation of the SE rate, we only need the imaginary part of the DGF. In this case, we get

$$\begin{aligned} &\mathrm{Im}\left\{ \overleftrightarrow{\mathrm{G}}_{\mathrm{EMISS}}(z_{\mathrm{DIP}}, z_{\mathrm{DIP}}, \omega) \right\} = \\ &= \int \frac{d\mathbf{k}_\perp}{(2\pi)^2} \frac{i}{2k_{\mathrm{VAC}}^2 \beta} \begin{bmatrix} k_{\mathrm{VAC}}^2 - k_x^2 & -k_x k_y & 0 \\ -k_x k_y & k_{\mathrm{VAC}}^2 - k_y^2 & 0 \\ 0 & 0 & k_{\mathrm{VAC}}^2 - \beta^2 \end{bmatrix}. \end{aligned} \tag{4.54}$$

We can now express Eq. 4.54 as below:

$$\begin{aligned}\mathrm{Im}\left\{\overleftrightarrow{\mathrm{G}}_{\mathrm{EMISS}}\left(z_{\mathrm{DIP}}, z_{\mathrm{DIP}}, \omega\right)\right\} = \\ = \int \frac{d\mathbf{k}_\perp}{(2\pi)^2} \frac{i}{2k_{\mathrm{VAC}}^2 \beta} \begin{bmatrix} k_{\mathrm{VAC}}^2 - k_x^2 & -k_x k_y & -k_x \beta \\ -k_x k_y & k_{\mathrm{VAC}}^2 - k_y^2 & -k_y \beta \\ -k_x \beta & -k_y \beta & k_{\mathrm{VAC}}^2 - \beta^2 \end{bmatrix},\end{aligned} \tag{4.55}$$

We observe that the integrand functions of the new non-zero entries actually give null contributions to the integral since they are odd functions of either k_x or k_y.

We aim to detect an imbalance in the SE rate between RCP and LCP light due to the cavity being influenced by Local Density of Optical States (LDOS). Hence, we decompose the total DGF in the CP basis.

Now, we define the following Hermitian projection operators

$$\begin{aligned}\hat{P}_f(\mathbf{k}_\perp) &= \left((\mathbf{k}_\perp, f\beta) \otimes (\mathbf{k}_\perp, f\beta)^\dagger\right) / |\mathbf{k}|^2 \\ \hat{P}_{\hat{n}_{s,f}(\mathbf{k}_\perp)} &= \hat{n}_{s,f}(\mathbf{k}_\perp) \otimes \hat{n}_{s,f}^\dagger(\mathbf{k}_\perp)\end{aligned} \tag{4.56}$$

where, $\hat{P}_f(\mathbf{k}_\perp)$ is the projector along the $\mathbf{k}$direction. At the same time, the other two are projectors on either the right ($s = 1$) or left ($s = -1$) CP basis for forward ($f = 1$) or backward ($f = -1$) directions.

Therefore, $\hat{n}_{s,f}(\mathbf{k}_\perp)$ are the CP unit vectors are defined as below:

$$\begin{aligned}\hat{n}_{s,f}(\mathbf{k}_\perp) = \mathcal{N}\Bigg(\hat{e}_x + \frac{fisk_{\mathrm{VAC}}\beta - k_x k_y}{\beta^2 + k_y^2}\hat{e}_y + \\ - \frac{isk_{\mathrm{VAC}}k_y + fk_x\beta}{\beta^2 + k_y^2}\hat{e}_z\Bigg), \\ \mathcal{N} = \left[1 + \frac{\left|fisk_{\mathrm{VAC}}\beta - k_x k_y\right|^2}{\left|\beta^2 + k_y^2\right|^2} + \frac{\left|isk_{\mathrm{VAC}}k_y + fk_x\beta\right|^2}{\left|\beta^2 + k_y^2\right|^2}\right]^{-1/2}.\end{aligned} \tag{4.57}$$

The solutions are obtained by solving the homogeneous system of Maxwell's equations in vacuum and using the CP unit vectors.

Therefore, for $z \neq z_{\mathrm{DIP}}$ the transverse electromagnetic field, we define

$$\overleftrightarrow{\mathrm{G}}^{\mathrm{EMISS}}_{s,f}(\mathbf{k}_\perp) = \hat{P}_{\hat{n}_{s,f}(\mathbf{k}_\perp)} \overleftrightarrow{\mathrm{G}}^{\mathrm{EMISS}}_{f}(\mathbf{k}_\perp) \hat{P}^{\dagger}_{\hat{n}_{s,f}(\mathbf{k}_\perp)} \tag{4.58}$$

which gives the decomposition of the radiative field in the CP basis as below:

$$\overleftrightarrow{\mathrm{G}}^{\mathrm{EMISS}}_{f}(\mathbf{k}_\perp) = \sum_{s=\pm 1} \overleftrightarrow{\mathrm{G}}^{\mathrm{EMISS}}_{s,f}(\mathbf{k}_\perp) \tag{4.59}$$

because,

$$\hat{P}_f(\mathbf{k}_\perp, f\beta) \overleftrightarrow{\mathrm{G}}^{\mathrm{EMISS}}_{f}(\mathbf{k}_\perp) \hat{P}_f(\mathbf{k}_\perp, f\beta)^{\dagger} = 0, \tag{4.60}$$

We note that the CPs do not mix because the emitter is in an isotropic, homogeneous medium (vacuum). Moreover, for $z = z_{\mathrm{DIP}}$ the angular spectrum components of the DGF in Eq. 4.55 show a trivial projection on the longitudinal direction (fixing $f = 1$).

Inside the chiral cavity, we solve the homogeneous problem in a vacuum, and we express the field as

$$\begin{aligned} \mathbf{E}^{\mathrm{HOM}}(\mathbf{r}, \omega) &= \int d\mathbf{k}_\perp \frac{e^{i\mathbf{k}_\perp \cdot \mathbf{r}_\perp}}{(2\pi)^2} \sum_{s,f=\pm 1} E^{\mathrm{HOM}}_{s,f}(\mathbf{k}_\perp) \hat{n}_{s,f}(\mathbf{k}_\perp) e^{if\beta z} = \\ &= i\omega\mu_0 \int_{\mathrm{V}} d^3 r' \overleftrightarrow{\mathrm{G}}_{\mathrm{REFL}}(\mathbf{r}, \mathbf{r}', \omega) \cdot \mathbf{j}(\mathbf{r}', \omega), \end{aligned} \tag{4.61}$$

where

$$\left(\nabla \times \nabla \times - \frac{\omega^2}{c^2} \right) \overleftrightarrow{\mathrm{G}}_{\mathrm{REFL}}(\mathbf{r}, \mathbf{r}', \omega) = 0, \tag{4.62}$$

where the spectral decomposition can be expressed as below:

$$\overleftrightarrow{\mathrm{G}}_{\mathrm{REFL}}(\mathbf{r}, \mathbf{r}', \omega) = \int \frac{d\mathbf{k}_\perp}{(2\pi)^2} \overleftrightarrow{\mathrm{G}}_{\mathrm{REFL}}(\mathbf{k}_\perp, \mathbf{r}', \omega) e^{i\mathbf{k}_\perp \cdot \mathbf{r}_\perp} e^{if\beta z}. \tag{4.63}$$

The total transverse field can be written as below:

$$\mathbf{E}(\mathbf{r},\omega) = \omega^2\mu_0 \sum_{s,f=\pm1} \Big[\overleftrightarrow{\mathrm{G}}^{\mathrm{EMISS}}_{s,f}(\mathbf{r}, z_{\mathrm{DIP}}, \omega) + \\ + \overleftrightarrow{\mathrm{G}}^{\mathrm{REFL}}_{s,f}(\mathbf{r}, z_{\mathrm{DIP}}, \omega) \Big] \cdot \mathbf{d}_{\mathrm{ge}}, \tag{4.64}$$

where $\overleftrightarrow{\mathrm{G}}_{\mathrm{REFL}}(\mathbf{r},\mathbf{r}',\omega) = \sum_{f,s=\pm1} \overleftrightarrow{\mathrm{G}}^{\mathrm{REFL}}_{s,f}(\mathbf{r}, z_{\mathrm{DIP}}, \omega)$ is the DGF accounting for cavity reflections and thus for the homogeneous contribution to the field.

To determine the homogeneous solution, we now apply the TMA approach as discussed in the section 4.4.1.1.

For our problem, we need two transfer matrices: one for the mirror located at $z = w/2$ and one for the mirror at $z = -w/2$, where w denotes the cavity width.

For the mirror at $z = w/2$, we may use the matrix as computed in Ref. [223], and discussed in the section 4.4.1.1.

For the mirror at $z = -w/2$ we must account for a global geometric rotation of π about the $x-$axis relative to the former mirror (see Figure 4.2. Basically, the mirrors' optical axes are reversed, though they are physically identical. So, for that, we need to recalculate the appropriate incident, reflected, and transmitted field components and compute the corresponding transfer matrix.

Therefore, for a given $\mathbf{k}_\perp$ we have [228]

$$\begin{aligned}
&\begin{bmatrix} E^{\mathrm{HOM}}_{1,1} \\ E^{\mathrm{HOM}}_{-1,1} \end{bmatrix} e^{-i\beta\frac{w}{2}} = \hat{M}^{-1}_{\mathrm{REFL}} \times \\
&\quad \times \begin{bmatrix} \omega^2\mu_0 \hat{n}^\dagger_{1,-1} \cdot \overleftrightarrow{\mathrm{G}}^{\mathrm{EMISS}}_{-1} \cdot \mathbf{d}_{\mathrm{ge}} e^{i\beta\left|\frac{w}{2}+z_{\mathrm{DIP}}\right|} + E^{\mathrm{HOM}}_{1,-1} e^{i\beta\frac{w}{2}} \\ \omega^2\mu_0 \hat{n}^\dagger_{-1,-1} \cdot \overleftrightarrow{\mathrm{G}}^{\mathrm{EMISS}}_{-1} \cdot \mathbf{d}_{\mathrm{ge}} e^{i\beta\left|\frac{w}{2}+z_{\mathrm{DIP}}\right|} + E^{\mathrm{HOM}}_{-1,-1} e^{i\beta\frac{w}{2}} \end{bmatrix}, \\
&\begin{bmatrix} E^{\mathrm{HOM}}_{1,-1} \\ E^{\mathrm{HOM}}_{-1,-1} \end{bmatrix} e^{-i\beta\frac{w}{2}} = \hat{M}^{1}_{\mathrm{REFL}} \times \\
&\quad \times \begin{bmatrix} \omega^2\mu_0 \hat{n}^\dagger_{1,1} \cdot \overleftrightarrow{\mathrm{G}}^{\mathrm{EMISS}}_{1} \cdot \mathbf{d}_{\mathrm{ge}} e^{i\beta\left|-\frac{w}{2}+z_{\mathrm{DIP}}\right|} + E^{\mathrm{HOM}}_{1,1} e^{i\beta\frac{w}{2}} \\ \omega^2\mu_0 \hat{n}^\dagger_{-1,1} \cdot \overleftrightarrow{\mathrm{G}}^{\mathrm{EMISS}}_{1} \cdot \mathbf{d}_{\mathrm{ge}} e^{i\beta\left|-\frac{w}{2}+z_{\mathrm{DIP}}\right|} + E^{\mathrm{HOM}}_{-1,1} e^{i\beta\frac{w}{2}} \end{bmatrix}.
\end{aligned} \tag{4.65}$$

In particular, this expression holds for a dipole that is not located in correspondence with either one or the other wall.

With the decomposition $\overleftrightarrow{\mathrm{G}}^{\mathrm{EMISS}}_{f}(\mathbf{k}_\perp) = \sum_{s=\pm1} \overleftrightarrow{\mathrm{G}}^{\mathrm{EMISS}}_{s,f}(\mathbf{k}_\perp)$ and solving the system, we retrieve the reflected DGF, which can be as well decomposed as $\overleftrightarrow{\mathrm{G}}^{\mathrm{REFL}}_{f}(\mathbf{k}_\perp) = \sum_{s=\pm1} \overleftrightarrow{\mathrm{G}}^{\mathrm{REFL}}_{s,f}(\mathbf{k}_\perp)$.

We solve for the homogeneous part, and we write it as below:

$$\begin{aligned}
\begin{bmatrix} E^{\mathrm{HOM}}_{1,1} \\ E^{\mathrm{HOM}}_{-1,1} \end{bmatrix} &= \omega^2\mu_0 \begin{bmatrix} \mathcal{G}^{\mathrm{REFL}}_{1,1} \hat{n}^\dagger_{1,1} \cdot \mathbf{d}_{ge} \\ \mathcal{G}^{\mathrm{REFL}}_{-1,1} \hat{n}^\dagger_{-1,1} \cdot \mathbf{d}_{ge} \end{bmatrix} \\
\begin{bmatrix} E^{\mathrm{HOM}}_{1,-1} \\ E^{\mathrm{HOM}}_{-1,-1} \end{bmatrix} &= \omega^2\mu_0 \begin{bmatrix} \mathcal{G}^{\mathrm{REFL}}_{1,-1} \hat{n}^\dagger_{1,-1} \cdot \mathbf{d}_{ge} \\ \mathcal{G}^{\mathrm{REFL}}_{-1,-1} \hat{n}^\dagger_{-1,-1} \cdot \mathbf{d}_{ge} \end{bmatrix}
\end{aligned}, \tag{4.66}$$

where $\overleftrightarrow{\mathrm{G}}^{\mathrm{REFL}}_{f}(\mathbf{k}_\perp) = \sum_{s=\pm1} \mathcal{G}^{\mathrm{REFL}}_{s,f}(\mathbf{k}_\perp) \hat{n}_{s,f}(\mathbf{k}_\perp) \otimes \hat{n}^\dagger_{s,f}(\mathbf{k}_\perp)$ is the final scattering DGF.

We can then find $\mathcal{G}^{\mathrm{REFL}}_{s,f}(\mathbf{k}_\perp)$ and express the total transverse electric field within the cavity as shown in Eq. 4.64.

we can express the SE rate in terms of the total DGF as

$$\begin{aligned}\gamma &= \frac{2\omega_0^2}{\hbar\varepsilon_0 c^2}\mathbf{d}_{\mathrm{ge}}^* \cdot \mathrm{Im}\left\{\overleftrightarrow{\mathrm{G}}_{\mathrm{TOT}}\left(\mathbf{r}_{\mathrm{DIP}}, \mathbf{r}_{\mathrm{DIP}}, \omega_0\right)\right\} \cdot \mathbf{d}_{\mathrm{ge}}, \\ \gamma_{\mathrm{R}} &= \frac{2\omega_0^2}{\hbar\varepsilon_0 c^2}\mathbf{d}_{\mathrm{ge}}^* \cdot \mathrm{Im}\left\{\overleftrightarrow{\mathrm{G}}_{\mathrm{TOT}}^{\mathrm{s}=1}\left(\mathbf{r}_{\mathrm{DIP}}, \mathbf{r}_{\mathrm{DIP}}, \omega_0\right)\right\} \cdot \mathbf{d}_{\mathrm{ge}}, \\ \gamma_{\mathrm{L}} &= \frac{2\omega_0^2}{\hbar\varepsilon_0 c^2}\mathbf{d}_{\mathrm{ge}}^* \cdot \mathrm{Im}\left\{\overleftrightarrow{\mathrm{G}}_{\mathrm{TOT}}^{\mathrm{s}=-1}\left(\mathbf{r}_{\mathrm{DIP}}, \mathbf{r}_{\mathrm{DIP}}, \omega_0\right)\right\} \cdot \mathbf{d}_{\mathrm{ge}},\end{aligned} \tag{4.67}$$

where γ_{R} and γ_{L} are SE rates for RCP and LCP light, respectively; $\omega_0 = \omega_{\mathrm{e}} - \omega_{\mathrm{g}}$ is the characteristic transition frequency of the two-level system, and

$$\overleftrightarrow{\mathrm{G}}_{\mathrm{TOT}}\left(\mathbf{r}_{\mathrm{DIP}}, \mathbf{r}_{\mathrm{DIP}}, \omega_0\right) = \sum_{s=\pm 1} \overleftrightarrow{\mathrm{G}}_{\mathrm{TOT}}^{\mathrm{s}=\pm 1}\left(\mathbf{r}_{\mathrm{DIP}}, \mathbf{r}_{\mathrm{DIP}}, \omega_0\right), \tag{4.68}$$

where

$$\begin{aligned}\overleftrightarrow{\mathrm{G}}_{\mathrm{TOT}}^{\mathrm{s}=\pm 1}\left(\mathbf{r}_{\mathrm{DIP}}, \mathbf{r}_{\mathrm{DIP}}, \omega_0\right) = \int \frac{d\mathbf{k}_\perp}{(2\pi)^2}\Bigg[&\overleftrightarrow{\mathrm{G}}_{s}^{\mathrm{EMISS}}\left(\mathbf{k}_\perp, \omega\right) + \\ &+ \sum_{f=\pm 1} \overleftrightarrow{\mathrm{G}}_{s,f}^{\mathrm{REFL}}\left(\mathbf{k}_\perp, z_{\mathrm{DIP}}, \omega\right) e^{if\beta z_{\mathrm{DIP}}}\Bigg],\end{aligned} \tag{4.69}$$

The emission term can be calculated from Eq. 4.55 by decomposing into the CP basis.

Also, we can define the partial LDOS for both CP states

$$\rho^s_{|\mathbf{d}_{\mathrm{ge}}|} \propto \hat{n}_{\mathrm{ge}} \cdot \mathrm{Im}\left\{\overleftrightarrow{\mathrm{G}}^{s}_{\mathrm{TOT}}\left(\mathbf{r}_{\mathrm{DIP}}, \mathbf{r}_{\mathrm{DIP}}, \omega_0\right)\right\} \cdot \hat{n}_{\mathrm{ge}}, \tag{4.70}$$

where $\hat{n}_{ge}$ is the unit vector along which the dipole is oriented. We calculate this DGF at the location of the two-level system. In the spontaneous decay, a photon of energy $\hbar\omega_0$ can be released for the given dipole orientation and position, which is indicated by LDOS, which denotes the number of modes per unit volume and frequency. Therefore, we observe from Eq. 4.70 and Eq. 4.67 that SE is strongly dependent on the mode distribution and position of the theoretical nodes and antinodes.

4.4.3 Results and discussions

For studying polarization-sensitive spontaneous emission, we consider Rubidium-85 (^{85}Rb) as a quantum emitter. We choose the atomic transition to be the D2 line for detailed analysis, i.e $5S_{1/2} \rightarrow 5P_{3/2}$, commonly used in quantum optics due to its sharpness and resonance with a vacuum wavelength near $\lambda_{\text{VAC}} = 780$ nm, with a reduced electric dipole matrix element $|\mathbf{d}_{ge}| = 5.98211ea_0$ [229], with e the absolute value of the electric charge, a_0 Bohr radius. We neglect the internal degeneracy or magnetic sub-levels; that is, we consider a pure two-level atomic system.

Therefore, we first find the SE rate for the considered system in vacuum, then study polarization-dependent results by placing the quantum emitter in a chiral cavity. Then we first study the imbalance between two CP by varying the cavity width for different fixed dipolar orientations; then we fix the cavity width and vary the dipolar position to study the imbalance in the SE rate.

4.4.3.1 Evaluation of SE in vacuum

We calculate the SE for this transition in free space. We consider only the emission contribution of the DGF. The calculation gives us $\gamma \approx 1.5279 \times 10^8 \text{s}^{-1}$. In free space, there is no preference for either RCP or LCP when there are no other influences; both rates are $\gamma/2$, which is half of the total one. It is worth mentioning that the DGF, which solves Maxwell's equations, accounts for evanescent (non-radiative) modes, but our calculation only focused on the propagating modes. Evanescent modes do not support the constructive interference required to form Fabry-Pérot cavity resonances. Therefore, they do not enhance SE for RCP and LCP modes.

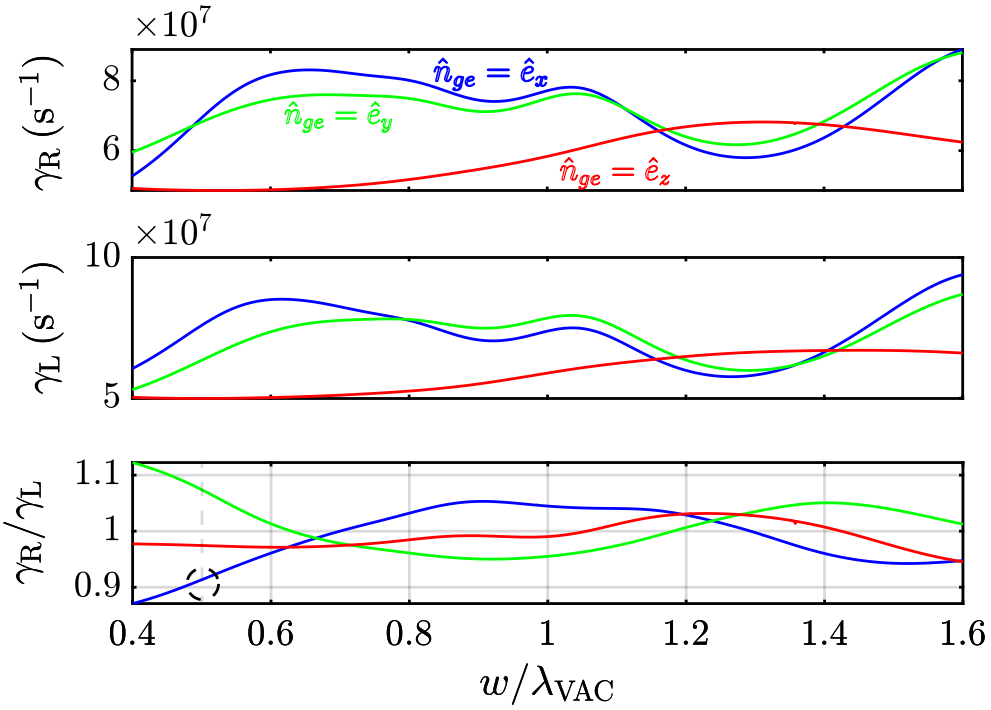

Figure 4.5 The panels illustrate, from top to bottom, the dependence of SE rate for RCP ight and LCP, and the ratio between these two emission rates associated with a ^{87}Rb emitter positioned at the origin of our reference frame, which is modified at a vacuum wavelength of approximately 780 nm. In each figure, the values are plotted as a function of the optical cavity width w and for several distinct fixed dipole orientations $\hat{n}_{\rm ge} = \hat{e}_{x,y,z}$, indicated by the blue ($\hat{e}_x$), green ($\hat{e}_y$), and red curves ($\hat{e}_z$), where the bottom plot includes a dashed black circle that marks the specific ratio observed when the dipole is oriented along the x-axis and the cavity width is set to half the vacuum wavelength at $w = 0.5\lambda_{\rm VAC}$.

4.4.3.2 Evaluation of SE varying the cavity width and for different fixed dipolar orientations

The SE rates are primarily dependent on the radiative field and its associated cavity modes for the given cavity length at least $0.4\lambda_{\rm VAC}$.

First, we consider a dipole at the origin of the reference frame, see Fig 4.2, and we calculate $\gamma_{\rm R}$ and $\gamma_{\rm L}$, see Eq. 4.67, by changing the width of the cavity from $0.4\lambda_{\rm VAC}$ up to $1.6\lambda_{\rm VAC}$. For the incidence angle of 20° close to the normal wall (z-axis), the cavity transmits RCP excitation and reflects LCP excitation.

In Fig 4.5 we observe the variation of SE from top to bottom panel for SE rate

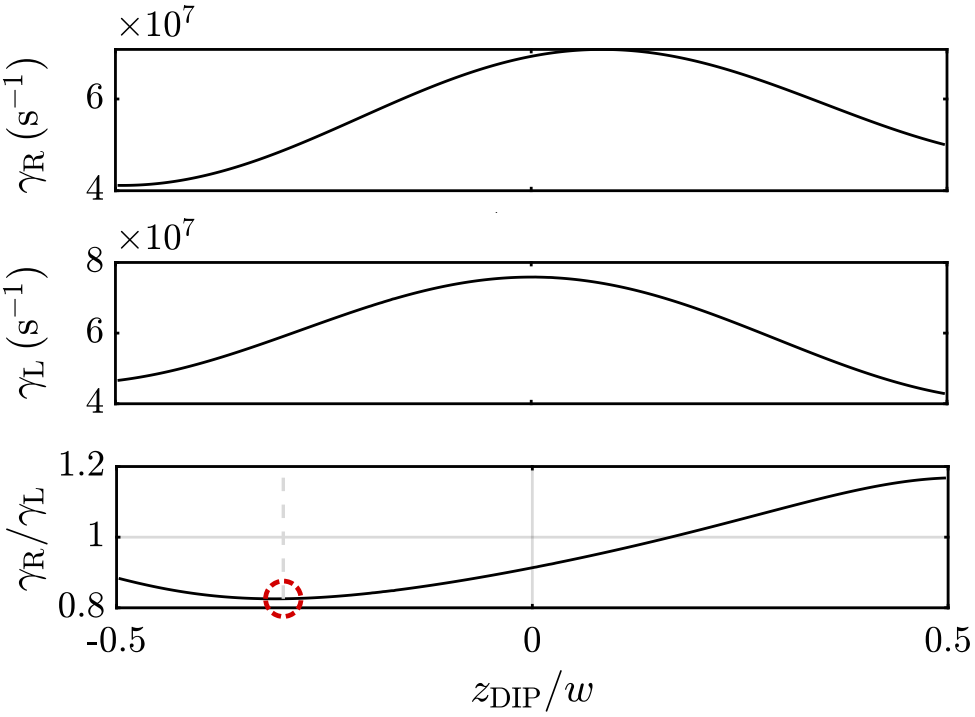

Figure 4.6 SE rate by a ^{87}Rb emitter at $\lambda_{\mathrm{VAC}} \simeq 780$ nm for RCP, LCP, and their ratio, respectively, from the top to the bottom panels. These quantities are illustrated as a function of the emitter position within a cavity of fixed width $w = 0.5\lambda_{\ rmVAC}$ and for fixed dipole orientation $\hat{n}_{\mathrm{ge}} = \hat{e}_x$. The red dashed circle in the bottom panel highlights the configuration of maximum imbalance between RCP and LCP SE rates, which is approximately 20%.

for right and left, and the ratio between the two as a function of the cavity wall width. Also, we observe this variation across different fixed dipolar orientations in the $\hat{\mathbf{e}}_x$, $\hat{\mathbf{e}}_y$, and $\hat{\mathbf{e}}_z$ directions, denoted by the blue, green, and red curves. The black dotted circle in the bottom panel highlights the dipole moment oriented along the x-axis and the cavity width, set to half the vacuum wavelength, i.e $w = 0.5\lambda_{\mathrm{VAC}}$.

We observe in the TAPCs that, due to a lack of cylindrical symmetry, the imbalance in the SE ratio between RCP and LCP is inverted when the dipolar orientation changes from $\hat{\mathbf{e}}_x$ to $\hat{\mathbf{e}}_y$. Physically, it signifies that the system has truncated the anisotropic photonic crystal, so the edge effects are introduced by the first $CaCO_3$ layer's extraordinary axis aligned with $\hat{\mathbf{e}}_x$. A $x-$dipole couples to the extraordinary mode, while a $y-$one to the ordinary one changes the accumulation of the reflection phase and shifts the Purcell resonance modes, which signifies that

the LDOS itself, see Eq. 4.70, is strongly dependent on the dipole orientation due to the effective anisotropy of the environment. For the dipole orientation along the z direction, the net imbalance is overall smaller than the one reported for the other two cases, which confirms that the polarization sensitivity of the cavity walls corresponds to the emission angle, where the dipole field is weaker.

4.4.3.3 Evaluation of SE for different dipolar positions

Now we fix the cavity width $w = 0.5\lambda_{\ rmVAC}$ and orientation along the x-direction, where we expect the interaction between the cavity walls and the emitter's position to be relatively strong; see Fig. 4.5. We change the dipole position from one part of the cavity wall to another. We study the dependence of the SE rate for right γ_{R} (top panel), left γ_{L} (mid panel), and the ratio $\gamma_{\mathrm{R}}/\gamma_{\mathrm{L}}$ (bottom panel) over z_{DIP}/w. In the bottom panel, the maximum imbalance CP-SE rate is highlighted in the red circle. We found approximately 20% for the given configurations.

Physically, it signifies that, due to the lack of mirror symmetry in the geometry of the system, such plots are not symmetric under the reflection transformation $z \to -z$.

4.4.3.4 Angular dependence of polarization dependence SE rate

Now we fix $z_{\mathrm{DIP}} = -0.3103w$ and modify the dipole orientation, as depicted in Fig. 4.7, which illustrates the zenithal (θ_{DIP}) and azimuthal (ϕ_{DIP}) dipole direction dependence of SE rate for right (a) γ_{R}, left (b) γ_{L}, and the ratio between the two CP (c) $\gamma_{\mathrm{R}}/\gamma_{\mathrm{L}}$.

We observe that, depending on the azimuthal and zenithal angle, CP-SE imbalance maxima and minima alternate periodically, repeating with a π period; see Fig. 4.7c. We express the dipole unit vector in spherical coordinates as $\hat{n}_{\mathrm{ge}} = (\sin\theta_{\mathrm{DIP}}\cos\phi_{\mathrm{DIP}}, \sin\theta_{\mathrm{DIP}}\sin\phi_{\mathrm{DIP}}, \cos\theta_{\mathrm{DIP}})$. Basically, when we rotate the dipole in the x-y plane, we change the relative phases of the circular components

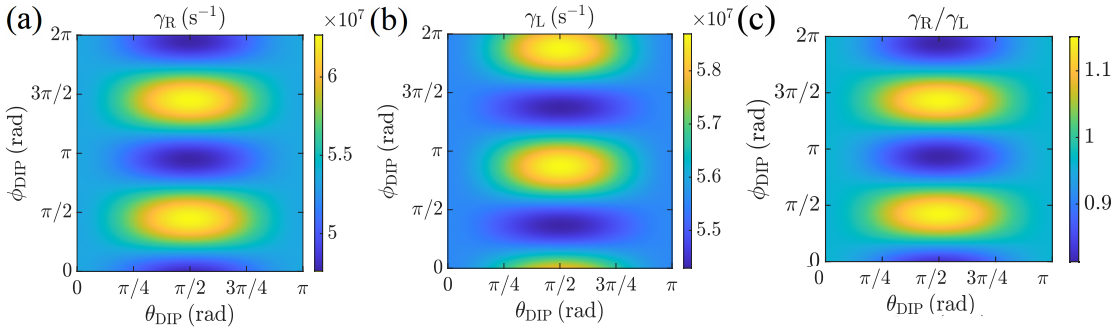

Figure 4.7 **(a,b)** SE rates for **(a)** RCP γ_R and **(b)** LCP γ_R, and **(c)** their ratio γ_R/γ_L, as a function of the dipole orientation accounted for by the zenithal and azimuthal angles θ, ϕ, respectively. All plots are obtained for ^{87}Rb emitter at $\lambda_{VAC} \simeq 780$ nm and fixed cavity width $w = 0.5\lambda_{VAC}$ and dipole position $z_{DIP} = -0.3103w$.

of the linearly polarized field, which changes the reflection phase. Interestingly, we can observe from Figs. 4.7(a),(b) that if the dipole is oriented along z, the SE is inhibited for both RCP and LCP light, meaning that the cavity is off-resonant and/or the atom is located at a node of mode functions. The dipolar orientation is random, as the process has no particular driving field, so the emission rate is averaged over orientations as follows:

$$\begin{aligned}
\gamma^{AV} &= \frac{1}{4\pi}\int_0^{2\pi} d\phi \int_0^{\pi} d\theta \sin\theta \gamma(\theta,\phi), \\
\gamma_R^{AV} &= \frac{1}{4\pi}\int_0^{2\pi} d\phi \int_0^{\pi} d\theta \sin\theta \gamma_R(\theta,\phi),, \\
\gamma_L^{AV} &= \frac{1}{4\pi}\int_0^{2\pi} d\phi \int_0^{\pi} d\theta \sin\theta \gamma_L(\theta,\phi).
\end{aligned} \tag{4.71}$$

where, $\gamma(\theta,\phi)$, $\gamma_R(\theta,\phi), \gamma_L(\theta,\phi)$ are given by Eq. 4.67 which denotes the total emission rate for a given dipole orientation given by zenithal θ and azimuthal angles ϕ, while γ_R^{AV} and γ_R^{AV} correspond to the orientation average rates for RCP and LCP excitations, respectively.

After performing these angular integrations we obtain the values $\gamma_R^{AV} = 5.47 \times 10^7\,\mathrm{s}^{-1}$ and $\gamma_L^{AV} = 5.63 \times 10^7\,\mathrm{s}^{-1}$, , still keeps $w = 0.5\lambda_{VAC}$ and $z_{DIP} = -0.3103w$. Consequently, with this configuration, we obtain an imbalance $\gamma_R/\gamma_L = 0.97$ for

the specific cavity geometry and position considered. Therefore, the calculated ratio between the averaged RCP and LCP emission rates is approximately 0.9704.

4.5 Concluding remarks

In this chapter, theoretically, we study the functionalities of the chiral cavity made of TAPCs. We study the polarization-dependent SE rate and compare it to the enhancement rather than the free-space decay rate. Our theoretical calculations mainly depend on the DGF approach and the TMA approach for studying the functionalities of TAPCs. We consider a pure two-level quantum emitter and, by averaging over random dipole orientations, observe that the system can produce a 3% CP-SE imbalance. Also, this imbalance is limited by effects such as dipole orientation averaging, which leads to a mixing of constructive and destructive interference contributions in a strongly anisotropic environment. Also, the planar cavity geometry, which mainly enabled LDOS manipulation for wave vectors collimated around the cavity. We observe that, for a fixed dipolar orientation, the imbalance can increase significantly, reaching up to 20%. But by controlling this limitation by adjusting dipole orientation through the design of advanced microcavities, it may be possible to achieve a high CP-induced SE rate. This is a promising platform for measuring chirality that can emit CP excitation at the sub-micrometer scale.

4.6 Author contribution

The work presented in this chapter is the result of a collaborative effort. The author contributed to refining the research concept and actively participated in implementing the theoretical and computational models. She was involved in the investigation and analysis of the results, including validation, data interpretation,

and the preparation of selected figures. The candidate also contributed to the manuscript's writing, revision, and editing, helping shape the final presentation of the findings.

Chapter 5

Conclusion

5.1 Summary of the thesis

This thesis is based on theoretical modeling of electromagnetic interaction and chiral molecules. In nano-optics, the interaction of electromagnetic radiation at the sub-wavelength scale is of primary importance. Also, in pharmacology, molecular chirality plays an important role because a drug's efficacy depends on its chiral composition. Therefore, chiral purity and selectivity are important for the development of new drugs. The linear, inherently weak chiroptical signal has a limited sensitivity, allowing measurement of chirality up to a milliliter in volume. This is why our perspective on measuring chirality with advanced techniques is that we can adjust the sensitivity limits and measure the enantiomeric imbalance in nanoliter volumes.

In this thesis, we developed analytical tools to model the propagation of light at the subwavelength scale. To that end, we focus on two advanced techniques for measuring chirality: first, NL optics with pump-probe spectroscopy, and second, a nanophotonic environment with a chiral cavity. To apply the NL optical phenomena, EIT and LWI in the chiral molecule fluorooxoirane, we investigated how the EIT and LWI enhance the DACS of molecules using optical pumping by

different CP excitations. In another work, we introduced a chiral cavity mirror as a nanophotonic environment and separately studied the modulation of the SE rates of LCP and RCP excitations.

The result obtained can be summed up as follows:

- We investigated EIT and LWI in a two-level approximation for the virtual chiral molecule fluoroxirane, which was excited by optical pumping. Thanks to the polarity and chirality of the fluoroxirane, we were able to observe this in a two-level system. For theoretical modeling, we use NL chiroptical interaction, introduce a perturbative approach to the density-matrix formalism, evaluate the electric and magnetic fields for optical excitation, and finally apply the chiral optical theorem to determine the ACS as a function of different optical parameters. We observe that the pump threshold intensity is highly dependent on the dephasing rate because these are coherent phenomena. For the decay rate ($\gamma \simeq 10^{13}$ s^{-1}) which is typical for the gas-phase molecular systems for a particular temperature and pressure, we find an unphysical minimum pump intensity $I_{\mathrm{P}}^{\mathrm{min}}$, but we manage to produce results with a decay rate ($\gamma_{\mathrm{rad}} \simeq 1.15 \times 10^{7}$ s^{-1}) for the radiative one through the laser cooling, for that minimum intensity $I_{\mathrm{P}}^{\mathrm{min}} \simeq 1$ kW/cm^2 is not unphysical for a particular molecular orientation. Thanks to CP-sensitive EIT and LWI, we achieve *diverging orientation-averaged CP dissymmetry factors* $\bar{\eta}_{\mathrm{dsf}} \to \infty$ with $I_{\mathrm{P}}^{\mathrm{min}} \simeq 1$ kW/cm^2. Thus, we systematically investigate the two NL optical phenomena and observe a strong dependence on the pump and signal polarizations and on molecular orientation.

- We investigate the polarization dependence SE in a chiral cavity composed of TAPCs for considering Rubidium-87 (^{87}Rb) as a quantum emitter. Thanks to the CP sensitivity of the chiral mirror, we are able to observe modulation in the SE rate rather than the free-space decay rate. For theoretical

modeling, we study the QED of the system using the TMA approach to evaluate the scattered field, which assesses TAPCs functionalities, and the DGF approach to determine the SE rate for different CP excitations. For a given vacuum wavelength, we engineered a mirror that reflects one CP and transmits the other at an incidence angle of 20°. The free space SE rate is calculated as $\gamma \simeq 1.5279 \times 10^8\,\mathrm{s}^{-1}$ without any imbalance between RCP and LCP excitations. But within the chiral cavity we obtain the SE rate for RCP as $\gamma_{\mathrm{R}}^{\mathrm{AV}} = 5.47 \times 10^7\,\mathrm{s}^{-1}$ and for LCP as $\gamma_{\mathrm{L}}^{\mathrm{AV}} = 5.63 \times 10^7\,\mathrm{s}^{-1}$, emitter at $\lambda_{\mathrm{VAC}} = 780$ nm placed at $z_{\mathrm{DIP}} = -0.3103w$ within a cavity of width $w = 0.5\lambda_{\mathrm{VAC}}$. These configurations produce a 3% CP-SE imbalance after averaging over random dipole orientations. Thus, we systematically investigate SE and observe polarization-dependent behavior for specific dipolar orientations/positions and cavity widths.

Our work on the EIT and LWI has great potential to develop a novel nonlinear spectroscopic technique. The technique can measure chirality at the single-molecule level with a commercial CW laser system. Also, our results related to the SE imbalance between two CPs suggest to us that designing proper microcavities with proper optical parameters can produce huge CP-induced SE rate, which is a promising area for the development of integrated circularly polarized single-photon sources and a CP lasing system. Therefore, this is another promising platform for studying chiral light-matter interaction.

5.2 Scope of future work

There are some interesting problems that can be pursued in the future, depending on the present results of my thesis. Some of the ideas are discussed below:

- **EIT and LWI for a particular time delay in chirality:**

Till now, we have not put any time delay between the pump and probe spectroscopy, so in the future, maybe we can add a time delay between the pump and signal and study nonlinear optical phenomena, such as EIT and LWI, as a function of time delay; maybe we'll observe some interesting results by investigating chiral light-matter interactions.

- **Transient grating in chiral medium:**

  If we consider the bi-anisotropic dispersion relation presented in this thesis, we may be able to explore Kerr nonlinear interaction in a chiral medium. When a chiral medium is used for incident TE and TM waves, cross-polarization occurs because the chiral medium can rotate the plane of polarization, though a standard transient grating is possible when the same polarization interferes in an achiral medium. Therefore, we can measure chirality by using a transient grating or self-diffraction.

5.3 List of Publications

- **Spontaneous emission of circularly polarized radiation in a chiral cavity**

  A. Alessandrini, **S. Pal**, L. di Mauro Villari, L. Assogna, M. Silvestri, M. Venturi, D. Tedeschi, C. Ferrante, and A. Marini,

  Photonics and Nanostructures - Fundamentals and Applications (submitted, 2026).

- **Electromagnetically induced transparency and lasing without inversion in chiral molecules**

  S. Pal, A. Sahoo, R. Adhikary, M. Venturi, A. Alessandrini, G. Salvitti, D. Tedeschi, C. Ferrante, M. Aschi, and A. Marini,

  Physics Letters A (submitted, 2026).

Bibliography

[1] Georges H. Wagnière. On the interaction of light with molecules: Pathways to the theoretical interpretation of chiroptical phenomena. In Nina Berova, Prasad L. Polavarapu, Koji Nakanishi, and Robert W. Woody, editors, *Comprehensive Chiroptical Spectroscopy, Volume 1: Instrumentation, Methodologies, and Theoretical Simulations*, pages 3–26. John Wiley & Sons, Hoboken, 2012. (cited on pages 1 and 26.)

[2] Eugene Hecht. *Optics*. Addison–Wesley, San Francisco, 4 edition, 2002. (cited on pages 1 and 2.)

[3] Augustin Jean Fresnel. Fresnel's prize memoir on the diffraction of light. In Henry Crew, editor, *The Wave Theory of Light: Memoirs of Huygens, Young and Fresnel*, pages 81–144. American Book Company, New York, 1900. English translation of "Mémoire sur la diffraction de la lumière" (1818). (cited on page 1.)

[4] Max Born and Emil Wolf. *Principles of Optics*. Cambridge University Press, Cambridge, 7 edition, 1999. (cited on pages 1 and 2.)

[5] H. D. Flack. Louis pasteur's discovery of molecular chirality and spontaneous resolution in 1848, together with a complete review of his crystallographic and chemical work. *Acta Crystallographica Section A*, 65(5):371–389, 2009. (cited on pages 1 and 2.)

[6] John David Jackson. *Classical Electrodynamics*. John Wiley & Sons, New York, 3 edition, 1998. (cited on pages 1, 12, 13, and 14.)

[7] Michael Faraday. Thoughts on ray vibrations. *Philosophical Magazine*, 28:345–350, 1846. (cited on page 1.)

[8] James Clerk Maxwell. *A Treatise on Electricity and Magnetism*. Clarendon Press, Oxford, 1873. (cited on page 1.)

[9] Max Planck. On the law of distribution of energy in the normal spectrum. *Annalen der Physik*, 4:553–563, 1901. (cited on page 2.)

[10] Albert Einstein. On a heuristic point of view concerning the production and transformation of light. *Annalen der Physik*, 17:132–148, 1905. (cited on page 2.)

[11] R. A. Beth. Mechanical detection and measurement of the angular momentum of light. *Physical Review*, 50(2):115–125, 1936. (cited on page 2.)

[12] L. Allen, M. W. Beijersbergen, R. J. C. Spreeuw, and J. P. Woerdman. Orbital angular momentum of light and the transformation of Laguerre–Gaussian laser modes. *Physical Review A*, 45(11):8185–8189, 1992. (cited on page 2.)

[13] Konstantin Y. Bliokh, Francisco J. Rodríguez-Fortuño, Franco Nori, and Anatoly V. Zayats. Spin–orbit interactions of light. *Physics Reports*, 592:1–38, 2015. (cited on page 2.)

[14] David L. Andrews and Mohamed Babiker, editors. *The Angular Momentum of Light*. Cambridge University Press, Cambridge, 2013. (cited on page 2.)

[15] C. Genet. Chiral light–chiral matter interactions: An optical force perspective. *ACS Photonics*, 9(1):1–15, 2022. (cited on page 2.)

[16] Anthony E. Siegman. *Lasers*. University Science Books, Sausalito, 1986. (cited on page 2.)

[17] Peter W. Milonni and Joseph H. Eberly. *Laser Physics*. Wiley, Hoboken, 2010. (cited on page 2.)

[18] Robert W. Boyd. *Nonlinear Optics*. Academic Press, London, 4 edition, 2020. (cited on pages 2, 13, 14, 15, 30, 33, 49, and 52.)

[19] Prasad L. Polavarapu. *Chiroptical Spectroscopy: Fundamentals and Applications*. CRC Press, Boca Raton, 1 edition, 2016. (cited on page 2.)

[20] Mengxin Ren, Eric Plum, Jingjun Xu, and Nikolay I. Zheludev. Giant nonlinear optical activity in a plasmonic metamaterial. *Nature Communications*, 3:833, 2012. (cited on page 2.)

[21] Laurence D. Barron. *Molecular Light Scattering and Optical Activity*. Cambridge University Press, Cambridge, 2 edition, 2004. (cited on pages 2, 8, 9, 10, and 20.)

[22] Edward U. Condon. Theories of optical rotatory power. *Reviews of Modern Physics*, 9(4):432–457, 1937. (cited on page 2.)

[23] William Thomson Kelvin. *The Molecular Tactics of a Crystal*. Clarendon Press, Oxford, 1894. (cited on page 2.)

[24] Georges H. Wagnière. *On Chirality and the Universal Asymmetry: Reflections on Image and Mirror Image*. Wiley-VCH, Weinheim, 2007. (cited on pages 3 and 9.)

[25] Ismo V. Lindell, Ari H. Sihvola, Sergei A. Tretyakov, and Ari J. Viitanen. *Electromagnetic Waves in Chiral and Bi-Isotropic Media*. Artech House, Boston, 1994. (cited on page 3.)

[26] David L. Andrews and Michael W. Tretton. Physical principles of circular dichroism. *Journal of Chemical Education*, 97(12):4487–4498, 2020. (cited on page 3.)

[27] Rebecca U. McVicker and Niamh M. O'Boyle. Chirality of new drug approvals (2013–2022): Trends and perspectives. *Journal of Medicinal Chemistry*, 67(4):2305–2320, 2024. Perspective. (cited on pages 3 and 11.)

[28] Koji Nakanishi, Nina Berova, and Robert W. Woody, editors. *Circular Dichroism and the Conformational Analysis of Biomolecules*. University Science Books, Mill Valley, 1994. (cited on page 3.)

[29] Olga Smirnova. A new age of molecular chirality. *Nature Physics*, 19(10):1379–1381, 2023. (cited on page 3.)

[30] Olga Smirnova, Yann Mairesse, and Serguei Patchkovskii. Opportunities for chiral discrimination using high harmonic generation in tailored laser fields. *Journal of Physics B: Atomic, Molecular and Optical Physics*, 48(23):234005, 2015. (cited on page 3.)

[31] R. Cireasa, A. E. Boguslavskiy, B. Pons, M. C. H. Wong, D. Descamps, S. Petit, H. Ruf, N. Thiré, A. Ferre, J. Suarez, et al. Probing molecular chirality on a sub-femtosecond timescale. *Nature Physics*, 11(8):654–658, 2015. (cited on page 3.)

[32] Yiqiu Tang and Adam E. Cohen. Optical chirality and its interaction with matter. *Physical Review Letters*, 104(16):163901, 2010. (cited on page 3.)

[33] Makoto Kuwata-Gonokami, Naoya Saito, Yasunori Ino, Martti Kauranen, Konstantins Jefimovs, Tero Vallius, Jari Turunen, and Yuri Svirko. Giant optical activity in quasi-two-dimensional planar nanostructures. *Physical Review Letters*, 95(22):227401, 2005. (cited on page 3.)

[34] Alexander O. Govorov, Zonghui Fan, Francisco J. Hernandez, Joseph M. Slocik, and Rajesh R. Naik. Theory of circular dichroism of nanomaterials comprising chiral molecules and nanocrystals: plasmon enhancement, dipole interactions, and dielectric effects. *Nano Letters*, 10(4):1374–1382, 2010. (cited on page 3.)

[35] Antoine Canaguier-Durand, James A. Hutchison, Cyriaque Genet, and Thomas W. Ebbesen. Mechanical separation of chiral dipoles by chiral light. *Angewandte Chemie International Edition*, 52(40):10533–10536, 2013. (cited on page 3.)

[36] Carlos Rodríguez, Álvaro Peña-Gallego, and J. Luis Alonso-Gómez. Chiroptical sensing: A conceptual introduction. *ChemPhotoChem*, 4(8):514–528, 2020. (cited on page 8.)

[37] David L. Nelson and Michael M. Cox. *Lehninger Principles of Biochemistry*. W. H. Freeman and Company, New York, 7 edition, 2017. (cited on pages 8, 9, and 10.)

[38] Giuliano Zanchetta, Makoto Nakata, Marco Buscaglia, Tommaso Bellini, and Noel A. Clark. Right-handed double-helix ultrashort dna yields chiral nematic phases with both right- and left-handed director twist. *Proceedings of the National Academy of Sciences*, 107(40):17497–17502, 2010. (cited on page 9.)

[39] William A. Bonner. The origin and amplification of biomolecular chirality. *Origins of Life and Evolution of the Biosphere*, 21(2):59–111, 1991. (cited on page 9.)

[40] Koji Tamura. Origin of amino acid homochirality: Relationship with the rna world and tRNA aminoacylation. *Journal of Bioscience and Bioengineering*, 106(6):516–523, 2008. (cited on page 9.)

[41] Lien Ai Nguyen, Hua He, and Chuong Pham-Huy. Chiral drugs: An overview. *International Journal of Biomedical Science*, 2(2):85–100, 2006. (cited on pages 9, 10, 11, and 75.)

[42] Sara R. Domingos, Carlos Pérez, and Melanie Schnell. Sensing chirality with rotational spectroscopy. *Annual Review of Physical Chemistry*, 73:231–252, 2022. (cited on page 9.)

[43] Guo-Qiang Lin, Qi-Dong You, and Jie-Fei Cheng. *Chirality in Drug Design and Development*. Marcel Dekker, New York, 2004. (cited on page 9.)

[44] Joseph Gal and Pedro Cintas. Early history of the recognition of molecular biochirality. In Pedro Cintas, editor, *Biochirality: Origins, Evolution and Molecular Recognition*, volume 333 of *Topics in Current Chemistry*, pages 1–40. Springer, Berlin, Heidelberg, 2013. (cited on page 9.)

[45] Francesco Perri, Christof Nilewski, and Patrick Kirsch. Enantiomeric natural products: Occurrence and biogenesis. *Journal of Natural Products*, 75(4):589–602, 2012. (cited on page 9.)

[46] Alan D. McNaught and Andrew Wilkinson. The r/s convention. In *IUPAC Compendium of Chemical Terminology (the "Gold Book")*. Blackwell Science, Oxford, 2 edition, 1997. (cited on page 10.)

[47] Donna G. Blackmond. The origin of the homochirality of biomolecules. *Cold Spring Harbor Perspectives in Biology*, 2(5):a002147, 2010. (cited on page 10.)

[48] Vladimir Avetisov and Vitalii Goldanskii. Mirror symmetry breaking at the molecular level. *Proceedings of the National Academy of Sciences*, 93(20):11435–11442, 1996. (cited on page 11.)

[49] Eiji Tokunaga, Toshiyuki Yamamoto, Etsushi Ito, and Norio Shibata. Understanding the thalidomide chirality in biological processes by the self-disproportionation of enantiomers. *Scientific Reports*, 8:1–10, 2018. (cited on page 11.)

[50] Taeko Asatsuma-Okumura, Tatsuya Ito, and Hiroshi Handa. Molecular mechanisms of the teratogenic effects of thalidomide. *Molecules*, 25(5):1–17, 2020. (cited on page 11.)

[51] John E. Mendelson, Dana McGlothlin, Debra S. Harris, Elyse Foster, Tom Everhart, Peyton Jacob, and Reese T. Jones. The clinical pharmacology of intranasal l-methamphetamine. *BMC Clinical Pharmacology*, 8:1–9, 2008. (cited on page 11.)

[52] Tetsuya Nishimura, Kazue Takahata, Yuri Kosugi, Takaaki Tanabe, and Shizuko Muraoka. Psychomotor effect differences between l-methamphetamine and d-methamphetamine are independent of murine plasma and brain pharmacokinetics profiles. *Journal of Neural Transmission*, 124:519–523, 2017. (cited on page 11.)

[53] Yan Wei, Lin Chang, and Kenji Hashimoto. Molecular mechanisms underlying the antidepressant actions of ketamine and its enantiomers. *Molecular Psychiatry*, 27:190–204, 2022. (cited on page 11.)

[54] R. Craven. Ketamine. *Anaesthesia*, 62(Suppl. 1):48–53, 2007. (cited on page 11.)

[55] Maria A. Gonzalez and coauthors. Chiral drugs: The fda perspective on manufacturing and control. *Journal of Pharmaceutical and Biomedical Analysis*, 11(8):583–592, 1993. (cited on page 11.)

[56] Mike Auerbach. Chiral separation and enantiomeric analysis: Critical importance in pharmaceutical development. *American Pharmaceutical Review*, 28, 2025. (cited on page 11.)

[57] Julius Adams Stratton. *Electromagnetic Theory*. McGraw-Hill, New York, 1941. (cited on page 13.)

[58] Gerald B Folland. *Fourier analysis and its applications*, volume **4**. American Mathematical Soc., 2009. (cited on page 13.)

[59] Andrew Lininger, Giovanna Palermo, Alexa Guglielmelli, Giuseppe Nicoletta, Madhav Goel, Michael Hinczewski, and Giuseppe Strangi. Chirality in light–matter interaction. *Advanced Materials*, 35(34):2107325, 2023. (cited on pages 18, 20, and 25.)

[60] Lauren A. Warning, Ali Rafiei Miandashti, Lauren A. McCarthy, Qingfeng Zhang, Christy F. Landes, and Stephan Link. Nanophotonic approaches for chirality sensing. *ACS Nano*, 15(10):15539–15566, 2021. (cited on pages 18, 20, 23, 24, and 25.)

[61] Kan Yao and Yongmin Liu. Enhancing circular dichroism by chiral hotspots in silicon nanocube dimers. *Nanoscale*, **10**(18):8779–8786, 2018. (cited on page 24.)

[62] Abdu Hussen Ali. High-performance liquid chromatography (hplc): A review. *Annals of Advances in Chemistry*, 6:010–020, 2022. (cited on page 25.)

[63] Christie Aroulanda and Philippe Lesot. Molecular enantiodiscrimination by nmr spectroscopy in chiral oriented systems: Concept, tools and applications. *Chirality*, 34:182–244, 2022. (cited on page 25.)

[64] M. A. Belkin, S. H. Han, X. Wei, and Y. R. Shen. Sum-frequency gener-

ation in chiral liquids near electronic resonance. *Physical Review Letters*, 87:113001, 2001. (cited on page 28.)

[65] Joshua Vogwell, Laura Rego, Olga Smirnova, and David Ayuso. Ultrafast control over chiral sum-frequency generation. *Science Advances*, 9:eadj1429, 2023. (cited on page 29.)

[66] J. D. Byers, H. I. Yee, T. Petralli-Mallow, and J. M. Hicks. Second-harmonic generation circular-dichroism spectroscopy from chiral monolayers. *Physical Review B*, 49(20):14643–14647, 1994. (cited on page 30.)

[67] T. Petralli-Mallow, T. M. Wong, J. D. Byers, H. I. Yee, and J. M. Hicks. Circular dichroism spectroscopy at interfaces: A surface second harmonic generation study. *The Journal of Physical Chemistry*, 97:1383–1388, 1993. (cited on page 31.)

[68] Qingkai Qian, Rui Zu, Qingqing Ji, Gang Seob Jung, Kunyan Zhang, Ye Zhang, Markus J. Buehler, Jing Kong, Venkatraman Gopalan, and Shengxi Huang. Chirality-dependent second harmonic generation of mos_2 nanoscroll with enhanced efficiency. *ACS Nano*, 14(10):13333–13342, 2020. (cited on page 31.)

[69] G. P. Agrawal. *Nonlinear Fiber Optics*. Academic Press, Amsterdam, 5 edition, 2012. (cited on page 31.)

[70] Lei Kang, Yuhao Wu, and Douglas H. Werner. Nonlinear chiral metasurfaces based on the optical kerr effect. *Advanced Optical Materials*, 11:2202658, 2023. (cited on page 31.)

[71] Peer Fischer and François Hache. Nonlinear optical spectroscopy of chiral molecules. *Chirality*, 17:421–437, 2005. (cited on page 33.)

[72] Vincenzo Amendola, Rémy Pilot, Marco Frasconi, Oronzio M. Maragò, and Maria Antonietta Iatì. Surface plasmon resonance in gold nanoparticles: A review. *Journal of Physics: Condensed Matter*, 29:203002, 2017. (cited on page 37.)

[73] Michael Schäferling, Daniel Dregely, Mario Hentschel, and Harald Giessen. Tailoring enhanced optical chirality: Design principles for chiral plasmonic nanostructures. *Physical Review X*, 2:031010, 2012. (cited on page 37.)

[74] Michael Schäferling, Xiaoyang Yin, Nader Engheta, and Harald Giessen. Helical plasmonic nanostructures as prototypical chiral near-field sources. *ACS Photonics*, 1:530–537, 2014. (cited on page 37.)

[75] Meng Cen, Jun Wang, Jian Liu, Hao He, Kai Li, Wenjun Cai, Ting Cao, and Yu-Jia Liu. Ultrathin suspended chiral metasurfaces for enantiodiscrimination. *Advanced Materials*, 34:2203956, 2022. (cited on page 37.)

[76] E. S. A. Goerlitzer, A. S. Puri, J. J. Moses, L. V. Poulikakos, and Nicolas Vogel. The beginner's guide to chiral plasmonics: Mostly harmless theory and the design of large-area substrates. *Advanced Optical Materials*, 9:2100378, 2021. (cited on page 38.)

[77] Aitzol Garcia-Etxarri and Jennifer A. Dionne. Surface-enhanced circular dichroism spectroscopy mediated by nonchiral nanoantennas. *Physical Review B*, 87:235409, 2013. (cited on page 38.)

[78] Mohammad H. Alizadeh and Björn M. Reinhard. Plasmonically enhanced chiral optical fields and forces in achiral split ring resonators. *ACS Photonics*, 2:361–368, 2015. (cited on page 38.)

[79] Shoukuan Zu, Qi Sun, Enjie Cao, Tomoya Oshikiri, and Hiroaki Mis-

awa. Revealing the chiroptical response of plasmonic nanostructures at the nanofemto scale. *Nano Letters*, 21:4780–4786, 2021. (cited on page 38.)

[80] Andreas Horrer, Yifei Zhang, Damien Gérard, Julien Béal, Mathieu Kociak, Julien Plain, and Rémi Bachelot. Local optical chirality induced by near-field mode interference in achiral plasmonic metamolecules. *Nano Letters*, 20:509–516, 2020. (cited on page 38.)

[81] Mitsuhiro Terakawa, Shinya Takeda, Yuji Tanaka, Go Obara, Takashi Miyanishi, Takashi Sakai, Takeshi Sumiyoshi, Hiroshi Sekita, Masashi Hasegawa, Pierre Viktorovitch, and Minoru Obara. Enhanced localized near field and scattered far field for surface nanophotonics applications. *Progress in Quantum Electronics*, 36:194–271, 2012. (cited on page 38.)

[82] Milton Kerker, David S. Wang, and Charles L. Giles. Electromagnetic scattering by magnetic spheres. *Journal of the Optical Society of America*, 73:765–767, 1983. (cited on page 38.)

[83] Guoxin Rui, Sisi Zou, Bin Gu, and Yi Cui. Surface-enhanced circular dichroism by localized superchiral hotspots in a dielectric dimer array metasurface. *Journal of Physical Chemistry C*, 126:2199–2206, 2022. (cited on page 39.)

[84] Lingling Ye, Jian Li, F. U. Richter, Yashar Jahani, Rui Lu, Byoungho R. Lee, Ming-Lun Tseng, and Hatice Altug. Dielectric tetramer nanoresonators supporting strong superchiral fields for vibrational circular dichroism spectroscopy. *ACS Photonics*, 10:4377–4384, 2023. (cited on page 39.)

[85] Federico R. Gomez, Jorge R. Mejia-Salazar, and Pablo Albella. All-dielectric chiral metasurfaces based on crossed-bowtie nanoantennas. *ACS Omega*, 4:21041–21047, 2019. (cited on page 39.)

[86] Ershad Mohammadi, Andreas Tittl, Kosmas L. Tsakmakidis, T. V. Raziman, and Alberto G. Curto. Dual nanoresonators for ultrasensitive chiral detection. *ACS Photonics*, 8(6):1754–1762, 2021. (cited on page 39.)

[87] E. Petronijevic, M. Centini, A. Belardini, G. Leahu, T. Hakkarainen, and C. Sibilia. Chiral near-field manipulation in au-gaas hybrid hexagonal nanowires. *Optics Express*, 25:14148–14157, 2017. (cited on page 39.)

[88] Y. Wang, Q. Wang, Q. Wang, Y. Wang, Z. Li, X. Lan, J. Dong, W. Gao, Q. Han, and Z. Zhang. Dynamically adjustable-induced thz circular dichroism and biosensing application of symmetric silicon-graphene-metal composite nanostructures. *Optics Express*, 29:8087–8097, 2021. (cited on page 40.)

[89] I. Zubritskaya, N. Maccaferri, X. Inchausti Ezeiza, P. Vavassori, and A. Dmitriev. Magnetic control of the chiroptical plasmonic surfaces. *Nano Letters*, 18(1):302–307, 2018. (cited on page 40.)

[90] G. Armelles, A. Cebollada, H. Y. Feng, A. Garcia-Martin, D. Meneses-Rodriguez, J. Zhao, and H. Giessen. Interaction effects between magnetic and chiral building blocks: A new route for tunable magneto-chiral plasmonic structures. *ACS Photonics*, 2(9):1272–1277, 2015. (cited on page 40.)

[91] H. Y. Feng, C. de Dios, F. Garcia, A. Cebollada, and G. Armelles. Analysis and magnetic modulation of chiro-optical properties in anisotropic chiral and magneto-chiral plasmonic systems. *Optics Express*, 25(25):31045–31055, 2017. (cited on page 40.)

[92] Abraham Vázquez-Guardado and Debashis Chanda. Superchiral light generation on degenerate achiral surfaces. *Physical Review Letters*, 120(13):137601, 2018. (cited on page 40.)

[93] Alexander O. Govorov, Zhiyuan Fan, Pedro Hernandez, Joseph M. Slocik,

and Rajesh R. Naik. Theory of circular dichroism of nanomaterials comprising chiral molecules and nanocrystals: Plasmon enhancement, dipole interactions, and dielectric effects. *Nano Letters*, 10(4):1374–1382, 2010. (cited on page 40.)

[94] Tatyana Levi-Belenkova, Alexander O. Govorov, and Gil Markovich. Orientation-sensitive peptide-induced plasmonic circular dichroism in silver nanocubes. *The Journal of Physical Chemistry C*, 120(22):12751–12756, 2016. (cited on page 40.)

[95] Fang Lu, Ye Tian, Mingzhao Liu, Dong Su, Hui Zhang, Alexander O. Govorov, and Oleg Gang. Discrete nanocubes as plasmonic reporters of molecular chirality. *Nano Letters*, 13(7):3145–3151, 2013. (cited on page 40.)

[96] Joseph M. Slocik, Alexander O. Govorov, and Rajesh R. Naik. Plasmonic circular dichroism of peptide-functionalized gold nanoparticles. *Nano Letters*, 11(2):701–705, 2011. (cited on page 40.)

[97] Hui Zhang and Alexander O. Govorov. Giant circular dichroism of a molecule in a region of strong plasmon resonances between two neighboring gold nanocrystals. *Physical Review B*, 87:075410, 2013. (cited on page 40.)

[98] Nadia A. Abdulrahman, Z. Fan, Taishi Tonooka, Sharon M. Kelly, Nikolaj Gadegaard, Euan Hendry, Alexander O. Govorov, and Malcolm Kadodwala. Induced chirality through electromagnetic coupling between chiral molecular layers and plasmonic nanostructures. *Nano Letters*, 12(2):977–983, 2012. (cited on page 40.)

[99] Hideyuki Shinmori and Chihiro Mochizuki. Strong chiroptical activity from achiral gold nanorods assembled with proteins. *Chemical Communications*, 53(49):6569–6572, 2017. (cited on page 41.)

[100] Sergio Dominguez-Medina, Lydia Kisley, Lawrence J. Tauzin, Anneli Hoggard, Bo Shuang, A. Swarnapali D. S. Indrasekara, Sishan Chen, Lin-Yung Wang, Paul J. Derry, Anton Liopo, Eugene R. Zubarev, Christy F. Landes, and Stephan Link. Adsorption and unfolding of a single protein triggers nanoparticle aggregation. *ACS Nano*, 10(2):2103–2112, 2016. (cited on page 41.)

[101] Qingfeng Zhang, Taylor Hernandez, Kyle W. Smith, Seyyed Ali Hosseini Jebeli, Alan X. Dai, Lauren Warning, Rashad Baiyasi, Lauren A. McCarthy, Hua Guo, Dong-Hua Chen, Jennifer A. Dionne, Christy F. Landes, and Stephan Link. Unraveling the origin of chirality from plasmonic nanoparticle–protein complexes. *Science*, 365(6458):1475–1478, 2019. (cited on page 41.)

[102] X. B. Shen, P. F. Zhan, A. Kuzyk, Q. Liu, A. Asenjo-Garcia, H. Zhang, F. J. Garcia de Abajo, A. Govorov, B. Q. Ding, and N. Liu. 3d plasmonic chiral colloids. *Nanoscale*, 6:2077–2081, 2014. (cited on page 41.)

[103] F. Lu, Y. Tian, M. Liu, D. Su, H. Zhang, A. O. Govorov, and O. Gang. Discrete nanocubes as plasmonic reporters of molecular chirality. *Nano Letters*, 13(7):3145–3151, 2013. (cited on page 41.)

[104] V. A. Gerard, Y. K. Gun'ko, E. Defrancq, and A. O. Govorov. Plasmon-induced cd response of oligonucleotide-conjugated metal nanoparticles. *Chemical Communications*, 47(26):7383–7385, 2011. (cited on page 41.)

[105] T. Levi-Belenkova, A. O. Govorov, and G. Markovich. Orientation-sensitive peptide-induced plasmonic circular dichroism in silver nanocubes. *The Journal of Physical Chemistry C*, 120(22):12751–12756, 2016. (cited on page 41.)

[106] V. M. Agranovich and D. L. Mills. *Surface Polaritons*. North-Holland, Amsterdam, 1982. (cited on page 41.)

[107] A. Boardman. *Electromagnetic Surface Modes*. John Wiley & Sons, New York, 1982. (cited on page 41.)

[108] H. Raether. *Surface Plasmons*. Springer-Verlag, Berlin, 1988. (cited on page 41.)

[109] J. N. Anker, W. P. Hall, O. Lyandres, N. C. Shah, J. Zhao, and R. P. Van Duyne. Biosensing with plasmonic nanosensors. *Nature Materials*, 7(6):442–453, 2008. (cited on page 41.)

[110] J. Homola. *Surface Plasmon Resonance Based Sensors*. Springer, Berlin, 2006. (cited on page 41.)

[111] G. Raschke, S. Kowarik, T. Franzl, C. Sonnichsen, T. A. Klar, J. Feldmann, A. Nichtl, and K. Kurzinger. Biomolecular recognition based on single gold nanoparticle light scattering. *Nano Letters*, 3:935–938, 2003. (cited on page 41.)

[112] Stefan A. Maier. *Plasmonics: Fundamentals and Applications*. Springer, New York, 2007. (cited on page 42.)

[113] Stefan A. Maier and Harry A. Atwater. Plasmonics: Localization and guiding of electromagnetic energy in metal/dielectric structures. *Journal of Applied Physics*, 98(1):011101, 2005. (cited on page 42.)

[114] W. Andrew Murray and William L. Barnes. Plasmonic materials. *Advanced Materials*, 19(22):3771–3782, 2007. (cited on page 42.)

[115] Yoon Young Lee, Ryeong Myeong Kim, Sang Won Im, Mani Balamurugan, and Ki Tae Nam. Plasmonic metamaterials for chiral sensing applications. *Nanoscale*, 12(1):58–66, 2020. (cited on page 42.)

[116] Jerome V. Moloney and Alan C. Newell. Nonlinear optics. *Physica D: Nonlinear Phenomena*, 44(1–2):1–37, 1990. (cited on page 45.)

[117] Claude Cohen-Tannoudji, Jacques Dupont-Roc, and Gilbert Grynberg. *Atom-Photon Interactions: Basic Processes and Applications*. John Wiley & Sons, New York, 1998. (cited on page 49.)

[118] Daniel Manzano. A short introduction to the lindblad master equation. *AIP Advances*, 10:025106, 2020. (cited on page 50.)

[119] Heinz-Peter Breuer and Francesco Petruccione. *The Theory of Open Quantum Systems*. Oxford University Press, Oxford, 2002. (cited on page 50.)

[120] Steven S. Andrews. Using rotational averaging to calculate the bulk response of isotropic and anisotropic samples from molecular parameters. *Journal of Chemical Education*, 81(6):877–886, June 2004. (cited on page 54.)

[121] Lukas Ohnoutek, Ji-Young Kim, Jun Lu, Ben J. Olohan, Dora M. Răşădean, G. Dan Pantos, Nicholas A. Kotov, and Ventsislav K. Valev. Third-harmonic mie scattering from semiconductor nanohelices. *Nature Photonics*, 16(2):126–133, 2022. (cited on page 55.)

[122] Lars Jensen, Marcel Swart, and Piet Th. van Duijnen. Microscopic and macroscopic polarization within a combined quantum mechanics and molecular mechanics model. *The Journal of Chemical Physics*, 122:034103, 2005. (cited on page 57.)

[123] Matteo Venturi, Raju Adhikary, Ambaresh Sahoo, Carino Ferrante, Isabella Daidone, Francesco Di Stasio, Andrea Toma, Francesco Tani, Hatice Altug, Antonio Mecozzi, Massimiliano Aschi, and Andrea Marini. Plasmon-enhanced circular dichroism spectroscopy of chiral drug solutions. *The Journal of Chemical Physics*, 159(15):154703, 2023. (cited on pages 63 and 75.)

[124] R. Adhikary, M. Venturi, G. Salvitti, A. Sahoo, C. Ferrante, P. Benassi, F. Di Stasio, A. Toma, H. Altug, M. Aschi, and A. Marini. Vibrational

circular dichroism of plasmonic nanostructures embedding chiral drugs. *Scientific Reports*, 15:13116, 2025. (cited on page 66.)

[125] K.-J. Boller, A. Imamoğlu, and S. E. Harris. Observation of electromagnetically induced transparency. *Physical Review Letters*, 66:2593–2596, 1991. (cited on pages 74 and 78.)

[126] S. E. Harris. Electromagnetically induced transparency. *Physics Today*, 50(7):36–42, 1997. (cited on page 74.)

[127] M. Fleischhauer, A. Imamoğlu, and J. P. Marangos. Electromagnetically induced transparency: Optics in coherent media. *Reviews of Modern Physics*, 77:633–673, 2005. (cited on pages 74 and 78.)

[128] L. V. Hau, S. E. Harris, Z. Dutton, and C. H. Behroozi. Light speed reduction to 17 metres per second in an ultracold atomic gas. *Nature*, 397:594–598, 1999. (cited on page 74.)

[129] C. Liu, Z. Dutton, C. H. Behroozi, and L. V. Hau. Observation of coherent optical information storage in an atomic medium using halted light pulses. *Nature*, 409:490–493, 2001. (cited on page 74.)

[130] M. D. Lukin and A. Imamoğlu. Controlling photons using electromagnetically induced transparency. *Nature*, 413:273–276, 2001. (cited on page 74.)

[131] J. Mompart and R. Corbalán. Lasing without inversion. *Journal of Optics B: Quantum and Semiclassical Optics*, 2:R7–R24, 2000. (cited on page 74.)

[132] A. M. Akulshin, S. Barreiro, and A. Lezama. Electromagnetically induced absorption and transparency due to resonant two-field excitation of quasidegenerate levels in Rb vapor. *Physical Review A*, 57:2996–3002, 1998. (cited on page 74.)

[133] M. D. Eisaman, A. André, F. Massou, M. Fleischhauer, A. S. Zibrov, and M. D. Lukin. Electromagnetically induced transparency with tunable single-photon pulses. *Nature*, 438:837–841, 2005. (cited on page 74.)

[134] M. Mücke, E. Figueroa, J. Bochmann, C. Hahn, K. Murr, S. Ritter, C. J. Villas-Boas, and G. Rempe. Electromagnetically induced transparency with single atoms in a cavity. *Nature*, 465:755–758, 2010. (cited on page 74.)

[135] M. F. Yanik, W. Suh, Z. Wang, and S. Fan. Stopping light in a waveguide with an all-optical analog of electromagnetically induced transparency. *Physical Review Letters*, 93:233903, 2004. (cited on page 74.)

[136] Q. Xu, S. Sandhu, M. L. Povinelli, J. Shakya, S. Fan, and M. Lipson. Experimental realization of an on-chip all-optical analogue to electromagnetically induced transparency. *Physical Review Letters*, 96:123901, 2006. (cited on page 74.)

[137] E. Waks and J. Vuckovic. Dipole induced transparency in drop-filter cavity-waveguide systems. *Physical Review Letters*, 96:153601, 2006. (cited on page 74.)

[138] N. Papasimakis, V. A. Fedotov, N. I. Zheludev, and S. L. Prosvirnin. Metamaterial analog of electromagnetically induced transparency. *Physical Review Letters*, 101:253903, 2008. (cited on page 74.)

[139] S. Zhang, D. A. Genov, Y. Wang, M. Liu, and X. Zhang. Plasmon-induced transparency in metamaterials. *Physical Review Letters*, 101:047401, 2008. (cited on page 74.)

[140] N. Liu, L. Langguth, T. Weiss, J. Kästel, M. Fleischhauer, T. Pfau, and H. Giessen. Plasmonic analogue of electromagnetically induced transparency

at the drude damping limit. *Nature Materials*, 8:758–762, 2009. (cited on page 74.)

[141] C. Kurter, P. Tassin, L. Zhang, T. Koschny, A. P. Zhuravel, A. V. Ustinov, S. M. Anlage, and C. M. Soukoulis. Classical analogue of electromagnetically induced transparency with a metal-superconductor hybrid metamaterial. *Physical Review Letters*, 107:043901, 2011. (cited on page 74.)

[142] A. H. Safavi-Naeini, T. P. Mayer Alegre, J. Chan, M. Eichenfield, M. Winger, Q. Lin, J. T. Hill, D. E. Chang, and O. Painter. Electromagnetically induced transparency and slow light with optomechanics. *Nature*, 472:69–73, 2011. (cited on page 74.)

[143] C. Wang, X. Jiang, G. Zhao, M. Zhang, C. W. Hsu, B. Peng, A. D. Stone, L. Jiang, and L. Yang. Electromagnetically induced transparency at a chiral exceptional point. *Nature Physics*, 16:334–340, 2020. (cited on page 75.)

[144] T. Müller, K. B. Wiberg, and P. H. Vaccaro. Cavity ring-down polarimetry (CRDP): A new scheme for probing circular birefringence and circular dichroism in the gas phase. *Journal of Physical Chemistry A*, 104:5959–5968, 2000. (cited on page 75.)

[145] S. S. Wesolowski and D. E. Pivonka. A rapid alternative to x-ray crystallography for chiral determination: Case studies of vibrational circular dichroism (VCD) to advance drug discovery projects. *Bioorganic & Medicinal Chemistry Letters*, 23:4019–4025, 2013. (cited on page 75.)

[146] J. K. Gansel, M. Thiel, M. S. Rill, M. Decker, K. Bade, V. Saile, G. von Freymann, S. Linden, and M. Wegener. Gold helix photonic metamaterial as broadband circular polarizer. *Science*, 325:1513–1515, 2009. (cited on page 75.)

[147] E. Plum, J. Zhou, J. Dong, V. A. Fedotov, T. Koschny, C. M. Soukoulis, and N. I. Zheludev. Metamaterial with negative index due to chirality. *Physical Review B*, 79:035407, 2009. (cited on page 75.)

[148] Y. Zhao, M. A. Belkin, and H. Altug. Twisted optical metamaterials for planarized ultrathin broadband circular polarizers. *Nature Communications*, 3:870, 2012. (cited on page 75.)

[149] E. Mohammadi, K. L. Tsakmakidis, A. N. Askarpour, P. Dehkhoda, A. Tavakoli, and H. Altug. Nanophotonic platforms for enhanced chiral sensing. *ACS Photonics*, 5:2669–2675, 2018. (cited on page 75.)

[150] G. Pellegrini, M. Finazzi, M. Celebrano, L. Duò, and P. Biagioni. Surface-enhanced chiroptical spectroscopy with superchiral surface waves. *Chirality*, 30:993–999, 2018. (cited on page 75.)

[151] C. Gilroy, S. Hashiyada, K. Endo, A. S. Karimullah, L. D. Barron, H. Okamoto, Y. Togawa, and M. Kadodwala. Roles of superchirality and interference in chiral plasmonic biodetection. *Journal of Physical Chemistry C*, 123:15195–15203, 2019. (cited on page 75.)

[152] A. O. Govorov. Plasmon-induced circular dichroism of a chiral molecule in the vicinity of metal nanocrystals: Application to various geometries. *Journal of Physical Chemistry C*, 115:7914–7923, 2011. (cited on page 75.)

[153] M. L. Nesterov, X. Yin, M. Schäferling, H. Giessen, and T. Weiss. The role of plasmon-generated near fields for enhanced circular dichroism spectroscopy. *ACS Photonics*, 3:578–583, 2016. (cited on page 75.)

[154] R. Adhikary, M. Venturi, G. Salvitti, A. Sahoo, C. Ferrante, P. Benassi, F. Di Stasio, A. Toma, H. Altug, M. Aschi, and A. Marini. Vibrational

circular dichroism of plasmonic nanostructures embedding chiral drugs. *Scientific Reports*, 15:13116, 2025. (cited on page 75.)

[155] P. Fischer and F. Hache. Nonlinear optical spectroscopy of chiral molecules. *Chirality*, 17:421–437, 2005. (cited on page 75.)

[156] D. Ayuso, A. F. Ordoñez, and O. Smirnova. Ultrafast chirality: the road to efficient chiral measurements. *Physical Chemistry Chemical Physics*, 24:26962–26985, 2022. (cited on page 75.)

[157] Marlan O. Scully and M. Suhail Zubairy. *Quantum Optics*. Cambridge University Press, Cambridge, 1997. (cited on page 85.)

[158] M. Elshakre. The dissociative ionization of CO_2 in the 800 nm intense laser field using time-of-flight (TOF) mass spectrometry. *International Journal of Mass Spectrometry*, 336:37–42, 2013. (cited on page 106.)

[159] C. M. Holland, Y. Lu, and L. W. Cheuk. Bichromatic imaging of single molecules in an optical tweezer array. *Physical Review Letters*, 131:053202, 2023. (cited on page 110.)

[160] K. H. Drexhage. Iv interaction of light with monomolecular dye layers. In E. Wolf, editor, *Progress in Optics*, volume 12, pages 163–232. North-Holland, Amsterdam, 1974. (cited on page 116.)

[161] Lukas Novotny and Bert Hecht. *Principles of Nano-Optics*. Cambridge University Press, New York, 2006. (cited on pages 116, 119, 124, and 134.)

[162] H. Chew. Transition rates of atoms near spherical surfaces. *J. Chem. Phys.*, 87(3):1355–1360, 1987. (cited on page 116.)

[163] H. Chew. Radiation and lifetimes of atoms inside dielectric particles. *Phys. Rev. A*, 38(7):3410–3416, 1988. (cited on page 116.)

[164] V. V. Klimov and V. S. Letokhov. Resonance coupling of an excited atom with surface plasmons in a cluster of two metallic nanoparticles. *Laser Phys.*, 15:61–75, 2005. (cited on page 116.)

[165] L. A. Blanco and F. J. Garcia de Abajo. Spontaneous light emission in complex nanostructures. *Phys. Rev. B*, 69:205414, 2004. (cited on page 116.)

[166] V. V. Klimov and D. V. Guzatov. Strongly localized plasmon oscillations in a cluster of two metallic nanoparticles and spontaneous emission. *Phys. Rev. B*, 75:024303, 2007. (cited on page 116.)

[167] J.-W. Liaw, C.-S. Chen, and J.-H. Chen. Fluorescence emission and radiative properties of dye molecules near a nanostructure: numeric simulation. *J. Quant. Spectrosc. Radiat. Transfer*, 111:454–462, 2010. (cited on page 116.)

[168] Dmitry V. Guzatov and Vasily V. Klimov. Spontaneous emission of an optically active molecule near a chiral nanoellipsoid. *Physical Review A*, 98(1):013823, 2018. (cited on pages 116 and 124.)

[169] D. V. Guzatov and V. V. Klimov. Spontaneous emission of a chiral molecule near a cluster of two chiral spherical particles. *Quantum Electronics*, 45(3):250–257, 2015. (cited on pages 116 and 124.)

[170] E. M. Purcell. Spontaneous emission probabilities at radio frequencies. *Physical Review*, 69:681, 1946. (cited on page 116.)

[171] F. De Martini, G. Innocenti, G. R. Jacobovitz, and P. P. Mataloni. Anomalous spontaneous emission time in a microscopic optical cavity. *Physical Review Letters*, 59:2955, 1987. (cited on page 116.)

[172] T. Fujisawa, T. H. Oosterkamp, W. G. van der Wiel, B. W. Broer, R. Aguado, S. Tarucha, and L. P. Kouwenhoven. Spontaneous emission

spectrum in double quantum dot devices. *Science*, 282:932–935, 1998. (cited on page 116.)

[173] Susumu Noda, Masayuki Fujita, and Takashi Asano. Spontaneous-emission control by photonic crystals and nanocavities. *Nature Photonics*, 1:449–458, 2007. (cited on page 116.)

[174] S. Takahashi, Y. Kinuta, S. Ito, H. Onishi, K. Yamashita, J. Tatebayashi, S. Iwamoto, and Y. Arakawa. Circularly polarized cavity mode emission from quantum dots in a semiconductor three-dimensional chiral photonic crystal. *Applied Physics Letters*, 126:081108, 2025. (cited on page 116.)

[175] Y. Yamamoto, S. Machida, and G. Björk. Microcavity semiconductor laser with enhanced spontaneous emission. *Phys. Rev. A*, 44:657–668, 1991. (cited on page 116.)

[176] E. Yablonovitch, T. J. Gmitter, and R. Bhat. Inhibited and enhanced spontaneous emission from optically thin algaas/gaas double heterostructures. *Phys. Rev. Lett.*, 61:2546–2549, 1988. (cited on page 116.)

[177] R. J. Glauber and M. Lewenstein. Quantum optics of dielectric media. *Phys. Rev. A*, 43:467, 1991. (cited on page 116.)

[178] G. Gabrielse and H. Dehmelt. Observation of inhibited spontaneous emission. *Physical Review Letters*, 55:67–70, 1985. (cited on page 116.)

[179] H.-R. Xia, C.-Y. Ye, and S.-Y. Zhu. Experimental observation of spontaneous emission cancellation. *Physical Review Letters*, 77:1032–1035, 1996. (cited on page 116.)

[180] E. Yablonovitch. Inhibited spontaneous emission in solid-state physics and electronics. *Physical Review Letters*, 58:2059–2062, 1987. (cited on page 116.)

[181] R. G. Hulet, E. S. Hilfer, and D. Kleppner. Inhibited spontaneous emission by a rydberg atom. *Physical Review Letters*, 55:2137–2140, 1985. (cited on page 116.)

[182] W. Jhe, A. Anderson, E. A. Hinds, D. Meschede, L. Moi, and S. Haroche. Suppression of spontaneous decay at optical frequencies: Test of vacuum-field anisotropy in confined space. *Physical Review Letters*, 58:666–669, 1987. (cited on page 116.)

[183] F. De Martini, M. Marrocco, P. Mataloni, L. Crescentini, and R. Loudon. Spontaneous emission in the optical microscopic cavity. *Physical Review A*, 43:2480–2497, 1991. (cited on page 116.)

[184] Sajeev John and Tran Quang. Spontaneous emission near the edge of a photonic band gap. *Physical Review A*, 50:1764–1769, 1994. (cited on page 116.)

[185] Daniel Kleppner. Inhibited spontaneous emission. *Physical Review Letters*, 47:233–236, 1981. (cited on page 116.)

[186] Gunnar Björk, Susumu Machida, Yoshihisa Yamamoto, and Kazuhiro Igeta. Modification of spontaneous emission rate in planar dielectric microcavity structures. *Physical Review A*, 44:669–681, 1991. (cited on page 116.)

[187] D. G. Deppe, C. Lei, C. Lin, and D. L. Huffaker. Spontaneous emission from planar microstructures. *Journal of Modern Optics*, 41:325–344, 1994. (cited on page 116.)

[188] Pavel Ginzburg, David J. Roth, M. E. Nasir, P. Segovia, A. V. Krasavin, James M. Levitt, Liisa M. Hirvonen, N. Wells, J. Kuhling, Dominic Richards, et al. Spontaneous emission in non-local materials. *Light: Science & Applications*, 6:e16273, 2017. (cited on page 116.)

[189] P. Goy, J. M. Raimond, M. Gross, and S. Haroche. Observation of cavity-enhanced single-atom spontaneous emission. *Physical Review Letters*, 50:1903–1906, 1983. (cited on page 116.)

[190] Kasey J. Russell, Tsung-Li Liu, Shanying Cui, and Evelyn L. Hu. Large spontaneous emission enhancement in plasmonic nanocavities. *Nature Photonics*, 6:459–462, 2012. (cited on page 116.)

[191] S. Noda, M. Fujita, and T. Asano. Spontaneous-emission control by photonic crystals and nanocavities. *Nature Photonics*, 1(8):449–458, 2007. (cited on page 117.)

[192] M. Pelton. Modified spontaneous emission in nanophotonics. *Nature Photonics*, 9(7):427–435, 2015. (cited on page 117.)

[193] A. Femius Koenderink. Plasmon nanoparticle array waveguides for surface enhanced spectroscopy and spontaneous emission control. *Nano Letters*, 9(12):4228–4233, 2009. (cited on page 117.)

[194] T. B. Hoang et al. Ultrafast spontaneous emission source using plasmonic nanoantennas. *Nat. Commun.*, 6, 2015. (cited on page 117.)

[195] Matthew Pelton. Modified spontaneous emission in nanophotonic structures. *Nature Photonics*, 9:427–435, 2015. (cited on page 117.)

[196] Zhiyuan Qian, Lian Shan, Xinyi Zhang, Qiang Liu, Yu Ma, Qihuang Gong, and Ying Gu. Spontaneous emission in micro-or nanophotonic structures. *PhotoniX*, 2:1–35, 2021. (cited on page 117.)

[197] Thang B. Hoang, Gleb M. Akselrod, Christos Argyropoulos, Jia Huang, David R. Smith, and Maiken H. Mikkelsen. Ultrafast spontaneous emission source using plasmonic nanoantennas. *Nature Communications*, 6:7788, 2015. (cited on page 117.)

[198] John C. Owens, Margaret G. Panetta, Brendan Saxberg, Gabrielle Roberts, Srivatsan Chakram, Ruichao Ma, Andrei Vrajitoarea, Jonathan Simon, and David I. Schuster. Chiral cavity quantum electrodynamics. *Nature Physics*, 18:1048–1052, 2022. (cited on page 117.)

[199] J. Feis, D. Beutel, J. Köpfler, X. Garcia-Santiago, C. Rockstuhl, M. Wegener, and I. Fernandez-Corbaton. Helicity-preserving optical cavity modes for enhanced sensing of chiral molecules. *Physical Review Letters*, 124:033201, 2020. (cited on page 117.)

[200] K. Voronin, A. S. Taradin, M. V. Gorkunov, and D. G. Baranov. Single-handedness chiral optical cavities. *ACS Photonics*, 9:2652–2659, 2022. (cited on page 117.)

[201] I. Mauro, M. Cencini, S. Ciattini, I. Cacciari, F. Mazzamuto, M. Ghulinyan, G. Farinelli, L. C. Andreani, C. Menotti, and F. Intonti. Chiral discrimination in helicity-preserving fabry-pérot cavities. *Phys. Rev. A*, 107(2):023512, 2023. (cited on page 117.)

[202] J. Bao, Z. Wang, Y. Liu, Y. Chen, H. Cheng, and J. Tian. Chirality enhancement using fabry–pérot-like cavity. *Photonics Research*, 8(3):339–344, 2020. (cited on page 117.)

[203] Z. Zeng, J. Zhang, L. Schliehe, Z. Sun, L. Hu, J. Wen, H. Zhang, Z. Xie, and C. Jin. Photo-induced chirality in a nonchiral crystal. *Science*, 371:1–6, 2025. (cited on page 117.)

[204] Hannes Hübener, Umberto De Giovannini, Christian Schäfer, Johan Andberger, Michael Ruggenthaler, Jérôme Faist, and Angel Rubio. Engineering quantum materials with chiral optical cavities. *Nature Materials*, 20:438–442, 2021. (cited on page 117.)

[205] G. S. Agarwal. *Quantum Statistical Theories of Spontaneous Emission and Their Relation to Other Approaches*. Springer, 2006. (cited on page 117.)

[206] Stefan Scheel, Ludwig Knöll, Dirk-Gunnar Welsch, and Stephen M. Barnett. Quantum local-field corrections and spontaneous decay. *Physical Review A*, 60:1590–1602, 1999. (cited on pages 117 and 135.)

[207] Johannes Feist, Antonio I. Fernández-Domínguez, and Francisco J. García-Vidal. Macroscopic qed for quantum nanophotonics: Emitter-centered modes as a minimal basis for multi-emitter problems. *Nanophotonics*, 9:4813–4831, 2020. (cited on pages 117 and 135.)

[208] Alessandro Ciattoni. Quantum electrodynamics of lossy magnetodielectric samples in vacuum: Modified langevin noise formalism. *Physical Review A*, 110:013707, 2024. (cited on pages 117 and 135.)

[209] Alessandro Ciattoni. Quantum-optical scattering by macroscopic lossy objects: A general approach. *Physical Review A*, 112:013704, 2025. (cited on pages 117 and 135.)

[210] A. A. Abrikosov, L. P. Gorkov, and I. E. Dzyaloshinski. *Methods of Quantum Field Theory in Statistical Physics*. Courier Corporation, 2012. (cited on pages 117 and 135.)

[211] Stefan Yoshi Buhmann. *Dispersion Forces I: Macroscopic Quantum Electrodynamics and Ground-State Casimir, Casimir–Polder and van der Waals Forces*, volume 247 of *Springer Tracts in Modern Physics*. Springer, 2013. (cited on pages 117 and 135.)

[212] A. G. Kofman, G. Kurizki, and B. Sherman. Spontaneous and induced atomic decay in photonic band structures. *Journal of Modern Optics*, 41:353–384, 1994. (cited on page 117.)

[213] S. Scheel, L. Knöll, and D.-G. Welsch. Spontaneous decay of an excited atom in an absorbing dielectric. *Physical Review A*, 60:4094–4104, 1999. (cited on page 117.)

[214] Yong Xu, Reginald K. Lee, and Amnon Yariv. Quantum analysis and the classical analysis of spontaneous emission in a microcavity. *Physical Review A*, 61:033807, 2000. (cited on page 117.)

[215] Ho Trung Dung, Ludwig Knöll, and Dirk-Gunnar Welsch. Spontaneous decay in the presence of dispersing and absorbing bodies: General theory and application to a spherical cavity. *Physical Review A*, 62:053804, 2000. (cited on page 117.)

[216] Stefan Scheel and Stefan Yoshi Buhmann. Macroscopic quantum electrodynamics: Concepts and applications. *Acta Physica Slovaca*, 58:675–809, 2008. (cited on pages 117 and 139.)

[217] W. L. Vos, R. Sprik, A. van Blaaderen, A. Imhof, A. Lagendijk, and G. H. Wegdam. Orientation-dependent spontaneous emission rates of a two-level quantum emitter in any nanophotonic system. *Physical Review A*, 80:053802, 2009. (cited on page 118.)

[218] Andrea Alessandrini, Leone di Mauro Villari, Luca Assogna, Matteo Silvestri, Matteo Venturi, Carino Ferrante, Paola Benassi, Davide Tedeschi, and Andrea Marini. High-performance chiral mirrors by twisted anisotropic photonic crystals. *Physical Review Applied*, 23:064027, 2025. (cited on page 118.)

[219] E. Reusch. Untersuchung über glimmercombinationen. *Annalen der Physik*, 214:628–638, 1869. (cited on page 118.)

[220] E. Reusch and A. Lakhtakia. Optical investigations on periodic multilayers of

mica. In *More Adventures in Contemporary Electromagnetic Theory*, pages 1–16. Springer, 2025. (cited on page 118.)

[221] R. A. Beth. Mechanical detection and measurement of the angular momentum of light. *Physical Review*, 50:115–125, 1936. (cited on page 118.)

[222] D. V. Guzatov, V. V. Klimov, and N. S. Popruykailo. Spontaneous radiation of a chiral molecule located near a halfspace of a bi isotropic material. *Optics and Spectroscopy*, 114(3):362–368, 2013. (cited on page 124.)

[223] Andrea Alessandrini, Leone di Mauro Villari, Luca Assogna, Matteo Silvestri, Matteo Venturi, Carino Ferrante, Paola Benassi, Davide Tedeschi, and Andrea Marini. High-performance chiral mirrors by twisted anisotropic photonic crystals. *Physical Review Applied*, 23(6):064027, 2025. (cited on pages 125, 126, and 143.)

[224] Gorachand Ghosh. Dispersion-equation coefficients for the refractive index and birefringence of calcite and quartz crystals. *Optics Communications*, 163:95–102, 1999. (cited on page 126.)

[225] Pochi Yeh. Electromagnetic propagation in birefringent layered media. *Journal of the Optical Society of America*, 69:742–756, 1979. (cited on page 131.)

[226] Pochi Yeh. Optics of anisotropic layered media: a new 4×4 matrix algebra. *Surface Science*, 96:41–53, 1980. (cited on page 131.)

[227] Stefan Scheel and Stefan Yoshi Buhmann. Macroscopic quantum electrodynamics: concepts and applications. *Acta Physica Slovaca*, 58:675–809, 2008. (cited on page 134.)

[228] M.-S. Tomaš. Green function for multilayers: Light scattering in planar cavities. *Physical Review A*, 51:2545–2559, 1995. (cited on page 144.)

[229] Rhona Hamilton, Benjamin M. Roberts, Sarah K. Scholten, Clayton Locke, Andre N. Luiten, Jacinda S. M. Ginges, and Christopher Perrella. Experimental and theoretical study of dynamic polarizabilities in the $5s_{1/2}$–$5d_{5/2}$ clock transition in rubidium-87 and determination of electric dipole matrix elements. *Physical Review Applied*, 19:054059, 2023. (cited on page 146.)

Funding

This work has been partially funded by the European Union – NextGenerationEU under the Italian Ministry of University and Research (MUR) National Innovation Ecosystem grant ECS00000041 – VITALITY – CUP E13C22001060006. This work has been supported by the European Union under grant agreement No. 101046424 within the framework of the XXXVIII cycle of the Ph.D. program at the Università degli Studi dell'Aquila. I gratefully acknowledge this support, which made my doctoral thesis and research activities possible.